The Impact of In-Cylinder Charge Motion on Lean Limit Extension and In-Pre-Chamber Mixture Preparation in a Homogeneous Ultra-Lean Engine

A thesis submitted for the degree of Doctor of Philosophy

by

Michael Peter Bunce

Department of Mechanical, Materials, and Manufacturing Engineering

University of Nottingham, UK

October 2021

Abstract

The perpetual desire to conserve fuel is driving strong demand for increased efficiency in spark ignited (SI) engines. A method being increasingly explored to accomplish this goal is lean combustion. Homogeneous ultra-lean combustion with $\lambda > 1.6$ has demonstrated the ability to both increase thermal efficiency and significantly reduce engine-out nitrogen oxides (NO_x) emissions due to the colder cylinder temperatures innate to combustion with high levels of dilution. The major limitation in developing lean and ultra-lean combustion systems is the less favorable ignition quality of the mixture. This has necessitated the development of higher energy ignition sources. A pre-chamber combustor application known as jet ignition is one such technology, having been researched extensively.

Differing types and magnitudes of charge motion are incorporated in SI engines to aid with mixture preparation. The influence of charge motion over lean SI combustion however is less well understood. Additionally, charge motion introduced in the main combustion chamber has the potential to translate to the pre-chamber, thereby affecting pre-chamber mixing and combustion. The effect of charge motion on mixing and combustion comprehensively throughout the engine cycle is unknown and has not been investigated. This study seeks to evaluate the impact of charge motion on mixture preparation and combustion processes in a jet ignition engine.

Experimental engine testing is undertaken to quantify the impact of differing levels and types of induced charge motion on pre-chamber and main chamber combustion. An analysis of high speed pressure data from the pre-chamber provides insight into how charge motion affects pre-chamber combustion stability, and how instabilities cascade to the main chamber combustion event. A set of simulations, matched to experimental engine results, is used to develop an understanding of charge motion influence over the complexities of in-pre-chamber phenomena that are not easily observed experimentally. From the synthesis of these data sets, a clear understanding of the role that charge motion plays in homogeneous highly dilute jet ignition engines emerges. This study quantifies the impact that charge motion has on lean limit extension and engine efficiency, identifies optimal charge motion type, and provides a roadmap for engine system optimization.

List of contents

Publications and awards related to this research

Publications:

Bunce, M., Cairns, A., Subramanyam, S. K. P., Peters, N., Blaxill, H., "Combustion Sensitivity to Charge Motion in a Dilute Jet Ignition Engine," Institution of Mechanical Engineers Internal Combustion Engines Conference, London, 2021.

Bunce, M., Cairns, A., Subramanyam, S. K. P., Peters, N., Blaxill, H., "The Influence of Charge Motion on Pre-Chamber and Main Chamber Combustion in a Highly Dilute Jet Ignition Engine." *Front. Mech. Eng* 6:629243, 2021. doi: 10.3389/fmech.2020.629243

Bunce, M., Cairns, A., Blaxill, H., "The Use of Active Jet Ignition to Overcome Traditional Challenges of Pre-Chamber Combustors Under Low Load Conditions." *International Journal of Engine Research*. November 2020. doi:10.1177/1468087420972555.

Bunce, M., Peters, N., Subramanyam, S. K. P., Blaxill, H., "Assessing the Low Load Challenge for Jet Ignition Engine Operation," Proceedings of the Institution of Mechanical Engineers Internal Combustion Engines Conference, Birmingham, 2019.

Bunce, M., Blaxill, H., Cooper, A., "Development of Both Active and Passive Pre-Chamber Jet Ignition Multi-Cylinder Demonstrator Engines," Pischinger, S. and Eckstein, L. (eds.), in 28th Aachen Colloquium Automobile and Engine Technology, Aachen, 2019, 907-942.

Bunce, M., Blaxill, H., Gurney, D., "Development of a Light Duty Gasoline Engine Incorporating Jet Ignition for Stable Ultra-Lean Operation," Proceedings of the JSAE Spring Technical Conference, Yokohama, 2019.

Bunce, M., Blaxill, H., Gurney, D., "Design and Development of a Jet Ignition Engine for Stable Ultra-Lean Operation," Proceedings of the Institution of Mechanical Engineers Internal Combustion Engines Conference, London, 2017.

Awards:

2020 Dugald Clerk Prize – Institution of Mechanical Engineers. The award is made annually to the author(s) of an original paper dealing with a subject with which the late Sir Dugald Clerk was associated, i.e. marine/automobile internal combustion engines, or for a contribution or achievement in that field. Awarded for the following paper: Bunce, M., Peters, N., Subramanyam, S. K. P., Blaxill, H., "Assessing the Low Load Challenge for Jet Ignition Engine Operation," Proceedings of the

Institution of Mechanical Engineers Internal Combustion Engines Conference, 2019.

List of illustrations

List of tables

Acknowledgements

I would like to acknowledge the technical support of the MAHLE Powertrain US Research & Development team: Dr. Nathan Peters, Sai Krishna Pothuraju Subramanyam, and Vamsie Sampath.

I would like to acknowledge my advisor, Prof. Al Cairns, who has greatly supported this work and whose guidance has been invaluable. I also thank my manager, Hugh Blaxill, for enabling me to pursue this work and for his encouragement throughout this process. Working with both Al and Hugh has made pursuing this degree much more enjoyable than it had any right to be.

I thank my parents, Dr. Diane Bunce and Dr. Jim Bunce, for their constant encouragement and support, as well as my brother Dr. John Bunce and sister-in-law Dr. Caissa Revilla-Minaya for their support.

Most of all I thank my deeply supportive and understanding wife Erika. Without her assistance and compassion this work would never have had a chance of being completed. This was especially true as we were forced to navigate work life, home life, and study life through a pandemic.

I dedicate this thesis to my daughter Antonia, now 5 years old, who thankfully never followed through on her many threats to break my laptop when I was too busy writing this thesis to play with her.

Notation

Abbreviations	**Units**
AFR: air-fuel ratio	-
AMR: adaptive mesh refinement	-
BDC: bottom-dead center	-
BEV: battery electric vehicle	-
BMEP: brake mean effective pressure	bar
BSCO: brake specific carbon monoxide emissions	g/kWh
BSFC: brake specific fuel consumption	g/kWh
BSHC: brake specific hydrocarbon emissions	g/kWh
$BSNO_x$: brake specific nitrogen oxides emissions	g/kWh
BTE: brake thermal efficiency	%
CAX: angle of X% fuel mass burned	degree
CAD model: computer aided design model	-
CAD: crank angle degrees	degrees
CAX-Y: crank angle duration of X-Y% fuel mass burned	degrees
CFD: computational fluid dynamics	-
CFD: computational fluid dynamics	-
CH_4: volumetric exhaust methane concentration	ppm
CI: compression ignition	-
CO: volumetric exhaust carbon monoxide concentration	ppm
CO_2: volumetric exhaust carbon dioxide concentration	ppm
CO_2e: carbon dioxide equivalent	tons
COV: coefficient of variation of IMEPg	%
CR: compression ratio	-
CSSR: cold start spark retard	-
CVCC: compound vortex controlled combustion	-
dATDC: degrees after top-dead center	degrees
dBTDC: degrees before top-dead center	degrees
DI: direct fuel injection	-
ECU: engine control unit	-
EGR: exhaust gas recirculation	-
EOI: end of injection angle	degrees
EVC: exhaust valve closing	degree
EVO: exhaust valve opening	degree
FMEP: friction mean effective pressure	bar
GHG: greenhouse gas	-
H_2: hydrogen fuel	-
H_2: hydrogen volumetric exhaust hydrogen concentration	ppm
HAJI: hydrogen-assisted jet ignition	-
HC: volumetric exhaust hydrocarbon concentration	ppm
HCCI: homogeneous charge compression ignition	-
HD: heavy duty	-
HEV: hybrid electric vehicle	-
ICE: internal combustion engine	-

IDI: indirect fuel injection	-
IMEPg: gross indicated mean effective pressure	bar
ITE: indicated thermal efficiency	%
IVC: intake valve closing	degree
IVO: intake valve opening	degree
LES: large eddy simulation	-
LNV: lowest normalized value of IMEPg	%
MFE: MAHLE flexible engine control unit	-
MJI: MAHLE Jet Ignition®	-
NEDC: new European drive cycle	-
NG: natural gas	-
NMEP: net mean effective pressure	bar
NO_x: volumetric exhaust nitrogen oxides concentration	ppm
O_2: volumetric exhaust oxygen concentration	ppm
PFI: port fuel injection	-
PHEV: plug-in hybrid electric vehicle	-
Pmax: maximum average cylinder pressure	bar
PMEP: pumping mean effective pressure	bar
ppm: parts per million	ppm
RANS: Reynolds Averaged Navier Strokes	-
RCCI: reactivity controlled compression ignition	-
Rmax: maximum rate of cylinder pressure rise	bar/degree
RPM: revolutions per minute	rpm
SI: spark ignited	-
SOI: start of injection	degree
SUV: sport utility vehicle	-
TDC: top-dead center	-
THC: volumetric exhaust total hydrocarbon concentration	ppm
TKE: turbulent kinetic energy	m^2/s^2
TTW: tank-to-wheels	-
VGT: variable geometry turbocharger	-

Variables	**Units**
C_f: flow coefficient	-
C_p: specific heat	J/kgK
$h_i(T)$: sensible enthalpy of exhaust constituent *i* at exhaust temperature T	J
K: water-gas reaction equilibrium constant	-
LHV_{fuel}: fuel lower heating value	MJ/kg
m: fuel oxygen:carbon ratio	-
$\dot{m}$: fuel mass flow rate	g/s
M_x: molar mass of constituent *x*	g/mol
MEP: mean effective pressure	bar
N: engine speed	rpm
n: fuel hydrogen:carbon ratio	-
$\dot{n}$: exhaust molar flow rate	mol/s
η_c: compressor efficiency	%
nf: fuel conversion efficiency	%
n_R: number of revolutions per power stroke	-
P: engine power	kW
p: pressure	bar
Q: air mass flow rate	g/s
$\dot{Q}_{fuel}$: fuel power supplied to the engine	kW
r_c: compression ratio	-
S_g: specific gravity of air	-
T: temperature	K
V_d: swept cylinder volume	cm^3
$\dot{W}$: work	J

Greek Letters	**Units**
ΔP: maximum pressure differential between pre-chamber and main chamber during the pre-chamber combustion event (delta pressure)	bar
γ: ratio of specific heats (gamma)	-
λ: relative air-fuel ratio (lambda)	-

Chapter 1

Introduction

1.1 Preface

The transportation sector remains a significant source of global Greenhouse Gas (GHG) emissions. A combination of societal and governmental pressure has resulted in increasingly stringent global regulation of GHG emissions from this sector. This factor has played a significant role in the establishment of multiple viable powertrain types for the passenger car market. Internal Combustion Engine (ICE)-based powertrains are now joined by battery electric and hydrogen fuel cell powertrains for sale in the market. These latter powertrains offer significant advantages over ICEs, including the absence of local criteria pollutant emissions and increased efficiency. The increased efficiency of these powertrains coupled with the generally lower carbon intensity of fuel production produces lower GHG emissions on a well-to-wheels basis.

However, these alternative powertrains face steep market cost barriers and are predicted to grow slowly in global market share over the next few decades. ICE-based powertrains are expected to continue to dominate the global passenger car market and vehicle fleet through at least 2030, as shown in a graph of EU passenger car sales by type (Fig. 1-1).

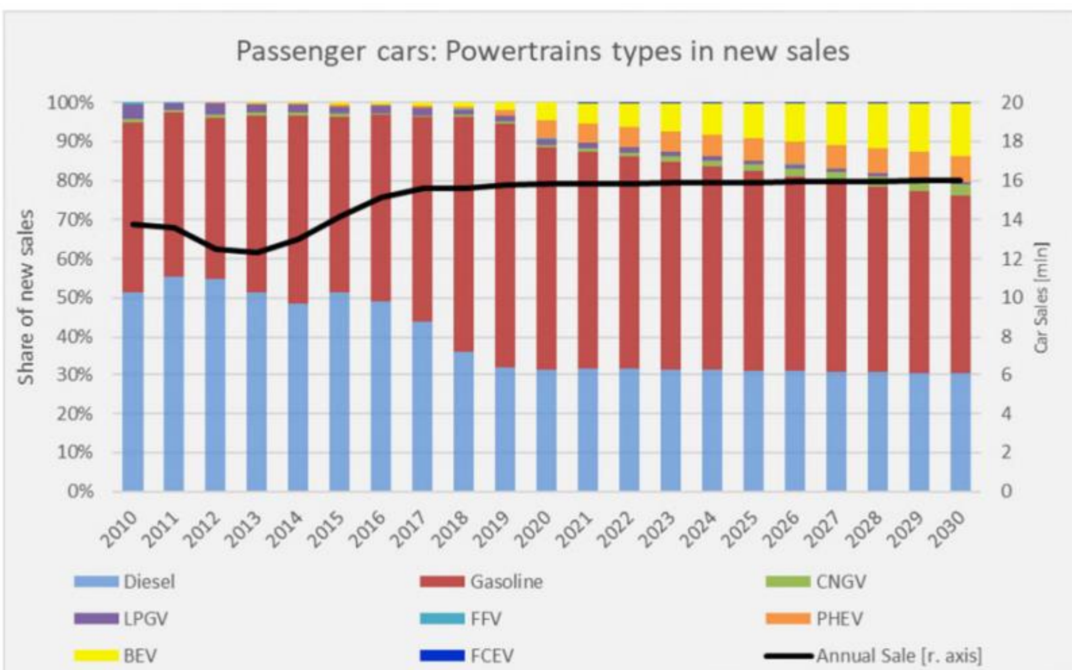

Figure 1-1: EU passenger car sales, historic and predicted, by vehicle type [1].

As can be observed in Fig. 1-1, ICE-based powertrains are expected to constitute the majority of new car sales in the EU through at least 2030. The majority of these are expected to have some degree of hybridization in the powertrain. In other global markets such as heavy duty on-road transportation and megawatt-scale industrial power generation, ICEs are expected to remain the dominant power source for even longer, albeit in some cases operating in hybrid powertrains utilizing low carbon fuels where available. It is therefore critical to continue to investigate pathways for significant GHG reduction in ICE powertrains. To meet upcoming GHG regulations, a step change in ICE efficiency is required. Figure 1-2 demonstrates the impact that increased ICE efficiency can have on EU passenger car fleet GHG emissions.

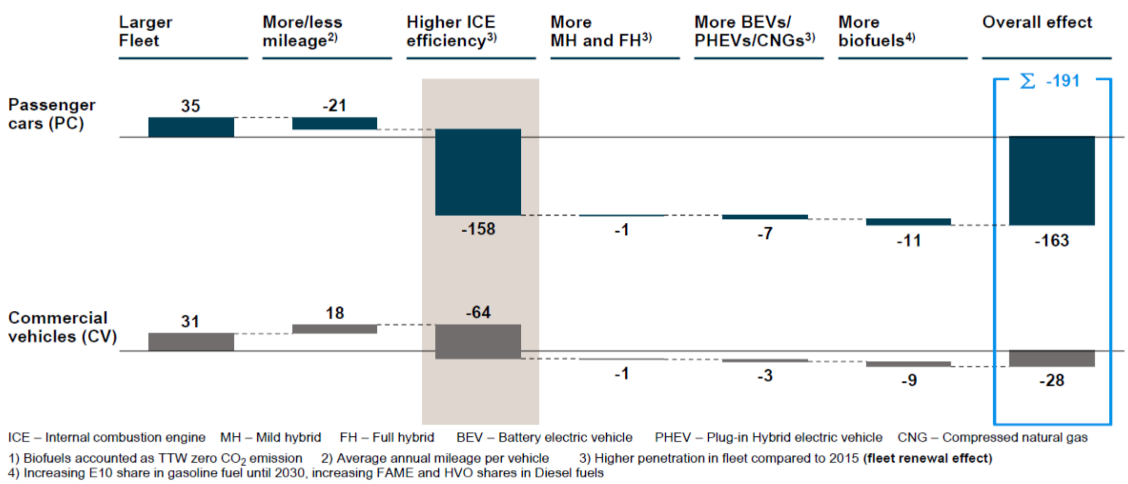

Figure 1-2: Tank-to-Wheels (TTW) GHG emissions in million tons CO_2 equivalent by influencing factor 2015 vs. 2030 in the EU passenger car fleet [2].

A method being explored to accomplish this step-change efficiency goal is dilute gasoline combustion [3,4]. A major limitation in developing dilute combustion systems is the less favorable ignition quality of the mixture. This has necessitated the development of higher energy ignition sources [5,6]. A pre-chamber combustor is one such technology [7-9] and such combustion concepts have already demonstrated the potential for stable main chamber combustion at high levels of dilution [10].

Pre-chamber combustion systems possess numerous parameters than can be optimized in order to increase efficiency, minimize engine-out emissions or aid practical engine operation. While many of these parameters have been studied extensively [11-13], one parameter for which there is minimal published data on its effect on pre-chamber combustor processes is charge motion. Charge motion refers to ordered motion of air or of air-fuel mixtures initiated in the intake system and formed in the cylinder through deliberately induced bulk air motion, which subsequently breaks down into smaller scales ahead of the ignition event. The bulk charge motion is typically designed to aid fuel-air mixing to minimize emissions. As these bulk motions break down into smaller scales this further aids fuel-air mixing. Charge motion also participates in the combustion process. The influence of charge motion on combustion of easily ignitable fuel-air mixtures is negligible, but the influence may be more prominent in difficult-to-ignite mixtures. Pre-chamber combustion, as well as nearly all high efficiency advanced combustion modes, maximizes ICE efficiency by enabling combustion of difficult-to-ignite mixtures, in this case mixtures with a significant excess of air participating in the turbulent combustion process. Investigating the influence of charge motion on pre-chamber combustor operation, and whether it can be used to further increase the efficiency potential of pre-chambers, is relevant.

1.2 Relevance

Pre-chamber combustors have garnered significant industry interest for a variety of applications in the past 5 years. Market applications under investigation or that have been commercialized include passenger car, heavy duty on- and off-road vehicle, motorsport, marine, small engine, and industrial power generation. One school of thought considers pre-chambers to be commodities for upfitting of existing engines with minimal system changes. Another school of thought, championed by this author, considers pre-chambers as integral elements of an engine system optimized for highly dilute high efficiency operation. As such, numerous parameters within the engine and peripheral systems must be optimized in order to maximize efficiency and robustness of the engine. This work focuses specifically on optimizing charge motion to increase concept viability and system efficiency. It is hoped that this work can be used as a part of a broader roadmap for better understanding and optimized pre-chamber combustion engines.

1.3 Research Objectives

The primary purpose of this work was to identify optimal charge motion for use in a homogeneous highly dilute pre-chamber combustion engine that extends the lean limit of the engine and increases efficiency. Experimental engine testing was performed at various operating conditions, coupled with correlated simulations in order to address these specific research objectives:

1) Identify the influence of varying types and levels of charge motion on in-cylinder combustion, and quantify its effect on key engine parameters including combustion stability, lean limit, burn duration, and thermal efficiency

2) Define the comprehensive effect that varying levels and types of charge motion have on the full engine cycle, including in-pre-chamber phenomena such as mixture preparation and pre-chamber combustion
3) Identify optimal charge motion type for use in pre-chamber-enabled highly dilute combustion systems and quantify the impact that optimized charge motion has on system efficiency.

1.4 Thesis Outline

The context of the work and the research objectives are described in Chapter One. Chapter Two, a literature review, provides a comprehensive description of the base high efficiency pre-chamber technology, the mechanisms for efficiency increase in highly dilute ICEs and a review of the current and researched uses of charge motion in ICEs. A review of the experimental engine platform and the details of the test plan employed in this study comprise Chapter Three. Chapter Four includes explanation of the limitations of the experimental approach in developing a fundamental understanding of in-pre-chamber phenomena. The chapter also incorporates a description of the simulation approach used in this study and explanation of how this was utilized to fill in the gaps in system understanding. The concept of pre-chamber applicability, the ability of the highly dilute pre-chamber combustion system to accommodate all aspects of modern engine map operation, is introduced in Chapter Five. Experimental engine results focus specifically on addressing low load operation limitations, a historic weakness of pre-chamber combustion concepts. This chapter also introduces the role that differing types and levels of charge motion can play in aiding operation in difficult-to-ignite regimes. In Chapter Six the concept of charge motion optimization is examined comprehensively through experimental engine results coupled to correlated simulation results to help explain complexities that cannot be experimentally observed. Chapter Seven concludes this study by summarizing the results and describing their relevance to the industry and the required future work.

Chapter 2

Literature Review

2.1 Introduction

Largely since the inception of the internal combustion engine in the mid-1800s it has served as the dominant power plant for global transportation [14]. The features and advantages of the Internal Combustion Engine (ICE) that led to its ubiquity are still relevant to today's transportation sector. These include: power-to-weight ratio of the engine, scalability of power, durability, cost, and ease of use and maintenance [9]. With the strain that an increasing global population, amongst other factors, places on resource utilization, the disadvantages of ICEs have drawn increasing scrutiny for at least the last 40 years [15]. The primary disadvantages with far reaching market and environmental implications are the relative inefficiency of fuel usage that is characteristic of ICEs and the chemical byproducts of the internal combustion process, many of which are detrimental to human health. Advances in ICE design and operation in recent decades have sought to address these disadvantages. The implementation of these and future advancements are critical to both ensuring the short-term viability of the ICE and minimizing its deleterious impact on the environment and human health.

2.2 Efficiency Loss in Engines

2.2.1 Sources of Efficiency Loss

To understand the scale of advancement needed in these areas, it is important to examine the operating principles of ICEs and, subsequently, the efficiency loss pathways. ICEs create an exothermic reaction by combusting fuel with an oxidizer, thereby converting the chemical energy of the fuel to thermal energy. This reaction occurs in an enclosed chamber bordered by a reciprocating piston. The expansion of the chamber during the combustion process converts a portion of the thermal energy to mechanical work. A crank-slider mechanism arrangement converts the reciprocal motion of the piston into rotational shaft work. This shaft work ultimately is used to drive the end application, which can be electrical power production, wheel rotation, propeller rotation etc. In conventional ICE transportation applications the working fluid of the engine is a combination of filtered ambient air and a petroleum-based fuel. Spark ignited (SI) engines, the dominant ICE mode in the US passenger car market and a mode controlling over 70% passenger car market share globally [16], ignite a mixture of gasoline and air using a thermo-electrical pulse from a spark plug. Passenger car engines in the US and Europe exclusively operate using a four-stroke cycle. This cycle defines the working fluid exchange process in the combustion chamber. The four “strokes” are defined by piston movement in specific directions and the functions of these movements. The process can be summarized as: 1) intake of working fluids driven by piston motion downward (volume expansion with an intake valve open), 2) compression of working fluids driven by piston motion upward in the closed system followed by 3) combustion, expansion of the combustion products forcing piston motion downward in the closed system, and 4) exhaust of the combustion products through an open exhaust valve driven by piston motion upward. Four-stroke SI passenger car engines are of most relevance to this thesis and will therefore be the focus of all subsequent discussion.

With the combustion reaction occurring in the closed chamber bordered by (and overlapping) the compression and expansion strokes, power generation can be effectively described by a relationship between pressure and volume as a surrogate for the effect of thermal energy on the reciprocating piston [9,17]. This methodology is also consistent with the most effective means by which to measure the thermodynamic impact of the combustion process in engines [18-20] i.e. pressure measurement. A common depiction of the combustion process in ICEs is therefore a measured or predicted value of pressure inside the combustion chamber versus the volume of that combustion chamber as dictated by the piston position. Another common depiction of this process uses logarithmic values of pressure and volume, as shown in Fig. 2-1. This latter approach provides a clear illustration of the higher pressure state of the combustion chamber contents resulting from the combustion event, analogous to the useful work generated by this event [21,22].

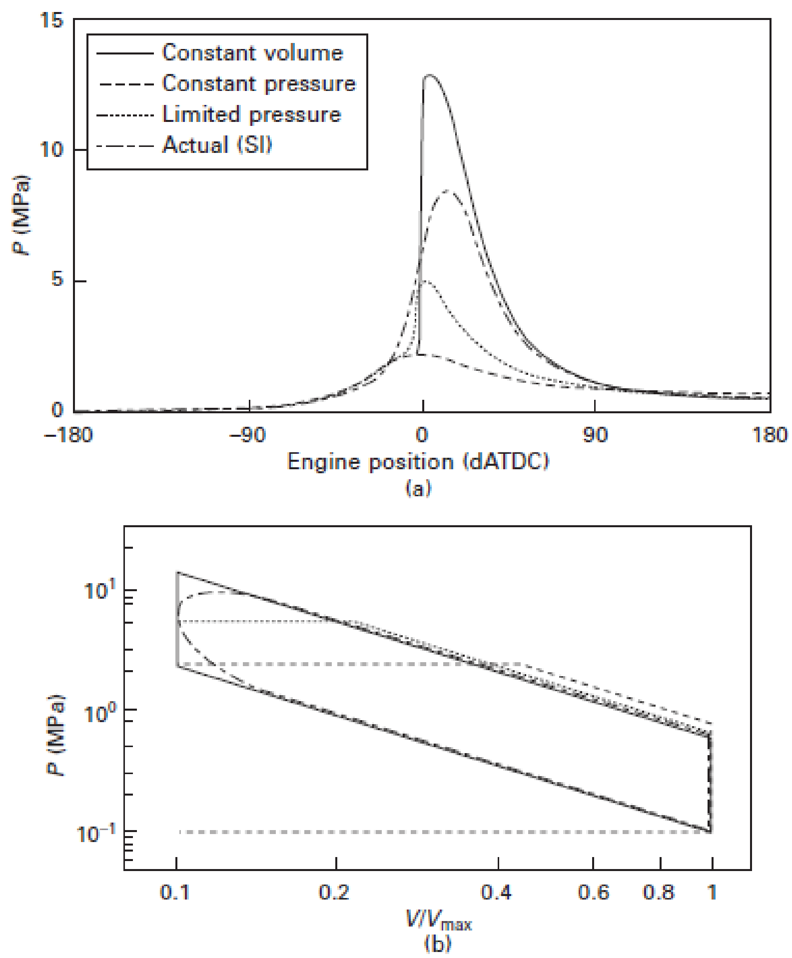

Figure 2-1: Representative in-cylinder pressure measurement and pressure-volume relationship for various cycles [23].

The collective impact of the efficiency loss pathways of the engine can be qualitatively demonstrated by a comparison of an ideal cycle with its real-world counterpart. An ideal cycle is a representation of the combustion process with several key assumptions: 1) it is a closed system that only considers pressure/temperature events in the combustion chamber with working fluids that are present and do not leave, 2) it assumes that the chemical-to-thermal conversion process of the working fluids is complete with no chemical exergy remaining, 3) it is an isentropic system meaning that there is no loss of thermal energy through conduction or convection to the environment as a result of compression, combustion, or expansion, and 4) there are no structural limitations of the physical engine to the combustion process, i.e. the engine can structurally withstand the pressure rise resulting from combustion with no loss-inducing accommodations needed [22-25].

There are two common approaches to expressing ideal efficiency in ICEs. The constant volume approach assumes that the totality of the combustion process is experienced by the system instantaneously, meaning that even though the continuous motion of the piston results in continuously varying chamber volume, volume is essentially fixed while combustion occurs [23,26,27]. In order to produce the maximum pressure, the constant volume ideal cycle assumes that combustion occurs when volume has reached a minimum, a position known as Top-Dead Center (TDC). This cycle is characterized by an instantaneous increase in chamber pressure at TDC that only decreases proportionately to the subsequent decrease in chamber volume during the expansion stroke.

The second ideal cycle type is known as the constant pressure method. This assumes that the combustion event produces a pressure that remains constant as the volume is increased during the expansion stroke [9,23]. Practically, the constant pressure approach assumes a combustion event with a finite duration that encompasses a significant portion of the expansion stroke. There is no sudden increase in pressure here; the pressure that the engine would experience at TDC in the absence of a combustion event is achieved and maintained over most of the subsequent expansion stroke resulting from the combustion event.

While both of these cycles generate work from the combustion-induced pressure rise, the constant volume approach produces a higher thermal or “fuel conversion” efficiency due to the pressure rise event occurring solely at a minimum volume condition, thereby maximizing the downward force on the piston. Real-world SI cycle pressure-volume curves lie between the two ideal cycles. A rapid but not instantaneous pressure rise event continues over a finite period of time, generating work on the piston in a manner that reflects a combination of the two ideal cycle approaches [9,23]. Figure 2-1 displays the constant volume and constant pressure ideal cycles as well as a real-world SI cycle. These cycles are compared using pressure traces versus piston position and logarithmic pressure and volume relationship.

As can be inferred from Fig. 2-1a, SI engines adhere more closely to constant volume ideal cycles than constant pressure in terms of the mechanics of the combustion-induced pressure rise event [28]. Examining Fig. 2-1b, the most apparent deviations from the ideal cycle occur during the combustion event, and with the addition of the gas exchange process. The latter accounts for both the open nature of the system during this phase, and for the fact that half of the cycle (two of the four strokes) is used to induce exchange of the working fluids. These two apparent deviations represent two specific types of efficiency losses experienced by real-world SI engines, namely real combustion and pumping losses, respectively. These and the remaining efficiency losses are described below:

Real combustion: This efficiency loss is introduced due to the fact the combustion process does not occur instantaneously but instead has a finite duration. This finite duration means that combustion can and typically does occur as the volume reduces (compression stroke) and as it expands (expansion stroke). Pressure rise during the compression stroke creates a downward force on the piston as it is moving upwards toward TDC, thereby minimizing the effectiveness of that work. Conversely pressure rise as the piston is moving downward more closely aligns to the constant pressure ideal cycle which is limited in its ability to create work as previously discussed. Real combustion loss is therefore due to both the finite duration combustion and the location of its energy release centroid relative to the piston position [29]. Ideally the centroid would occur precisely at TDC with equal combustion durations before and after this point. In real-world applications the ideal location for this centroid is slightly after the piston reaches TDC due to the asymmetric nature of fuel combusting in the cylinder relative to the TDC position of the piston [30,31].

Incomplete combustion: The ideal cycles assume a complete conversion of fuel chemical energy to thermal energy in the combustion process. In practical application, this process is incomplete. The chemical kinetics that drive the fuel conversion process are controlled by two key partially interrelated parameters: temperature of the reaction site and relative proportion of fuel to oxidizer at the reaction site [32]. The ability of the process to maintain a suitably high reaction site temperature is dependent on the thermal energy produced at the reaction and the surrounding environment. If local environmental factors induce a rapid transfer of thermal energy away from the reaction site, the chemical kinetics of combustion can be arrested. This is often manifested as the production of intermediate combustion species or, in more extreme cases, completely unconverted fuel [32-34]. Secondly, the proportion of fuel to oxidizer dictates the composition of the resulting species. Local variations in mixture proportion, specifically resulting in fuel-rich conditions can also produce intermediate combustion species, with subsequent reactions arrested due to lack of oxidizer.

Heat transfer: One of the most significant deviations from the ideal cycle, and one of the most significant sources of efficiency loss in ICEs is heat transfer. There are two general categories of heat transfer: in-cylinder and exhaust. Thermal energy produced during combustion is transferred to the physical barriers of the combustion chamber through conduction (combustion flame contact with chamber walls) and convection. Due to the nominal delta in temperature between the working fluid (especially during compression) and combustion products (mostly during expansion), and the chamber barrier, heat transfer is induced. Thermal energy is also lost to the exhausted combustion products due to the heat capacity of these products and, generally, an expansion ratio equivalent to the compression ratio (CR) that does not allow enough expansion to reduce the working fluid back down to the initial temperature prior to the exhaust stroke [35]. Some of this thermal energy can be recovered as useful work using heat recovery technologies that are ancillary to the ICE, but the energy recovery rates of these are typically low and reducing heat losses directly from the ICE presents a much clearer pathway for overall system efficiency gain.

Ideal cycle: This category of efficiency loss occurs due to the fact that the ideal cycle assumes an isentropic process but a real-world combustion event is an exothermic reaction that is irreversible [9,23,36]. If a real-world system were in fact closed and the working fluid remained in the chamber, the cycle could not return to its initial state due to the 1) lack of time to reach equilibrium, 2) loss of thermal energy through the chamber walls, and 3) the inability of the combustion process to reverse itself and reconvert the thermal energy into chemical energy held in a working fluid [23,37]. Real-world ICEs are open systems that exchange combustion products with replacement fuel and air each cycle in order to ensure that the system returns to the initial state temperature and pressure. Similarly, compression and expansion are polytropic processes. The thermal energy generated by compression also transfers to the surrounding material and exits the system through conduction. The Carnot cycle describes how a peak efficiency is limited by the upper and lower bound temperatures in the system [9,37-39].

Pumping: As the engine must acquire a new working fluid every cycle, it is responsible for the exhaust of the previous cycle’s combustion products and the intake of the subsequent cycle’s fuel-air mixture. These products travel quickly through exhaust and intake valves. The diameter of these valves is generally limited by the geometry of the combustion chamber [9]. Piston motion during the exhaust and intake strokes forces flow through these restrictions leading the ICE to expend work to induce gas exchange. This can be exacerbated by the throttling feature of SI engines. Engine power is controlled by quantity of fuel combusted in the cylinder. As SI engines can only operate in a narrow band of air-to-fuel ratios, a throttle is present in the intake to proportionately control the quantity of air present in the cylinder as well. At low power levels in particular, the restriction placed on the system by the throttle leads to significant efficiency loss.

Friction: Power generation in an ICE is contingent on its ability to ensure that the bulk of the work generated in the combustion chamber is used to drive downward movement of the piston. This means that the piston must seal with the liner to minimize leakage during the combustion phase and expansion stroke, which it does through the use of sealing rings. The presence of continuously moving components in contact with each other results in energy loss through friction. Numerous contact points of moving components in ICEs translate into many points of friction loss. This can be mitigated somewhat with the use of lubricants, low friction coatings, and attention to component surface finish [40,41].

Other losses: While the following are not thermodynamic losses, they do represent aspects of ICE design and operation that are given significant consideration by engine manufacturers and have a direct bearing on engine efficiency.

Knock: In SI engines, ignition of the fuel-air mixture is initiated and therefore controlled by the time at which the spark plug is activated. “Abnormal combustion” results when ignition occurs locally in the combustion chamber independent of spark timing or independent of the primary combustion event induced by the spark plug. The latter event is known as knock, whereby a local fuel-air mixture auto-ignites before being consumed by the encroaching flame front initiated by the spark plug. Initiation of combustion causes pressure and therefore temperature to rise in the unburned portion of the combustion chamber. This localized pressure rise can cause auto-ignition, resulting in irregular and localized spikes in heat release which can cause considerable damage to engine components such as the piston and piston rings. The primary means by which to avoid knock is to reduce the geometric CR of the engine which in turn reduces background pressure and temperature in the combustion chamber [42]. This reduction in CR limits the thermal efficiency of the engine according to the following equation:

$$n_f = 1 - \frac{1}{r_c^{\gamma-1}} \qquad \text{Eq. 2-1}$$

Where n_f is fuel conversion or thermal efficiency, r_c is the CR, and γ is the ratio of specific heats.

Component protection: In modern ICEs there are typically many ancillary subsystems, the operation of which can necessitate occasionally inefficient operation of the ICE itself. As an example, the use of turbochargers is becoming increasingly common for ICEs. Turbochargers are operated using the exhaust enthalpy of the ICE. While the ICE can generate a wide range of exhaust temperatures, turbochargers cannot necessarily tolerate this same wide range of temperatures. Therefore, at certain conditions such as high speed and high load operation ICEs are operated with rich fuel-air mixtures in order to reduce exhaust temperature while still achieving the desired load [43]. As mentioned previously, rich operation has the added negative effect of increasing the incomplete combustion loss of the engine.

Figure 2-2 shows a map of brake specific fuel consumption (BSFC) for a typical modern SI engine. The map is annotated to show the primary efficiency loss pathways in each speed and load region of the map. While certain losses such as friction are omnipresent, friction becomes dominant at higher engine speeds. Here rubbing friction increases due to rotational speeds of components such as the crankshaft and camshafts [44]. Likewise in-cylinder heat transfer loss is dominant at lower engine speeds when there is more residence time for heat to dissipate from the cylinder wall through the engine block and head, thereby reducing the average temperature of the cylinder wall and driving a greater delta temperature between combustion products and cylinder surface [45]. Higher in-cylinder pressure and temperature at high load introduces the probability of knock occurring. The most effective method to actively reduce knock at these conditions is to retard spark timing, shifting the centroid of combustion further away from the TDC position. This lowers combustion temperatures but also introduces a significant real combustion loss as the centroid occurs further away from its optimum location. The later combustion process also leads to increased heat loss to the exhaust due to the higher temperature of the in-cylinder contents at the time of exhaust valve opening [43]. The need to reduce exhaust temperature at high speed, high load conditions is dictated by turbocharger component temperature limitations in turbocharged applications such as the example shown. An effective method to reduce exhaust temperatures in this region is to operate rich of stoichiometric. Rich operation, by definition providing a lower quantity of oxidizer than required for complete conversion of fuel during the combustion process, leads to an incomplete combustion loss. Finally, low load operation efficiency suffers deficiencies due to both the high degree of throttling needed to achieve the load and the limited CR which limits ideal efficiency and elongates burn duration. As can be clearly inferred from Fig. 2-2, efficiency in a modern SI passenger car engine is compromised, sometimes severely, by the requirement that engine operation encompasses a wide range of speeds and loads in order to meet operator demand for power and torque. The most effective modern high efficiency engine technologies are flexible enough to mitigate these compromises in multiple regions of the engine map.

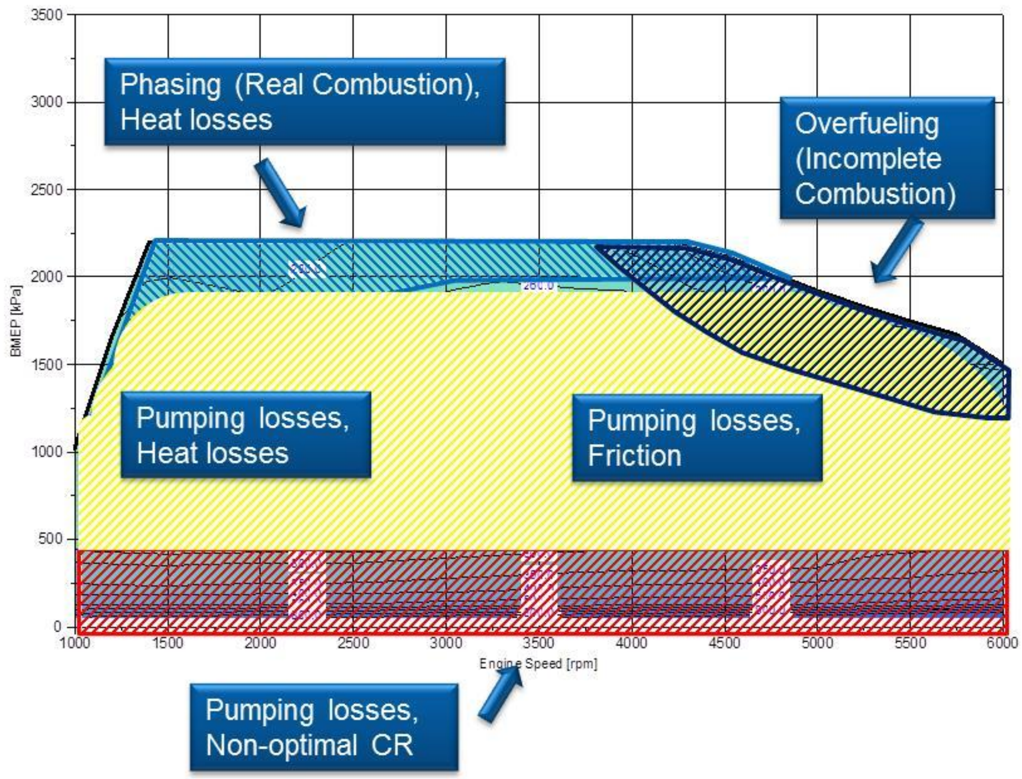

Figure 2-2: BSFC engine map from the MAHLE DI3 Downsizing demonstrator engine with dominant efficiency losses by region [46].

Figure 2-3 presents an energy analysis that depicts the loss pathways for fuel energy in an engine similar to the one depicted in Fig. 2-2, and how the relative magnitudes of these pathways change at different speed and load conditions. The x-axis is brake mean effective pressure (BMEP) in bar. It is notable that the most significant loss pathway, heat transfer (combined in-cylinder and exhaust), remains the largest detriment to engine efficiency throughout the engine map. It is therefore not coincidental that many advanced combustion technologies that successfully achieve step changes in engine peak efficiency are occasionally described as “low temperature combustion” concepts [47].

In Fig. 2-3, note that at 1.5 bar BMEP the pumping loss due to throttling is a significant percentage of the total fuel energy. This loss diminishes as BMEP is increased and the engine is de-throttled and boosted. Incomplete combustion loss increases substantially at the highest BMEP due to enrichment (normalized air-fuel ratio, or lambda = 0.79) and retarded combustion phasing, both of which also contribute to a decrease in in-cylinder heat loss.

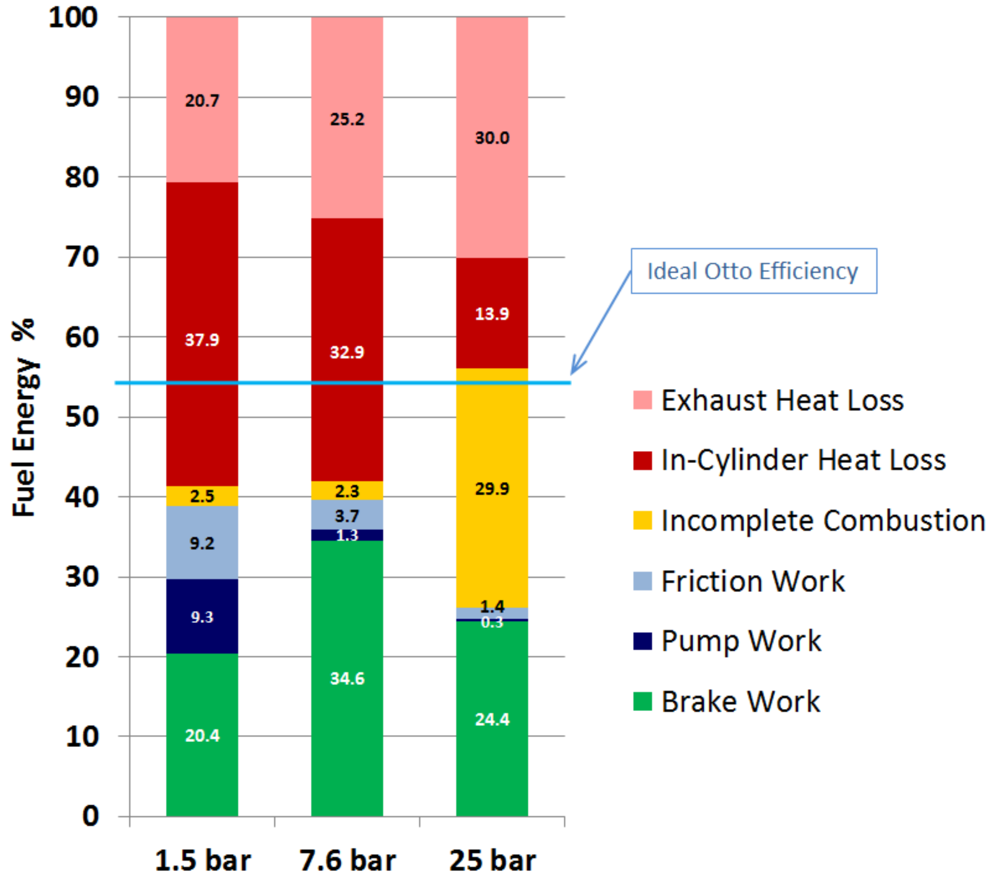

Figure 2-3: Energy loss analysis for the 1.5L MAHLE DI3 engine at 3000 rpm and various loads. Data courtesy of MAHLE Powertrain UK.

Some of the fuel energy that is dissipated through the loss pathways can be recovered. Only a few of the pathways lend themselves to energy recovery; a method that has been investigated for the past couple decades involves utilizing the heat transferred to the exhaust to perform work in service of an ancillary subsystem in the vehicle. Waste heat recovery technologies, some of which have been commercialized, take advantage of the relatively high heat flux in an exhaust system to provide continuous heat to a boiler or other Rankine cycle device [16, 48]. While this is a promising and in many cases cost/benefit positive application, Fig. 2-4 demonstrates the thermodynamic limitations of recovering the energy present in the exhaust. The x-axis is BMEP in bar and the y-axis is percent of total fuel energy at a given BMEP. The analysis in Fig. 2-4 is based on the 2nd Law of Thermodynamics and contrasts the exergy or energy availability in the exhaust with the energy present in the exhaust as determined by the 1st Law of Thermodynamics. While exhaust temperature and, under certain conditions, pressure are elevated versus atmospheric values and there is chemical energy contained in the emissions constituents, only a relatively small proportion of this energy can be extracted to perform useful work in a dedicated application [38]. Waste heat recovery therefore cannot be used to significantly offset the base engine efficiency loss associated with heat transfer; this loss pathway is more effectively addressed through combustion and in-cylinder processes that reduce heat transfer at the source of heat generation [49,50].

Note that the most exergy is available at the highest BMEP condition due to the elevated pressure of the exhaust and the availability of species capable of exothermic reactions in the exhaust resulting from rich operation. Exergy is a relatively small percentage of exhaust energy at the low and mid load conditions.

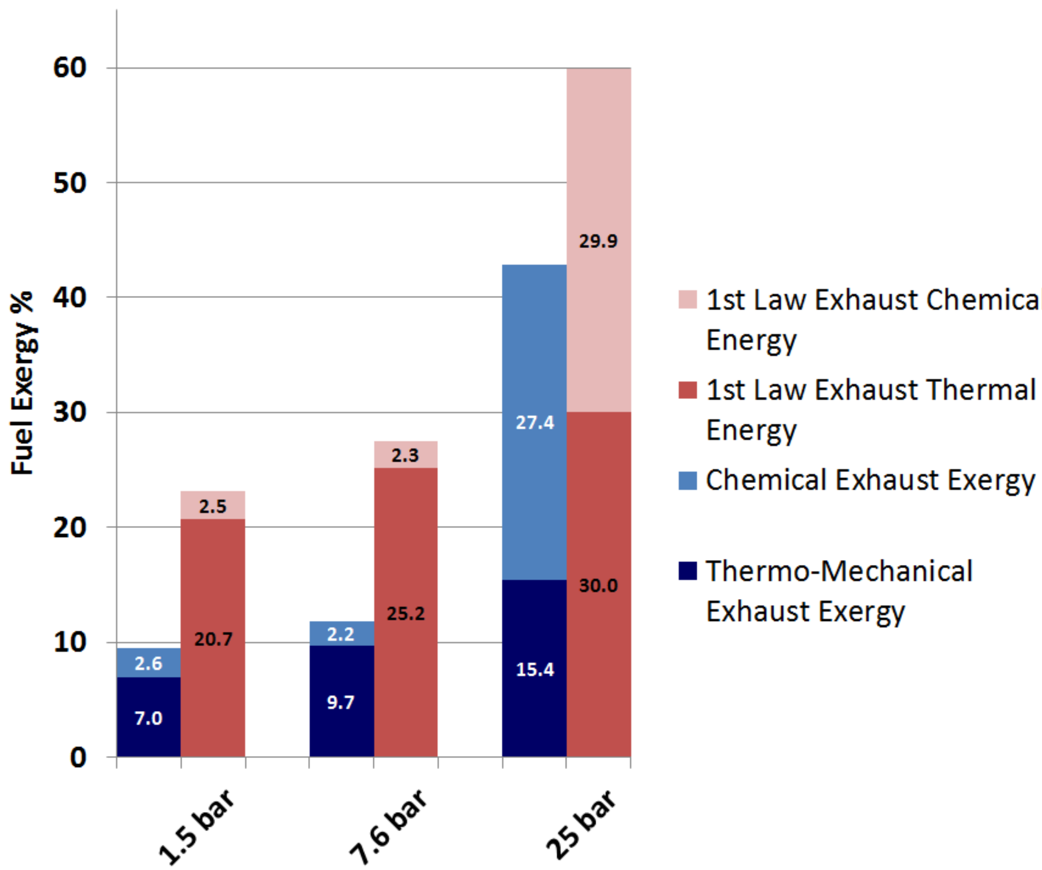

Figure 2-4: 2nd Law exergy loss analysis at 3000 rpm and various loads. Data courtesy of MAHLE Powertrain UK.

2.2.2 Technologies to Minimize Efficiency Loss

The following section describes selected ICE technologies that have been developed for the purpose of minimizing one or more of the efficiency loss pathways described above.

Direct Fuel Injection (DI): Prior to the advent of DI for SI engines, fuel was typically injected in the intake manifold or in the individual intake ports. Port Fuel Injection (PFI) allows for relatively low fuel pressure requirements and therefore reduced parasitic loss on the engine and relatively homogeneous fuel-air mixing. There are however two prominent disadvantages to PFI. Firstly, the fuel injected in the port displaces air that would otherwise enter into the cylinder, resulting in a reduced full load volumetric efficiency for the engine. Secondly, PFI does not allow fuel targeting or other fueling-based combustion strategies. DI technology enables fuel injection directly into the cylinder. While higher fuel pressures are necessary to overcome the higher background pressure of the cylinder, pumping losses are decreased due to the elimination of the air displacement effect. Spray targeting and multiple injection events in the same cycle to optimize operation such as cold start are possible with DI. The DI provides an additional benefit in that the injected fuel must undergo a phase change from liquid to vapor in the cylinder as opposed to the port. This phase change requires energy input from the system which in turn reduces the temperature of the compressed fuel-air mixture. As knock is highly sensitive to local pressure and temperature, this “charge cooling effect” reduces knock and allows for more optimal combustion phasing (reducing real combustion loss in otherwise knock-limited engine map regions) and/or increased CR (reducing ideal cycle loss). DI SI engines currently have significant market penetration and the controllability and efficiency benefits of this technology make it complimentary to other modern SI engine technologies such as downsizing [51-54].

Engine Downsizing (Rightsizing): The advent of DI injection and especially boost system development breakthroughs such as high capacity, active geometry, and multi-stage boost systems has enabled engine downsizing. Engine downsizing is a mode of engine operation with both component-level and system-level considerations that is intended to not only increase peak engine efficiency but drive cycle average efficiency as well. The technology is self-descriptive and involves replacing large displacement naturally aspirated or moderately boosted engines with smaller engines that are more heavily boosted in order to achieve similar peak power levels. The smaller displacement requires the engine to operate at higher BMEP levels in order to achieve similar peak power levels. As pumping loss reduces significantly with increased load, downsized engines display higher efficiency than corresponding non-downsized engines at common power levels and averaged over a drive cycle. Though the more highly loaded downsized engines encounter higher friction due to component sizing safety factors, this is compensated by the reduced pumping loss at the engine peak efficiency speed and load, resulting in generally higher efficiency than a corresponding non-downsized engine [55-58], as is described in Fig. 2-5. Downsizing requires the engine to achieve higher specific power output than the corresponding baseline engine. This headroom is provided by changes to the engine and ancillary systems including lower restriction intake design and valve size, high efficiency boosting system and charge air cooler, DI injection strategies, and lower CR, though the latter is tempered by leveraging the charge cooling effect of DI to reduce knock [59].

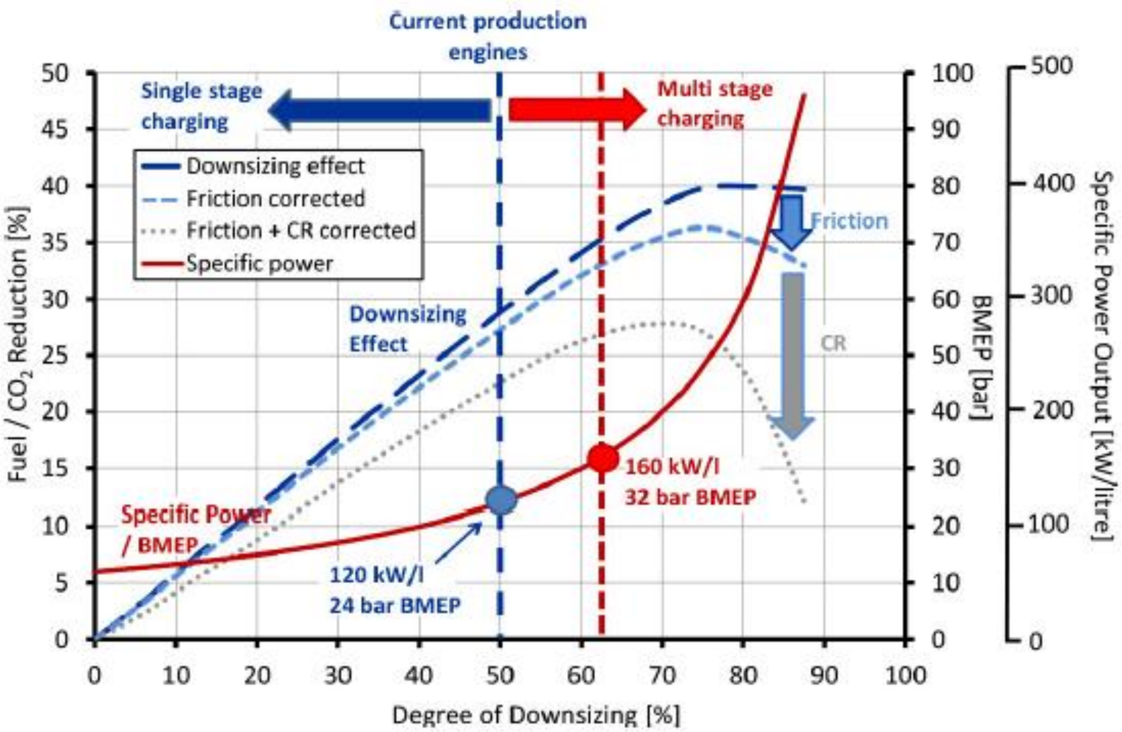

Figure 2-5: Benefits and limitations of engine downsizing with regards to specific power output and fuel/CO_2 reduction [46].

Over-Expansion: While knock is a big impediment to further increasing CR, it is not in and of itself a limit to further increasing the expansion ratio. The Atkinson cycle engine, developed by James Atkinson in the 1880s [60] sought to decouple what was until then an inextricable relationship between the compression and expansion ratios. The inherent lack of charge density with the smaller compression stroke was addressed by turbocharging in Ralph Miller's patent of the Miller cycle engine in 1957 [61]. While Atkinson's and Miller's engine concepts included mechanical linkages in the crankshaft and connecting rod to physically decouple compression and expansion in a common cylinder, subsequent innovations have also included the use of variable valvetrain systems to independently adjust charge flow during the intake and exhaust strokes [51]. The increased expansion ratio reduces the temperature of the post-combustion in-cylinder charge, thereby returning the charge to a pressure and temperature condition closer to its original state. This modification to the Otto cycle results in a reduced ideal cycle efficiency loss that overcompensates for the increased friction in modern mechanical linkage-based systems [62-64].

Dilution via Exhaust Gas Recirculation (EGR): EGR is a technology that involves siphoning a portion of the exhaust gases from the engine, cooling the gas, and re-entering it into the cylinder. It was originally conceived as an emissions control technology for diesel engines [65]. As NO_x emissions are sensitive primarily to temperature, an added diluent acting as a heat sink lowers engine-out NO_x by limiting bulk combustion temperatures. EGR is rich with high heat capacity molecules such as N_2 that trap thermal energy and is relatively low in O_2 which, in excess, could increase NO_x formation [65]. When applied to SI engines, EGR has an added effect on efficiency. The higher heat capacity of the EGR reduces combustion temperatures which in turn reduces in-cylinder heat loss and increases the value of the ratio of specific heats, further increasing the ideal cycle efficiency. Additionally, the introduction of EGR necessitates engine de-throttling, reducing pumping loss [66]. There is a limit to the EGR dilution tolerance of SI engines that is dictated both by poor kernel development during ignition and slow flame front propagation during the combustion process. Both of these factors are temperature dependent and so the heat capacity of EGR is both an efficiency benefit under nominal operation and ultimately a deficit to dilution tolerance [67,68]. One method that is used to expand the EGR dilution tolerance has been increased charge motion, primarily tumble, in the cylinder. High degrees of charge motion serve to stretch the flame front into areas of otherwise challenging propagation, and the additional turbulent kinetic energy in the cylinder serves to increase bulk flame speeds. This charge motion benefit to flame front propagation can be counterweighed by inadvertent stretching of the kernel during ignition which can extinguish the kernel at certain conditions [69].

Dilution via Excess Air: As an alternative to EGR dilution, dilution with excess air has been studied extensively in SI engines [70]. The benefits are similar to EGR dilution, with the exception of the ratio of specific heats (γ) and oxygen availability. The ratio γ is a product not just of temperature of the working fluid but also of its constituents. The constituents of air give it a higher γ value than EGR, therefore the efficiency potential is higher [71]. This is reflected in the potential for lower in-cylinder heat loss. A lean system does not need the added complexity of an EGR valve and cooler, but air dilution does prohibit the sole use of a 3-way catalyst to control emissions in passenger car engines because this catalyst is effective only at nominally stoichiometric conditions. Additionally, as described by the Zeldovich mechanism [72], NO_x emissions increase in the near lean region, with a peak at approximately λ=1.1. Therefore, to minimize the burden on the aftertreatment system, λ values in this region must be avoided.

Similar to EGR dilution, poor kernel formation and slow flame front propagation resulting from λ flammability limits of specific fuels dictate a lean limit of the engine, a limit that rarely exceeds λ=1.4-1.6 in modern SI engines using conventional spark plugs [9]. A method to increase dilution tolerance is stratification of the fuel in the cylinder as enabled by DI fuel systems [73]. In this configuration, a multi-pulse strategy or careful spray targeting is employed to ensure a near-stoichiometric mixture at the spark plug to promote rapid kernel formation. The remaining stratification in the cylinder means that fuel is consumed at a variety of λ values. While this approach typically results in significantly lower engine-out hydrocarbon (HC) and carbon monoxide (CO) emissions than with EGR dilution, these emissions and NO_x are still relatively high compared with a homogeneous lean approach [75,75]. The high emissions levels at low temperature lean conditions have resulted in complex and costly emissions control solutions in production applications [76].

2.3 Dilute SI Combustion

Introducing high levels of homogeneous dilution, through the use of either EGR or excess air, has been definitively proven to increase the thermal efficiency of ICEs. The necessary mechanism to achieving stable, highly dilute SI operation is transcending the lower flame speed and flammability limit of the fuel encountered under highly dilute operation. Traditional centrally mounted spark plugs are typically insufficient to ensure stable lean operation at λ values greater than 1.6 or EGR values greater than 30%. This limitation is manifested as misfires due to poor kernel formation and partial burning due to excessive flame stretch and ultimately arrested flame development, both conditions contributing to reduced efficiency and elevated HC and CO emissions in addition to being characterized by poor combustion stability [5,70,71,73,77].

In recent decades this combustion stability limitation has hastened the development of advanced ignition systems. These systems generally fall into three categories: 1) systems that increase the electrical energy available for ignition, 2) systems that rapidly distribute the electrical or thermo-chemical energy generated during the ignition process throughout the combustion chamber, and 3) systems that combine these two methods [78].

Systems that increase electrical energy availability during the ignition process seek to ensure robust kernel formation and reduce the sensitivity of this process to either a stretching and extinguishing event in high charge motion environments, or rapid heat loss due to dilution [76]. Systems such as long duration or increased discharge spark plugs are examples of these systems. Other similar systems such as plasma and corona ignition both increase electrical energy and provide the electrical energy in such a way that it is more efficiently converted to thermo-chemical energy inside the combustion chamber. Plasma ignition, as the name implies, generates plasma directly as an output of the ignition system.

The benefit of distributing ignition energy throughout the combustion chamber, either inherently or as a function of the ignition process, is that the multiple flame fronts that propagate from the resulting ignition points need to traverse less physical space and individually consume less fuel in order for the combustion process to achieve completion. In this case the reduced flame speed resulting from dilution is not directly addressed but indirectly mitigated by effectively segmenting the fuel-air mixture in the main chamber with individual ignition points responsible for the combustion process only in a given segment. The simplest and most practical approach to achieve this goal is the use of multiple spark plugs in the combustion chamber. The Chrysler “Hemi” hemispherical combustion chamber is a well-known example of the “twin-spark” approach, though this was not originally conceived as a high dilution enabling technology. The limitation with this approach is the non-ideal placement of the ignition source, by definition nearly flush mounted with the combustion chamber roof, as are conventional single spark plugs. As such the ability of this type of concept to promote stable, highly dilute operation is limited by premature flame truncation and wall interactions [79,80].

2.4 Pre-Chamber Combustion

2.4.1 Pre-Chamber History

2.4.1.1 Passenger Car Applications

As can be inferred from the description above, technologies that can both increase the electrical or thermo-chemical ignition energy in the system and can distribute the ignition energy throughout the combustion chamber possess a strong potential to induce stable, highly dilute combustion. A prominent technology that accomplishes both is a combustion concept known as jet ignition. Jet ignition is combustion process that results from the use of a pre-chamber combustor. Before the principles of jet ignition are discussed, it is useful to understand the development and incorporation of pre-chambers throughout the history of the ICE. As will be illustrated, the pre-chamber is a relatively simple component that has demonstrated versatility through its use in a variety of applications.

A pre-chamber is a proportionally smaller chamber directly connected to the combustion chamber. Its historical uses have spanned low pressure fuel delivery, spark plug protection, and use as an ignition system in and of itself.

The first ICEs to utilize pre-chambers were diesel engines. Prior to the advent of direct fuel injection, diesel engines utilized indirect injection (IDI) [81]. One common method to achieve this fueling configuration included the use of a pre-chamber that housed the fuel injector, as originally developed by L'Orange [82,83]. Fuel is injected at relatively low pressure into the pre-chamber during the compression stroke. The pre-chamber also preserves a portion of the charge motion generated in the diesel engine during the intake stroke. This charge motion, typically swirl hence the alternative name “swirl chamber”, translates to the pre-chamber ensuring that the fuel in the pre-chamber mixed adequately with the incoming air [84]. Combustion then initiates in the pre-chamber and continues in the main chamber as the local pressure rise in the pre-chamber forces the burned and burning contents to transfer to the main chamber. Communication pathways between the chambers vary from an open throat to a nozzle with multiple small orifices. Prominent examples of the IDI diesel pre-chamber are displayed in Fig. 2-6.

This IDI configuration was developed out of necessity due to the lack of an implementable solution for high pressure diesel fuel injection for many decades. The pre-chamber in the case of IDI offers a containment area for fuel as the main chamber is pressurized, preventing it from entering crevice volumes in the chamber such as the top land of the piston which would greatly reduce efficiency and increase HC and soot emissions. Even during the early adoption of high pressure diesel fuel injection systems, pre-chambers were still in use as late as the late 1990s due to the ability to maintain a flat top piston crown design, allowing diesel engines to achieve relatively high CRs largely independently of the size of the pre-chamber volume [85]. Modern DI diesel engines generally utilize inset bowls in the piston crown corresponding to the injector spray pattern in order to a) avoid liquid fuel impingement on the surface of the piston, and b) prevent the swirl motion in the combustion chamber from disintegrating as the piston approaches TDC.

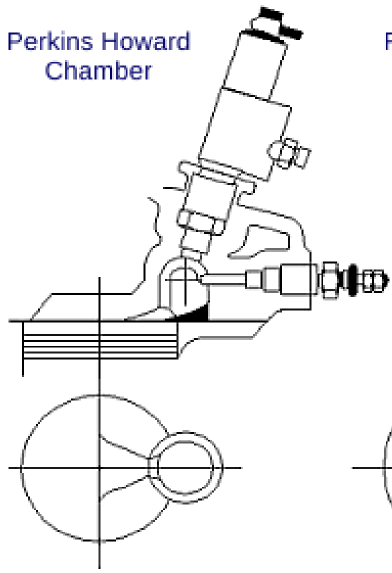

Figure 2-6: Examples of prominent IDI diesel pre-chamber engines [86].

This configuration was translated to SI engines through Sir Harry Ricardo's patent for the Ricardo 3-valve pre-chamber engine on which he first began development in 1903 [87]. This is a 2-stroke SI engine that utilizes a relatively large pre-chamber separated by a throat passage to the main chamber (shown in Fig. 2-7). A rich fuel-air mixture is delivered directly to the pre-chamber via a pre-chamber valve, while a lean mixture is delivered to the main chamber through a conventionally located intake valve. This forced stratification, remarkably advanced for the year in which it was conceived, resulted in a lean burn engine.

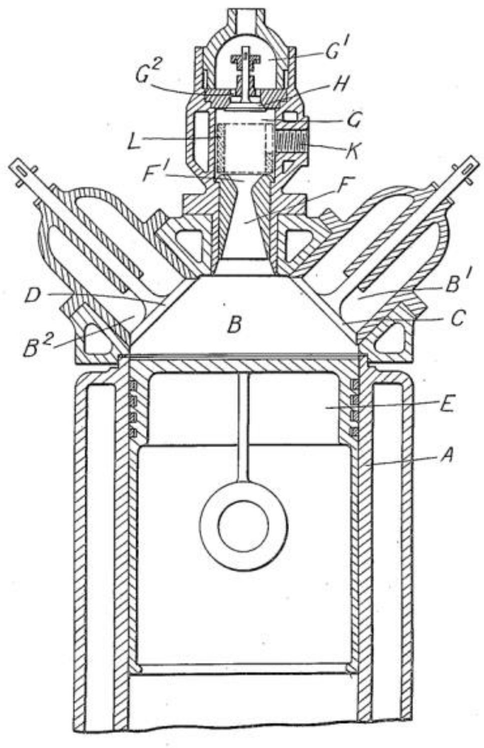

Figure 2-7: Ricardo 3-valve pre-chamber engine [88].

It is constructive to examine the differences in form and function between pre-chambers used in diesel engines and gasoline engines. While IDI diesel pre-chambers are intended as containment units for the system fuel prior to combustion, SI pre-chambers typically contain a percentage of the system fuel mass that is approximately proportional to their volume. This means that the majority of the system fuel in SI combustion chambers that contain a pre-chamber is located in the main chamber whereas ideally none of the fuel in IDI diesels is located in the main chamber prior to combustion. This alludes to the differing functionality of the two pre-chamber configurations: the IDI diesel pre-chamber is a fuel delivery surrogate; the SI pre-chamber is a tool for ignition enhancement. Differences between diesel compression ignition (CI) and gasoline pre-chambers are detailed in Table 2-1.

With the 3-valve engine providing the template for the use of a pre-chamber as an enabling technology for lean SI combustion, subsequent variations were investigated by researchers at several global automotive engine manufacturers [89-93]. Nearly all of the variants subsequently patented contained pre-chambers that appear, qualitatively if not explicitly, to possess a smaller volume than that of the Ricardo 3-valve engine. As is often cited in the development of small displacement SI engines surface-to-volume ratio increases as combustion chamber displacement decreases. With combustion occurring in this smaller volume, there is a greater surface area through which the thermal energy generated during the combustion process can transfer resulting in increased heat transfer losses as a percentage of fuel energy [94]. This surface-to-volume effect applies to pre-chambers as well but there is a key difference: the main system contribution of the fuel ignited in the pre-chamber is to generate thermo-chemical energy to ignite the remaining fuel in the main chamber. It is primarily the ignited main chamber fuel that contributes to the pressure rise that drives piston motion downward. There is a pressure rise in the main chamber resulting from the entering pre-chamber combustion products but it is negligible because the percentage of fuel used in this process and the jet expulsion phase typically begins and ends completely during the compression stroke when conventional main chamber combustion phasing is employed. Therefore, a practical system optimization pathway would be to minimize the quantity of fuel that is “sacrificed” for ignition, i.e. the quantity of fuel that is burned in the pre-chamber while still generating adequate thermo-chemical energy through this process to ignite the main chamber contents. Larger volume pre-chambers, with superior surface-to-volume ratios, require more pre-chamber fuel in order to ensure an ignitable fuel-air ratio at the spark plug. Smaller volume pre-chambers, though they experience heat loss as a higher percentage of the fuel consumed, require less fuel in order to ensure adequate pre-chamber combustion and therefore result in higher system efficiency. This relationship was made more explicit in the work of Gussak on the subject in the latter half of the last century [95-101], and it is hypothesized to be the reason for the gradual reduction in pre-chamber volume with patents subsequent to Ricardo’s.

Table 2-1: Differences between CI and SI pre-chamber combustion systems.

Parameter	Pre-Chamber Combustion System Type	
	CI	**SI**
fuel delivery to pre-chamber	directly via fuel injector	directly via fuel injector, check valve / indirectly via piston motion
pre-chamber mixture preparation requirements	translate main chamber charge motion to pre-chamber to promote fuel-air mixing	none inherent
fuel location	all fuel in pre-chamber	throughout both chambers, air-fuel ratio can differ between chambers
ignition mode	auto-ignition when local stoichiometric mixture is achieved in the pre-chamber	spark plug ignites pre-chamber contents
gas exchange to main chamber	piston motion during expansion stroke scavenges pre-chamber	pressure rise in pre-chamber forces contents to exit into main chamber
main chamber combustion	burned products expand in the main chamber	burned pre-chamber contents form torches or jets that ignite the main chamber fuel-air
primary benefit	use of low fuel injection pressure	enables knock mitigation, dilute operation
primary benefit category	mechanical system	Combustion

Some SI pre-chamber concepts developed subsequently to the Ricardo 3-valve removed the separate pre-chamber fueling feature [89-92]. In these designs, fuel is injected conventionally into the main chamber and piston motion during the compression stroke forces a portion of this fuel-air mixture proportional to the pre-chamber volume to enter the pre-chamber. This type of design, which is commonly termed passive pre-chamber, reduces hardware, controls, and packaging complexity and provides a more stable combustion event at lean air-to-fuel ratios when compared to a conventional SI engine, though enleanment capability is limited when compared against a separately fueled, or active, pre-chamber.

The most prominent automotive production application of the pre-chamber concept in the latter half of the 20th century is the Honda Compound Vortex Controlled Combustion (CVCC) engine which was in production from the early-to-mid 1970s [102]. The concept is shown in Fig. 2-8. During this period when emissions control for automotive engines was first becoming stringently regulated in the United States lean combustion was thought of as a viable low engine-out emissions alternative to catalytic conversion of emissions constituents in the exhaust pipe. The increasing stringency of emissions regulation eventually made catalytic conversion of exhaust emissions a *defacto* mandate. The 3-way catalyst became a standard component for automobiles and its requirement for stoichiometric operation rendered lean combustion unfavorable at the time [103].

The CVCC, as with most pre-chamber concepts developed and commercialized up to that time, incorporated a throat separating the pre-chamber and main chamber large enough to keep the flame front intact as combustion proceeded from the pre-chamber to the main chamber. Qualitatively appearing similar to a blowtorch, this approach relies on a reactive flame to continue its propagation through the remainder of fuel-air mixture. Without the challenge of generating and maintaining a spark kernel in a lean environment, combustion proceeds and moderate enleanment is achieved. As a result this and similar concepts are commonly termed torch ignition systems.

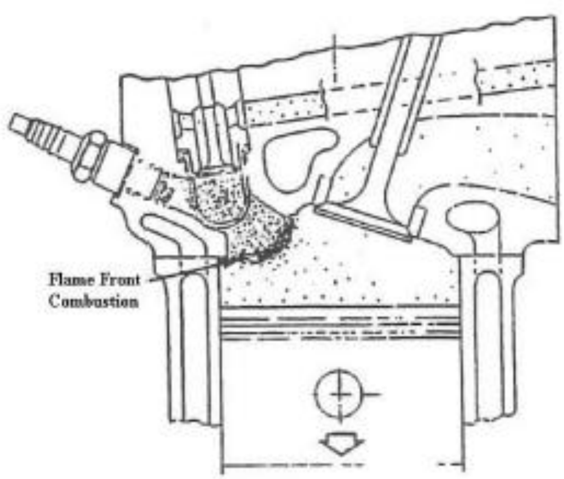

Figure 2-8: Honda CVCC pre-chamber engine [102].

Commercial pre-chamber igniter usage in the light duty passenger car segment was largely extinguished by the late 1970s due to the advent of competing emissions control technologies such as catalytic converters. Though they presented an emissions control solution robust enough to encompass the highly varied operating conditions of passenger car engines, catalytic converters incorporated large quantities of precious metals and therefore represented a significant add-on cost to passenger cars. This presented a scaling issue when applied to larger engines, with add-on emissions control cost outpacing the proportional cost of the engine and peripherals [104].

2.4.1.2 Heavy Duty Gaseous Fuel Applications

In a separate development beginning approximately in the late 1970s, natural gas became a prevalent fuel in the large bore power generation sector, with fuel usage costs making it a serious competitor to existing diesel fuel [105], especially given the fact that key natural gas fuel properties somewhat leant themselves to highly efficient lean operation. Many large bore stationary power engine manufacturers began adding natural gas variants to their existing diesel engine product line. The confluence of these factors made the prospect of lean burn natural gas-fueled large bore engines for stationary power attractive to manufacturers and consumers. Pre-chamber technology, long familiar to heavy duty diesel engine manufacturers and researchers, and in parallel having been established as a lean combustion-enabler for SI engines, was therefore developed for this new class of large bore natural gas-fueled engines.

In one notable example, Caterpillar developed a natural gas-fueled variant of its 3600 diesel engine series in 1991 (Fig. 2-9). This variant incorporated a pre-chamber combustor (Fig. 2-10) to ignite lean natural gas mixtures. Other large bore engine manufacturers such as Wartsila, Waukesha, and Jenbacher also commercialized pre-chamber lean burn natural gas engines during this period. While many of the pre-chamber applications that were commercialized in the industry were passive designs, numerous patents filed by engine manufacturers during this time period indicate substantial research interest in active systems as well [106].

Parameter	Value	Units
Bore	280	mm
Stroke	300	mm
Displacement	147.8	L
Cylinders	8	-
Power	2460	kW
Torque	24700	Nm

Figure 2-9: Caterpillar G3600 engine incorporating pre-chamber combustors [107].

Figure 2-10: Passive pre-chamber for use in Caterpillar G3600 engine [108].

2.4.2 Jet Ignition

2.4.2.1 Introduction

An alternative to torch ignition was first researched by Nicolai Semenov in the 1950s [109-111], followed shortly by pioneering research by Lev Gussak that led to a commercial application in the Volga sedan engine. This combustion mode, relying on similar components but with a significantly different combustion mechanism to torch ignition, is known as jet ignition. While it retains the pre-chamber combustor, jet ignition differs primarily from its antecedent by the manner in which combustion translates from the pre-chamber to the main chamber. Torch igniters are generally designed to promote continuous flame front propagation from pre-chamber to main chamber, with different mixture preparation conditions in each to promote rapid kernel development at the spark plug and robust early flame generation. With jet ignition systems, particularly in Gussak's designs, the relatively large diameter throat that separates the two chambers is replaced by a nozzle containing one or more small orifices with diameters smaller than the quench diameter of the combusted fuel's flame. With this design the pre-chamber flame front is quenched and combustion is *discontinuous* as it translates between the chambers [95-101].

Without the reactivity of the sustained flame front, jet ignition systems must rely on other mechanisms to successfully achieve main chamber combustion. Jet ignition systems initiate combustion in the main chamber through fuel chemical kinetic, thermal, and turbulent effects, as is described below:

1) Fuel chemical kinetic – similarly to advanced pre-mixed auto-ignition concepts such as Homogeneous Charge Compression Ignition (HCCI) or Reactivity Controlled Compression Ignition (RCCI) [112-114], main chamber ignition is reliant to a large degree on the decomposition of fuel molecules eventually achieving an intermediate hydrocarbon species that forms chain branching reactions. In this manner, chemical kinetics plays a key role in a successful jet ignition process. The difference between jet ignition and the aforementioned advanced auto-ignition concepts is that in jet ignition a conventional combustion process is underway in the pre-chamber and then temporarily arrested through flame quenching. The process then effectively restarts in the main chamber [115,116].
2) Thermal – though the flame front generated in the pre-chamber is extinguished as contents exit through the nozzle orifice or orifices, the contents remain at an elevated temperature. This elevated temperature prevents a permanent arresting of the chemical kinetic process begun during pre-chamber combustion [117].
3) Turbulent – while not a direct trigger for ignition, the gas exchange process and turbulence generated by the high velocity jets play a role in determining when the re-ignition events occur in the main chamber. A secondary effect of the small diameter orifice(s) is that a greater degree of pressure is generated in the pre-chamber while the nozzle acts as a restriction to the generated pressure wave. This pressure gradient between pre-chamber and main chamber forces gas exchange to the main chamber which is manifested as "jets" that travel at high velocities. This velocity causes a delay to the re-ignition process until jet momentum has reduced, and to some extent entrains the unburned fuel-air mixture of the main chamber [118].

With the absence of a flame front, jet-induced ignition in the main chamber resembles an auto-ignition process. A conventional flame front propagates quickly from each auto-ignition site aided by the entrainment of unburned charge.

Table 2-2 compares the operating approach of torch ignition with jet ignition.

Table 2-2: Differences between torch ignition and jet ignition pre-chamber combustion systems.

Parameter	Pre-Chamber Combustor Functional Approach	
	Torch Ignition	**Jet Ignition**
throat/orifice size	> quenching diameter	<< quenching diameter
charge velocity, pre-chamber to main chamber	similar to laminar flame speed	irrespective of laminar flame speed
heat loss through chamber communication path	Low	very high
main chamber ignition mode	continuous flame front	auto-re-ignition of radical intermediate combustion species
main chamber ignition location	at throat/orifice exit	distributed between orifice exit and main chamber surface
main chamber burn duration potential	moderately fast	very fast
enleanment capability vs. conventional SI	Moderate, lambda~1.8	High, lambda≥2

While the quenching effect of jet ignition resulting from the relatively small orifice diameter results in increased heat transfer loss to the nozzle, the primary advantage of jet ignition is the ability to distribute the ignition site(s) in the main chamber some distance away from the orifice exit. With a multi-orifice nozzle, the result is a distributed multi-point ignition system, an achievement that is by definition not possible with a torch ignition system. As is discussed in previous sections, this type of ignition system possesses clear benefits for promoting stable combustion of very lean mixtures. For example, Gussak was able to achieve a homogeneous $\lambda = 2$ condition with his patented jet ignition concept, a value that had not been published as achievable by a torch ignition system to that point [97]. To achieve this so-called ultra-lean capability (beyond conventional SI enleanment, $\lambda > 1.6$) direct fueling to the pre-chamber became a necessity.

Yamaguchi, researching a jet ignition system similar to Gussak's, confirmed that there is both a minimum orifice diameter below which the main chamber re-ignition process is compromised, and a maximum orifice diameter above which the jet ignition process gradually transforms into a torch ignition process. There is therefore a clear optimum range of orifice diameters, irrespective of other factors, where jet radical species formation is maximized and heat loss as the jets pass through the nozzle orifices is not unduly detrimental to jet reactivity [117].

A resurgence of interest in pre-chamber-initiated lean combustion in the early 1990s led Dr. Harry Watson to explore the concept of optimum radical formation in the pre-chamber through the use of hydrogen injection [119-124]. The concept of using hydrogen (H_2) as a fuel supplement to increase flame speeds in conventional SI engines had been researched previously, but Watson applied this concept to pre-chamber combustion in a jet ignition engine in order to generate a greater degree of H_2 and other highly reactive intermediate species in the jets, thereby creating a higher reactivity jet. This research, in one sense a fundamental exploration of jet reactivity resulted in a Hydrogen-Assisted Jet Ignition (HAJI) engine capable of achieving $\lambda = 5$ [125].

The ability to achieve SI lambdas well beyond what had up to that time been achievable led to another conclusion: thermal efficiency does not increase continuously with enleanment. In fact Watson's research shows that in a HAJI engine, peak thermal efficiency is achieved near $\lambda = 1.7$ for the conditions tested [126]. Different pre-chamber and main chamber fuels shift this "peak efficiency lambda" slightly but generally efficiency peaked at a λ that was shy of the lean limit. Figure 2-11 illustrates this effect. Watson's results strongly indicated that the reason for this was a precipitous increase in incomplete combustion loss as the engine is enleaned, likely due to the drop in temperature of the combustion chamber surfaces. In this way the reduced combustion temperatures inherent to ultra-lean operation are both an efficiency benefit and eventual limitation.

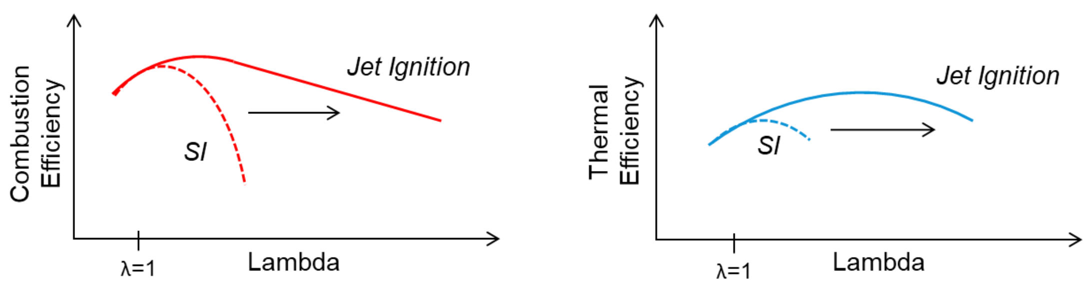

Figure 2-11: Illustrated trends in combustion efficiency (left) and thermal efficiency (right) with enleanment.

While a means of directly fueling the pre-chamber is not a pre-requisite for jet ignition combustion, all published ultra-lean-enabling homogeneously mixed concepts contain directly fueled pre-chambers. A directly fueled pre-chamber allows for separate fuels to be injected in pre-chamber and main chamber. Considering the characteristically small volume of jet ignition pre-chambers, the majority of these concepts fueled the pre-chamber with a gaseous fuel such as natural gas, propane, or, in the case of HAJI, hydrogen. The reasoning behind the use of a gaseous fuel for pre-chamber combustion is stated explicitly by Watson: the gaseous fuels considered have wide flammability limits compared to gasoline and there is no danger of “wall wetting”, i.e. having liquid fuel pool onto the surfaces of the pre-chamber. When pool burning occurs in the pre-chamber, there is a distinct danger of soot generation that damages the spark plug and fuel delivery device. Heavy duty stationary natural gas applications also, by definition, use a gaseous pre-chamber fuel. Since this is the primary, and for many decades only, commercial application of pre-chambers in ICEs, gaseous fuel delivery hardware, operating strategy, and general understanding are well established in pre-chambers [127].

2.4.2.2 MAHLE Jet Ignition

MAHLE Powertrain has been developing a jet ignition concept known as MAHLE Jet Ignition® (MJI) since 2007 through the research of Attard [10,128-130] and this author [3,4,131]. MJI was originally conceived as a non-hydrogen fueled variant of the HAJI concept. In an effort to make the technology more commercially viable, MJI research focused on developing a common fueled liquid gasoline variant for passenger car applications. The key differentiator between MJI and its antecedents is the incorporation of modern DI fuel injector technology in the pre-chamber. The use of a micro-flow DI fuel injector allows for precise, consistent metering of small quantities of fuel each cycle and precise targeting of the fuel spray within the pre-chamber. The high pressure capabilities of modern DI fuel injection systems also enable relatively late fuel injection in the pre-chamber which in turn allows the fuel strategy to exploit the local charge motion interior to the pre-chamber during the compression stroke. This is necessary to minimize particulate formation during the pre-chamber combustion event. Direct fuel injection also provides the opportunity for injection late in the cycle. A fuel injection event that occurs too early can result in “over-mixing”, producing an overly dilute mixture near the spark plug, posing a risk of misfire. A fuel injection event late in the compression stroke is therefore desired in order to ensure an ignitable mixture near the spark plug and maximize the quantity of auxiliary injected fuel that participates in the pre-chamber combustion event. This innovation to the jet ignition concept is viewed as critical for 1) successful operation with a liquid pre-chamber fuel, and 2) efficient, judicious use of the pre-chamber fuel in order to ensure a strong system efficiency increase. The MJI pre-chamber prototype assembly is displayed in Fig. 2-12. Figure 2-13 illustrates the importance of precise control over pre-chamber fuel quantity by displaying the sensitivity of engine efficiency to minute changes in pre-chamber injected fuel quantity. Shown in Figure 2-14 is the “over-mixing” effect of early fuel injection in the pre-chamber, demonstrating why late injection enabled by the DI injector is optimal.

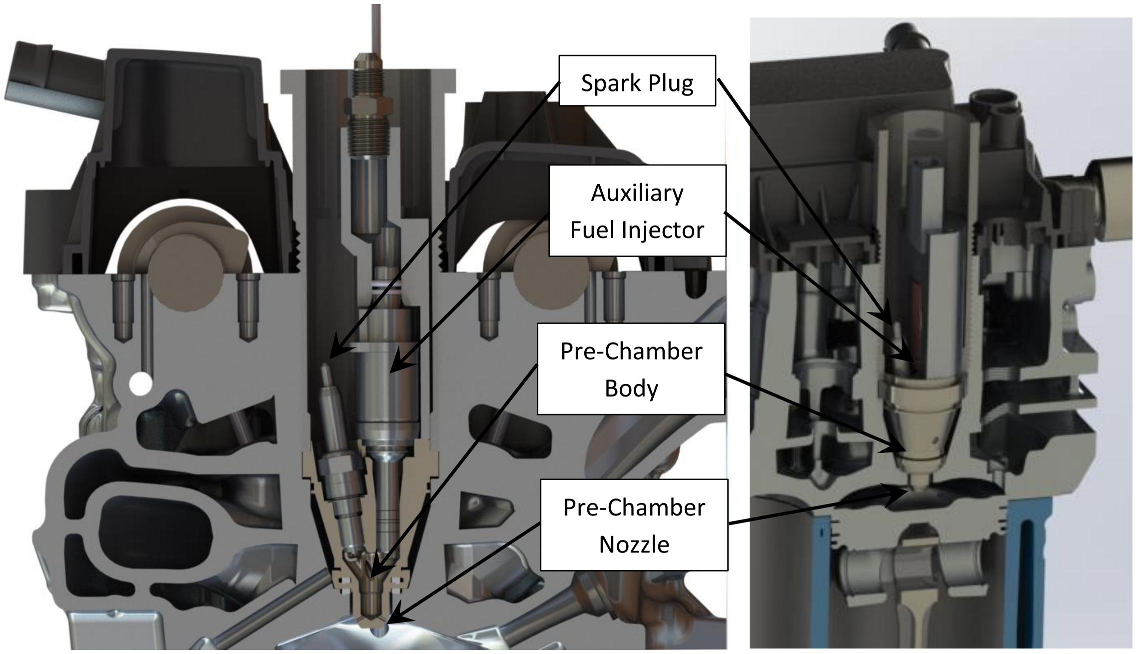

Figure 2-12: Cutaway of the MJI pre-chamber (left) and MJI pre-chamber assembly (right) in a typical passenger car engine [3].

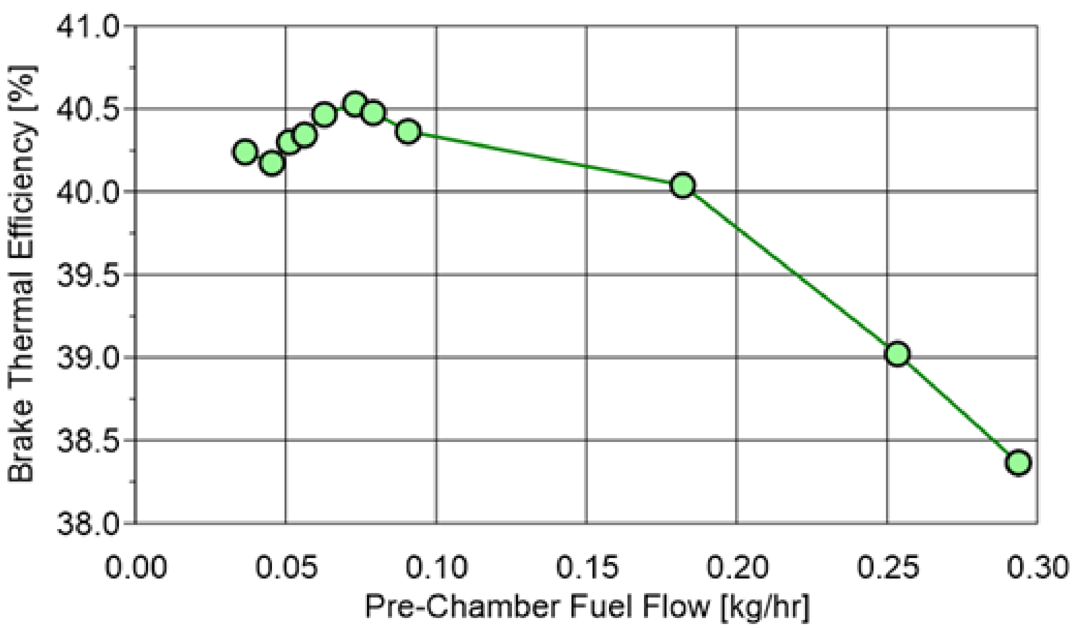

Figure 2-13. Brake thermal efficiency trends with pre-chamber fuel injection quantity, 1.5L DI3, CR = 15.1, speed = 3000 rpm, BMEP = 10 bar, λ = 1.7.

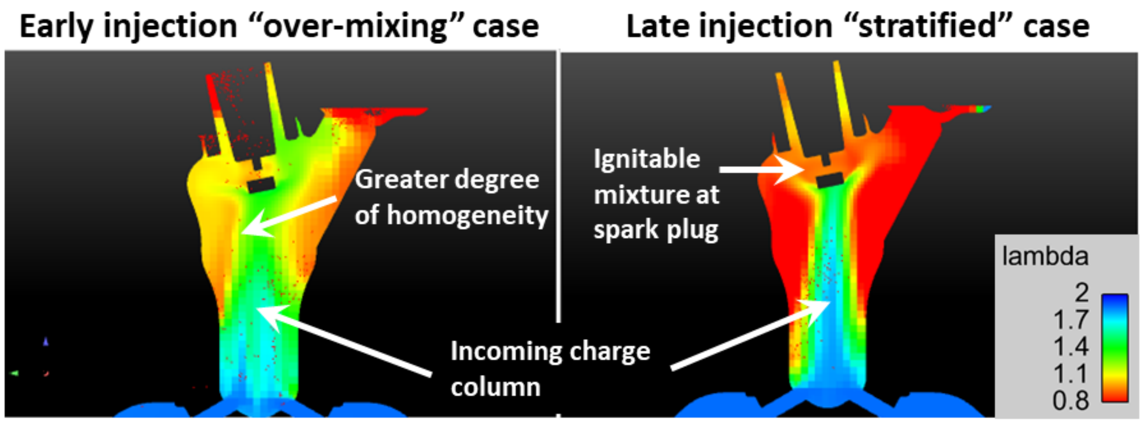

Figure 2-14: Mixture preparation with early (left) and late fuel injection (right) timing in the pre-chamber at time of spark with constant pre-chamber fuel quantity.

Aside from the fuel injection system, MJI incorporates the characteristics of many jet ignition concepts developed since the early 1990s, namely a small volume pre-chamber (< 5% of the clearance volume) and a multi-orifice nozzle with orifice diameters that promote a high degree of flame quenching. The quenching and re-ignition process was confirmed through images taken from an optically accessible engine, and confirmed using a computational fluid dynamics (CFD) combustion simulation that was correlated to experimental engine test data [132]. Images from the optical engine are shown in Fig. 2-15. The images in this figure show luminous jets, with no backlighting, emerging from the pre-chamber. No intensifying was used for these images. The false color scale indicates relative temperatures, with the white color indicative of peak flame temperatures, the red band indicative of flame front temperatures, and yellow indicative of recently burned product temperatures. The flame content in these jets is minimal. The jets subsequently create distinct ignition sites in the main chamber, visible at the leading edges of the jets, particularly in the bottom row of images. These ignition sites produce distinct flame fronts that consume the charge, eventually joining during this process. More details of this study are provided in [4]. A CFD model depiction of the jet ignition process is displayed in Fig. 2-16.

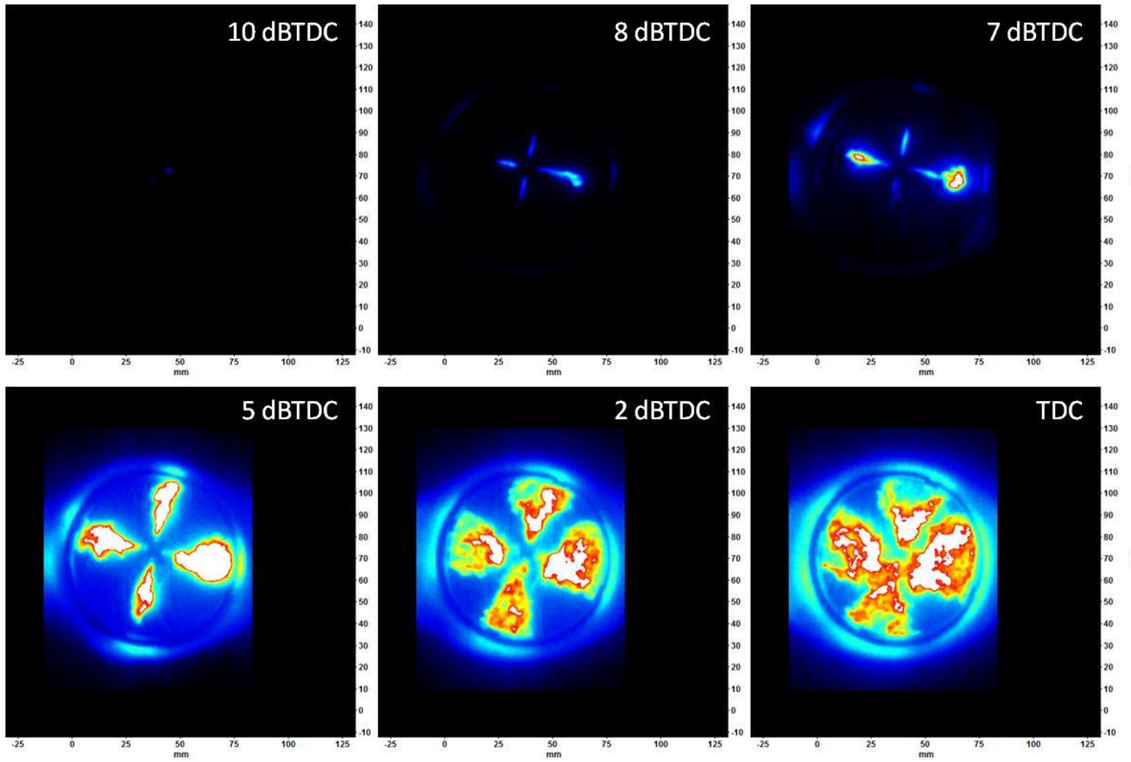

Figure 2-15: Chemiluminescence high speed images of the jet ignition process (Speed: 1500 rpm, gross indicated mean effective pressure: 5.5 bar, λ = 1.2, CR10) [4].

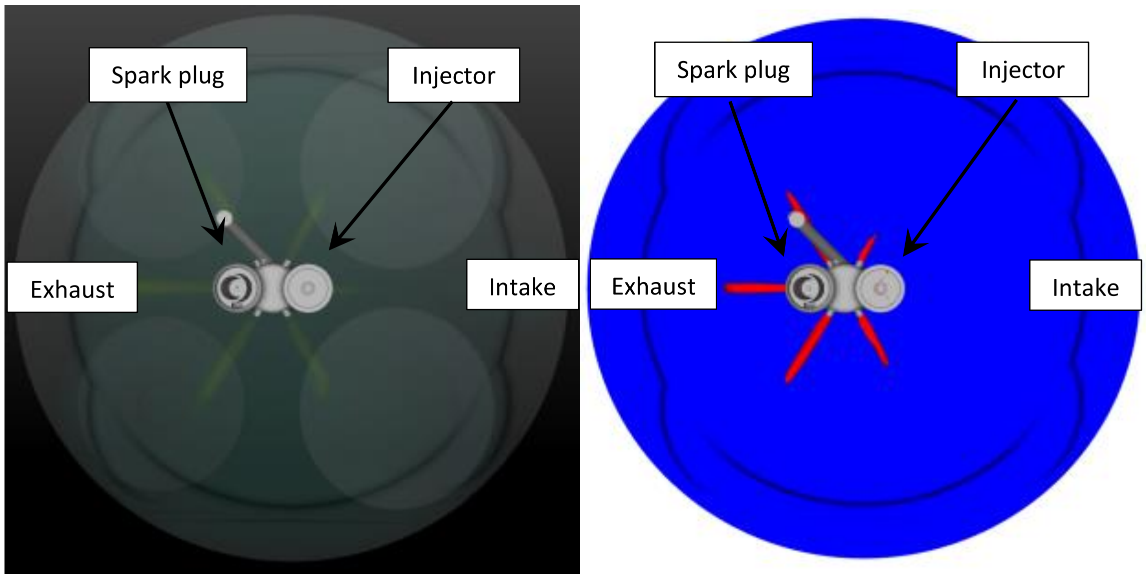

a) -9 crank angle degrees (CAD)

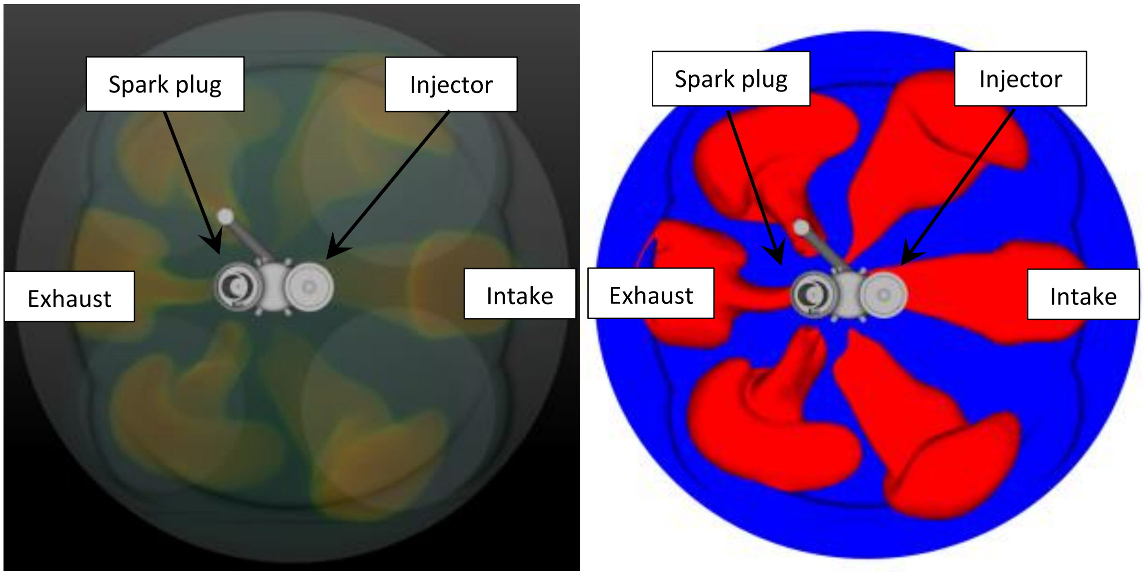

b) 2 CAD

Figure 2-16: CFD combustion model temperature visualization before (top) and after (bottom) TDC. Left: temperature range (0-2400K), Right: Isosurface at 1500K [132].

Development of the liquid fueled pre-chamber concept did indeed prove challenging. Initial research was plagued by significant wall wetting resulting in rapid plugging of the pre-chamber fuel injector. Combustion in each cylinder also proved to be more sensitive to pre-chamber internal geometry and fuel injector nozzle variation than did that of the gaseous-fueled concept [4]. Figure 2-17, an image of the fuel injection event taken from the CFD model, illustrates the challenge associated with optimizing a liquid fuel injection concept.

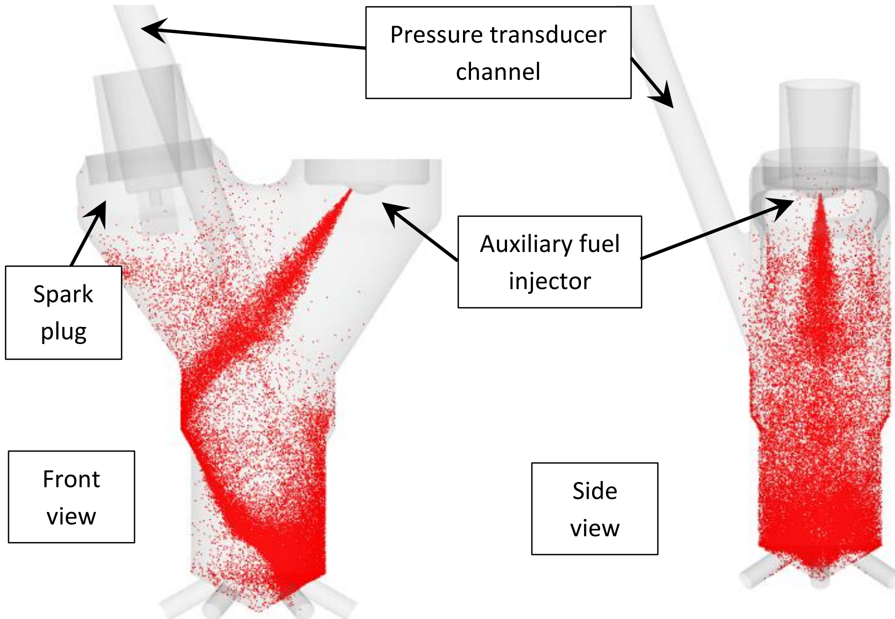

Figure 2-17: Front and side view of spray pattern within a MJI pre-chamber, 10 crank angle degrees after injection [132].

Ultimately MAHLE Powertrain developed patents concerning the geometric features of the pre-chamber and the fuel spray / charge motion interaction of a liquid gasoline-fueled pre-chamber concept. Peak Brake Thermal Efficiency (BTE) published to-date in a MJI engine is 42% [3], representing an increase of approximately 15% above the highest reported production SI engine at the time, and 10% above the highest reported production-intent SI engine at the time of this writing. A subsequent MJI engine study in review has demonstrated a peak BTE > 43.5% and a minimum BSFC < 190 g/kWh with the use of advanced lubricants and gasoline-range fuels. Figure 2-18 displays recorded peak BTE and projected peak BTE for a 1.5L 3-cylinder MJI engine utilizing various technology packages.

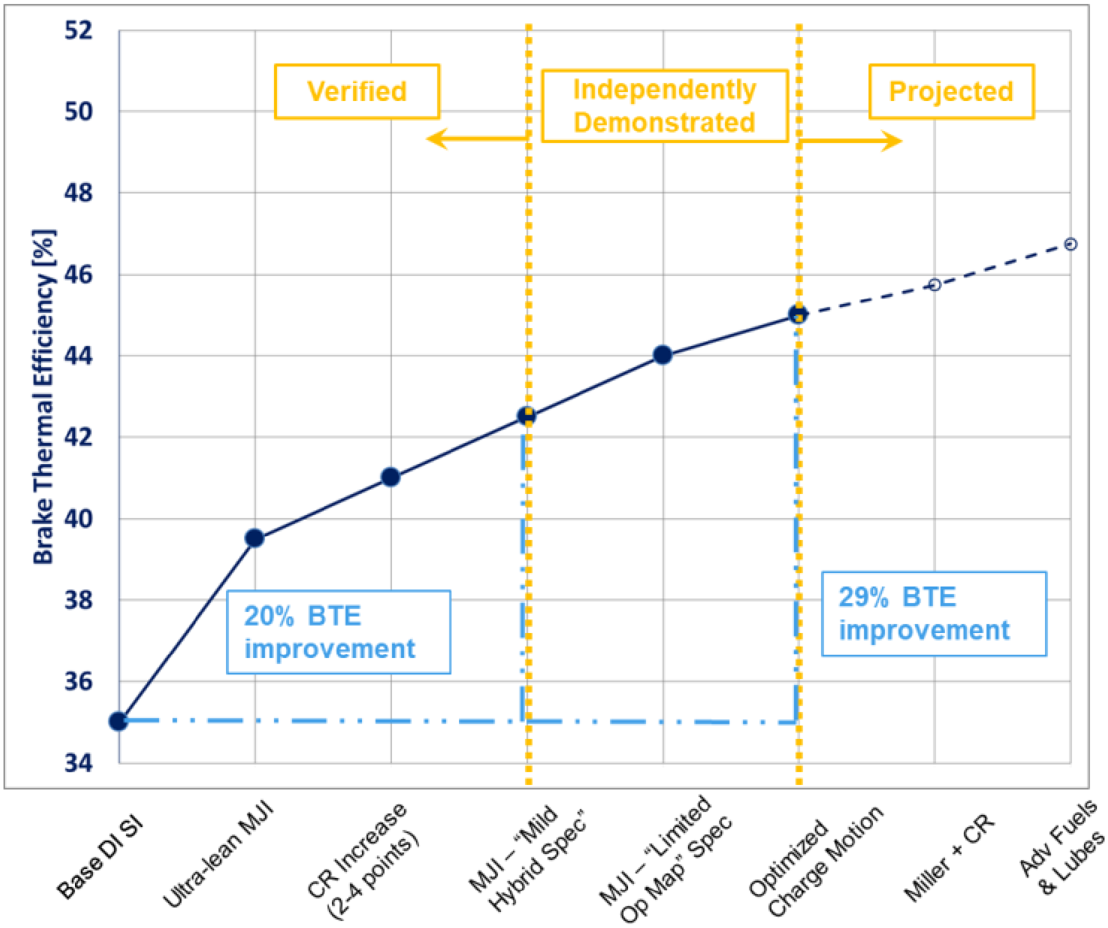

Figure 2-18: Demonstrated and potential BTE of the MJI concept.

Jet ignition concepts generally and MJI specifically possess numerous parameters that can be optimized in order to increase thermal efficiency, minimize engine-out emissions, or aid practical engine operation. While many of these parameters have been studied extensively by MAHLE Powertrain and others [4,96,109,111,118], one parameter for which there is minimal published data on its effect on jet ignition combustion processes is charge motion.

2.5 Powertrain Hybridization

2.5.1 Plug-In Hybrid Electric Vehicles

The increasing stringency of legislated CO_2 and fuel economy levels in the automotive industry in all global regions has driven considerations for significant changes to powertrain structure. This trend has accelerated in recent years as legislation begins meeting the limits of ICE-only strategies for increasing efficiency. This situation has led to a diversity of modern viable powertrain options, from ICE-centric powertrains to Battery Electric Vehicles (BEV). The macro trend of increased powertrain electrification applies to powertrains that contains ICEs, and therefore the majority of ICE vehicles are expected to become Hybrid Electric Vehicles (HEVs) in the next 10-15 years [133]. HEVs encompass a large spectrum of functionality, from parallel auxiliary electric assistance to direct drive of the axles with the ICE providing battery charging capability. Some of these HEV configurations are self-contained while others, such as Plug-in Hybrid Electric Vehicles (PHEV), draw electricity from the grid.

Currently vehicle CO_2 intensity (inversely related to fuel economy in countries that regulate fuel economy instead of CO_2 directly) is regulated at the tailpipe. However, a growing industrial consensus is that this methodology does not comprehensively reflect the actual CO_2 intensity of the vehicle, as it neglects considerations such as vehicle manufacturing and recycling, resource extraction, and grid CO_2 intensity for powertrains that draw electricity from the grid. Incorporating a comprehensive life cycle CO_2 assessment changes the calculus of future powertrain selection. Figure 2-19 presents a MAHLE Powertrain analysis of life cycle CO_2 intensity of PHEVs for varying electric driving ranges, i.e. differing battery sizes. The dashed yellow curve represents the average grid CO_2 intensity of the midwestern region of the US, where the author is based. The blue curve represents the combined PHEV life cycle CO_2 intensity as a function of electric driving range capacity, demonstrating that there is an optimum battery size that can be selected for this particular example (C-segment passenger car). The horizontal green lines represent the comparable life cycle CO_2 of BEVs of varying driving range. Typical modern electric vehicle driving range is 400km. Therefore, a PHEV for this application can demonstrate a lower life cycle CO_2 intensity than does a comparable BEV. A PHEV also retains the ability to operate in "BEV-mode" where localized tailpipe criteria emissions are heavily regulated. While a life-cycle CO_2 assessment of vehicles is not currently absorbed into legislation in a meaningful way, regulators may take life cycle CO_2 considerations into account in the future as the CO_2 intensity of the grid and of resource extraction fall under stricter scrutiny. Based on this analysis, it is clear that there remains a need not just for HEV powertrain development but also to continue to increase the thermal efficiency of the base engine in cost-effective ways.

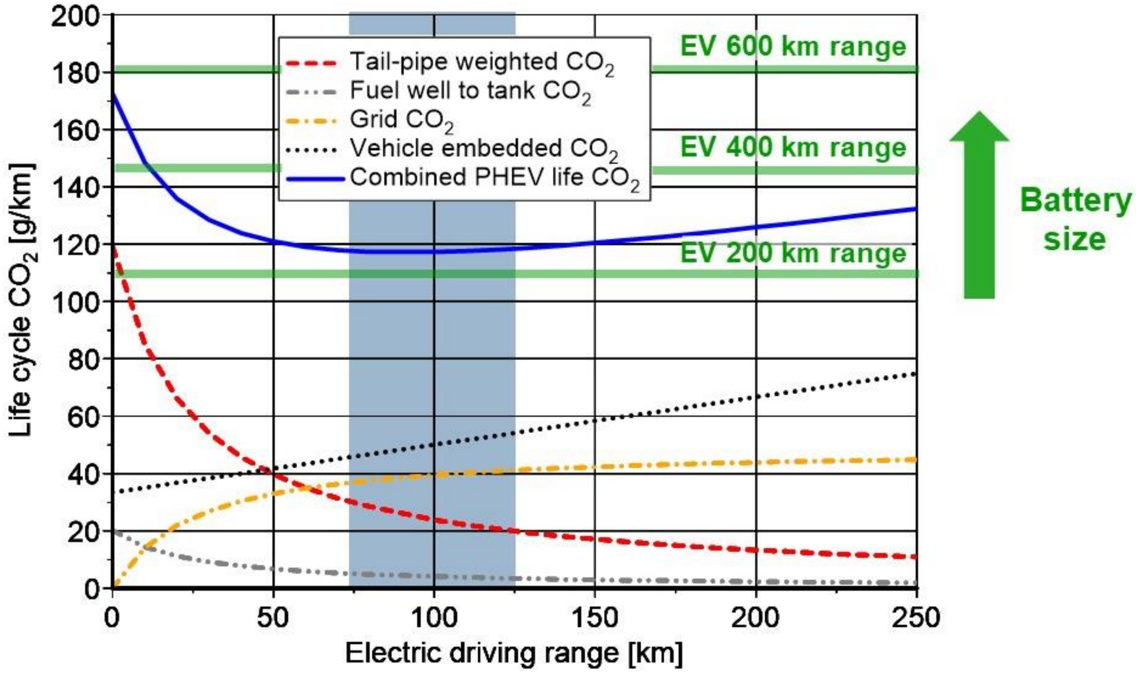

Figure 2-19: Life cycle CO_2 comparison of PHEV powertrains versus BEVs with varying electric driving ranges [133].

Increasing ICE efficiency in step-changes, such as introduction of high levels of dilution, is necessary in order to ensure viability of the ICE in the current legislative environment, and to allow it to serve as a bridge technology to fully electrified (battery, fuel cell) or zero tailpipe CO_2 (zero-carbon fuel ICE) future powertrains that require significant infrastructure investment for mass market penetration. Hybridization alone cannot accommodate upcoming legislation, and combustion-based high efficiency ICE solutions are needed as well. Figure 2-20 shows an analysis of powertrains with various technology and hybridization levels and their expected performance in a small cross-over Sport Utility Vehicle (SUV) across the New European Drive Cycle (NEDC). From this analysis it is clear that 1) increasing levels of powertrain electrification are necessary, and 2) combustion-based efficiency increases are impactful and must be developed in concert with HEV advances. With increasing complexity of HEV powertrain solutions, however, there is significant downward cost pressure on new additive technologies. Relatively low cost, high efficiency technologies such as jet ignition may therefore be ideal in HEV applications.

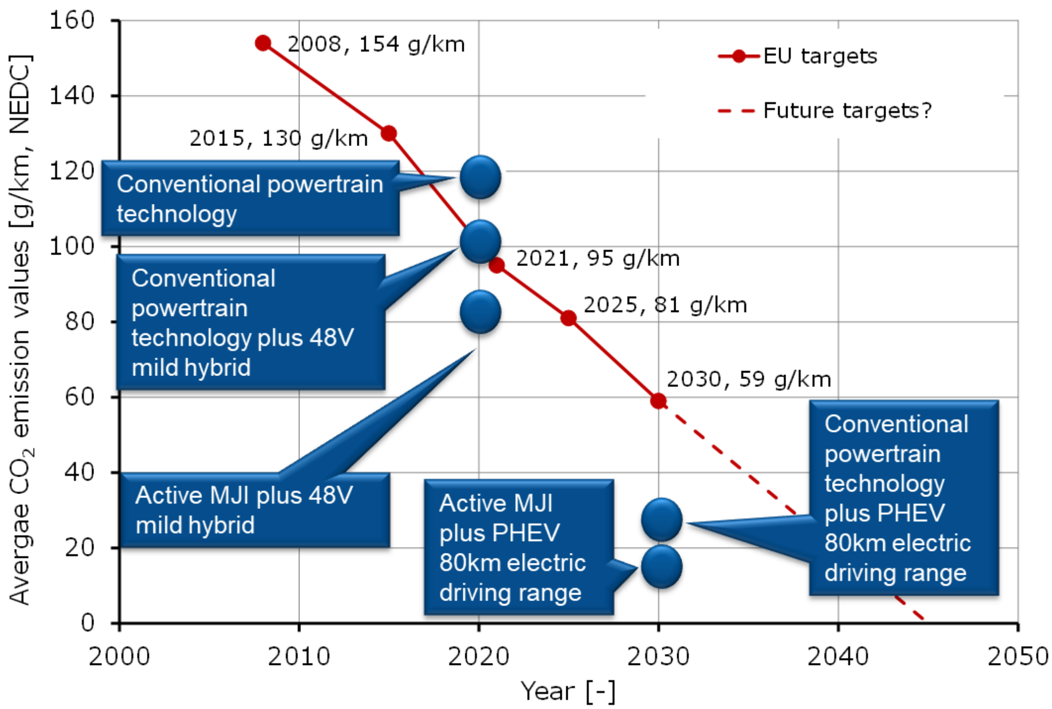

Figure 2-20: Fleet average CO_2 targets, with examples for 1400 kg compact cross-over SUV [133].

2.5.2 Hybridization with Jet Ignition Engines

Due to its simplified componentry and synthesis with existing technologies, passive jet ignition presents only a minimal cost increase over the baseline engine cost. Active jet ignition has a higher technology barrier to clear than passive, both because of the additional component complexity but also because homogeneous ultra-lean operation is a fundamentally different way to operate a modern SI engine. The thermal environment is drastically different due to the reduction in temperature, the air handling system must be optimized to manage low temperature, and lean aftertreatment must be optimized for effective catalysis of a low NO_x output. These ancillary system changes are required regardless of which technology is used to enable ultra-lean operation. However, each of these ancillary system changes are employed or have been employed in automotive applications. Lean aftertreatment, for example, is a necessary component of diesel engine emissions control. Ultra-lean jet ignition engines have a narrower λ window, higher exhaust temperatures, and produce engine-out CO and NO_x emissions orders of magnitude lower than diesel engines. Therefore, existing lean aftertreatment systems used in diesel engines can be cost-optimized for ultra-lean jet ignition operation. Passive and active jet ignition are therefore attractive additive technologies for increasing engine efficiency in HEV powertrains.

As some or all of the burden of propulsion shifts from the ICE to the electric motor in HEV powertrains, less versatility is required of the combustion system. This reduced versatility requirement means that less coverage of the traditional engine operating map is needed and there is a reduced need for transient operation, both of which provide greater control over engine operating temperatures. HEV powertrains, therefore, are ideal platforms for low cost advanced combustion modes that typically suffer due to the need to encompass operation over the full engine map and maintain combustion stability during transients.

While passive and active jet ignition have both demonstrated the ability to encompass the full engine operating map, the reduced versatility requirement does enable further optimization. For instance, reduced need for high speed / high load excursions eliminates the knock considerations for these conditions, enabling an increase in CR. With the electric motor providing low power operation, ICE catalyst heating operation can occur outside of the traditional low speed and load requirements. This enables physical and operational modifications to the jet ignition engine that provide a further increase in efficiency. Figure 2-21 illustrates the reduction in map-wide BSFC associated with the reduced combustion system versatility requirement of HEVs.

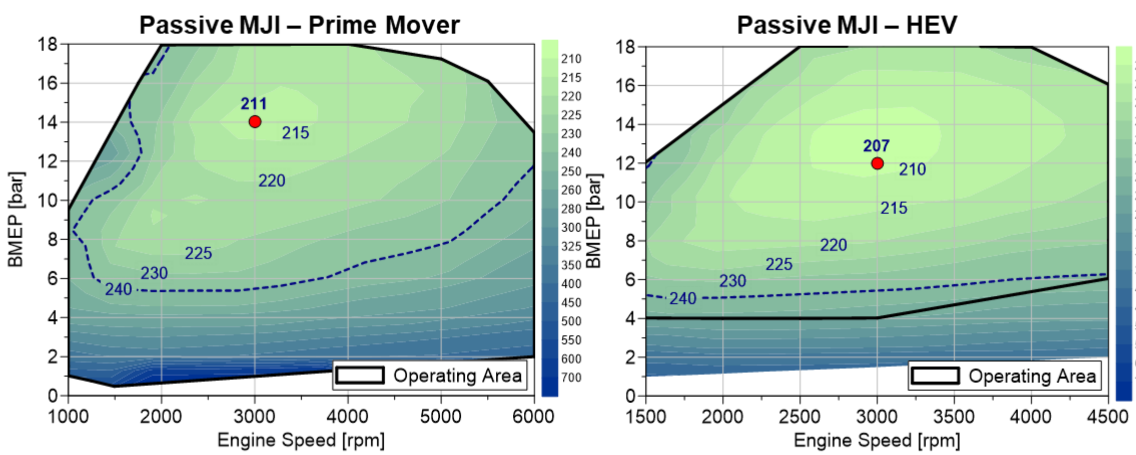

Figure 2-21: Passive MJI engine operation in a prime mover application (left) and a HEV application (right) [134].

All of the previously discussed advantages of the reduced versatility requirement for passive jet ignition engines apply equally to active jet ignition engines. Due to the approximately doubled air flow requirement for active jet ignition, these engines tend to place a strain on the boost system and have a smaller operating envelope than passive jet ignition applications. Reduced engine map coverage therefore is consistent with the needs of active jet ignition. Additionally, the greater control over engine operating temperatures and reduced lambda fluctuations, both due to the reduced need for transients, benefits the lean aftertreatment system, allowing for further cost-optimization of the system. Set out in Fig. 2-22 are the predicted operating map requirements of passive and active jet ignition in a common engine platform, which demonstrates how these requirements can be complimentary to jet ignition operation.

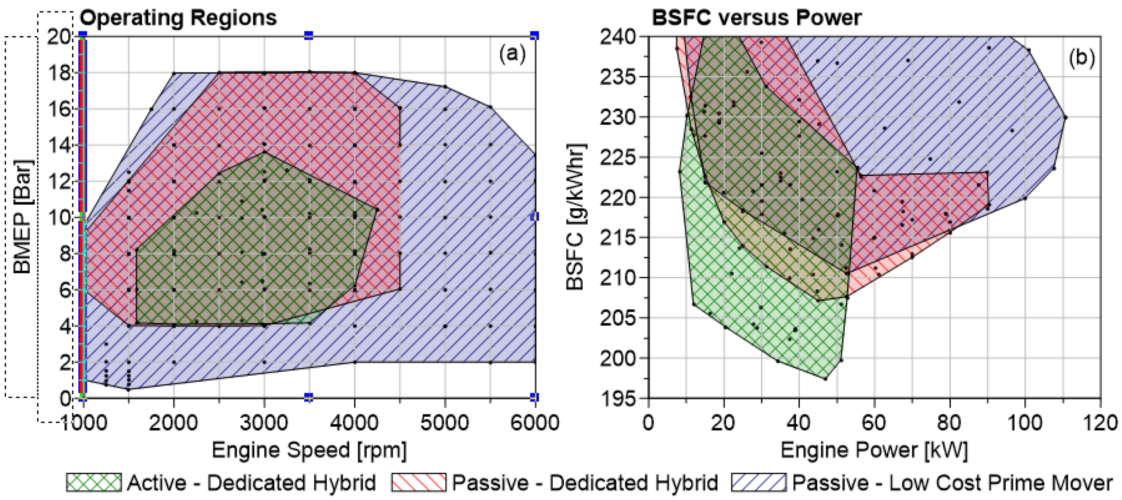

Figure 2-22: Passive MJI 1.5L 3-cylinder engine operation in a prime mover application (left) and a HEV application (right) [134].

2.6 Charge Motion

2.6.1 Charge Motion in SI Engines

Charge motion in SI engines is typically used to drive or enhance mixture preparation in the cylinder. With the advent of DI SI engines, the role of charge motion in mixture preparation has become especially critical to ensuring proper combustion and low emissions. The pervasive type of charge motion used in SI engines is tumble, which typically interacts with the bulk of the injector spray. Tumble requires certain length scales and tends to degrade as the piston nears TDC [135-137], though this effect is highly dependent on combustion chamber geometry, especially CR and bore-to-stroke ratio. It tends to devolve into a general non-ordered turbulent kinetic energy (TKE) with high velocity but no uniform flow field, though bulk tumble flow motion can persist in some combustion chamber geometries, which may lead to distortion of the flame front during propagation if not properly optimized. This persistence, however, is not considered ideal and is typically avoided. As such tumble motion tends to not contribute strongly to combustion in and of itself, but high levels of TKE present during the combustion process can increase turbulent flame speed, thereby increasing combustion burn rate [9]. This effect is particularly useful for lean engines, as it helps compensate for the reduction in laminar flame speed inherent in the colder lean combustion environment. High levels of turbulence can, however, have the detrimental effect of stretching the spark kernel, resulting in misfires and also increase in-cylinder heat loss.

Swirl is generally not purposefully used in production SI engines as it provides little mixture preparation benefit. It does not degrade near TDC to nearly the same extent as tumble therefore it is a potentially useful form of charge motion for lean combustion concepts. Literature and previous simulations performed by MAHLE Powertrain have shown contradictory effects of swirl on lean combustion [138-140].

Figure 2-23 depicts swirl motion and tumble motion in a typical combustion chamber.

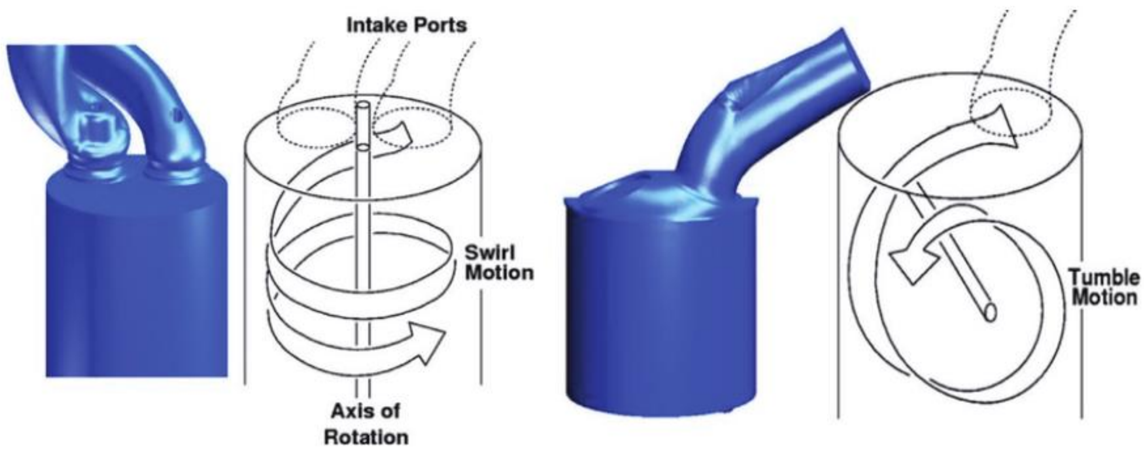

Figure 2-23: Illustration of swirl motion (left) and tumble motion (right) [141].

The pioneering work of Quader on the nature of lean combustion in SI engines is informative in this area [5,77,142]. Through combustion block experiments, Quader demonstrated that charge motion has a competing influence on kernel formation and flame front propagation in lean combustion systems. High levels of charge motion, regardless of type, can have the effect of stretching the flame kernel resulting in misfires. Contrarily, high levels of charge motion prove beneficial to increasing flame speed as the flame slowly consumes the lean charge. Stratified lean combustion with targeted mixture preparation to ensure an ignitable mixture near the spark plug is one potential solution that has been proposed to mitigate the kernel formation challenge of high tumble dilute engines [143,144]. Alternatively, pre-chamber concepts have the potential to effectively separate and quarantine the spark plug from the majority of the main combustion chamber flow field. This could potentially lead to high levels of TKE in the main chamber being beneficial to reducing burn duration and increasing enleanment while reducing or eliminating the adverse effect on kernel formation.

2.6.2 Charge Motion in Jet Ignition Engines

In practice however jet ignition pre-chambers possess two unique elements not considered in this generalized assessment of lean combustion. Firstly, the pre-chamber has its own unique charge motion generated by the nozzle geometry and the upward motion of the piston during the compression stroke. Internal pre-chamber geometry and component placement are also factors that can influence in-pre-chamber charge motion. Not only does the pre-chamber have its own charge motion dynamic separate from that of the main chamber, but a recent study [145] has shown that main chamber charge motion does translate to the pre-chamber, asymmetrically depending on the charge motion type. Secondly, as is discussed in previous sections, the jet ignition combustion process relies on the generation of auto-ignition or re-ignition sites in the main chamber. These sites, by definition, are untethered to a physical ignition source and their location is dictated by complex thermo-chemical and turbulent interaction. The effect of charge motion on the nature of these ignition sites and their location is unknown.

2.7 Summary

There are numerous technologies to address efficiency loss in SI engines. The use of high levels of dilution has been proven to be one such promising technology. However, in order to ensure stable combustion with high levels of dilution, a high energy distributed ignition source is needed. Jet ignition, a subcategory of pre-chamber combustion, has been proven to be an effective enabling technology for this combustion mode, and has periodically entered production in a variety of applications since the mid-20th century.

While there are many pathways for further optimization of jet ignition engines, one underexplored pathway is that of charge motion. Charge motion is typically used in SI engines for the purpose of mixture preparation and is not commonly thought of as a significant participant in the combustion process. However, when applied to dilute combustion systems, literature has shown some impact on the combustion process.

The aim of the current work is to add to the current understanding of the jet ignition combustion process by detailing the effects that swirl, tumble, general TKE, and combinations thereof have on each stage of the jet ignition process: 1) mixture preparation in the pre-chamber, 2) combustion in the pre-chamber, and 3) main chamber combustion. Data of this nature is not currently in the public domain, and this research is intended to provide a detailed understanding by which charge motion can be optimized to increase the efficiency potential of jet ignition combustion systems.

Chapter 3

Experimental Methodology

3.1 Introduction

In order to fully understand the influence of charge motion on all aspects of engine operation, multiple research platforms were employed. While computational fluid dynamics (CFD) simulation described in Chapter 4 provided fundamental insight on in-pre-chamber processes that are typically shielded from direct experimental observation in metal engines, a multi-cylinder thermodynamic engine was needed in order to quantify the impact of charge motion on efficiency. Specifically, the multi-cylinder engine provided a true measure of burn duration, combustion stability, combustion efficiency and thermal efficiency in an environment closely representative of real-world vehicle operation. The engine results accounted for key performance influences such as heat loss, cyclic engine speed variation and cycle-to-cycle combustion variation that are typically not captured effectively in simulation or require a high degree of computational intensity to model. The engine was therefore used to measure engine combustion and efficiency response to varying levels and types of charge motion.

Set out in Section 3.2 are details of the engine hardware used, including descriptions of the pre-chamber and the intake port inserts used to generate the varying levels and types of charge motion. This section also includes quantification of the relative change in charge motion through the use of an industry standard static air flow rig. The static air flow rig provided an accurate comparative measure of tumble ratio and swirl number for the charge motion variants considered. While these measurements have some correlation with simulated results, the static air flow rig results are considered most accurate and consistent for comparative purposes. Described in Section 3.3 is an outline of the manner in which the testing was performed. Finally, Section 3.4 includes description of the performance metrics, both for the overall system and for the pre-chamber specifically, that are of most interest in assessing the impact of charge motion.

3.2 Experimental Setup

3.2.1 Engine Specification

The jet ignition engine used as the research platform in the currently reported study was a 1.5L in-line turbocharged 3-cylinder based on the 1.2 liter MAHLE DI3 Downsizing demonstrator whose development has been well documented [46]. The DI3 engine was originally presented in 2008 to demonstrate the potential fuel economy and efficiency benefits of engine downsizing. The engine was developed by MAHLE Powertrain using MAHLE components and was not based on any production engine designs. The DI3 achieved peak BMEP of 30 bar, representing an engine power of 120 kW/L. This engine is pictured in Fig. 3-1. Beginning in 2016, MAHLE Powertrain developed a 1.5L version of the DI3 engine, intended for commercial sale to vehicle manufacturers, with the major specification change being an elongated stroke. It is this version of the DI3 that formed the basis of the research platform used in this study.

Key Features
Integrated exhaust manifold
BMTS turbocharger with electronic waste gate
Central DI - 200 bar system
Variable valve timing with 60 CAD authority
Cooled EGR system
Split cooling circuits for head and block

Figure 3-1: 1.2L MAHLE DI3 engine.

The MJI technology had been developed in parallel to the DI3 engine development timeline. In 2016, the decision was made to incorporate MJI into the 1.5L DI3 engine. This MJI engine was intended to be a fully configurable research platform capable of experimental investigations and optimization activities that were inhibited by previous reliance on production engine base hardware for MJI engine demonstration. Furthermore, one of the main goals of this program was to create a prototype demonstrator that could inform the development of a dedicated MJI modular engine for use in series and parallel hybrid powertrains known as the MAHLE Modular Hybrid Powertrain. The development of this engine sought to leverage the results of the MJI DI3 engine variant in order to inform the design of a clean-sheet MJI engine optimized for high efficiency hybrid powertrain operation. The Modular Hybrid Powertrain was first presented in 2019 and is a candidate for commercial sale. Figure 3-2 depicts the parallel development of the DI3 engine and the MJI concept from 2006-2020. When these activities were joined, the results were two distinct research platforms: 1) the MJI DI3 research engine platform described in this study, and 2) the MAHLE Modular Hybrid Powertrain.

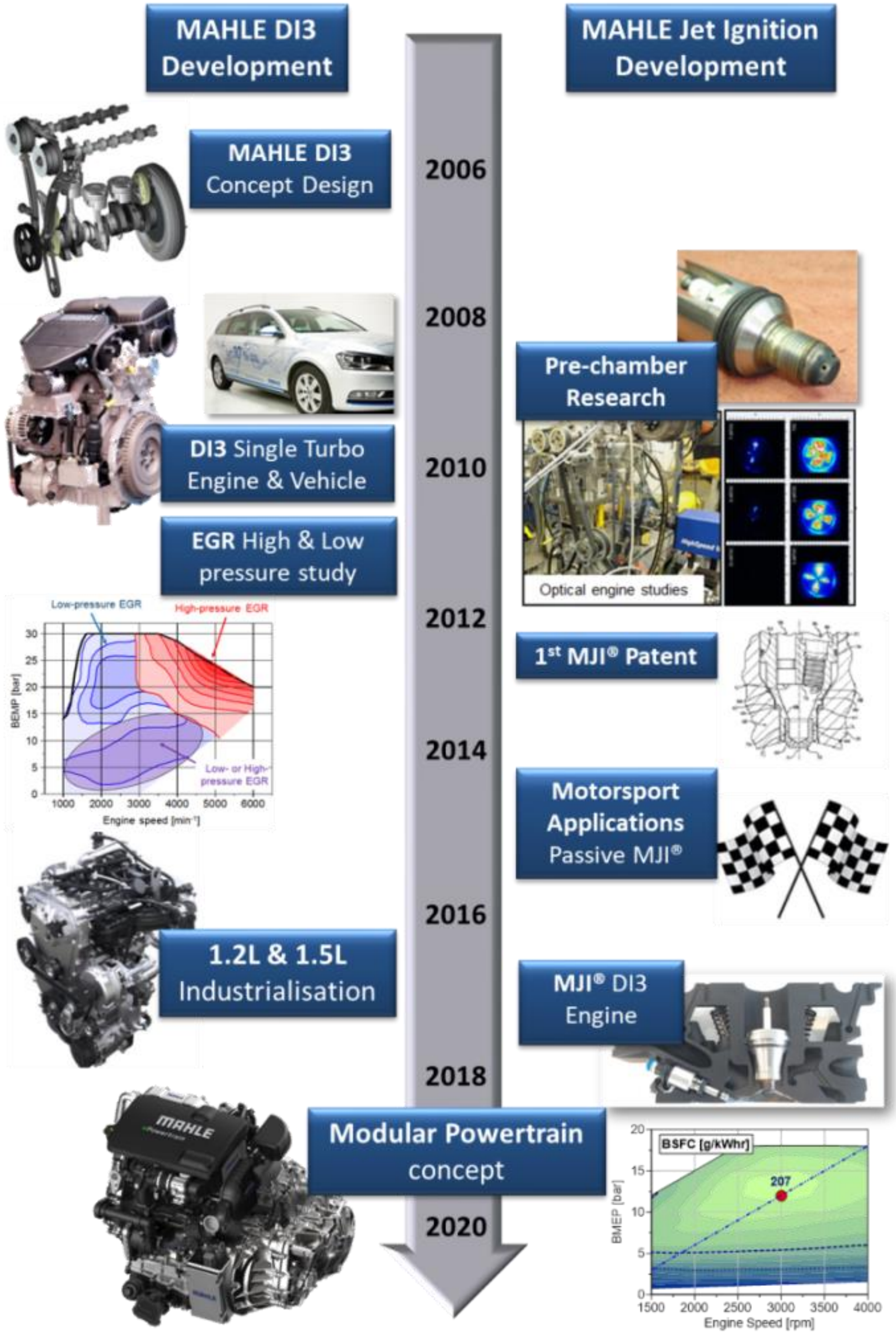

Figure 3-2: MAHLE DI3 and MJI development timelines.

The MJI DI3 engine was designed to be a configurable research platform. The engine can accommodate operation with a conventional spark plug, a passive pre-chamber, and an active pre-chamber. The engine has the ability operate with either side DI or PFI for main chamber fueling. The PFI configuration was used exclusively for this study. It also has the ability to operate in twin-spark mode, with an offset spark plug that can be used in parallel to either a centrally mounted spark plug or a pre-chamber. The engine uses standard cam timings.

MJI DI3 engine specifications are listed in Table 3-1. Renderings of the MJI DI3 engine are shown in Fig. 3-3. The properties of the pump grade gasoline fuel are shown in Table 3-2.

Table 3-1: MJI DI3 engine specifications.

Engine Configuration	In-line 3 cylinder
Displaced volume	1500 cm^3
Stroke	92.4 mm
Bore	83 mm
Compression Ratio	8.5:1-16:1; 14:1 and 15:1 used for the present study
Number of Valves per Cylinder	4
Fuel Injection Configuration	DI or PFI main chamber (PFI used exclusively in the present study), micro-flow DI prototype injectors for pre-chamber
Fuel Type	Pump Grade US Premium Gasoline (both chambers)
Fuel Injection Pressure	4 bar main chamber; 100 bar pre-chamber (BMEP > 2 bar), 30 bar pre-chamber (BMEP ≤ 2 bar)
Valvetrain Configuration	Variable phasing on intake and exhaust valves, 60 cam-degree phasing authority
Cam timing (Phasing authority: 60 cam-degrees)	40 cam-degrees advanced intake cam, 20 cam-degrees exhaust cam used for all test points in the present study
Number of Pre-Chamber Nozzle Orifices; Diameter	6 orifices; 1.2 mm diameter
Pre-Chamber Volume	1.0 cm^3
Piston Geometry	Flat-top with valve cutouts
Cylinder Head Geometry	Pent-roof with centrally mounted pre-chamber
Boost System	Variable-geometry turbocharger
Control System	MAHLE Flexible ECU (MFE)

Table 3-2: Gasoline fuel properties.

RON	97
MON	87
AKI	92
Sensitivity	10
Density @ 15˚C (kg/m3)	740
LHV, MJ/kg	42.6
Ethanol, Vol%	10

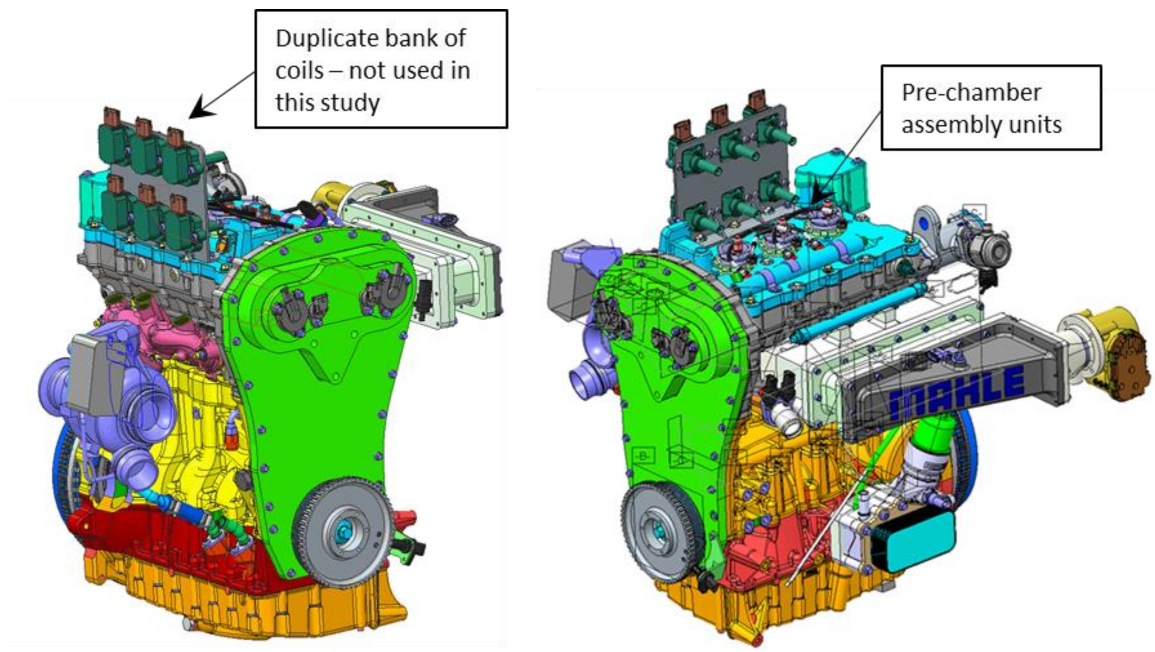

Figure 3-3: 1.5L MJI DI3 engine computer aided design (CAD model) renderings.

The engine incorporated an identical pre-chamber assembly into each cylinder, described in greater detail in the subsequent section. Both main chamber PFI and pre-chamber auxiliary DI fuel pressure were provided externally in the test cell and were nominally set to 4 bar and 100 bar, respectively. At BMEP values below 2 bar, pre-chamber fuel pressure was lowered to 30 bar in order to lower the minimum permissible auxiliary fuel injection quantity. This lower fuel quantity range accounted for the reduced charge density at the low load conditions.

The friction penalty for operating a fuel pump to feed the high pressure pre-chamber DI is small due to the low fuel flow rate used by the pre-chamber. Fluid power calculations were used to determine the fuel penalty associated with compressing the pre-chamber fuel to levels required for the engine. The power required to compress the fuel to the working pressure was calculated using the isentropic compression equation,

$$\dot{W} = \frac{\dot{m} \cdot c_p \cdot T_1}{3600 \cdot \eta_c}\left[\left(\frac{p_2}{p_1}\right)^{\frac{\gamma-1}{\gamma}} - 1\right] \qquad 3\text{-}1$$

where $\dot{m}$ is the fuel mass flow rate, c_p is the specific heat, T_1 is the temperature, η_c is the compressor efficiency, p_1 and p_2 are the pressures in and out of the compressor, respectively, and γ is the ratio of specific heats. For these calculations, a conservative compressor efficiency of 60% and a fuel pressure of 100 bar were assumed. The resulting impact on the brake efficiency values presented here would be less than 0.1%. This friction penalty was disregarded for the purposes of this study. In a production application, a combined high pressure and low pressure fuel stream pump, as used in applications that have both PFI and DI injectors, would be used to supply fuel to the two injectors at de-coupled pressures. These pumps are commercially available for passenger car engines that alternate DI and PFI injection for cold start and emissions purposes, however they are not optimized for the imbalance in fuel injection quantity inherent to active pre-chambers. Therefore, for this study pre-chamber fuel was pressurized using an external floating piston pressure vessel. The optimal injection pressure for the pre-chamber fuel injector was determined in a previous study.

Engines operating lean by definition require an excess of air for a given quantity of fuel. For lean boosted applications such as the one considered in this study, this puts a particular strain on the engine boosting system. Not only is greater than normal air quantity required to maintain the desired λ, but the lower combustion temperatures that result from high efficiency lean operation produce lower exhaust temperatures as well. Figure 3-4 shows a 35% reduction in exhaust temperature at constant load from λ = 1 to λ =2 at a part load condition. Despite the increased exhaust flow rate produced by the higher intake air flow requirement, the reduction in exhaust temperature compromises the exhaust enthalpy available for the turbine. After an evaluation of a variety of boost system configurations [146], a variable geometry turbocharger (VGT) was identified as providing sufficient intake air pressure for the engine map. The VGT used in this study was a commercially available unit, and it provided a significant cost advantage over electrically assisted boosting systems. The VGT turbocharger is shown in Fig. 3-5.

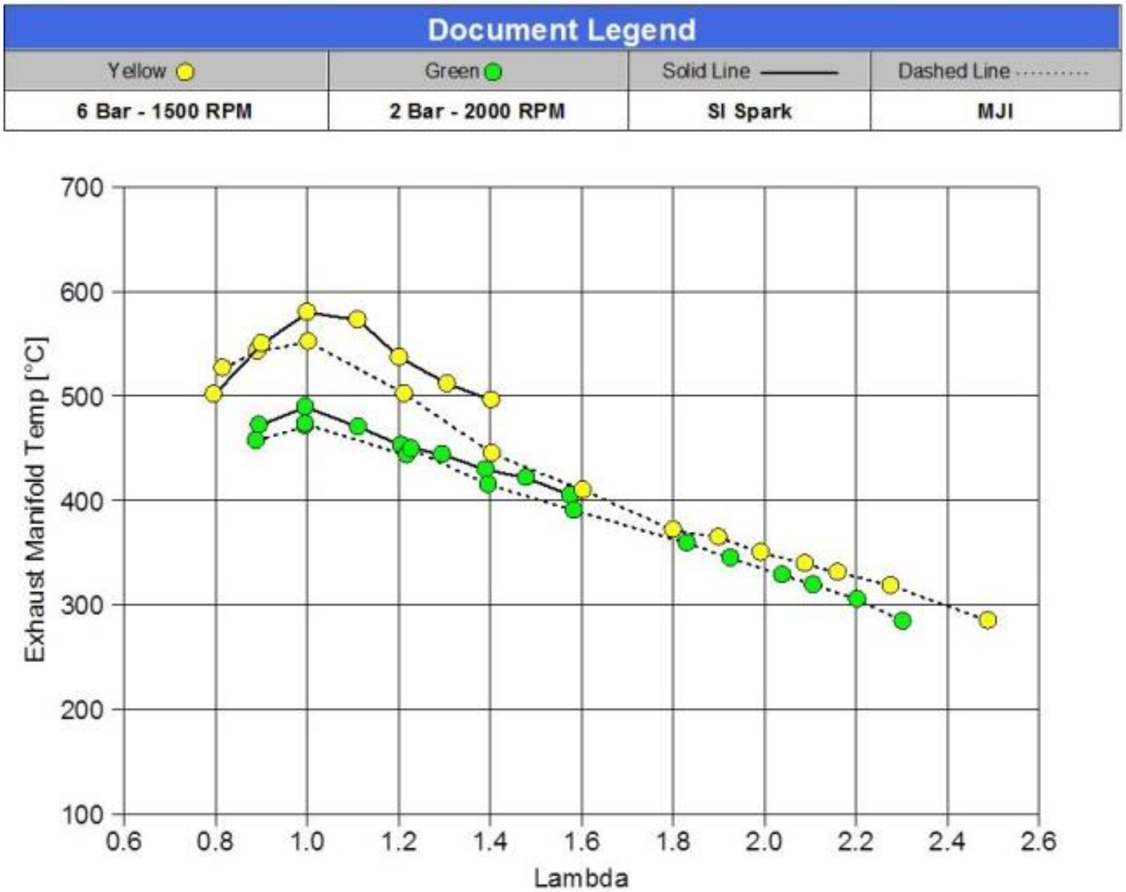

Figure 3-4: Exhaust temperature trends with enleanment, CR14, load in BMEP.

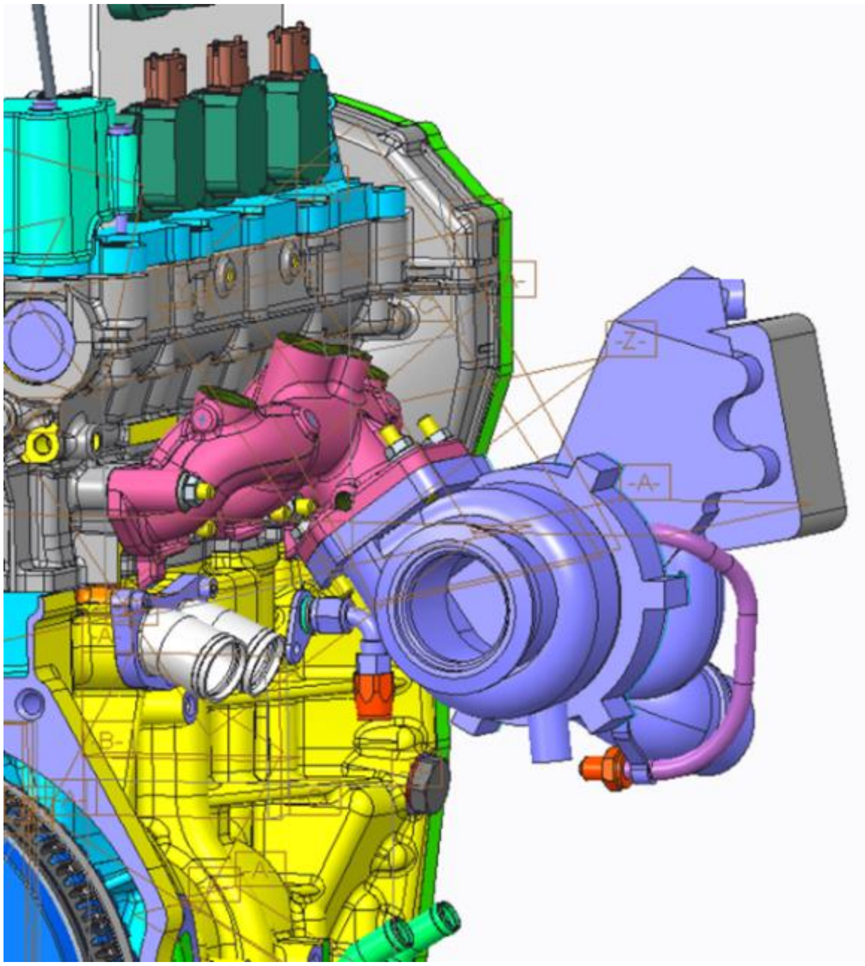

Figure 3-5: CAD model rendering of VGT turbocharger installed on MJI DI3 engine.

Multiple pistons were designed to accommodate a wide range of CRs from 8.5:1 to 16:1. The piston crown design was a flat top design with cutouts to accommodate the valves and a center volume that was manipulated to form a shallow bowl or pop-up for each of the pistons to accommodate the desired CR. This was done for the purpose of consistency and to reduce the effect that differences in piston crown design might have on in-cylinder charge motion, combustion, and heat losses. The CRs used in this study are 14:1 and 15:1, displayed in Fig. 3-6. The 14:1 CR has been previously established as an appropriate CR for the “majority lean” MJI strategy whereby the engine is operated with high levels of dilution throughout the full engine map, ultimately achieving an airflow limited full load equivalent to that of a comparable naturally aspirated engine, approximately 13-18 bar BMEP. The 15:1 CR was used for certain tests in this study in order to ensure that the engine would achieve knocking conditions under lean operation. Because lean operation is an effective tool for mitigating knock, even an exceptionally high SI engine CR of 14:1 does not necessarily ensure that knocking occurs under high load lean conditions in this engine. Rather, the engine more typically achieves a mechanical limit such as peak cylinder pressure (Pmax) or maximum rate of cylinder pressure rise (Rmax) than a knock limit. The Pmax limit for the engine was a peak average of 120 bar, and Rmax limit was a peak of 6 bar/degree crank. One of the purposes of this study was to contrast engine performance sensitivity to charge motion under non-knock-limited conditions with performance sensitivity under knock-limited conditions. Therefore, the higher CR of 15:1 was used for the knock-centric testing. Both sets of pistons utilized identical top-land height and ring pack, which allowed crevice volumes to be maintained.

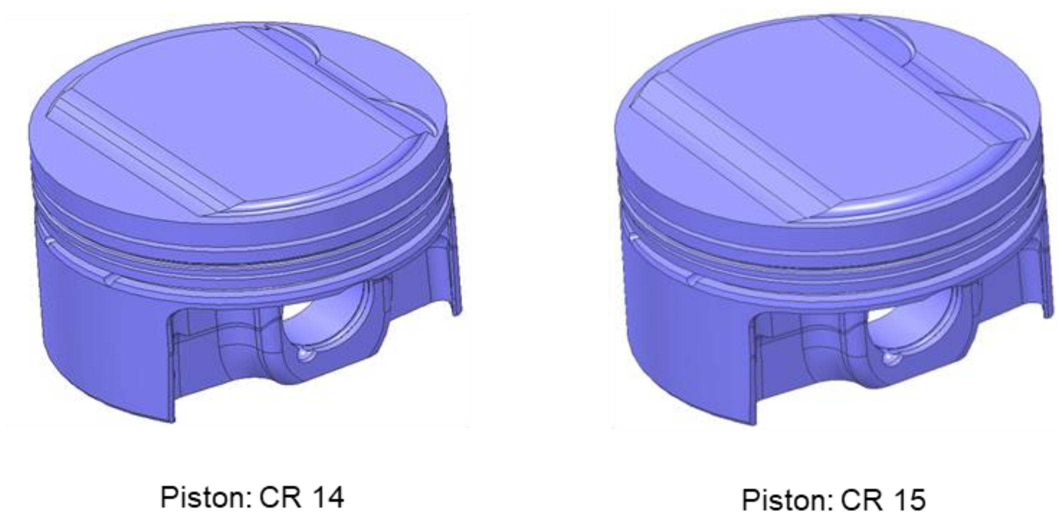

Figure 3-6: CAD model rendering of 14:1 CR piston (left) and 15:1 CR piston (right).

Engine speed was controlled by a motoring dynamometer. AVL Indicom data acquisition software was used to monitor engine measurements in real time, record data, and control the engine dynamometer. The engine itself was controlled using MAHLE's Flexible Engine control unit (ECU), known as MFE. MFE is a fully flexible ECU solution with controls strategy and software developed by MAHLE Powertrain, providing full control over all calibratable parameters (Fig. 3-7). The MFE communicated with a Delphi IDM4 injector driver box, which was used to control the pre-chamber fuel injectors.

The pre-chamber fuel injection event was controlled manually. The relevant calibratable parameters are end of injection angle (EOI) and injection pulsewidth. Pulsewidth-fuel quantity relationships were determined by static characterization curves provided by Delphi, and confirmed using a dedicated fuel flow meter, described below.

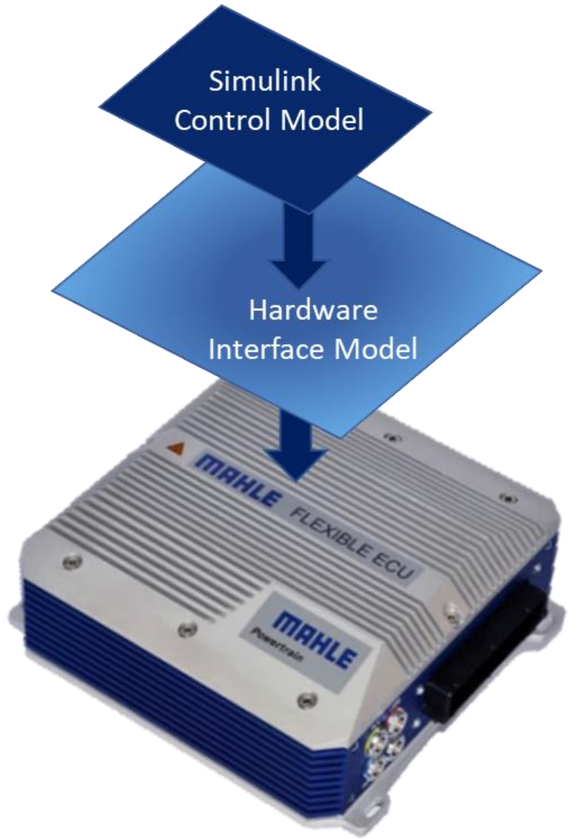

Figure 3-7: MAHLE Flexible ECU (MFE).

At each operating condition, the MFE varied throttle position and main chamber fuel quantity to achieve a commanded BMEP at the commanded overall λ in a closed loop mode. Commanded λ was controlled via a wide-band oxygen (O_2) sensor located in the exhaust manifold. This sensor reading was verified with calculated λ from measured exhaust emissions and from air flow and fuel flow measurements. Exhaust emissions were measured using an AVL AMA i60 emissions bench that contained CO_2, CO, total hydrocarbons (THC), methane (CH_4), O_2, and NO_x analyzers. As the engine was enleaned beyond λ=1.4, the limit of non-auxiliary fueled ignitability, auxiliary fuel was introduced and the pulsewidth of the pre-chamber DI was gradually increased to maintain the coefficient of variation (COV) of IMEPg less than 3%. The lean limit or other ignitability limit was considered achieved once COV achieved 3%. Main chamber and pre-chamber fuel flow rates were measured using a MicroMotion Coriolis flow meter and Bronkhorst M13 Coriolis flow meter, respectively. Unless otherwise stated all efficiency and fuel consumption metrics were calculated using total fuel flow to both chambers. Table 3-3 lists the specifications of the instrumentation used for testing. All specifications in this table are manufacturer specifications, with the exception of the high speed pressure transducer full scale error values, which were provided as an output of third party calibration of these instruments immediately preceding the testing performed in this study.

Table 3-3: Specifications of key instrumentation.

Instrument	Notes	Full Scale	Full Scale Error	Use
			%	
Thermocouple	K-type used exclusively	1370˚C	+/- 0.75	Multiple in intake, exhaust, oil loop, coolant
Low speed pressure transducer		Various	+/- 0.25	Multiple in intake, exhaust, oil loop, coolant
Fuel flowmeter	Bronkhorst M13 Micro-Coriolis	600 g/h	+/- 0.2	Pre-chamber fuel flowrate
Fuel flowmeter	MicroMotion Coriolis	125 kg/h	+/- 0.1	Main chamber fuel flowrate
Air flowmeter	Flowsonix	500 kg/hr	+/- 2	Engine air flow
Toque meter	HBM	500 N-m	+/- 0.5	Engine brake torque
High speed pressure transducer	AVL GH14 - 1 for each cylinder	150 bar	+/- 0.1	Crank angle-resolved pre-chamber pressure
High speed pressure transducer	Kistler 6041 - 1 for each cylinder	200 bar	+/- 0.2	Crank angle-resolved main chamber pressure
High speed pressure transducer	Kistler 6041 - located in cylinder #1 port	200 bar	+/- 0.2	Crank angle-resolved intake port pressure

An intercooler was used to control intake air temperature downstream of the compressor. This intercooler held intake air temperature to a maximum of 40˚C for non-boosted conditions. Under boosted operation, the intercooler held intake air temperature to a maximum of 60˚C. The latter figure represents a maximum intercooler-out temperature that a production engine would likely experience.

Figure 3-8 shows the engine installed in the test cell at MAHLE Powertrain's test facility in Plymouth, Michigan. Figure 3-9 depicts a schematic of the engine as installed in the test cell.

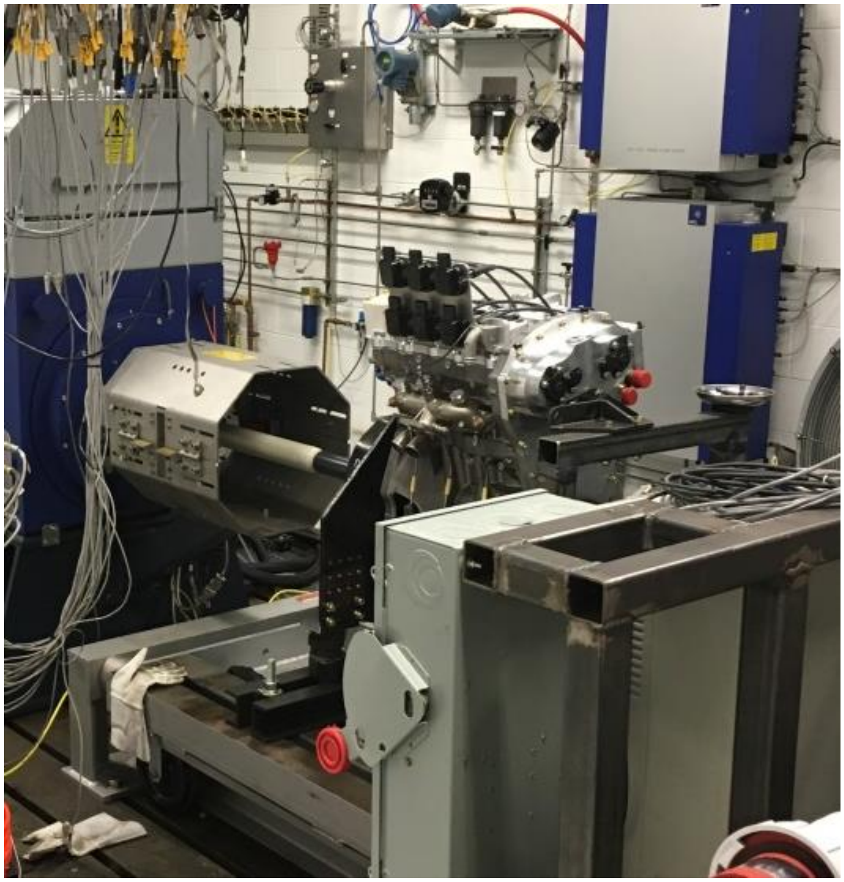

Figure 3-8: MJI DI3 engine installed in the test cell at MAHLE Powertrain's test facility in Plymouth, Michigan.

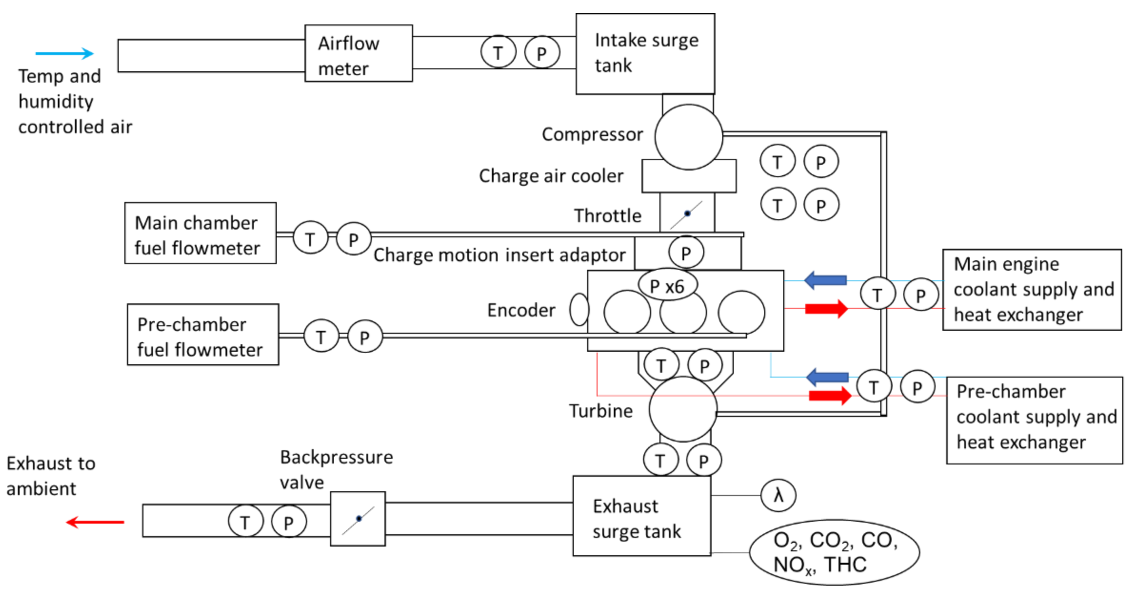

Figure 3-9: Schematic of the MJI DI3 engine as installed in the test cell.

Low speed data was recorded and averaged over a 30 second interval. This data included temperature, pressure, and flowrate information from added instrumentation, all sensor outputs, test cell conditions, exhaust emissions, and ECU commands and feedback. Three of these 30 second intervals were recorded and averaged consecutively, and the three averages were averaged to constitute a final result. These three averages were evaluated internally for consistency. High speed pressure data (main chamber – Kistler 6041, pre-chamber – AVL GH14) was acquired from each of the three main chambers and pre-chambers, and the intake port of one cylinder, with the log beginning simultaneous to the start of the low speed data log. High speed data was acquired for 300 consecutive cycles and then averaged. Figure 3-10 depicts the location of the main chamber high speed pressure transducer. The transducer was flush-mounted against the combustion chamber roof.

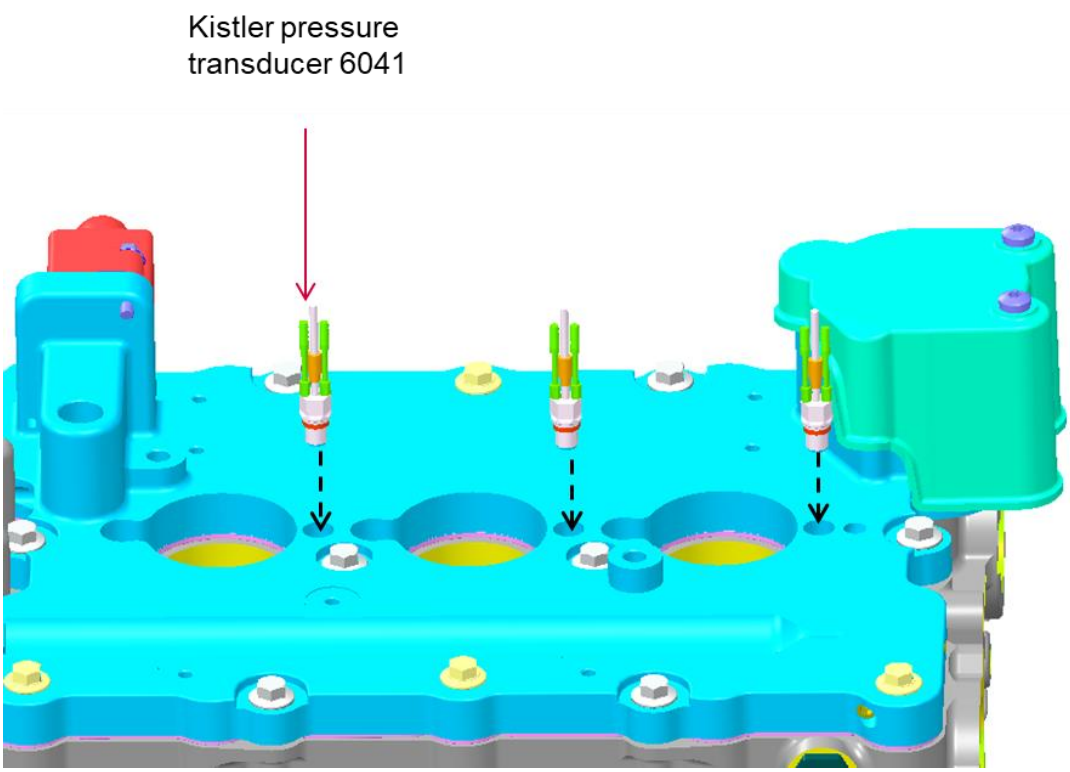

Figure 3-10: CAD model rendering of main chamber high speed pressure transducer placement relative to the pre-chamber cavity.

3.2.2 Pre-Chamber Specification

MJI applications retro-fitted in production engine cylinder heads must adhere to strict packaging constraints. For the MJI DI3 engine, however, more packaging freedom was afforded due to the ability to redesign the cylinder head to suit the assembly footprint. Therefore, the emphasis in the pre-chamber assembly design was on functionality and ease of access rather than adhering to a specific packaging constraint. The hardware considered for this study qualifies as prototype-level and would need to undergo significant modifications in a production scenario, while maintaining or improving upon the performance presented in this study. Figure 3-11 shows the cavities for the pre-chamber assemblies in the cylinder head.

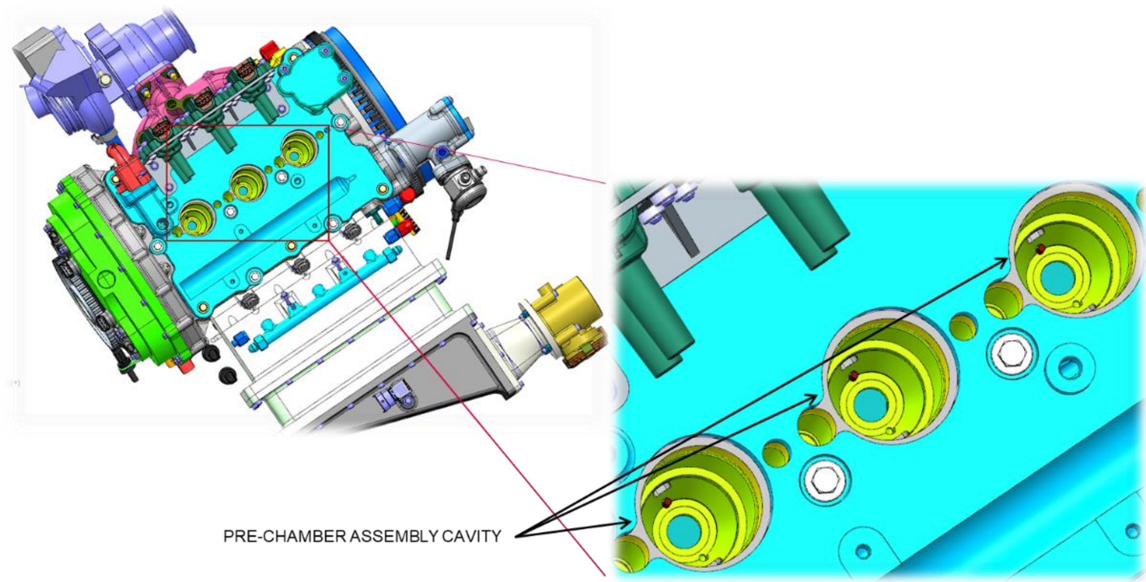

Figure 3-11: Pre-chamber assembly cavities in cylinder head.

The active pre-chamber assembly housed a fuel injector, spark plug, and high-speed pressure transducer. The pre-chamber body and nozzle were separate pieces to allow for the use of interchangeable hardware. Both components were made from stainless steel in order to withstand the high temperatures of the pre-chamber combustion event and to inhibit corrosion from the adjacent water jacket. The parent material of the cylinder head was aluminum. Some assembly features were designed to accommodate the differing rates of thermal expansion between the pre-chamber assembly components and the cylinder head. A rigid spring, also made of stainless steel, sat atop the pre-chamber body to prevent deformation under high temperature and high cylinder pressure conditions. Likewise, a clamp mounted above the fuel injector contained Belville washers to prevent deformation of the injector under high in-pre-chamber pressure conditions. A threaded collar shouldered on the rigid spring and was torqued to seal the full assembly in the cylinder head. Fuel connections, the braided steel pressure transducer cable, and a rubber coil extender are routed through the collar to join connections mounted on the cam cover. Because the pressure transducer cannot be flush-mounted in the pre-chamber, a small channel was added that broke into the pre-chamber volume and then terminated at the pressure transducer face, constituting approximately 10% of the total pre-chamber volume. Because of this small volume channel, some ringing was apparent on the pre-chamber pressure trace and was filtered during processing. The pre-chamber pressure transducer was used for research purposes only and is not intended as a production feature.

One non-production-intent solution implemented in this engine was a dedicated coolant jacket line that serves only the pre-chambers, with inlets and outlets on top of the cylinder head that connected to an external coolant rig. The coolant jackets encompassed the bodies of the pre-chambers to reduce the thermal loading of the in-pre-chamber components. By putting these coolant jackets on a dedicated external circuit, the coolant in the circuit was quickly and easily drained prior to removal of the pre-chamber assemblies. This procedure ensured that no coolant would leak into the cylinders upon removal of the pre-chambers. It also allowed for direct control over pre-chamber coolant flowrate and inlet temperature for parametric studies. In the present study, coolant inlet temperature was matched to the inlet temperature of the coolant in the cylinder head, in anticipation of a production-intent common coolant circuit. The external rig used for coolant control was an AVL water-cooled pressure transducer rig.

Typical connections from the ignition coil to the spark plug are of inadequate length, so a coil extender was used. This extender consisted of a rubber insulated electrical lead connected to a rubber boot. The lead snaked through the pre-chamber assembly with the boot fitting over the back of the spark plug. An M8 size spark plug was used in the pre-chamber. While not ideal, and likely not a production solution given its small size, this spark plug was employed due to its limited space claim and ability to minimize overall pre-chamber assembly package size.

Figure 3-12 provides a cutaway view of the assembly mounted in the cylinder head. Figure 3-13 shows the full active pre-chamber assembly. Figure 3-14 shows the high speed pressure transducer and coil extender installation in the pre-chamber.

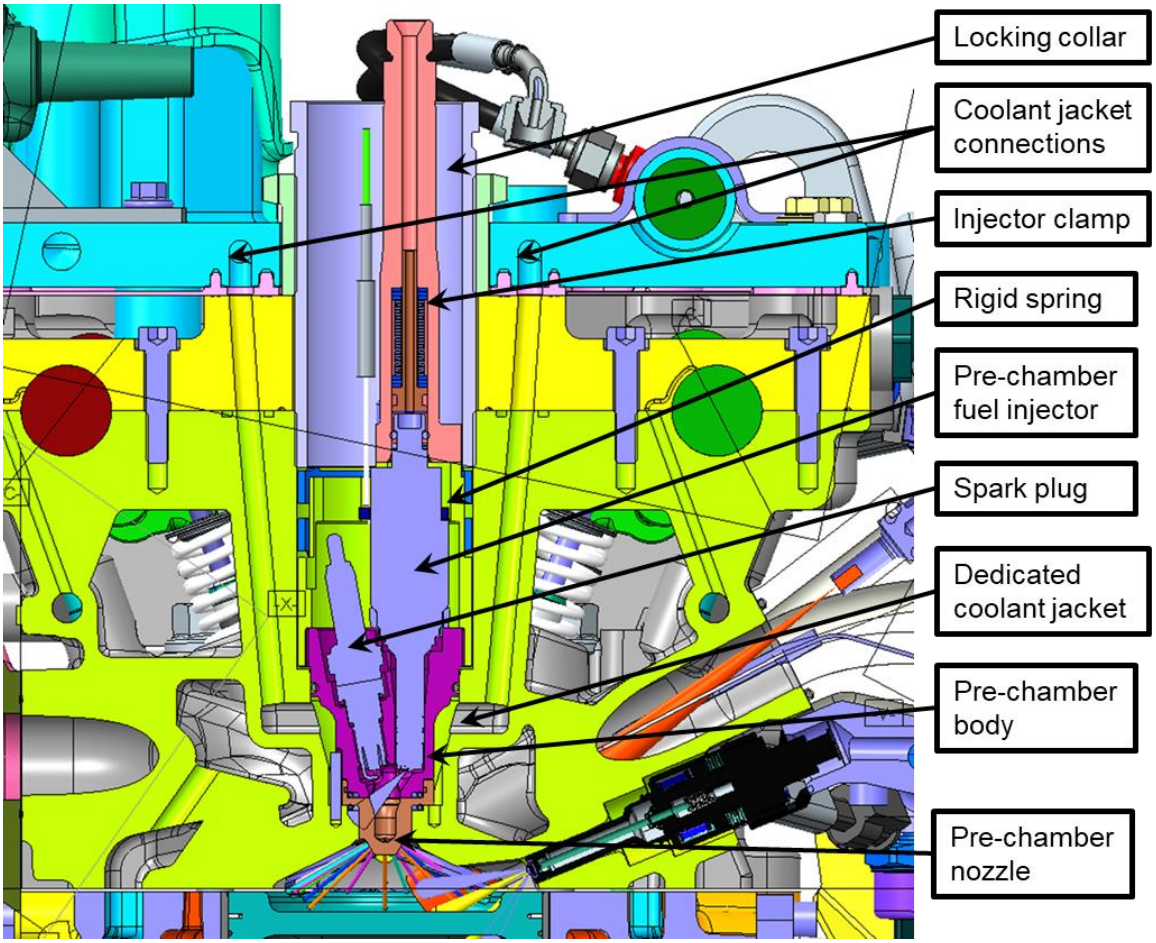

Figure 3-12: Annotated CAD model cutaway image of the active pre-chamber assembly.

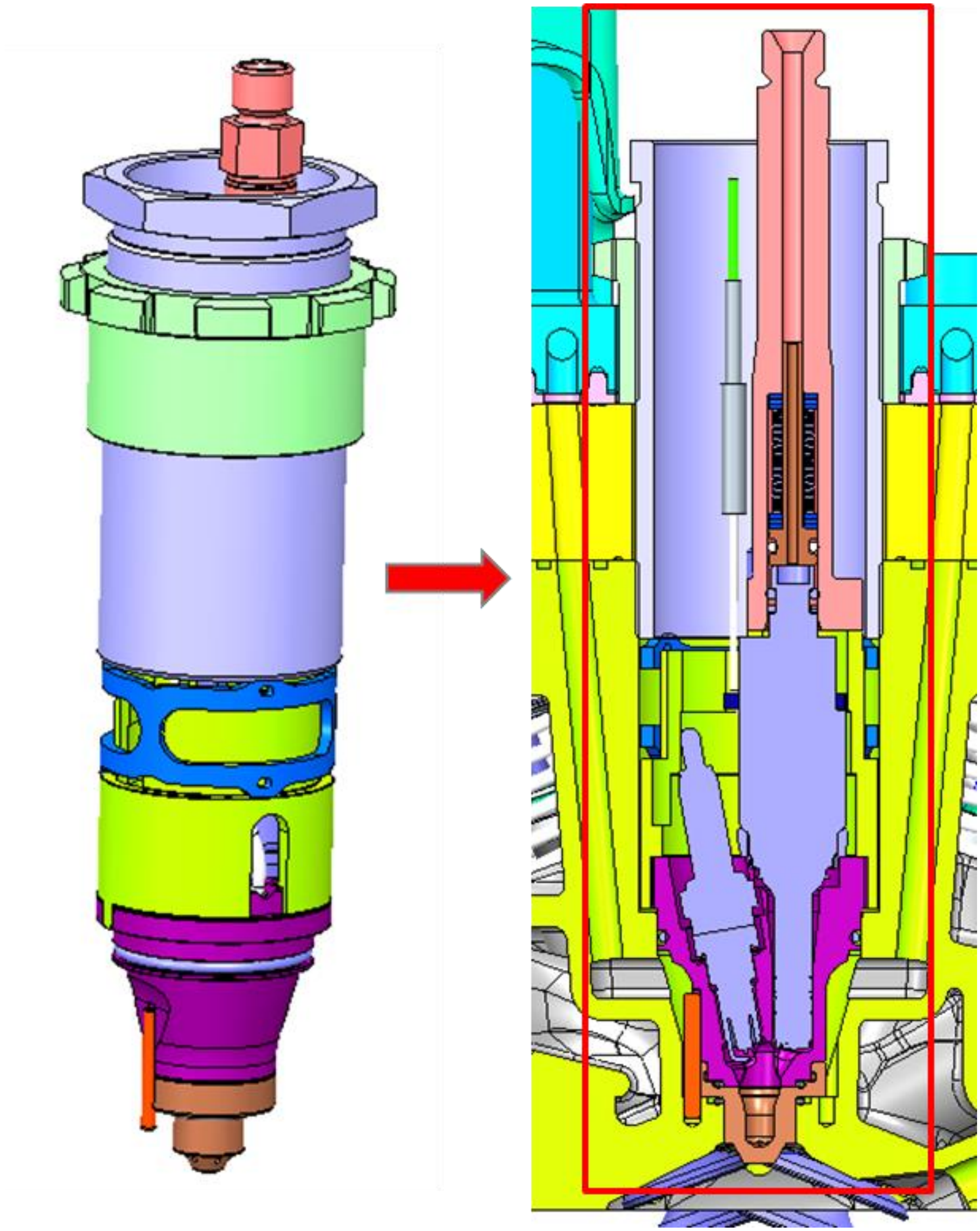

Figure 3-13: CAD model image of the full active pre-chamber.

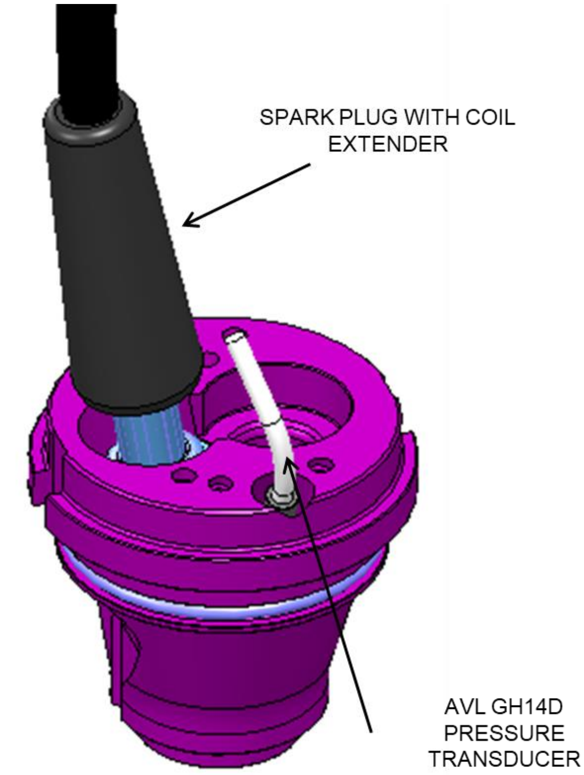

Figure 3-14: CAD model image of the in-pre-chamber pressure transducer and coil extender installation.

The pre-chamber constantly experiences a combustion event that occurs with a near-stoichiometric mixture to ensure optimal operation. The pre-chamber body itself therefore remains relatively hot even when the main chamber combustion temperatures reduce under lean conditions. Additionally, the pre-chamber nozzle experiences high temperature gas flow during the jetting process. Therefore, it is critical to maintain physical connection between elements of the pre-chamber and nozzle and the cylinder head. Figure 3-15 shows a thermal analysis that contrasts the average temperature profile throughout the valve bridges and combustion chamber roof with and without the pre-chamber nozzle present. With the nozzle present, and using a clearance fit between nozzle and cylinder head, there is inadequate transfer of heat from the pre-chamber and nozzle to cylinder head. This results in excessive heat concentrated in the nozzle, increasing the likelihood of pre-ignition should pre-mixed fuel come in contact with it during the compression stroke. However, with a slight interference fit (Fig. 3-16), there is much greater heat dissipation from the pre-chamber and nozzle to the cylinder head. Note the difference in scales between Figs. 3-15 and 3-16. The slight interference fit was therefore used for the assembly in this engine. Multiple removals and installations of the assembly over the course of this project caused the contact surfaces to wear, therefore a nickel-impregnated anti-seize was used to coat the contact surfaces during each installation. The nozzle was fabricated using stainless steel. Other materials, including those both more and less thermally conductive than steel, have been investigated internally for use in specialized applications.

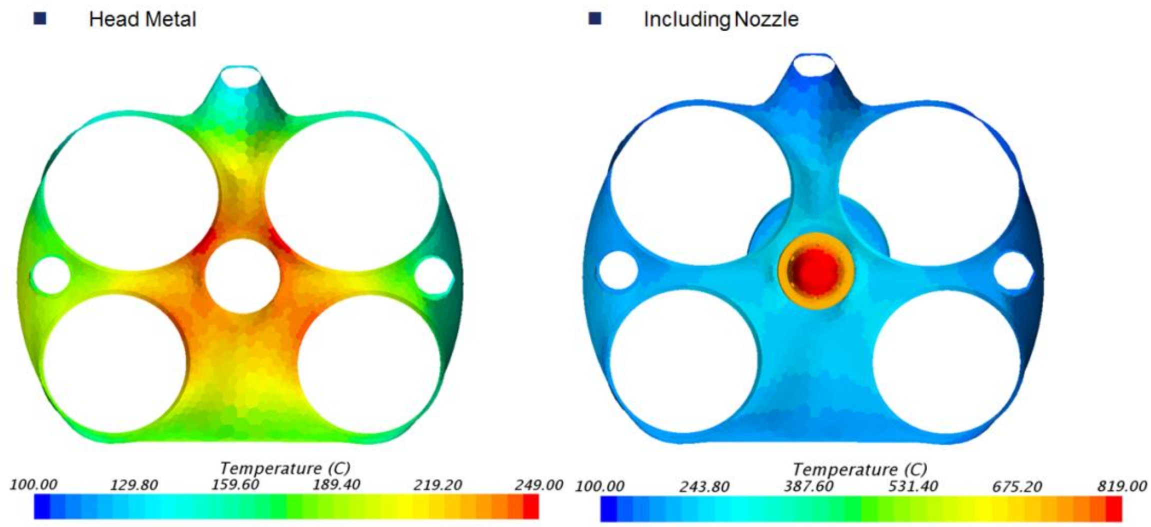

Figure 3-15: Thermal analysis of clearance fit pre-chamber nozzle under full load conditions.

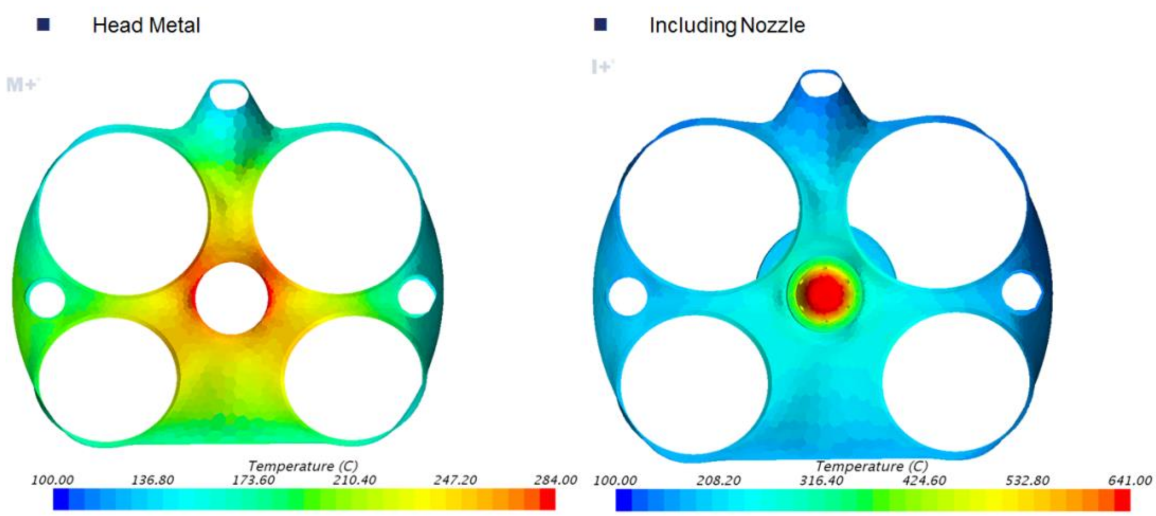

Figure 3-16: Thermal analysis of interference fit pre-chamber nozzle under full load conditions.

Pre-chamber and nozzle geometric specifications were determined using patented relationships [17,24] developed as part of previous projects [1,2,18]. For this study, a single set of pre-chamber hardware was used in order to ensure consistency of the performance comparisons. The pre-chamber volume chosen was 1cc. This volume was determined using the pre-chamber sizing rule-of-thumb that pre-chamber volume should be between 1% and 5% of the engine clearance volume [109]. The lower bound on the volume range is approximately the minimum volume that can be maintained without overly quenching the spark event through excessive heat loss through the pre-chamber walls. The upper bound on the volume range is approximately the maximum volume that can be maintained without the pre-chamber combustion process consuming so much system fuel that torque and thermal efficiency are compromised. The engine used in these experiments used two CRs (14:1 and 15:1) throughout the testing, thereby producing two distinct clearance volumes (Table 3-4). The target pre-chamber volume range was determined for both engine configurations. The minimum and maximum pre-chamber volumes therefore were the interior values in this range. The selected 1cc volume is the median. This pre-chamber volume has also been thoroughly established as optimal for this particular engine through previous research.

Table 3-4: Pre-chamber volume specification.

Engine	Displacement	1.5	1.5	L
	Cylinders	3	3	
	Displ/Cyl	0.5	0.5	L/cyl
	Bore/Stroke	0.9	0.9	
	Stroke	92.4	92.4	mm
	Bore	83	83	mm
	CR	14	15	
	Swept Vol	499940.2	499940.2	mm3
	Swept Vol	499.9402	499.9402	cc
	Clearance Vol	35.71001	33.32934	cc
Pre-Chamber	P/C Vol 5%	1.785501	1.666467	cc
	P/C Vol 1%	0.3571	0.333293	cc

The selected pre-chamber employed a y-shaped layout with the spark plug and fuel injector mounted parallel to each other. This layout removed the spark plug from the high velocity pre-chamber inlet charge column. This charge column, formed by charge from the main chamber entering the pre-chamber, prioritizes transportation of the lean main chamber contents to the spark plug, especially after the pre-chamber injection event has ended and there is no fuel plume perpendicular to and spanning the column. The velocity of the column itself can impede spark kernel formation. This is compounded by the lean charge it carries. Figure 3-17 illustrates the impact of the charge column on pre-chamber mixing dynamics in a central spark plug configuration and the y-shape configuration.

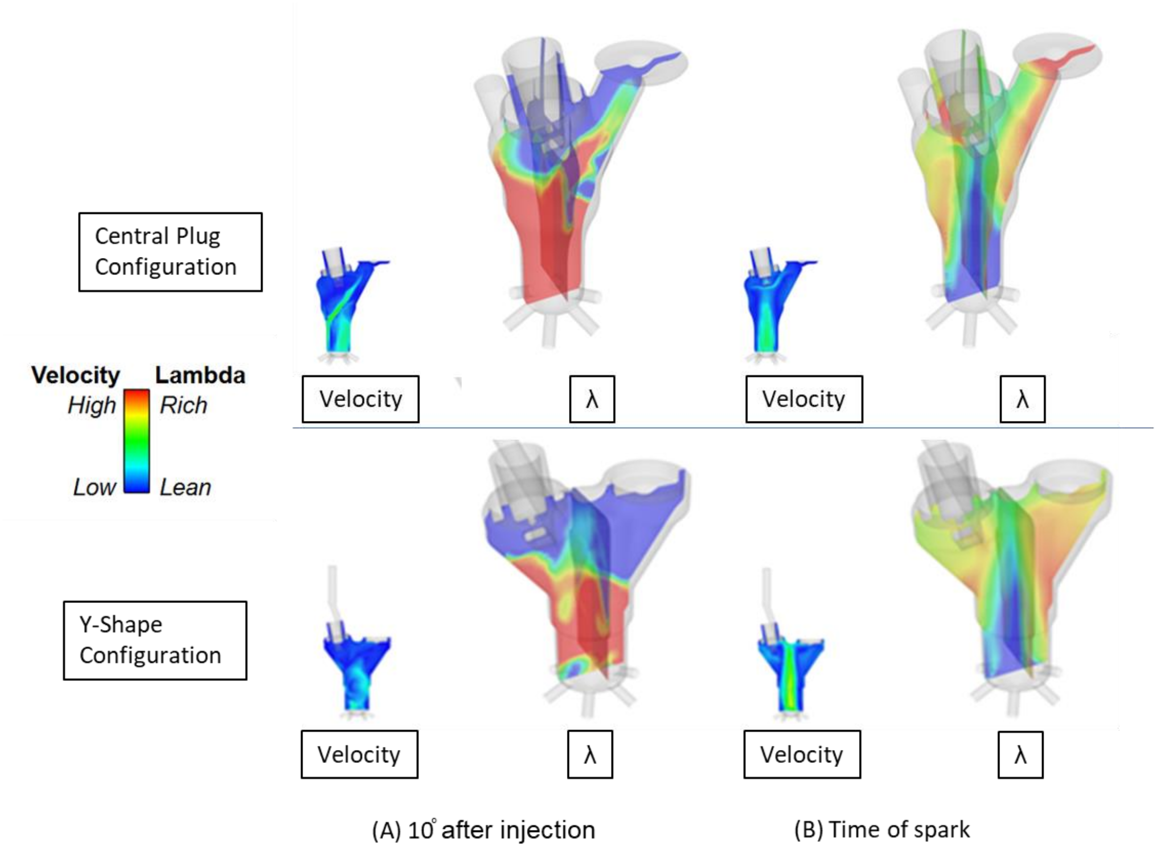

Figure 3-17: Qualitative comparison of velocity and λ distribution in the Central Plug and Y-Shape pre-chamber configurations a) 10 CAD after the conclusion of the pre-chamber injection event and b) at time of spark, taken from CFD simulation.

The 6-hole nozzle was indexed to the pre-chamber body through the use of a connecting peg, and the pre-chamber body was indexed to the combustion chamber using a locking mechanism built into the assembly collar. Figure 3-18 shows one these indexing features. Ensuring consistent indexing of all the various subsystem components to each other ensures that the spark plug and fuel injector placement maintain a constant spatial relationship with the nozzle orifices, and that the orifices produce jets that oriented to the main chamber in a consistent way across all tests. Any differences in the transfer of charge motion from the main chamber to the pre-chamber are a product of the motion type itself, and are not due to any positional differences related to the pre-chamber nozzle indexing to the cylinder head. Previous work has shown minimal impact on main chamber combustion performance to small changes in pre-chamber nozzle indexing under lean auxiliary-fueled conditions, but this work did not involve testing focused on charge motion influence on in-pre-chamber processes.

Figure 3-18: Indexing feature between pre-chamber body and collar.

The nozzle was indexed to the cylinder head through the use of a dowel feature, visible in Fig. 3-19. The nozzle was sealed against the head using a copper crush gasket which partially crushed as the assembly clamp is torqued. The crush gasket sealed potential intrusion of combustion gases past the interference fit of the nozzle in the cylinder head from the coolant jacket around the pre-chamber body. Evidence of leakage past this gasket would manifest as gas bubbles in the pre-chamber coolant line exiting the cylinder head. No gas bubbles were observed in this study.

A second crush gasket was used to seal the nozzle to the pre-chamber body (Fig. 3-20). This gasket prevented coolant from entering into the pre-chamber volume and from pre-chamber combustion gases entering the water jacket. No coolant leakage was observed interior to the pre-chamber in this study. The crush gaskets were replaced after each de-installation.

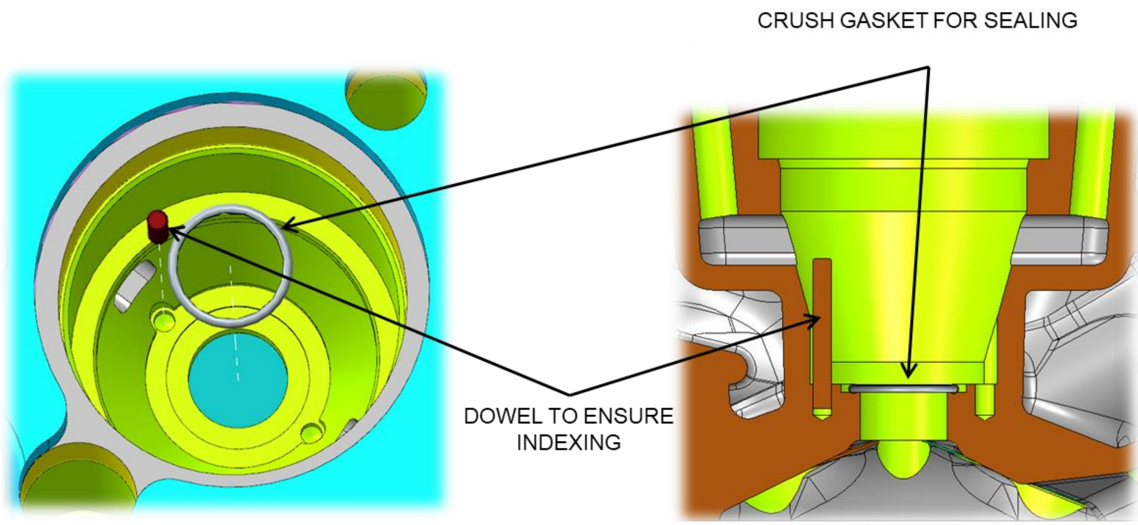

Figure 3-19: Indexing dowel feature and pre-chamber-to-cylinder head crush gasket seal.

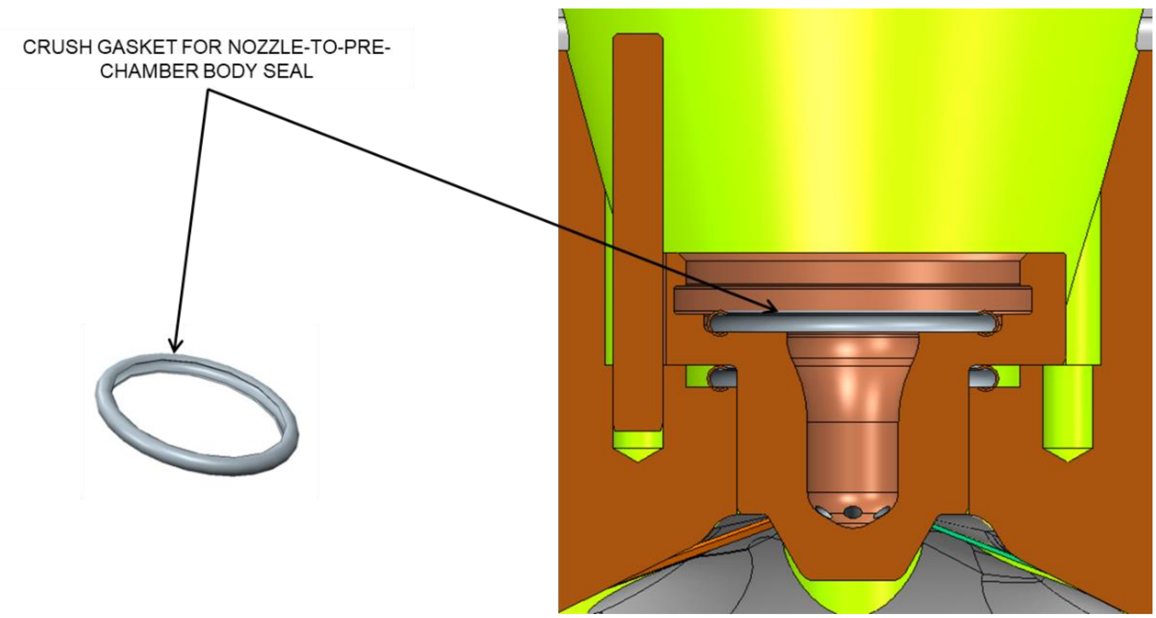

Figure 3-20: Pre-chamber-to-nozzle crush gasket seal.

The pre-chamber fuel injector is a third generation prototype micro-flow solenoid direct injector co-developed by MAHLE Powertrain and Delphi and supplied by Delphi. The decision was made to pursue a solenoid injector rather than piezo in order to minimize the cost delta between a baseline engine and an active pre-chamber engine. The injector nozzle provides spray targeting that is conducive to rapid vaporization and low risk of injector plugging. The injector achieves low flowrates due to modifications to the injector seat and pintle area. At 100 bar injection pressure, typical pulse width values used are below 1 ms but, unlike in traditional solenoid fuel injectors, these values are in the non-ballistic linear range of the injector. The ballistic range occurs at pulse widths below 0.3 ms, which are avoided in order to ensure consistent fuel injection and minimize shot-to-shot variation in injection quantity.

Pre-chamber injection timing was relatively late in the compression stroke, typically ending at approximately 40 degrees before TDC (dBTDC), or a maximum of 10 degrees before the most advanced spark timings used. This late injection timing prevents fuel from escaping into the main chamber prior to spark timing, helping to ensure consistent pre-chamber fuel quantity at spark timing across all cylinders. The late injection timing also prevents the over-mixing effect described in Chapter 2.

Appropriate pre-chamber fuel injected quantity was determined as a percentage of total system fuel quantity, and was generally held to a value of 5% of less. Fuel quantities higher than this percentage produced noticeable increases in pre-chamber burn duration and subsequent main chamber burn duration, and a corresponding drop in engine performance.

To perform comparative studies against an engine baseline, a spark plug insert was designed to fit within the pre-chamber assembly cavity and provide central spark plug operation. In this case, an insert containing threads to hold a spark plug was inserted in the pre-chamber assembly cavity and mounted using the same assembly clamp used for the pre-chamber. The spark plug used in the spark plug insert was an M10 size. Figure 3-21 shows the spark plug insert mounted in the engine. Figure 3-22 shows the view of the spark plug insert installation from the top of the cam cover.

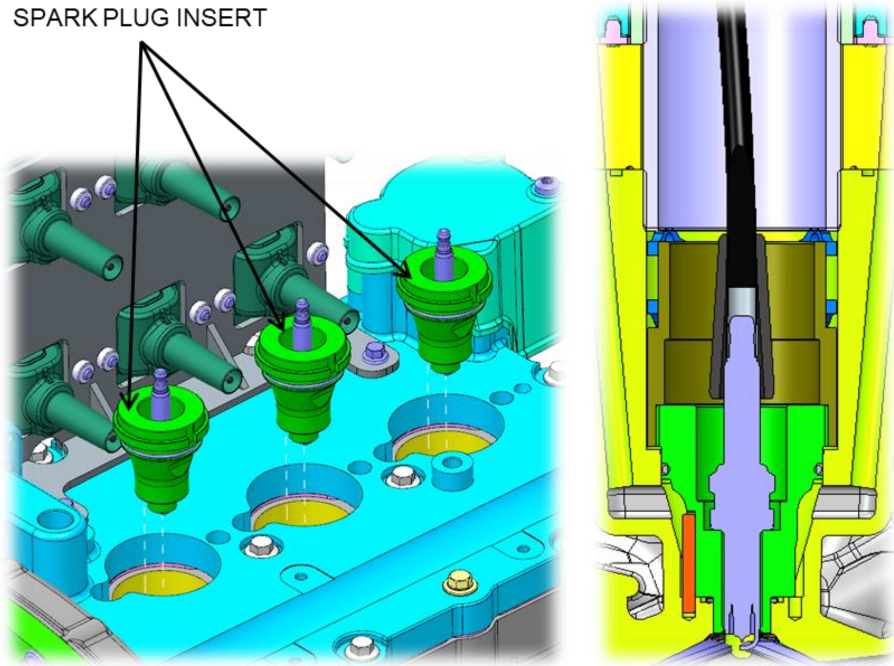

Figure 3-21: Spark plug insert assembly.

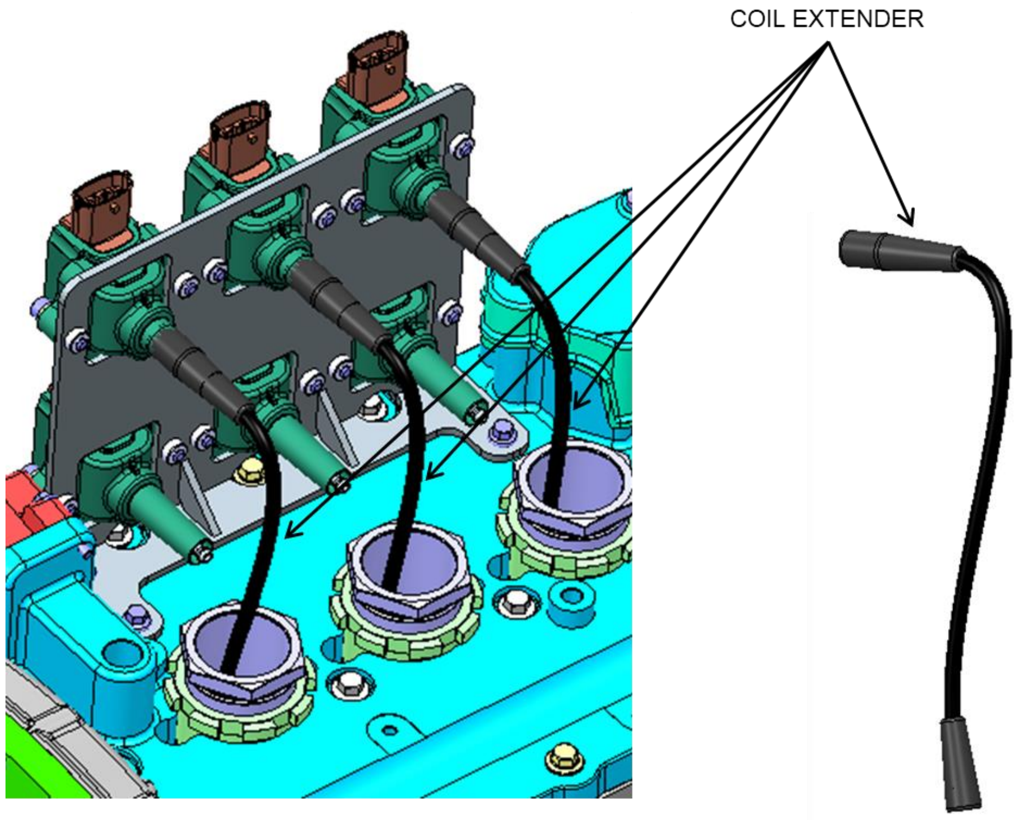

Figure 3-22: View from the top of the cam cover of the spark plug insert assembly.

Figures 3-23 and 3-24 depict the installation of the pre-chamber fuel rail and the active pre-chamber assembly installation in the cylinder head, respectively. Note the second bank of ignition coils. These were installed for use in a twin-spark arrangement that was not investigated as part of this study.

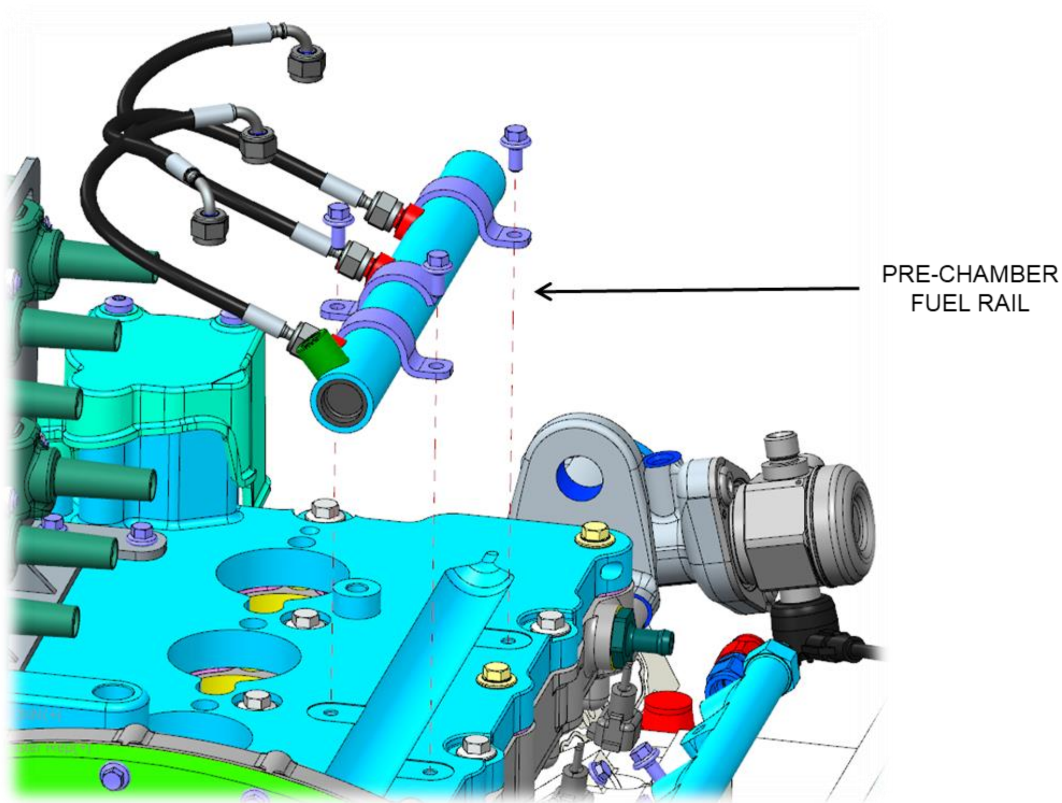

Figure 3-23: Pre-chamber injector fuel rail installation on the cam cover.

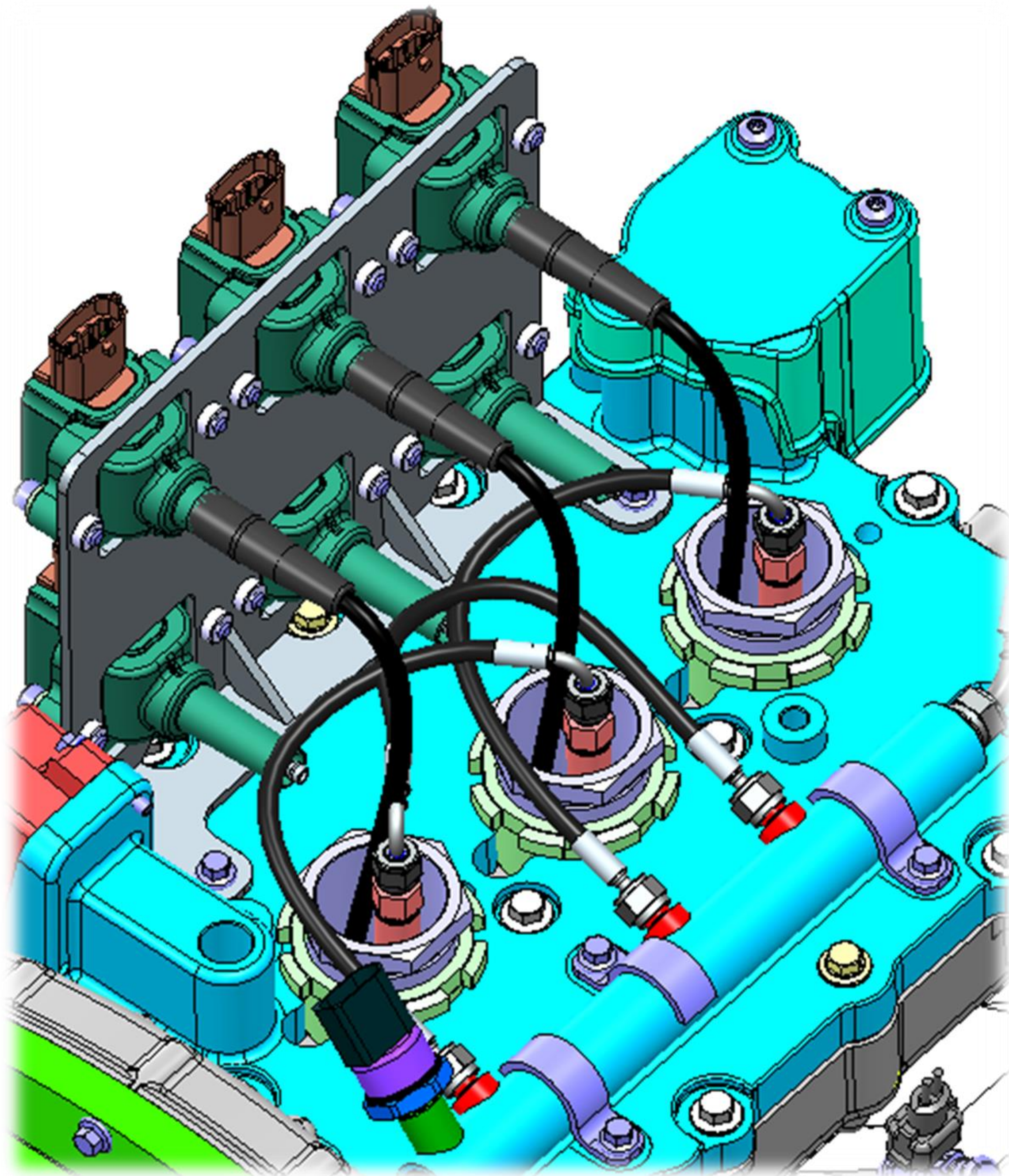

Figure 3-24: View from the top of the cam cover of the active pre-chamber assembly.

While this study explores the influence of charge motion across a constant pre-chamber geometry, there is a possibility that individual pre-chamber geometric features can be tailored to fully exploit the benefits of different charge motion levels and types. While such an investigation is beyond the scope of this study, this is a topic that warrants further consideration. An understanding of the impact of charge motion-tailored pre-chamber geometries could be especially useful in applications where the pre-chamber must be adapted to an existing engine with little to no ability to adjust existing charge motion, such as in heavy duty diesel engine conversions to spark ignited natural gas, propane, or hydrogen operation. The results of the currently reported study are intended to help lay the initial groundwork for such future studies.

3.2.3 Inducement of Charge Motion

3.2.3.1 Charge Motion Inserts

The engine incorporated features in the intake port and an additional intake spacer that allowed the use of inserts to induce varying levels and types of charge motion beyond those of the baseline engine. Four charge motion cases were evaluated in this study: baseline, increased tumble, introduction of swirl, and a combination of swirl and tumble (denoted as “swumble” in subsequent sections). The baseline configuration used no inserts and represents a moderate tumble engine consistent with tumble levels in modern DI SI engines (a tumble ratio of approximately 3). The inserts were designed to induce some relative change in tumble ratio and swirl number compared to the baseline.

An adaptor was designed for placement between the intake manifold and port. The adaptor incorporated slots in which a tumble insert could be installed. This insert consisted of a horizontal plate with a leading edge that dropped. This insert forced intake air to flow through only the top half of the adaptor, directing air flow in a tumble pattern. Figure 3-25 shows an exploded assembly view of the intake system, including the adaptor. Figure 3-26 shows a close-up view of the adaptor with the tumble insert.

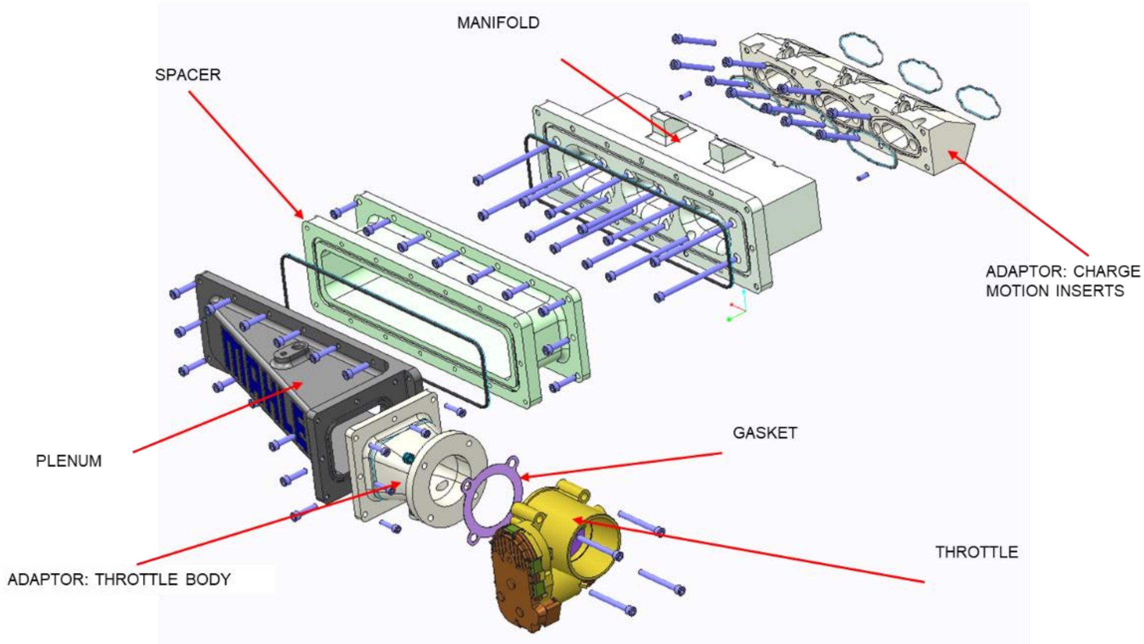

Figure 3-25: Exploded assembly view of the intake system.

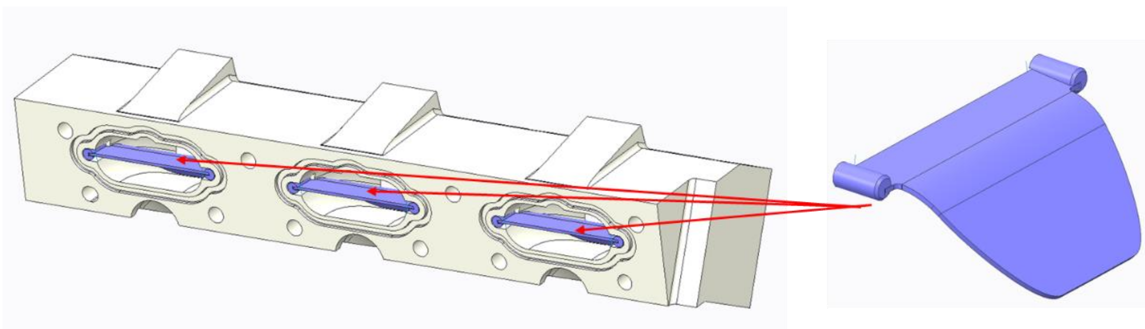

Figure 3-26: Intake adaptor with tumble inserts installed.

While many modern SI engines possess some degree of tumble, swirl is an unusual charge motion type for SI engines. To induce swirl in the MJI DI3 engine, a splitter plate was incorporated into the intake port. The plate had a slight incline across its width. This caused intake air flow to bias towards one side of the manifold, inducing swirl motion in the combustion chamber. Figure 3-27 depicts the splitter plate installation in the intake port. When not in use, pins were inserted into the rounded dowel holes on the sides of the port in order to prevent air flow from being directed through these channels and influencing overall charge motion direction and severity. Figure 3-28 depicts these pins being inserted into the intake port dowel holes. The splitter plate used in testing is shown in Fig. 3-29.

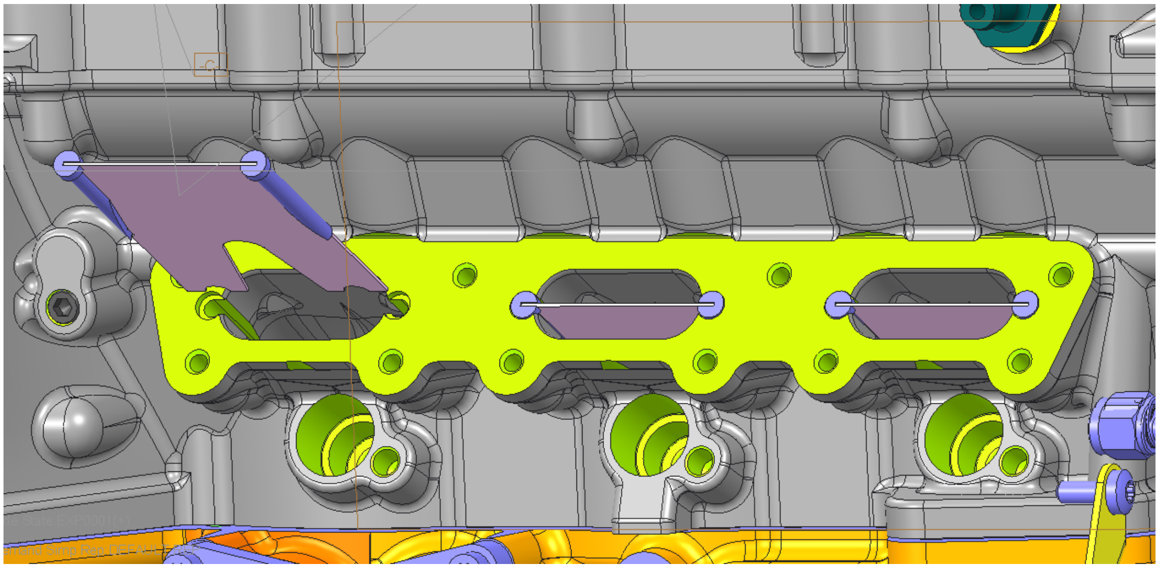

Figure 3-27: Intake port with splitter plates installed.

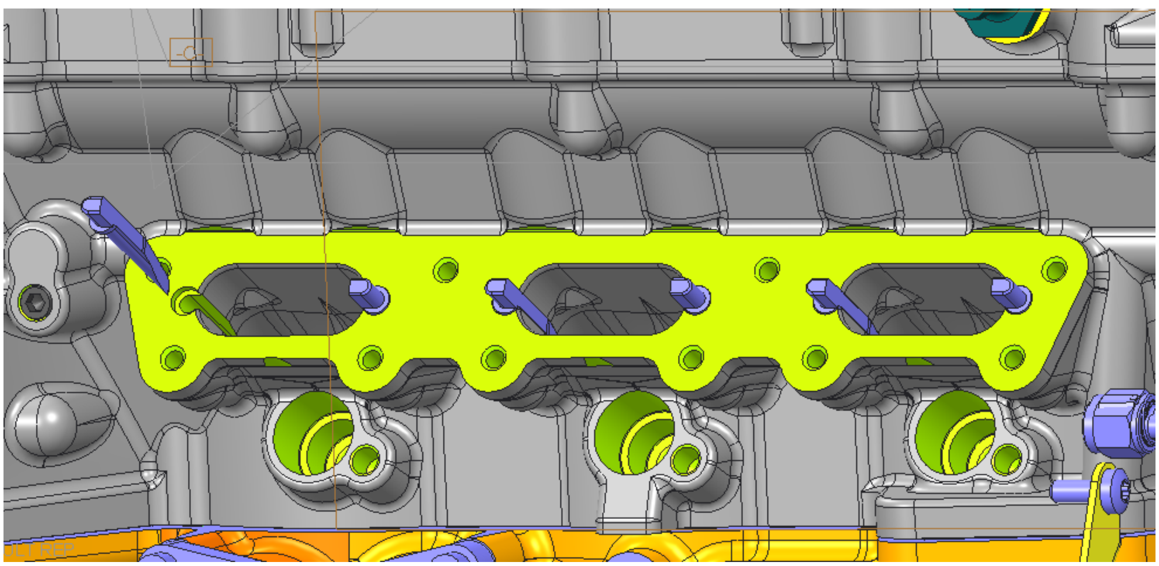

Figure 3-28: Intake port with pins installed.

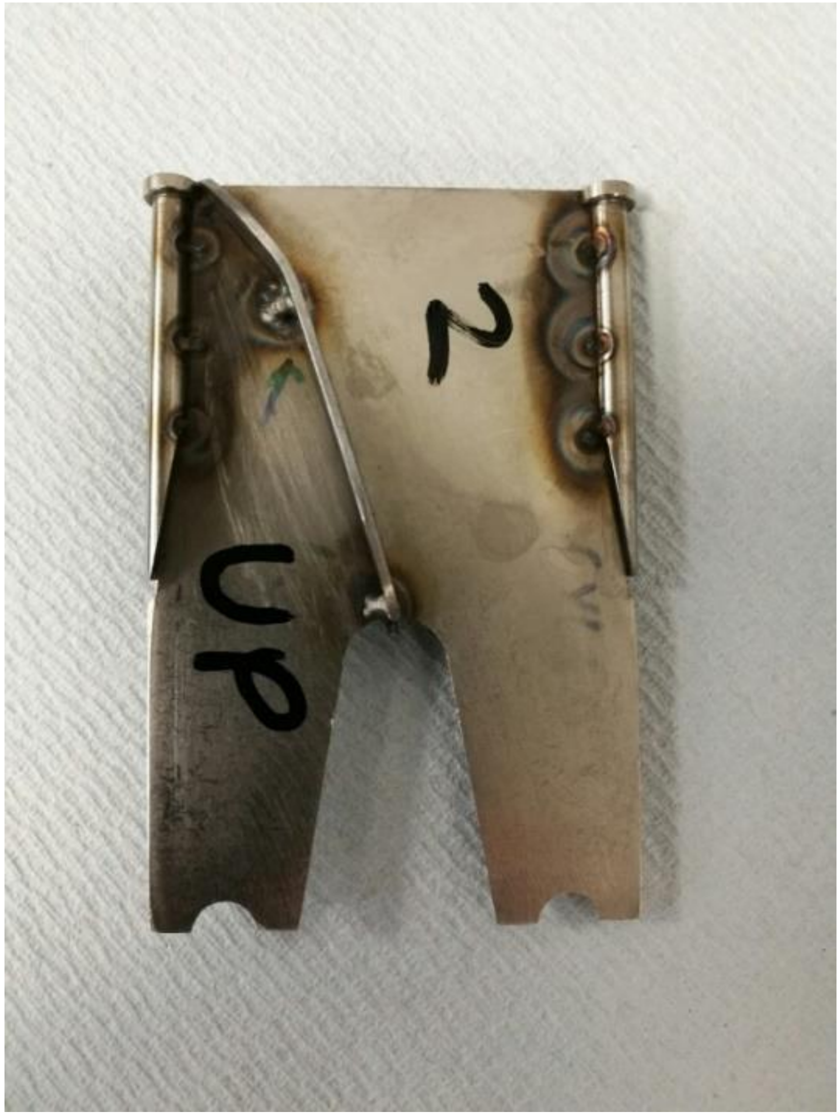

Figure 3-29: Splitter plate.

In order to induce swumble motion, the splitter plate and tumble insert were installed in series. This configuration, while not expected to be fully additive, provided both increased tumble over the baseline variant, and swirl.

The addition of the charge motion inserts increased the restriction in the intake system, reducing the volumetric efficiency of the engine. This impact to volumetric efficiency was expected to vary considerably with speed and load. The testing methodology sought to account for it by adjusting the comparison basis based on the specific speeds and loads considered. Modern engines employ less invasive approaches to generating charge motion, including tailored intake port design, valve masking, and piston crown design. The approach used in this study however provided the degree of flexibility necessary to generate a valid comparison amongst the different charge motion types and levels.

In Figure 3-30, with the inserts installed, it is clear that the splitter plate used for inducing swirl is in the path of the PFI fuel spray. The shape of the splitter was designed to specifically minimize impingement of the fuel spray on the plate. Figure 3-31 provides another view of the trajectory of the PFI fuel spray through the intake adaptor.

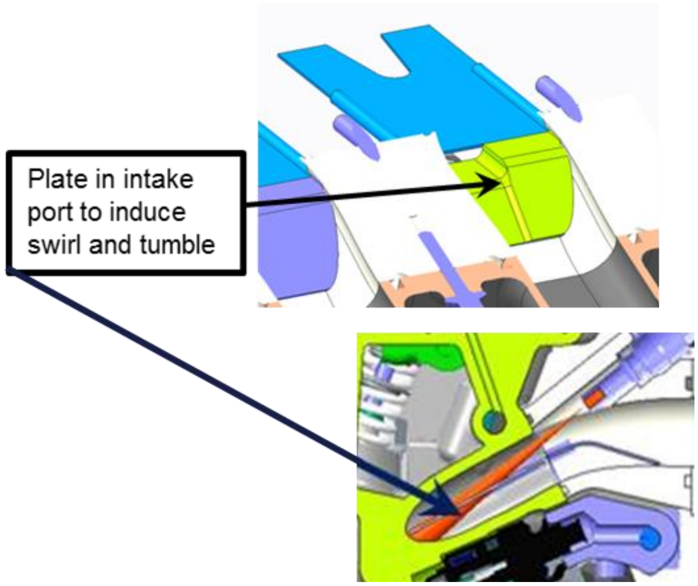

Figure 3-30: PFI fuel spray interaction with charge motion inserts.

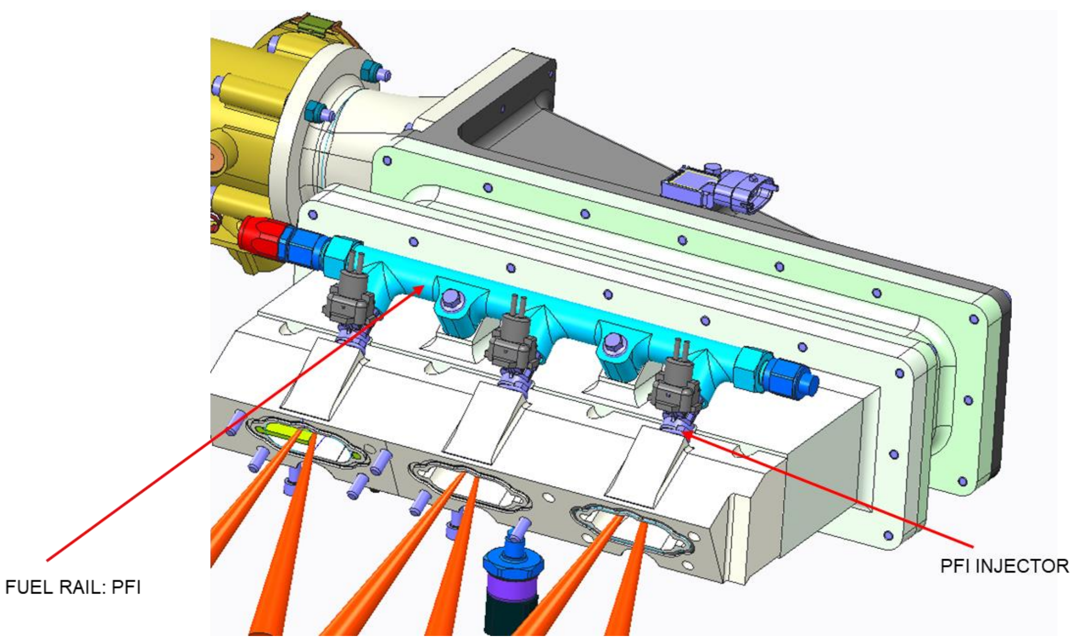

Figure 3-31: PFI fuel spray through the intake adaptor.

3.2.3.2 Air Flow Rig

The MPT Air Flow Rig was used to evaluate tumble ratio and swirl number of the MJI DI3 engine cylinder head in baseline configuration and with the charge motion inserts installed. The Air Flow Rig uses a blower to force air through one of the cylinder head's intake ports, into the combustion chamber, and out through a pipe connected to the combustion chamber. Flow control is implemented through a data acquisition and control unit. Air is pulled through the cylinder head, rather than pushed through, by a blower in order to emulate the function of the piston during the intake stroke, as the downward piston motion pulls intake air into the combustion chamber. The angular rotation of the air is then measured using an air rotation meter located downstream of the pipe connected to the combustion chamber. Data from this meter is interpreted by the software to determine the tumble and swirl generated by the cylinder head and intake system. The Air Flow Rig is pictured in Fig. 3-32. The schematic diagram is pictured in Fig. 3-33 and the air rotation meter is pictured in Fig. 3-34.

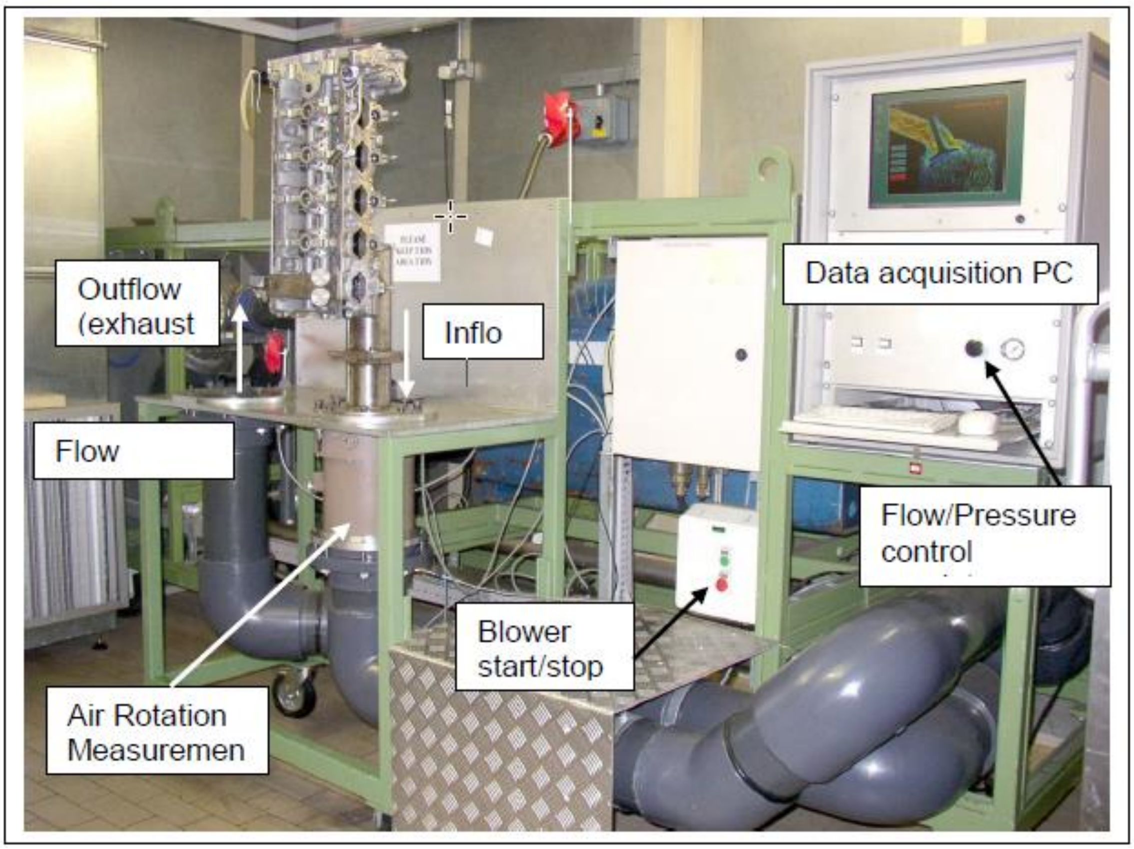

Figure 3-32: The MPT Air Flow Rig installed at MPT's facility in Northampton, UK.

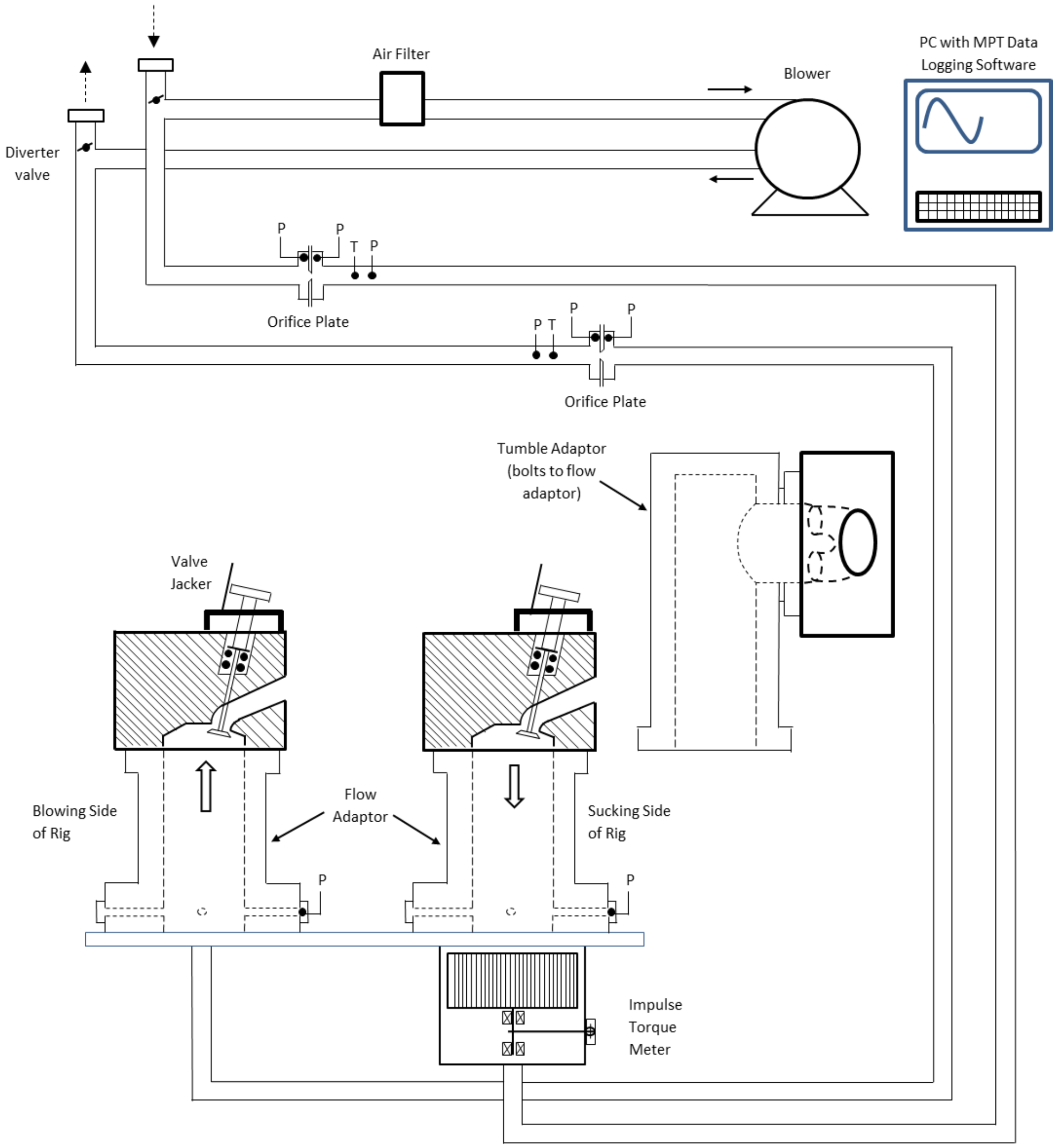

Figure 3-33: Air flow rig schematic diagram.

Figure 3-34: The air rotation meter.

The Air Flow Rig forced air to flow through the cylinder head, while valve lift was adjusted statically in 1 mm increments. The stock valve springs were replaced by softer springs, and jacking screws were installed so as to provide a manual means by which to adjust valve lift incrementally (Fig. 3-35). Static measurements were performed at each valve lift increment.

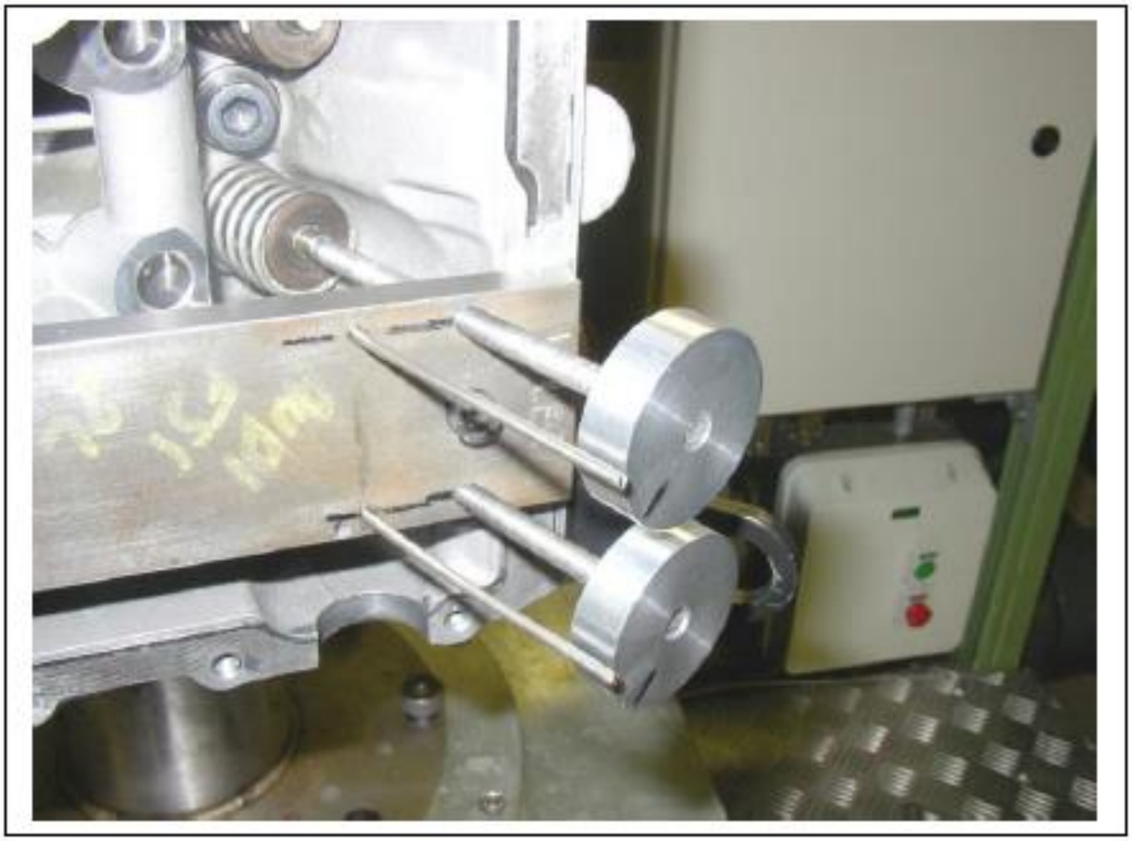

Figure 3-35: Jacking screws and thumb wheel rotators to allow for manual adjustment of valve lift during testing.

Data output from the Air Flow Rig produced non-dimensional tumble vs. lift and swirl vs. lift curves that were agglomerated from the static tests at the individual valve lift tests. In order to determine the singular tumble ratio and swirl number, the areas under the respective curves were integrated. Figure 3-36 shows a typical data set produced by the Air Flow Rig data acquisition system. The cylinder head evaluated in this example was from a typical production SI engine, therefore it generated nearly no swirl motion. All charge motion variants used in this study were evaluated for both tumble and swirl in separate tests. The flow coefficient, C_f, is calculated by the software using the following equation:

$$C_f = Q * \sqrt{\frac{S_g}{(P_o - P_1)}} \qquad \text{3-2}$$

Where Q is the air flow rate, S_g is the specific gravity of air, P_o is the pressure upstream of the valve, and P_1 is the pressure downstream of the valve. Table 3-5 lists the relative change in tumble ratio and swirl number for each of the three charge motion insert configurations versus the baseline. The baseline corresponds to a conventional SI intake port with no inserts, producing very low swirl and a tumble ratio of approximately 3. As is seen in the table, the tumble insert produced a modest 13% increase in tumble versus the baseline, with a further decrease in swirl. The minor swirl decrease is not significant due to the low baseline level. The swirl plate attenuated the tumble level of the baseline by 39% and produced an increase of over 1000% in swirl number. The addition of the tumble insert and swirl plate produced a swumble variant with a tumble level similar to that of the tumble insert on its own, with a moderate 75% increase in swirl number. While not necessarily a parametric spread of relative charge motion values, these inserts succeeded in producing the desired charge motion type at levels reasonably distinct from the baseline.

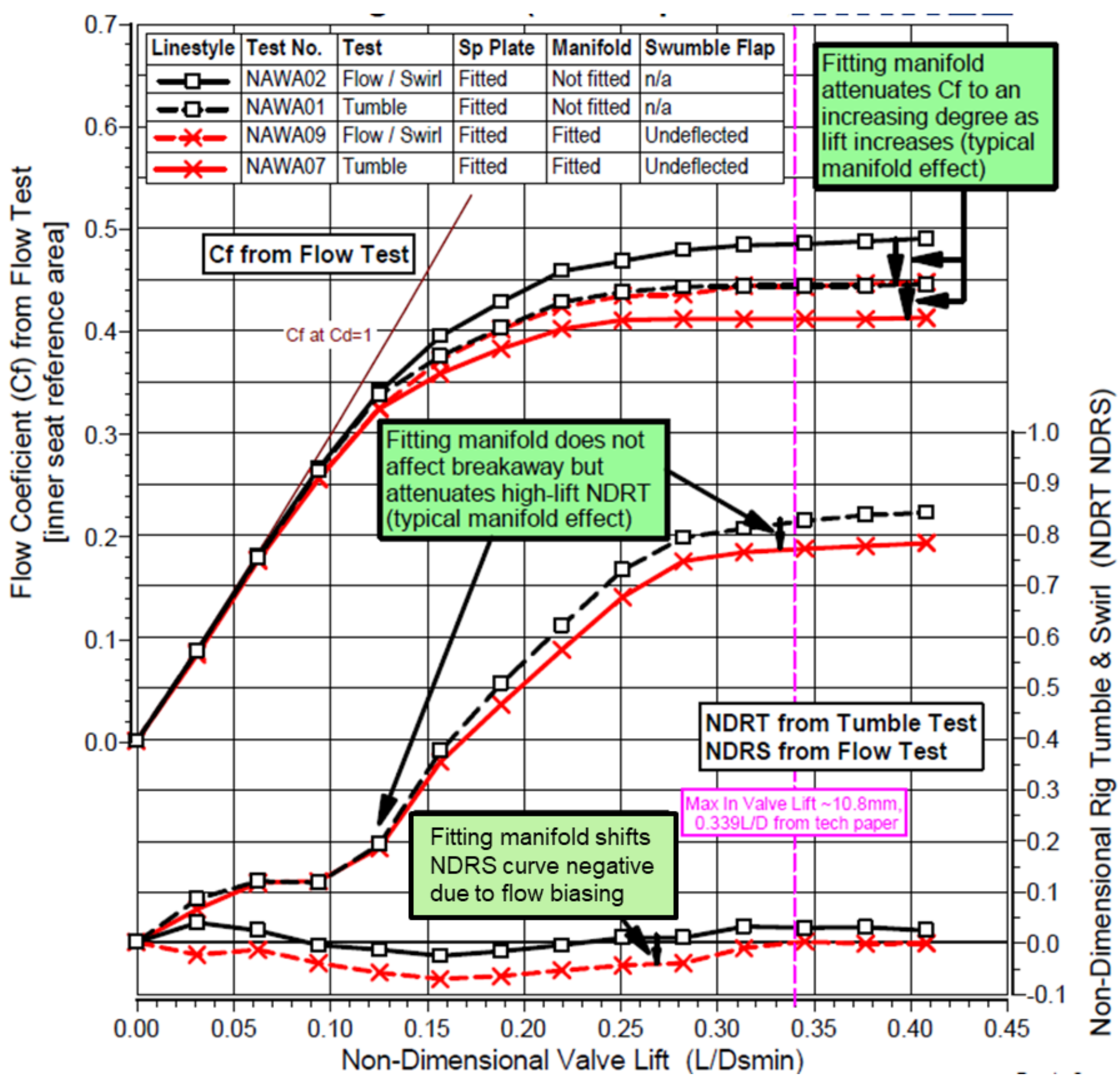

Figure 3-36: Example data set from the Air Flow Rig showing non-dimensional tumble and swirl and flow coefficient versus non-dimensional valve lift.

Table 3-5: Relative change in tumble ratio and swirl number with various intake port insert configurations, relative to the baseline configuration.

Configuration	Relative Tumble Ratio	Relative Swirl Number
Baseline	-	-
Tumble	+13%	-25%
Swirl	-39%	+1075%
Swumble	+13%	+75%

3.2.4 Direct Pre-Chamber Sampling

In order to develop a hypothesis for jet ignition combustion performance under low load spark retard conditions, and how it may or may not be impacted by different types of charge motion, baseline in-pre-chamber conditions needed to be fully understood. In order to directionally assess the effect of charge motion on inhibiting pre-chamber combustion, a direct measurement of pre-chamber gases needed to be made.

A Cambustion fast CO_2 analyzer was used to sample contents directly from the pre-chamber during fired engine operation. The resulting crank angle-resolved CO_2 trace was used to calculate a residual gas fraction inside the pre-chamber at time of spark.

Two methods of sampling directly from the pre-chamber were employed and the results were compared for validation purposes. In the sampling valve method, a fast response solenoid valve was connected to a port that broke through to the pre-chamber volume. The valve was commanded open and closed, allowing a small volume of pre-chamber contents to be sampled by the CO_2 analyzer in short duration increments. Care was taken to ensure that the proper minimum amount of sample gas was provided to the analyzer, and the time during which the valve sampled was swept throughout the cycle until reasonable convergence was achieved.

In the continuous sampling method (Fig. 3-37), the analyzer probe was connected directly to a port at the top of the pre-chamber body. A thin capillary connected this port to the pre-chamber volume. The analyzer constantly sampled pre-chamber contents throughout the cycle. While invasive, the minimum required volume was a fraction of the pre-chamber contents, and so pre-chamber combustion could be maintained. The resulting CO_2 trace was used to calculate residual gas fraction inside the pre-chamber.

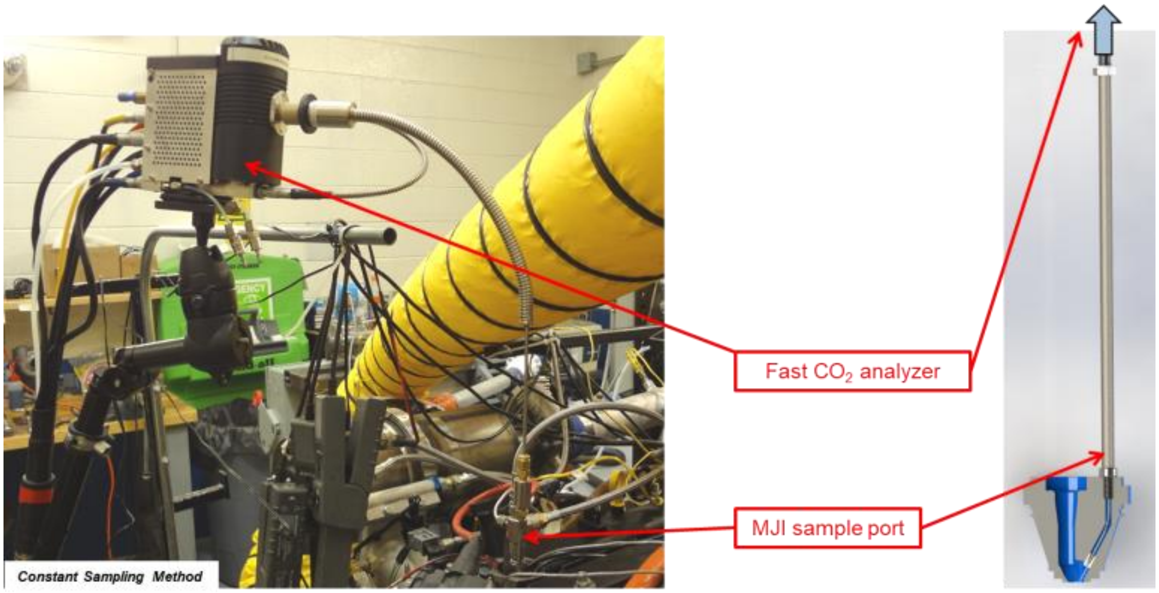

Figure 3-37: Constant sampling method for measuring pre-chamber residual fraction.

Experiments were performed to examine the influence that various pre-chamber parameters had on in-pre-chamber residual gas fraction. These parameters included auxiliary fueling quantity and angle of injection. Tests were performed at a value of $\lambda = 1.4$. At this value, the engine could be operated both with and without auxiliary pre-chamber fuel and still maintain acceptable COVs. Auxiliary fuel injection timing and quantity were adjusted parametrically at a constant engine speed, load, and angle of 50% fuel mass burned (CA50) and combustion and in-pre-chamber residual fraction response was observed.

3.3 Experimental Procedure

The following experimental procedures refers to operation of the MJI DI3 engine. This engine served as the primary experimental test bed in this study.

3.3.1 Data Consistency

Data quality was monitored using a series of daily check points that spanned stoichiometric non-auxiliary fueled pre-chamber operation and lean auxiliary fueled pre-chamber operation. At these daily check points, fuel injector pulsewidth, throttle position, and spark timing were fixed. A moving average of the following parameters was calculated, while a range of +/- 5% of the corresponding average valve was deemed an acceptable range of variation to proceed with the test proper: IMEPg, indicated thermal efficiency (ITE), crank angle duration of 10%-90% fuel mass burned (CA10-90), CA50, friction mean effective pressure (FMEP), COV, fuel flow rate (main chamber and pre-chamber), λ, and NO_x. These parameters were chosen due to their indication of engine health (ITE, FMEP, COV, fuel flow rate), engine control stability (λ), and high degree of sensitivity to minute changes in engine setup or ambient conditions (CA10-90, CA50, NO_x). If any of these parameters exceeded the +/- 5% threshold, the source of error was identified and rectified, and the daily check point was re-recorded until the parameters fell within the +/- 5% threshold.

A daily check moving average was established for each of the four charge motion variants evaluated, since they were expected to produce differences in the parameters used to establish daily check success criteria. Each charge motion variant was thus evaluated against a moving average of daily check data for that specific charge motion variant only.

The daily check point sample log is shown in Fig. 3-38.

Log no.	Speed	BMEP	Abs. Inlet Pressure	Int CAM	Exh CAM	Lambda	CA50	P/C Inj. Pressure	P/C Inj. Timing	P/C Inj. PW	PFI Pressure	PFI Inj. Timing	Oil Temp
#	rpm	bar	kPa	deg	deg	Active MJI	deg ATDC	bar	deg BTDC	ms	kPa	deg BTDC	°C
1	1500	**Motoring**	WOT	Baseline	Baseline		-	100	0	0	470	420	25
2	1500	6	Max	Baseline	Baseline	1	8	100	0	0	470	420	90
3	1500	6	Max	Baseline	Baseline	1.6	8	100	50	2	470	420	90

Figure 3-38: Daily check point test plan.

3.3.2 Error Analysis

The monitoring of the daily check point ensured that day-to-day variation in engine behavior was minimized. High speed pressure transducers were calibrated immediately preceding this testing. A TDC probe was used to verify TDC angle every 2 weeks. Additionally, logged test data was evaluated for its consistency. Of the three 30 second data logs of the low speed data, key data metrics including BMEP, CA50, COV, and λ must be within 2 standard deviations of the mean. If any of the three data logs did not comply, the test point was rerun. If, upon this rerun, the data still did not comply, the test was cancelled, and a daily check point was performed in order to assess the issue causing the error and to address it.

With the data acquisition complete, each sweep test plan was evaluated for internal error. If any error appeared systemic, i.e. more than 20% of the data points were determined to be outliers, the dataset was abandoned and rerun. For the sweeps of λ at constant load, the load held constant was the primary evaluation criterion. In various tests the load metric was IMEPg, net mean effective pressure (NMEP), or BMEP. In each case, the load was averaged, and any individual logs that contained a load outside of a band of 2 standard deviations from the mean was identified as an outlier and removed from the dataset.

For sweeps of load at constant λ, the same outlier standard was applied to the λ values. For sweeps of spark timing at constant load, the load used (typically NMEP) was used as the primary criterion for evaluating outliers. For the sweeps involving constant load, it was common for the number of outlier data points in a given set to be between 0 and 2 in a set of at least 20 data points. For the sweeps involving constant λ, there were rarely any outliers in a given dataset.

3.3.3 Calibration

Several engine parameters were not varied as part of this study. These parameters were optimized in previous studies and constituted a preliminary engine calibration in this study. The most notable of these parameters include cam timing and engine back pressure.

Because of the addition of λ as an engine variable, multiple cam timing optimization scenarios can be realized. Common scenarios employed include maximizing BTE, maximizing combustion efficiency, and minimizing NO_X across the engine map. For the current study, a maximum BTE strategy was used, whereby cam timings were chosen such that BTE was maximized across the full engine map.

Figure 3-39 shows an example of engine sensitivity to cam timing at a 3000 rpm, 12 bar BMEP, λ = 1.8 condition. At this condition, BTE is maximized when the exhaust cam timing is retarded from the park position and the intake cam timing is advanced somewhat from park position. Park position for the MJI DI3 engine corresponds to no valve overlap. The retarded exhaust cam and advanced intake cam timings demonstrate the positive impact on BTE provided by increased valve overlap.

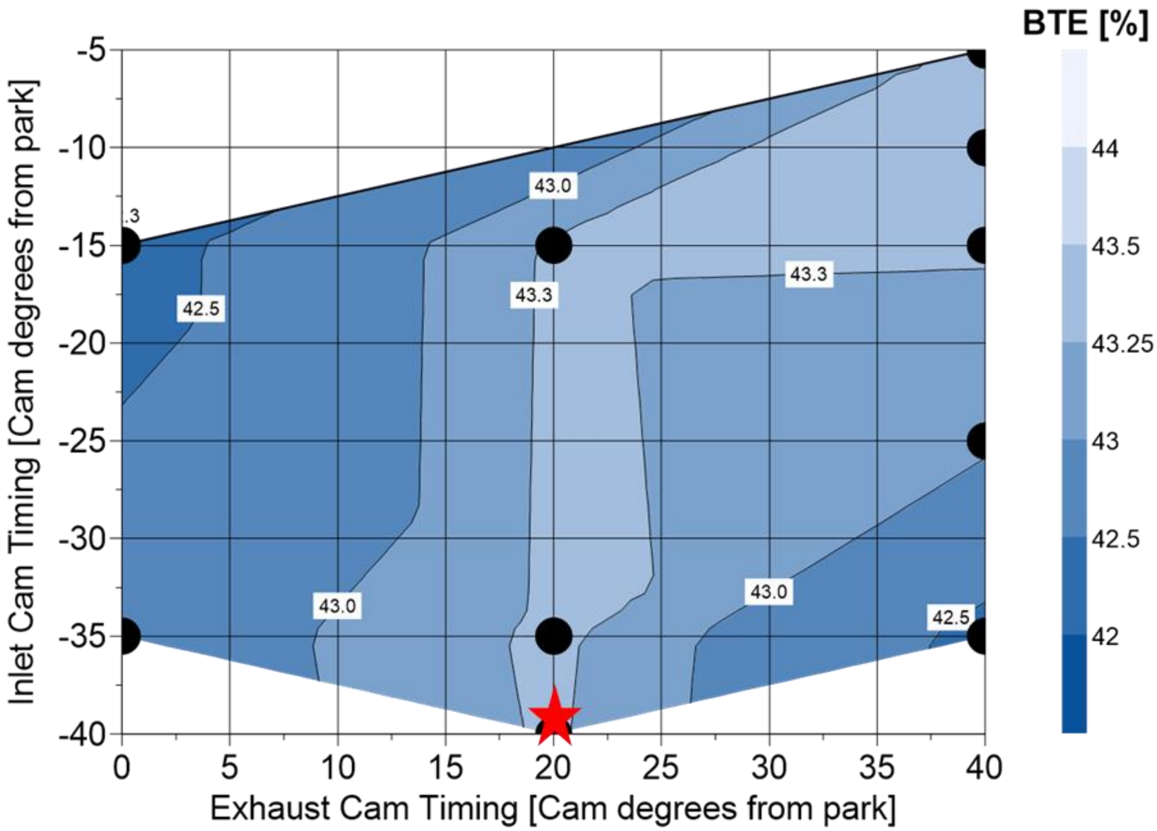

Figure 3-39: Example BTE sensitivity to cam timing at 3000 rpm, 12 bar BMEP, λ = 1.8.

The results from Fig. 3-39 applied relatively consistently across the engine. In all test points evaluated as part of this study, the optimal exhaust cam timing was 40 degrees retarded from park position. The optimal intake cam timing varied from 20 degrees advanced park position at part and high load conditions, to park position at low load conditions. The reason for the shift towards more overlap for the higher load conditions was hypothesized to be the benefits of internal residuals. At high load lean conditions, heavy boost was needed to provide the necessary air flow. The addition of internal EGR reduced the strain on the boost system by retaining some O_2 in the combustion chamber for the subsequent cycle. This led to lower intake manifold pressure and reduced pumping work, as evidenced by Fig. 3-40. The selected cam timing therefore maximized BTE while reducing intake manifold pressure.

Additionally, internal EGR retains some artefact of combustion temperature as it mixes with the incoming fresh charge. Lean operation reduces bulk combustion temperatures, which results in lower in-cylinder heat loss. However, the reduced combustion temperatures, coupled with the low ignitability lean charge, can lead to an arrested late burning process, placing downward pressure on combustion efficiency. The additional hot residuals mitigate this process, producing higher combustion efficiencies, with an influence significant enough to impact BTE as well.

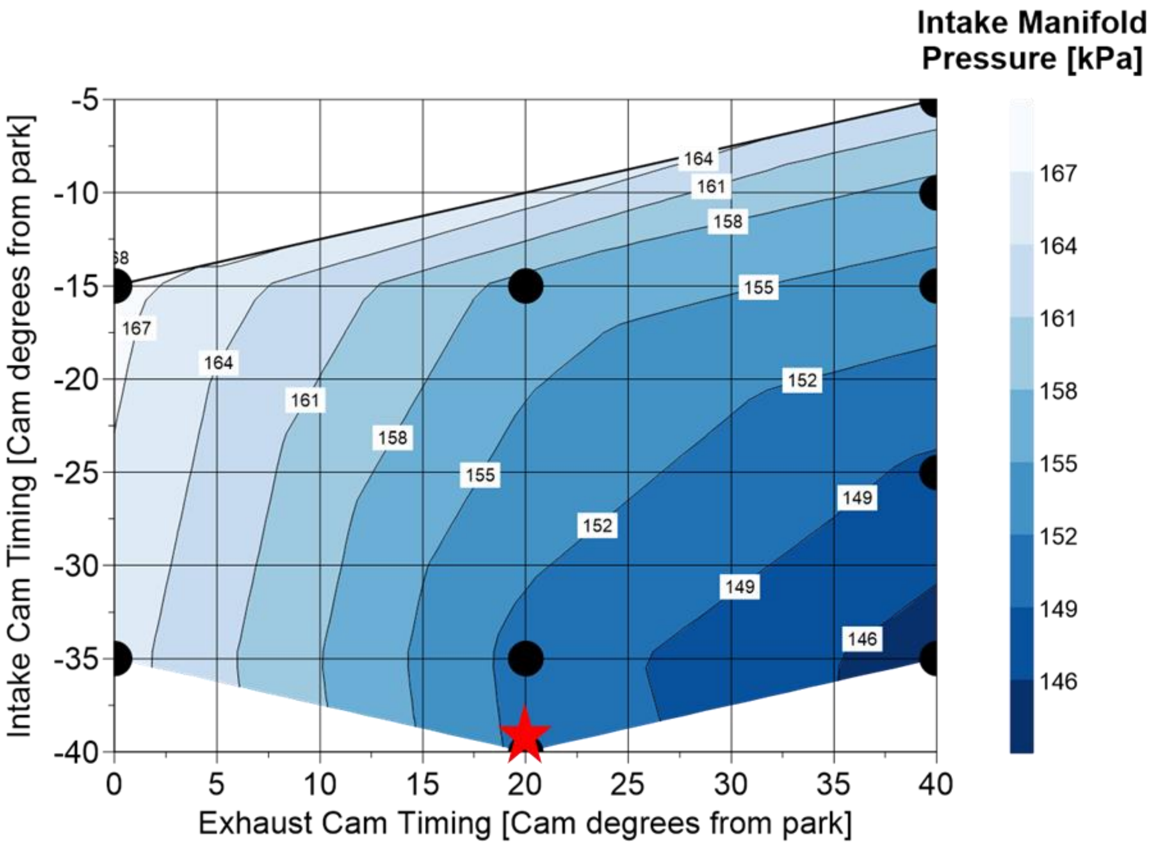

Figure 3-40: Example intake manifold pressure sensitivity to cam timing at 3000 rpm, 12 bar BMEP, λ = 1.8.

A back pressure valve was added to the engine downstream of the turbine. The back pressure added to the engine from manipulation of the valve accounts for the back pressure that would be encountered on a productionized version of the engine due to the addition of aftertreatment. A relationship between exhaust mass flowrate and catalyst inlet pressure was established using MPT's database of values from production engines between 1.2L and 1.8L displacement. Data was taken from the database that related exhaust mass flowrate to catalyst inlet pressure across all engine speeds, and a 2nd order polynomial was fit to this dataset. The polynomial equation was then used in the test cell to control back pressure valve position dynamically in order to achieve the desired upstream exhaust pressure. The 2nd order polynomial curve fit and resulting equation are shown in Fig. 3-41.

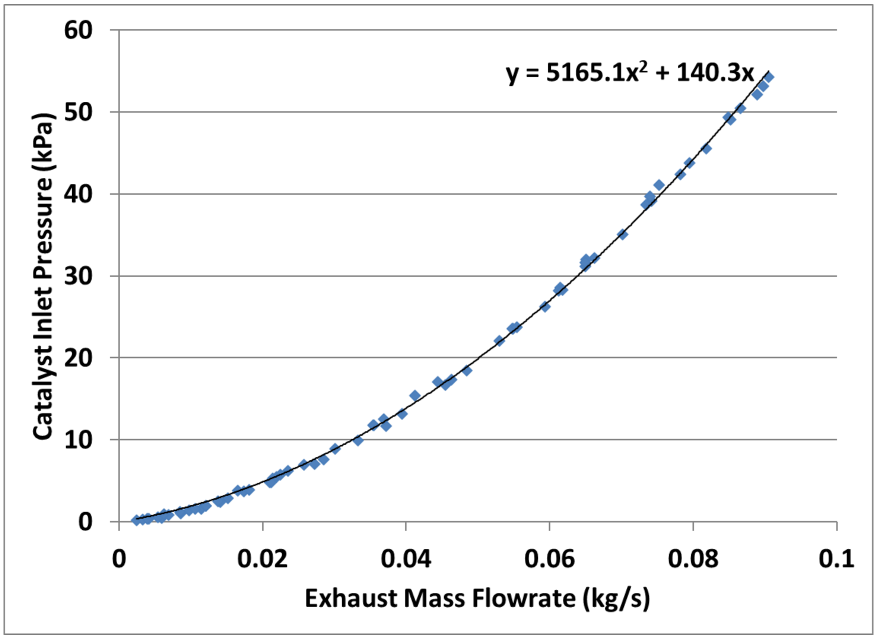

Figure 3-41: Relationship between exhaust mass flowrate and catalyst inlet pressure taken from MPT's database of production engines between 1.2L and 1.8L displacement.

3.3.4 Test Procedure

The following sections describe the test procedure for the MJI DI3 engine tests performed during this study. The engine was used to experimentally quantify the impact of charge motion on performance by comparing data using all 4 charge motion variants. Three categories of operating condition were investigated:

1) Non-knock-limited operation – a speed / load condition that does not exhibit any knock tendency under lean conditions.

2) Knock-limited operation – a speed / load condition that does exhibit a tendency to knock under lean conditions and therefore requires spark retard to avoid knock in this region.

3) Cold start spark retard (CSSR) operation – a speed / load condition consistent with the catalyst light-off conditions of modern production engines, requiring a late combustion event.

Multiple types of engine tests were performed in order to evaluate engine performance and sensitivity to charge motion across all 3 categories of operating conditions. The following subsections describe the type of tests performed and the operating condition types evaluated.

3.3.4.1 Sweeps of λ

For conditions 1 and 2, λ sweeps were performed, whereby speed and load were held constant as the λ of the engine was increased from 1.0 to or beyond its lean limit in increments of 0.1. This was done by gradually opening the throttle across the λ sweep and, when needed, applying boost pressure gradually until the desired load and λ were achieved. The lean limit defined in these tests is the λ at which consistent detectable misfires prevent the engine from holding its proscribed operating conditions, or the point at which the boost system of the engine is incapable of providing enough airflow to maintain the desired load with further enleanment. For the latter limit, data taken beyond this lean limit is viewed as inconsistent with the remainder of the dataset since two major variables (λ and load) begin to change rather than one (λ).

Sweeps of λ were performed at three speed/load conditions. These were 1500 rpm, 6 bar BMEP; 4000 rpm, 8 bar BMEP; and 3000 rpm, 13 bar IMEPg. The 1500 rpm point was chosen because it constitutes mid-load operation with little likelihood of knock occurring. The 4000 rpm point was chosen in order to demonstrate charge motion performance sensitivity at a higher engine speed, where burn duration, especially late burn duration, has a more significant influence on overall combustion performance. The 3000 rpm point was chosen due to its relatively high likelihood of experiencing knock, even under lean conditions, at the elevated 15:1 CR. The 3000 rpm point also corresponds to approximately the peak BTE point within the lean engine map.

The condition 1 λ sweeps also provided a comparison of the relative change in charge motion sensitivity from λ =1 to the lean limit. Understanding how the sensitivity to charge motion correlates with regressive mixture ignitability can provide an indication of the merits of charge motion optimization for passive jet ignition engines.

For condition 1, BMEP was used as the constant load parameter due to the reduced influence of pumping losses for a non-boosted condition that achieves wide open throttle when lean. For condition 2, IMEPg is used as the constant load parameter due to the significant influence of pumping losses associated with heavy boosting.

For both conditions, the pre-chamber fuel injector was used to provide auxiliary fuel when the engine achieves λ = 1.4. As the engine is enleaned, the pre-chamber fueling quantity is increased. With all charge motion variants, the pre-chamber auxiliary fuel is kept to the minimum allowable value to maintain COV < 3%. The baseline and tumble variants utilized nearly identical quantities of auxiliary fuel versus λ, while the swirl and swumble variants generally required approximately double this quantity at the leanest conditions tested (λ > 1.8). For all variants across all data points, the maximum fuel mass injected using the pre-chamber fuel injector was approximately 1.5% of the fuel mass injected through the main chamber fuel injector.

For the knock limited condition 2, CA50 was advanced at each λ point with each charge motion variant until the engine achieved a previously established speed-sensitive knock amplitude threshold as calculated from the main chamber high speed pressure transducers that represented a no/light knock condition. These results were confirmed qualitatively in real-time using an acoustic knock tube. No knock or pre-ignition was detected in the pre-chambers, which is consistent with the results of other tests of this engine / pre-chamber configuration.

Conditions 1 and 2 operated with approximately 60 degrees of valve overlap, which was determined to be optimal for thermal efficiency at these conditions. Both the 1500 rpm and 4000 rpm points that constituted condition 1 achieved wide open throttle near the lean limit of the engine, with only mild boost being employed throughout the testing at these points. For the 3000 rpm point (condition 2) wide open throttle was achieved in the near-lean region, with a maximum boost pressure of approximately 1.5 bar near the lean limit. At both conditions, back pressure was applied via a back pressure valve in order to mimic the effect of a catalyst. The use of the back pressure valve ensured a negative delta pressure across the engine at all conditions.

The test lineup for the 1500 rpm and 4000 rpm condition 1 points are depicted in Figs. 3-42 and 3-43, respectively. The test lineup for the 3000 rpm condition 2 point is depicted in Fig. 3-44. Note that at this condition the engine is too knock-limited at the near-stoichiometric λ values to be able to acquire data. The elevated CR of 15:1 essentially guarantees this result, by design, in order to maintain some degree of knock into the ultra-lean region. The lineup therefore starts in the near-lean region where the added dilution reduces knock.

1500 6 bar Lambda Sweep										
Set Points : Coolant =90 ; CAC =40 ; Oil =90										
Point no.	**Speed**	**BMEP**	**Int CAM**	**Exh CAM**	**Lambda**	**P/C Inj. Pressure**	**P/C Inj. Timing**	**PFI Pressure**	**PFI Inj. Timing**	**CA50**
#	**rpm**	**bar**	**deg**	**deg**	**-**	**bar**	**deg BTDC**	**bar**	**deg BTDC**	**dBTDC**
1	1500	6	-20	40	1	100	50	3	420	8
2	1500	6	-20	40	1.1	100	50	3	420	8
3	1500	6	-20	40	1.2	100	50	3	420	8
4	1500	6	-20	40	1.3	100	50	3	420	8
5	1500	6	-20	40	1.4	100	50	3	420	8
6	1500	6	-20	40	1.5	100	50	3	420	8
7	1500	6	-20	40	1.6	100	50	3	420	8
8	1500	6	-20	40	1.7	100	50	3	420	8
9	1500	6	-20	40	1.8	100	50	3	420	8
10	1500	6	-20	40	1.9	100	50	3	420	8
11	1500	6	-20	40	2	100	50	3	420	8
12	1500	6	-20	40	2.1	100	50	3	420	8

Figure 3-42: Test lineup for the 1500 rpm point – Condition 1.

4000 8 bar Lambda Sweep										
Set Points : Coolant =90 ; CAC =40 ; Oil =90										
Point no.	**Speed**	**BMEP**	**Int CAM**	**Exh CAM**	**Lambda**	**P/C Inj. Pressure**	**P/C Inj. Timing**	**PFI Pressure**	**PFI Inj. Timing**	**CA50**
#	**rpm**	**bar**	**deg**	**deg**	**-**	**bar**	**deg BTDC**	**bar**	**deg BTDC**	**dBTDC**
1	4000	8	-20	40	1	100	50	3	420	8
2	4000	8	-20	40	1.1	100	50	3	420	8
3	4000	8	-20	40	1.2	100	50	3	420	8
4	4000	8	-20	40	1.3	100	50	3	420	8
5	4000	8	-20	40	1.4	100	50	3	420	8
6	4000	8	-20	40	1.5	100	50	3	420	8
7	4000	8	-20	40	1.6	100	50	3	420	8
8	4000	8	-20	40	1.7	100	50	3	420	8
9	4000	8	-20	40	1.8	100	50	3	420	8
10	4000	8	-20	40	1.9	100	50	3	420	8
11	4000	8	-20	40	2	100	50	3	420	8
12	4000	8	-20	40	2.1	100	50	3	420	8
13	4000	8	-20	40	2.2	100	50	3	420	8

Figure 3-43: Test lineup for the 4000 rpm point – Condition 1.

3000 rpm Peak Efficiency Lambda Sweep										
Set Points : Coolant =90 ; CAC =40 ; Oil =90										
Point no.	**Speed**	**IMEPg**	**Int CAM**	**Exh CAM**	**Lambda**	**P/C Inj. Pressure**	**P/C Inj. Timing**	**PFI Pressure**	**PFI Inj. Timing**	**CA50**
#	**rpm**	**bar**	**deg**	**deg**	**-**	**bar**	**deg BTDC**	**bar**	**deg BTDC**	**dBTDC**
1	3000	13	-20	40	1.2	100	50	3	420	MBT
2	3000	13	-20	40	1.3	100	50	3	420	MBT
3	3000	13	-20	40	1.4	100	50	3	420	MBT
4	3000	13	-20	40	1.5	100	50	3	420	MBT
5	3000	13	-20	40	1.6	100	50	3	420	MBT
6	3000	13	-20	40	1.7	100	50	3	420	MBT
7	3000	13	-20	40	1.8	100	50	3	420	MBT
8	3000	13	-20	40	1.9	100	50	3	420	MBT
9	3000	13	-20	40	2	100	50	3	420	MBT
10	3000	13	-20	40	2.1	100	50	3	420	MBT

Figure 3-44: Test lineup for the 3000 rpm point – Condition 2.

3.3.4.2 Sweeps of Pre-Chamber Fueling Parameters

At the 1500 rpm point, pre-chamber fueling parameters were exercised in a parametric manner in order to capture potential sensitivities to charge motion. Sweeps of the two critical pre-chamber fuel injection parameters, end of injection angle and pulsewidth, were performed at a λ of 1.7 in order to ensure stable lean combustion.

Pre-chamber end of injection angle was varied from 120 dBTDC and 0 dBTDC in 20 crank angle degree increments. Injection pressure was held constant. With a constant pulsewidth, the differences in background pressure would create a non-constant fueling quantity in the pre-chamber. To avoid this, pre-chamber fuel flowrate was baselined at the nominal 50 dBTDC injection timing, and this flowrate was held constant through minor manual pulsewidth adjustments throughout the injection angle sweep. This test lineup is shown in Fig. 3-45.

1500 rpm 6 bar P/C Angle										
Set Points : Coolant =90 ; CAC =40 ; Oil =90										
Point no.	Speed	BMEP	Int CAM	Exh CAM	Lambda	P/C Inj. Pressure	P/C Inj. Timing	PFI Pressure	PFI Inj. Timing	CA50
#	rpm	bar	deg	deg	-	bar	deg BTDC	bar	deg BTDC	dBTDC
1	1500	6	-20	40	1.7	100	50	3	420	8
2	1500	6	-20	40	1.7	100	0	3	420	8
3	1500	6	-20	40	1.7	100	20	3	420	8
4	1500	6	-20	40	1.7	100	40	3	420	8
5	1500	6	-20	40	1.7	100	60	3	420	8
6	1500	6	-20	40	1.7	100	80	3	420	8
7	1500	6	-20	40	1.7	100	100	3	420	8
8	1500	6	-20	40	1.7	100	120	3	420	8

Figure 3-45: Test lineup for the pre-chamber injection timing sweep – Condition 1.

Pre-chamber injection pulsewidth was varied from 0 ms to 1.6 ms in 0.2 ms increments at a constant end of injection angle. Due to the constant end of injection angle, the change in pulsewdith corresponded to a linear change in injected fuel quantity. This test lineup is shown in Fig. 3-46.

1500 rpm 6 bar P/C Quantity											
Set Points : Coolant =90 ; CAC =40 ; Oil =90											
Point no.	Speed	BMEP	Int CAM	Exh CAM	Lambda	P/C Inj. Pressure	P/C Inj. Timing	P/C Inj. PW	PFI Pressure	PFI Inj. Timing	CA50
#	rpm	bar	deg	deg	-	bar	deg BTDC	ms	bar	leg BTD(	dBTDC
1	1500	6	-20	40	1.7	100	50	0	3	420	8
2	1500	6	-20	40	1.7	100	50	0.2	3	420	8
3	1500	6	-20	40	1.7	100	50	0.2	3	420	8
4	1500	6	-20	40	1.7	100	50	0.3	3	420	8
5	1500	6	-20	40	1.7	100	50	0.35	3	420	8
6	1500	6	-20	40	1.7	100	50	0.5	3	420	8
7	1500	6	-20	40	1.7	100	50	0.65	3	420	8
8	1500	6	-20	40	1.7	100	50	0.85	3	420	8
9	1500	6	-20	40	1.7	100	50	1	3	420	8

Figure 3-46: Test lineup for the pre-chamber injection pulsewidth sweep – Condition 1.

3.3.4.3 Sweeps of Engine Load

Another test to evaluate charge motion sensitivity under condition 2 knock-limited operation was a sweep of engine load at a constant speed of 3000 rpm and a constant λ of 1.7. The purpose of this test was to observe how comparative combustion performance amongst the charge motion variants changed from low loads up to knock-limited loads, and whether charge motion has a significant enough influence over knocking behavior that it dictates the knock-limited full load capacity under lean conditions.

BMEP was swept from 4 bar up to the load limit as dictated by excessive misfire cycles caused by overly retarded spark timing. Increments of 2 bar BMEP were used up to mid-load, and then 0.5 bar increments were used. The data was compared on an IMEPg scale. The test lineup is shown in Fig. 3-47.

3000 rpm lean load sweep										
Set Points : Coolant =90 ; CAC =40 ; Oil =90										
Point no.	Speed	BMEP	Int CAM	Exh CAM	Lambda	P/C Inj. Pressure	P/C Inj. Timing	PFI Pressure	PFI Inj. Timing	CA50
#	rpm	bar	deg	deg	-	bar	deg BTDC	bar	deg BTDC	dBTDC
1	3000	4	-20	40	1.7	100	50	3	420	MBT
2	3000	6	-20	40	1.7	100	50	3	420	MBT
3	3000	8	-20	40	1.7	100	50	3	420	MBT
4	3000	9	-20	40	1.7	100	50	3	420	MBT
5	3000	9.5	-20	40	1.7	100	50	3	420	MBT
6	3000	10	-20	40	1.7	100	50	3	420	MBT
7	3000	10.5	-20	40	1.7	100	50	3	420	MBT
8	3000	11	-20	40	1.7	100	50	3	420	MBT
9	3000	11.5	-20	40	1.7	100	50	3	420	MBT
10	3000	12	-20	40	1.7	100	50	3	420	MBT
11	3000	12.5	-20	40	1.7	100	50	3	420	MBT
12	3000	13	-20	40	1.7	100	50	3	420	MBT
13	3000	13.5	-20	40	1.7	100	50	3	420	MBT

Figure 3-47: Test lineup for the 3000 rpm lean load sweep – Condition 1.

3.3.4.4 Spark Retard Sweeps

For condition 3, a sweep of spark timing was performed at a constant speed, load, and λ with fluids chilled to 25˚C in order to emulate a CSSR catalyst heating condition. The specified speed and load are consistent with CSSR conditions for modern production engines, as confirmed by multiple engine manufacturers when developing the test plan. NMEP was held as the constant load parameter due to the reduced disparity in pumping losses amongst the charge motion variants at this condition, and for the traditional specification of NMEP as the relevant load for CSSR conditions.

Spark timing was retarded in order to generate a CA50 range from 0 degrees after TDC (dATDC) in 3 crank angle degree increments to the CA50 retard limit, as defined by the standard deviation of IMEPg achieving a limit of 0.4 bar or lowest normalized value of IMEPg (LNV) dropping below 40%. The equation for LNV is shown in Equation 3-3. These latter values excessive combustion instability and misfire cycle frequency. The base SI PFI engine CA50 retard limit was approximately 60 dATDC, and the pre-chamber charge motion variants were evaluated against this baseline performance.

$$LNV = \frac{IMEPg_{min}}{IMEPg} * 100 \qquad (3\text{-}3)$$

The key parameters involved in evaluation of CSSR performance included: combustion stability, specific exhaust enthalpy, and combined THC and NO_x emissions. Specific exhaust enthalpy increases as more of the combustion process is pushed into the expansion stroke and the mean in-cylinder gas temperature in proximity to EVO rises. Therefore, the CA50 retard limit greatly influences this parameter. Both criteria emission constituents are also influenced by combustion temperature history, and so CA50 retard limit has an influence here as well. Figure 3-48 shows the test lineup for evaluating condition 3 performance.

1500 rpm CSSR Spark Sweep										
Set Points : Coolant =25 ; CAC =20 ; Oil =25										
Point no.	**Speed**	**NMEP**	**Int CAM**	**Exh CAM**	**Lambda**	**P/C Inj. Pressure**	**P/C Inj. Timing**	**PFI Pressure**	**PFI Inj. Timing**	**CA50**
#	**rpm**	**bar**	**deg**	**deg**	**-**	**bar**	**deg BTDC**	**bar**	**deg BTDC**	**dATDC**
1	1500	2	-20	0	1.2	33	120	3	420	0
2	1500	2	-20	0	1.2	33	50	3	420	3
3	1500	2	-20	0	1.2	33	50	3	420	6
4	1500	2	-20	0	1.2	33	50	3	420	9
5	1500	2	-20	0	1.2	33	50	3	420	12
6	1500	2	-20	0	1.2	33	50	3	420	15
7	1500	2	-20	0	1.2	33	50	3	420	18
8	1500	2	-20	0	1.2	33	50	3	420	21
9	1500	2	-20	0	1.2	33	50	3	420	24
10	1500	2	-20	0	1.2	33	50	3	420	27
11	1500	2	-20	0	1.2	33	50	3	420	30
12	1500	2	-20	0	1.2	33	50	3	420	33
13	1500	2	-20	0	1.2	33	50	3	420	36
14	1500	2	-20	0	1.2	33	50	3	420	39
15	1500	2	-20	0	1.2	33	50	3	420	42
16	1500	2	-20	0	1.2	33	50	3	420	45
17	1500	2	-20	0	1.2	33	50	3	420	48
18	1500	2	-20	0	1.2	33	50	3	420	51
19	1500	2	-20	0	1.2	33	50	3	420	54
20	1500	2	-20	0	1.2	33	50	3	420	57
21	1500	2	-20	0	1.2	33	50	3	420	60
22	1500	2	-20	0	1.2	33	50	3	420	63

Figure 3-48: Test lineup for the CSSR spark timing sweep – Condition 3.

3.4 Data Analysis

3.4.1 Overall Engine Performance Metrics

Key engine performance metrics are defined in this section. Firstly, the load parameters are defined, as various engine tests employ different load metrics depending on the comparative influence of other parameters such as pumping work. Mean effective pressure is defined as:

$$MEP = \frac{P * n_R}{N * V_d} \tag{3-4}$$

Where P is engine power, n_R is the number of revolutions per power stroke, N is the engine speed, and V_d is swept cylinder volume.

The nature of MEP is dictated by the nature of the power term in Eq. 3-4. IMEPg uses power calculated as the work performed by the piston during the compression and expansion strokes. NMEP includes the pumping work associated with the exhaust and intake strokes. Since pumping mean effective pressure (PMEP) is typically work performed by the engine to transfer its working fluids, PMEP is nearly always a negative but is used as a positive term. Therefore, NMEP is typically lower than IMEPg. In engines, IMEPg, NMEP, and PMEP are calculated using data from the high speed in-cylinder pressure transducer. This is viewed as relatively high fidelity data when input data is entered correctly. The difference between IMEPg and BMEP is the friction mean effective pressure (FMEP), which encompasses the losses due to mechanical friction in the engine and driveline. BMEP is calculated from the measured shaft torque value at the engine driveline, with FMEP calculated as the difference between the IMEPg and BMEP values. FMEP is usually shown as a positive term despite the fact that it constitutes a power loss, so it is subtracted from NMEP. The relationships of these parameters are:

$$IMEPg = NMEP + PMEP \tag{3-5}$$

$$BMEP = NMEP - FMEP \tag{3-6}$$

In the present study, the introduction of the intake port inserts to generate charge motion affected the PMEP of the engine for a given operating point differently amongst the variants. These differences became most prominent under high intake air flow conditions, where the restriction caused by an insert significantly limited the ability of the engine to induct the required air quantity. This resulted in an adjustment of the throttle or increased boost pressure in order to compensate for the restriction. Under high flow conditions, therefore, the operating load held constant was IMEPg, which disregarded the pumping work required to provide the necessary air for the dictated fueling quantity and λ. Under lower air flow conditions, this restriction was much less prominent and could be disregarded, so lower load conditions used BMEP as the constant load term. BMEP is a more accurate reflection of real-world engine power and is the preferred load comparison term for multi-cylinder engines with realistic FMEP values.

Air-fuel ratio (AFR) and λ (normalized AFR) were measured from a wide-band O_2 sensor in the exhaust manifold or collector. For this testing, as in most engine testing, a production O_2 sensor was used. This sensor is a foundational sensor for the ECU, with fueling, throttle, and boost control dictated by the real-time sensor values. These production sensors are known for being increasingly imprecise the further away from stoichiometric conditions the engine operates. The wide dilution range tolerance of the jet ignition engine necessitates a high fidelity measurement of λ. For this study, an alternative measurement of a parameter known as Brettschneider AFR was used. Brettschneider AFR is calculated from the exhaust emissions to provide a high fidelity steady-state measurement of AFR. The O_2 sensor was correlated against this AFR measurement, and the offset was evaluated for consistency and accounted for in the control strategy. The Brettschneider AFR is calculated by:

$$\mathrm{AFR} = \left(\frac{[\mathrm{CO_2}] + \frac{[\mathrm{CO}]}{2} + [\mathrm{O_2}] + \left(\frac{n}{4} \cdot \frac{K}{K + [\mathrm{CO}]/[\mathrm{CO_2}]} - \frac{m}{2} \right) \cdot \left([\mathrm{CO_2}] + [\mathrm{CO}] \right) + \frac{[\mathrm{NO}]}{2}}{\left(1 + \frac{1}{[\mathrm{O_2}]_{\mathrm{Air}}} \cdot \frac{H}{2} \cdot \frac{M_{\mathrm{air}}}{M_{\mathrm{H_2O}}} \frac{[\mathrm{CO}]/[\mathrm{CO_2}]}{K + [\mathrm{CO}]/[\mathrm{CO_2}]} \right) \cdot \left(1 + \frac{n}{4} - \frac{m}{2} \right) \cdot \left([\mathrm{CO_2}] + [\mathrm{CO}] + [\mathrm{HC}] \right)} \right) \cdot \mathrm{AFR}_{\mathrm{stoic}} \tag{3-7}$$

Where *[XX]* corresponds to the dry volume fraction of the specific exhaust constituent, $[XX]_{air}$ refers to the dry volume fraction of O_2 in the ambient air, K refers to the water-gas reaction equilibrium constant, n and m refer to the fuel H:C ratio and O:C ratio, respectively, M_{air} and M_{H2O} refer to the molar mass of air and water, respectively, and AFR_{stoich} refers to the stoichiometric AFR of the fuel being used.

In the subsequent results Chapters, trends of several performance characteristics with enleanment are guided by a fuel energy breakdown based on the Thermodynamic First Law. The following explains the efficiency loss pathways included in this analysis.

The fuel supplied to the engine was measured by two Coriolis mass flowmeters, one dedicated to the main chamber fuel supply and the other dedicated to the pre-chamber fuel supply. The mass flowrates, $\dot{m}_{fuelp/c}$ and $\dot{m}_{fuelm/c}$, and lower heating value of the fuel, LHV_{fuel}, were used to determine the fuel power supplied to the engine, $\dot{Q}_{fuel}$, in accordance with Eq. 3-8.

$$\dot{Q}_{fuel} = (\dot{m}_{fuelp/c} + \dot{m}_{fuelm/c}) \cdot LHV_{fuel} \tag{3-8}$$

The brake thermal efficiency, BTE, was then computed using the brake power, P_{brake}, measured by the dynamometer.

$$BTE = \frac{P_{brake}}{\dot{Q}_{fuel}} \cdot 100 \tag{3-9}$$

High-speed pressure transducers mounted in the main chamber of the engine enabled the computation of $PMEP$ and $NMEP$. Using $NMEP$ and $BMEP$, $FMEP$ was calculated using,

$$FMEP = NMEP - BMEP \tag{3-10}$$

The MEP's were then used to determine pumping and friction power using equation 3-11:

$$P = \frac{MEP \cdot V_d \cdot N}{1200} \tag{3-11}$$

The exhaust heat loss is a measure of the sensible heat leaving the engine through the exhaust pipe. The power for each exhaust constituent species was defined as,

$$p_i = \frac{\dot{n}}{3600} \cdot 4.184 \cdot v_i \cdot \left[h_i(T_e) - h_i\left(T_{ref}\right)\right] \tag{3-12}$$

Where $\dot{n}$ is the exhaust molar flow rate, v_i is the exhaust volume fraction of constituent i, $h_i(T_e)$ is the sensible enthalpy of exhaust constituent i at exhaust temperature T_e, and $h_i\left(T_{ref}\right)$ is the sensible enthalpy of exhaust constituent i at the reference temperature of 25°C. The total exhaust power is then the summation of the power of all the constituent species.

The fuel energy lost due to incomplete combustion is a measure of the amount of high calorific value species present in the exhaust stream. This is also recorded as the combustion efficiency. In this analysis, H_2, CO, and THC were considered. H_2 was calculated using water-gas shift reactions. The power lost due to incomplete combustion was calculated using these species mass flow rates multiplied by their respective lower heating values.

The final category considered in this analysis was in-cylinder heat loss. This was calculated as the balance of the fuel power after all other categories were calculated. Therefore, this category also included other loss pathways, such as blow-by, which were not measured in this study. Heat transfer associated with engine and pre-chamber circuit coolant was not performed.

3.4.2 Pre-Chamber Performance Metrics

The high speed in-pre-chamber pressure measurement was used to evaluate pre-chamber combustion performance and stability. In this study, three metrics were used to describe pre-chamber combustion. The first was pre-chamber Pmax which is defined as the peak pressure inside the pre-chamber during the pre-chamber combustion event. The second is ΔP, defined as the maximum pressure differential between pre-chamber and main chamber during pre-chamber combustion, corresponding to the angle at which the pre-chamber pressure achieves a local maximum. Finally, pre-chamber combustion duration is the length of the pre-chamber pressure rise above that of the main chamber pressure in units of crank angles. The start and end locations are defined by the crossover points between main chamber and pre-chamber pressure. An example pressure trace is given in Figure 3-49 and annotated to further illustrate these pre-chamber combustion metrics.

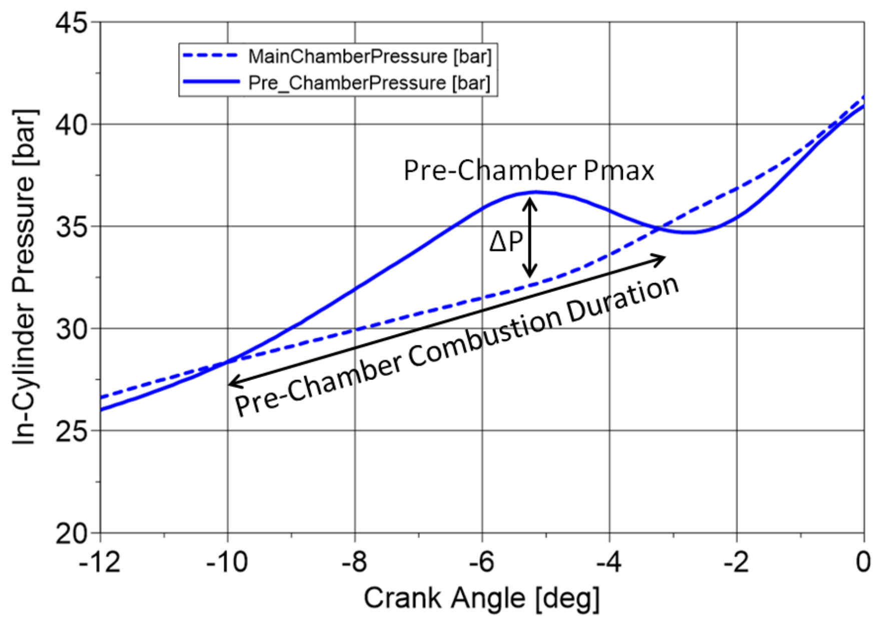

Figure 3-49: Pre-chamber pressure trace (solid line) and main chamber pressure trace (dashed line) during the pe-chamber combustion event with key pre-chamber combustion performance metrics annotated.

The variability of combustion metrics used in this study is captured by the coefficient of variation, a similar calculation but a distinct parameter from main chamber COV. This is defined by equation 3-13 as the standard deviation of variable i, s_i, normalized by the mean of variable i, $\bar{x}_i$.

$$COV_i = \frac{s_i}{\bar{x}_i} \tag{3-13}$$

The standard deviation was normalized by the mean of the same variable for all parameters in this study except for the COV of the angle of pre-chamber Pmax which was normalized by the mean of the pre-chamber combustion duration. This was done in order to ensure that the statistical analysis of the variability of the angle of pre-chamber Pmax was largely unaffected by spark timing which impacted the mean of that variable.

While several methods for aggregated indicative pre-chamber combustion stability were proposed, these metrics have not yet been evaluated extensively across the full engine operating map and across a wide range of engine operating parameters and pre-chamber geometries. It was therefore unclear which metric or metrics most accurately reflect true pre-chamber combustion stability, and which were most useful in predicting main chamber combustion stability behavior. These methods were employed in this study in order to determine which pre-chamber combustion metrics were most sensitive to charge motion, and which metrics if any actually reflected a potential transference of induced charge motion from the main chamber to the pre-chamber.

3.5 Summary

This chapter included details of the experimental platforms and test procedures used in this study. The MJI DI3 engine was described in detail, as was its use as a versatile test platform for studies that explore fundamental behavior. The design of the active pre-chamber assembly allowed for precise indexing with respect to the cylinder head to ensure consistent jet expulsion angular position within the combustion chamber. The pre-chamber assembly also incorporated a dedicated coolant jacket network with controllable temperature and flowrate to mimic a fully integrated cylinder head cooling jacket in a production-intent design scenario.

The engine incorporated a suite of sensors providing high accuracy data, including exhaust emissions, various temperatures and pressures, and high speed pressure from the pre-chambers and main chambers. The engine was controlled using the MFE, providing full manual control over specified parameters and closed-loop control to maintain load and λ within a dataset.

Direct in-pre-chamber sampling provided information about EGR evolution in the pre-chamber throughout the engine cycle. A thin capillary was inserted into the pre-chamber body, with vacuum pressure extracting a sample of the pre-chamber gases to measure CO_2 on a crank angle basis using a fast CO_2 emissions analyzer. Data from this experiment provided information about EGR sensitivities to engine parameters such as pre-chamber fuel quantity and main chamber λ, underpinning hypotheses on engine stability degradation under heavily throttled low load conditions.

The MJI DI3 engine incorporated inserts in the intake runner and port to induce varying levels and types of charge motion in the engine beyond the base intake port-induced tumble. The inserts were designed and evaluated using the MPT Air Flow Rig, which determined the static tumble ratio and swirl number of the intake system of the engine by recording data at manual intake valve lift increments and then integrating under the resulting valve lift curve. The inserts designed for this study produced moderate increases in tumble versus the baseline port, introduced swirl with a reduction in tumble versus the baseline port, and introduced a combination of swirl and increased tumble versus the baseline port. The relative changes in these values were quantified using the Air Flow Rig.

In order to evaluate combustion performance sensitivities to the charge motion variants, test plans were designed to probe performance under knock-limited, non-knock-limited, and CSSR operating conditions. These tests were designed to evaluate a broad range of operating scenarios, with a specific focus on induced combustion differences amongst the charge motion variants across λ, load, and spark timing ranges.

Data analysis included a fuel energy loss analysis based on the 1st Law of Thermodynamics using measured engine system parameters. Pre-chamber combustion stability was also analyzed using measured data from the high speed pressure transducers.

The experimental platforms and testing methodologies described in this chapter underpin the results and key findings presented in subsequent chapters. While the engine data describes real-world combustion response to charge motion, the detail provided by engine measurement is insufficient to fully grasp the underlying causal relationships, especially those related to differences in pre-chamber mixture preparation. In order to develop a comprehensive understanding of these sensitivities, the experimental approach described in this chapter is coupled with simulation. The simulation tool and methodology used are described in the next chapter.

Chapter 4

Modeling Techniques

4.1 Introduction

The previous chapter included discussion of the experimental platforms used in this study, particularly the MJI DI3 engine. This multi-cylinder engine platform provides the bedrock data of this study, with thorough examinations of engine performance sensitivity to charge motion under a variety of operating scenarios. The results from this engine provide valuable insight into combustion sensitivities on cycle-by-cycle and average bases. Despite the ample level of instrumentation on the engine, in-pre-chamber and in-cylinder processes can only be inferred, without any direct insight. A CFD model is needed in order to fully explore these fundamental processes. The CFD model allows observation of phenomena that are typically shielded from direct experimental observation, such as in-pre-chamber mixture preparation.

This chapter includes description of the CFD model setup and the key parameters most relevant to this study of charge motion sensitivities. The modeling methodology employed in this study takes precedence from previous work by the author and his colleagues to develop a model correlated to experimental single cylinder engine data. With the model correlated against experimental data, it was then used in a predictive manner for a wide range of engine applications across multiple market segments with success. For this study, correlation criteria with MJI DI3 experimental data was established on a macro level for the main chamber, whereby the matching was performed against the cylinder pressure trace at key event locations. While the exercise should not be considered a rigorous evaluation of model correlation to experimental data, the criteria used enables a high degree of confidence for qualitative assessment of the results.

The validity of this quasi-correlated approach will be described in this chapter. With the model results providing directionally indicative information, the appropriate interpretation of model outputs will be posited in this chapter. In this study, the model is used as an explanatory addendum to the experimental results. The model connects the level and type of induced charge motion to the measured combustion performance by describing the connective in-cylinder phenomena, including mixture preparation and combustion progress. In this way it also describes how charge motion induced in the intake port translates from predictable ordered motion in the main chamber to less easily predicted semi-ordered motion in the pre-chamber.

4.2 CFD Model

4.2.1 Model Setup

The numerical simulations were performed using Converge software version 3.0.21, which is a general purpose commercially available CFD code for calculating chemically reacting flow regimes. In the context of engine simulations, this code is able to simulate flows within complex geometries with moving boundaries. The CFD code is applied to a CAD file of the engine in STL format. The CAD file consists of the combustion chamber including wetted interior volume of the pre-chamber, the piston crown geometry, the liner, the intake ports upstream to the manifold boundary, and the exhaust ports downstream to the manifold boundary. The pre-chamber geometry includes the pressure transducer channel. The liner is created in the CFD code by specifying the engine bore. The piston boundary includes the crown geometry and the top ring. The moving boundaries consist of the piston boundary moving vertically within the liner and the intake and exhaust valves moving in and out of the combustion chamber at their respective valve angles. These movements are synchronized numerically to correspond to the physical synchronization in the engine. The cylinder chosen to be representative of engine performance is cylinder 1, and the CAD file corresponds to this cylinder geometry. An image of the CAD model is shown in Fig. 4-1.

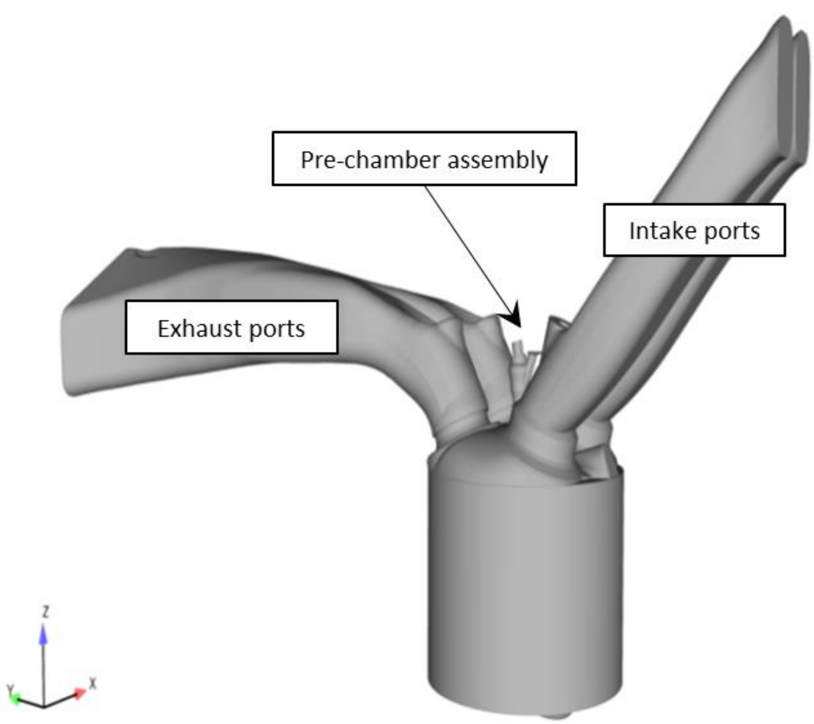

Figure 4-1: CAD image wetted volume of the MJI DI3 engine geometry.

Data input to the model includes engine geometric features, as well as valve lift information and piston height at the TDC location. Intake air flow conditions are taken from the experimental engine's high speed crank angle-resolved intake pressure measurement and confirmed using measured air flow from the air flow meter. Likewise, exhaust pressure is specified using exhaust pressure measurements from the engine, in this case the measurement is time averaged. Measured intake air temperature is input. Fuel flow parameters are taken from measured fuel injection pressure and injector pulsewidth cylinder 1, and are confirmed using the measured main chamber and pre-chamber fuel flow values. Calculated AFR in the model is cross-referenced with measured λ, providing a further confirmation of air and fuel flow parameter accuracy.

Metal surface boundary temperatures are specified using indicative values taken from temperature measurements on the engine that are in proximity to the specified boundaries. These estimates are well established for boundaries such as valve faces, liner, and piston crown, and were compared with data found abundantly in literature for light duty engines. In the initial model development stages, pre-dating this study, pre-chamber boundary temperature was determined using an iterative process that also involved proximal temperature measurements. All boundary temperatures are parameterized using a single value across the boundary. This is not reflective of the complex stratification of temperature across surfaces that is experienced the engine. This is especially prominent in the pre-chamber, where a wall-wetting event occurs when the pre-chamber fuel injector impinges liquid fuel on the opposite pre-chamber wall. This event results in a "cold spot" occurring at this location as the heat rapidly transfers from the wall section to the fuel, causing most of it to vaporize. This effect is not captured in this model.

The CFD code automatically produces a mesh throughout the interior surfaces of the geometry. The code employs a strategy known as Adaptive Mesh Refinement (AMR) to adaptively increase grid resolution where fluid flow is under-resolved as determined by gradients in temperature, pressure, or species. This allows fine mesh resolution in areas of interest while maintaining computationally efficient. In the simulations in this study, base grid size was 4mm. In the pre-chamber, AMR reduced grid size to 0.25 mm based on temperature gradients and 0.5mm based on pressure gradients. This level of grid refinement enabled detailed characterization of the cold flow field within the pre-chamber prior to spark timing, with even finer resolution of the flame front subsequent to spark timing as it consumed charge within the small volume of the pre-chamber. In the main chamber, AMR reduced grid size to 0.5mm based on temperature gradients and 1mm based on pressure gradients. In the intake, AMR reduced grid size to 1mm based on pressure gradients. The use of AMR effectively enables detailed tracking of the processes of interest in this study: in-pre-chamber mixture preparation, the pre-chamber combustion event, formation of the reactive jets, and the jet ignition process within the main chamber. Notably, this approach allows detection of minute differences in the in-pre-chamber flow field induced by the charge motion variants. Figure 4-2 shows an example of AMR as grid mesh resolution is increased to define the flame front and burned zone in greater detail than the surrounding volumes. Figure 4-3 shows this same AMR effect within the spark gap during spark kernel formation. The accuracy implications of differing levels of AMR embedding are demonstrated and discussed in Section 4.2.3.

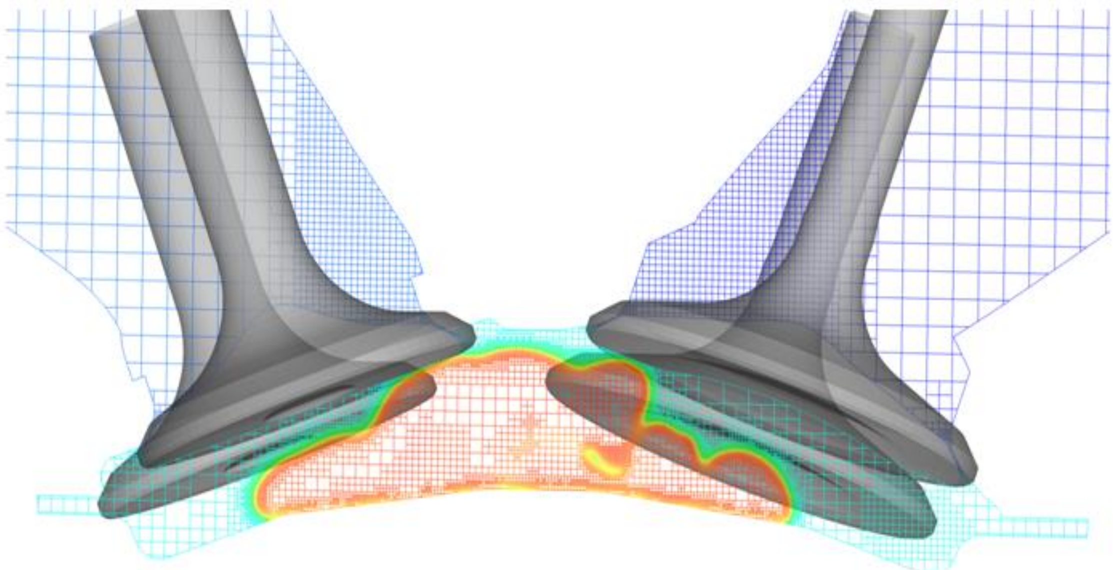

Figure 4-2: Cross section within the CFD mesh showing the AMR technique during main chamber flame propagation.

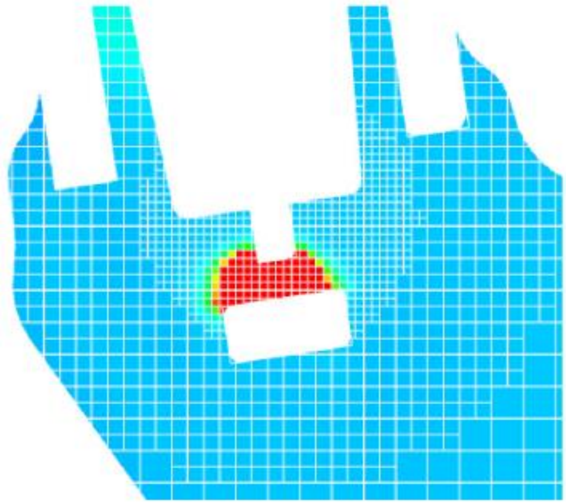

Figure 4-3: Cross section within the CFD mesh showing the AMR technique during spark kernel formation.

Rather than induce tumble or swirl motion artificially, the CFD model simulated the charge motion inserts in the intake port to generate model results analogous to the experimental data. The inserts were imported to the model using their respective CAD models, with location relative to the valve matched to the experimental installation. In order to resolve the flow upstream of the inserts, the intake ports were lengthened. This approach allowed the inserts to disrupt the ordered air flow in a similar manner to their physical function in the engine. Placing the intake boundary where the inserts begin would not generate the directional charge motion desired due to lack of proper directional air flow moving past the inserts.

Previous CFD effort by the author [132] has established that simplified combustion models such as G-equation, a turbulent flamelet-based model, are insufficient to capture pre-chamber and especially main chamber combustion processes in a jet ignition engine. This is due to turbulent flamelet-based models' inability to account for the flame quenching effect induced by the pre-chamber nozzle, as is described later. Instead a detailed chemistry approach is needed. The model used in this study adopts this approach, using an integrated chemistry solver available in the code, known as SAGE. This solver performs direct integration of detailed chemical mechanisms using reaction information in the CHEMKIN format within each grid cell. This detailed chemical kinetics approach adequately captures the pre-chamber combustion event, the partial quenching effect of the species as they move through the pre-chamber nozzle orifices, the jet ignition process whereby the jets form distinct auto-ignition sites within the main chamber, and the final flame propagation stage. Conversely, alternative combustion models such as G-equation rely on high turbulence intensity fluid flow regimes to dictate flame front location. This approach generally fails to capture the quenching effect instigated by the pre-chamber nozzle. The highly turbulent jets that proceed through the main chamber are therefore treated as distinct flame fronts, with no accommodation for auto-ignition site formation. In the author's experience this approach yields an incorrect understanding of combustion phenomena in jet ignition engines, leading to optimization pathways that are directionally opposed to demonstrated engine behavior.

The fuel used in the simulations is iso-octane in order to avoid the computational complexity associated with multi-component fuels. A skeletal reaction mechanism of iso-octane, developed by Jia and Xie [147], was used in this study. The particular mechanism was validated extensively in the literature against SI and HCCI experimental engines, with a particular emphasis on ignition phenomena, burn rate comparison, and exhaust emissions. The reaction mechanism involves 38 distinct species in 69 reactions. Jia and Xie developed the mechanism specifically for lean combustion systems (initially HCCI). The mechanism was developed through comparisons with a wide variety of experimental data from shock tube, rapid compression machine, stirred reactor, and HCCI single cylinder engine research platforms. In addition to achieving strong correlation to the experimental data, Jia and Xie found the skeletal mechanism identically matched results from more detailed mechanisms [148] in a fraction of the computational time. The good performance under lean conditions in particular has caused this mechanism to achieve wide adoption [149-151].

The main chamber is simulated using a fully pre-mixed fuel and air assumption. This assumption is generally consistent with a PFI configuration. The direct injection event in the pre-chamber is simulated using atomization and droplet formation models that use the equations developed by O'Rourke and Amsden [152]. The result of droplet collision can involve bouncing, stretching, reflexive separation, or coalescence. Spray/wall interaction was modeling using methodology developed by Naber and Reitz [153]. This modeling methodology was developed by the authors in coordination with Delphi (the supplier of the pre-chamber fuel injectors used in this study) as part of previous work. The validity of this modeling approach to the pre-chamber injection event has not been confirmed through experimental means. Confirmation of fuel spray behavior and spray/wall interaction inside the pre-chamber would require complex optical diagnostics that are beyond the scope of the current study and should be the subject of a dedicated research area. The pre-chamber injector spray pattern in a static environment and corresponding static flow curves were imported into the CFD code in order to ensure realistic fuel injector behavior. Fuel injector spray penetration and spray angle results for several injection pressure are displayed in Fig. 4-4. Spray pattern and plume width data for the injection pressure used in the CFD are displayed in Fig. 4-5. Figure 4-6 shows the static flow curves for several pre-chamber fuel injectors. This data was incorporated into the CFD model to ensure accurate representation of pre-chamber fuel injector operation.

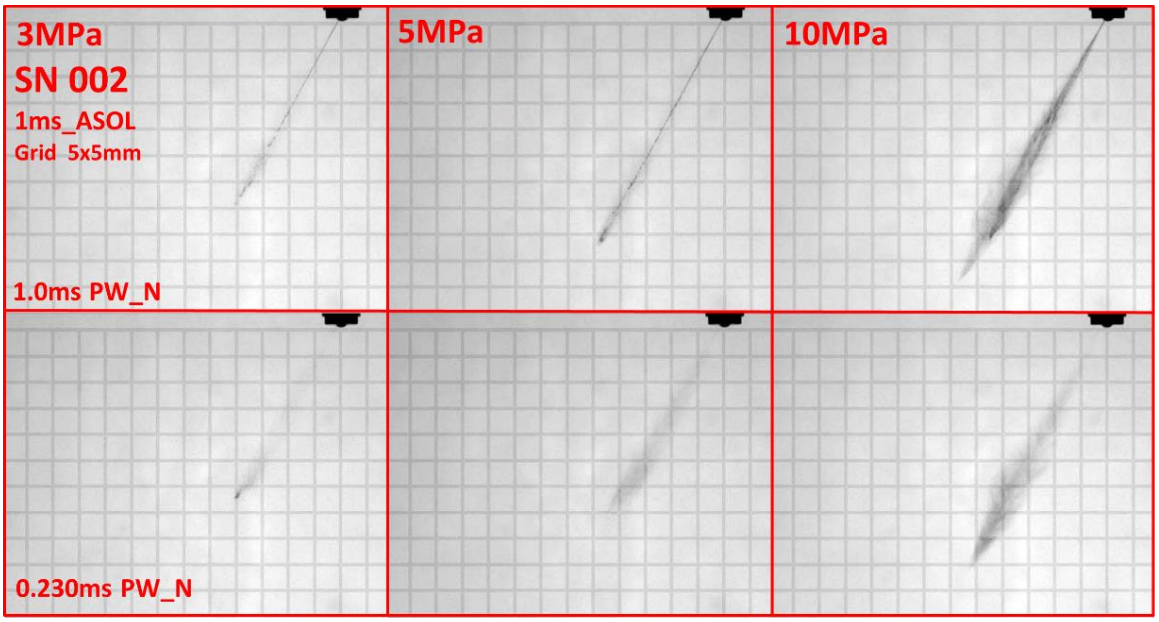

Figure 4-4: Pre-chamber fuel injector penetration, angle, and spray plume behavior for multiple static fuel injection pressure levels; Spray pattern information was used as a CFD input.

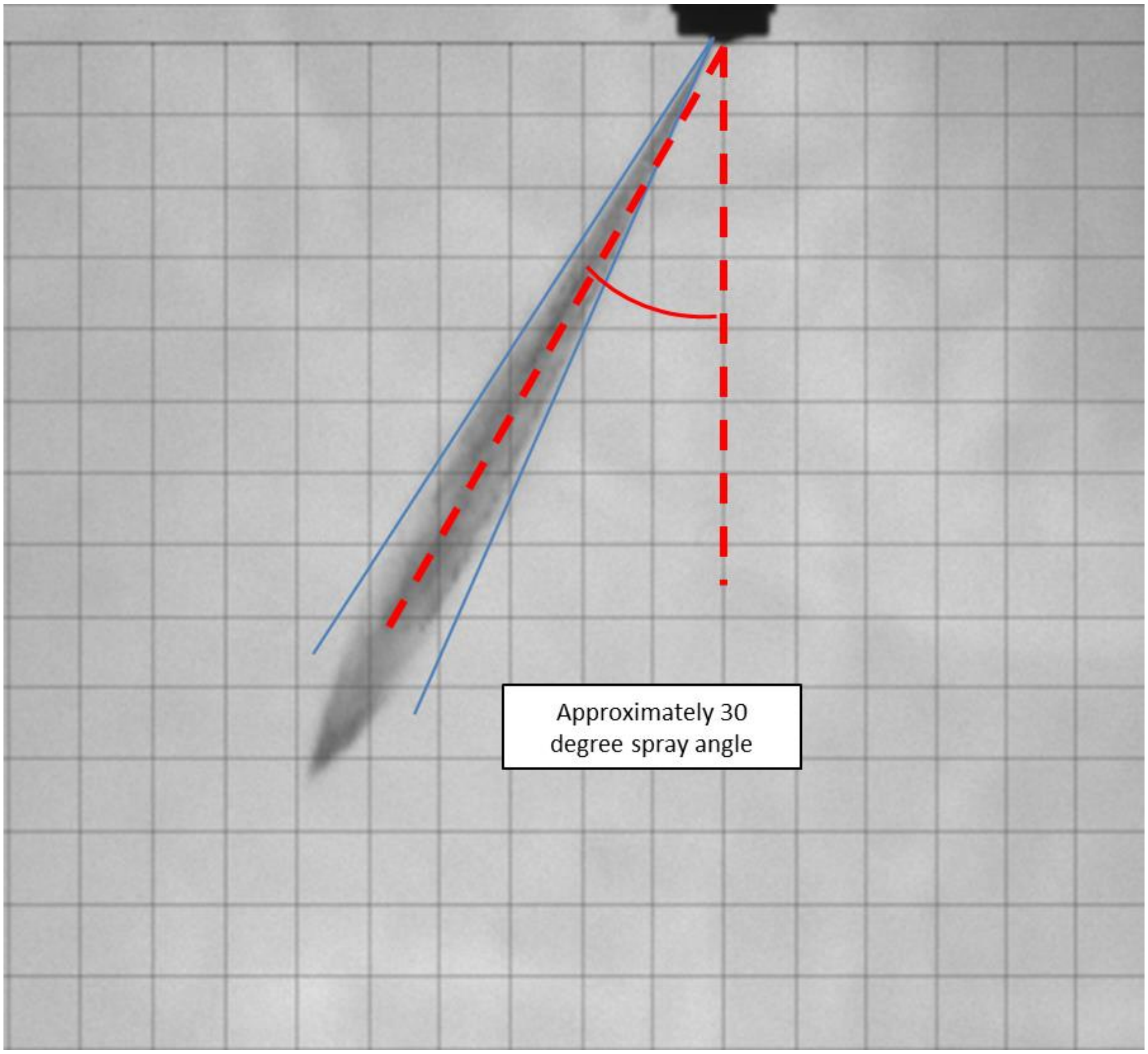

Figure 4-5: Pre-chamber fuel injector spray angle and plume angle at 10 MPA injection pressure, 1 ms pulsewidth; Spray pattern information was used as a CFD input.

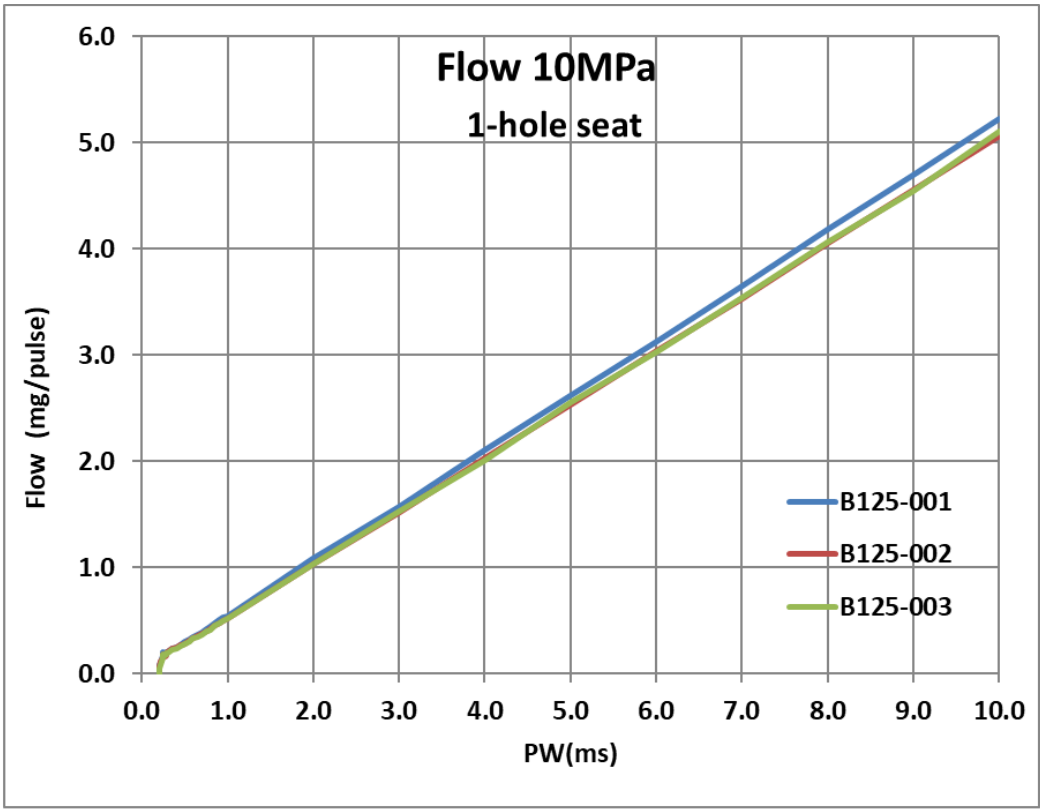

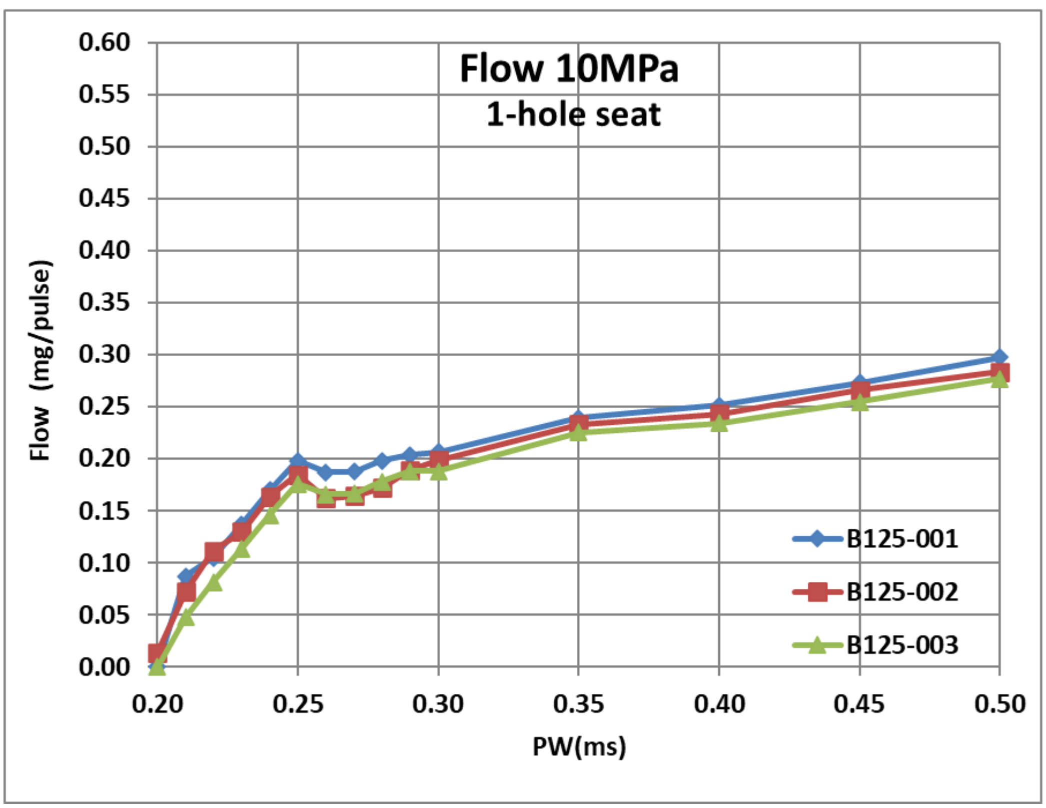

Figure 4-6: Pre-chamber fuel injector flow curves; flow information was used as a CFD input.

It should be noted that possibly because of the lack of validated fuel spray behavior, the pre-chamber pressure trace is typically the harder of the two in-cylinder pressure traces to match with experimental data. This is true in the author's own work and in the body of research generally [154,155]. Therefore in-pre-chamber events, particularly mixture preparation, can be considered to be approximated by CFD with no current feasible means of validation beyond the indirect and macro-level matching of main chamber pressure traces. CFD results from the pre-chamber are considered directionally indicative of actual events in this study.

CFD simulations were initialized at intake valve opening (IVO). Each simulation was run for 3 cycles and the results from the third cycle were compared with experimental data. The first cycle was initialized using an estimated residual fraction in the cylinder. The second cycle was initialized with residual contents resulting from the first cycle's combustion event. This multi-cycle approach allows the residual content and constituents to stabilize so that the third cycle in each sequence is initialized with residual contents in the cylinder that are representative of actual levels in the experiment. Practically this manifests as second and third cycle cylinder pressure and heat release results matching relatively closely. Additional cycles beyond the third offer minimal additional benefit. This is a commonly accepted approach for ensuring accurate residual content initialization [156].

The simulation methodology approach used in this study was developed through experience from previous studies. The process flow diagram of the CFD simulation approach is provided in Fig. 4-7. This approach has been used successfully in a wide range of commercial MJI programs.

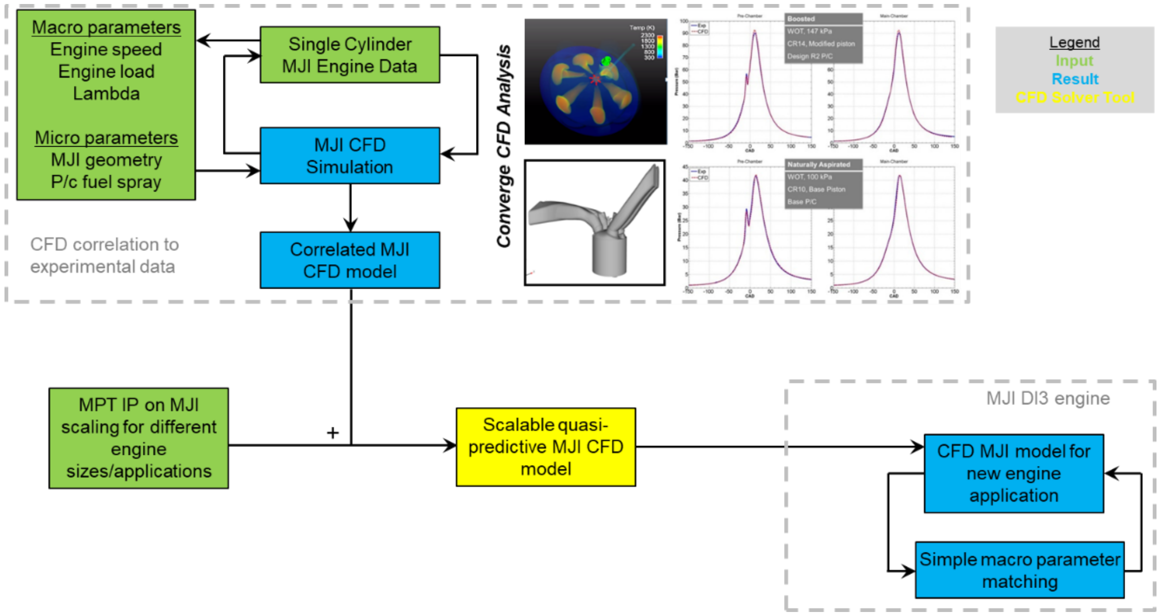

Figure 4-7: CFD methodology flow chart.

Initially, a CFD model of a single cylinder jet ignition engine was created. The methodology and sub-models were refined in an iterative arrangement as the model was correlated against a steady state experimental result. Correlation criteria including allowable error ranges on key model calculated parameters such as trapped mass in the cylinder at intake valve closing (IVC), cylinder pressure at time of ignition, and peak cylinder pressure. When the model results for these parameters fell within the respective allowable error bands, the validity of the establish modeling methodology was interrogated across macro engine parameters. These included different engine speeds, engine loads, compression ratio, and pre-chamber and main chamber lambda values. Modeling methodology and sub-models were again iterated until correlation was achieved across these macro parameters. The robustness of this correlation was then evaluated for its ability to track engine response as a function of changes to micro engine parameters. These encompassed parameters that were mostly specific to the pre-chamber such as small changes to pre-chamber geometry and pre-chamber fuel injection parameters such as quantity and injection angle. Once again, correlation was ensured by iterating the modeling methodology, sub-models, etc. until the model accurately predicted engine performance sensitivity to changes in micro parameters, and then this methodology was re-applied across macro parameters. The end result of this comprehensive process was CFD model that achieved correlation to experimental results across macro and micro engine parameters with a high degree of confidence.

With correlation established, MPT scaling relationships were incorporated into the model. These scaling relationships encompassed pre-chamber geometry and engine operation sensitivities across a wide range of engine bore sizes, combustion chamber geometries, and fuel types. When used in concert with the modeling methodology that produced results correlated to experimental data, a scalable quasi-predictive CFD model was established that can be scaled to the desired engine application and provide predicted engine performance results with a high degree of confidence.

This scalable quasi-predicted model was applied to the MJI DI3 engine. Simple macro parameter correlation, described later this in this chapter, was established. The comprehensive iterative correlation process established previously establishes the validity of the modeling approach to the MJI DI3 engine, and therefore the simple macro parameter correlation was considered adequate for the purpose of this study. As was previously established, in-pre-chamber processes are indicative only in this simulation approach, so further refinement of the model when applied to the MJI DI3 engine would not necessarily provide greater accuracy to processes of interest such as in-pre-chamber mixture preparation and its sensitivity to charge motion differences. Processes such as translation of induced charge motion in the main chamber to the pre-chamber are evaluated qualitatively any way, so further refinement provides only minimal value here.

4.2.2 Turbulence Model

Turbulence in the active flow domain was modeled using a Reynolds Averaged Navier Stokes (RANS) k-ε turbulence model. Within the unsteady flow field, enhanced mixing due to turbulence is accounted for with the addition of turbulent viscosity, conductivity, and diffusion terms. The addition of turbulent diffusion coefficients causes the smallest flow scale size to be increased. In typical RANS simulations, the smallest flow scale grid size is 0.1 mm. A further increase of the grid resolution beyond this value offers no improvement in model accuracy since there is no longer any smaller scale turbulence to resolve. Because of this pegging of minimum grid size within the active flow domain, AMR can be strategically introduced to resolve the smallest necessary grid size in high turbulence environments such as the pre-chamber while the remainder of the grid outside of the active flow field or even outside of the area of high turbulence can remain coarse.

While this RANS-based approach significantly reduces computational time and complexity, it does not capture very small scale turbulence fluctuations in the flow field. These fluctuations can alter flame shape, and perhaps of most relevance to the current study, jet shape and characteristics. The jet expulsion event tends to be highly turbulent, as is apparent from images taken from optical engines. The RANS simulation cannot capture the smaller scale turbulence present in the jet flow field, instead capturing jet qualities akin to mean flow values. Qualitatively, this results in jet shapes in the RANS simulation that look overly smooth when compared to optical engine observations. Brief studies of Large Eddy Simulation (LES) models, which do capture these small scale turbulent effects, show qualitative jet shape and behavior similar to optical engine observations. The jet qualities of note extracted from the RANS simulations, such as jet velocity and penetration length, can therefore be used for comparative purposes amongst the charge motion cases evaluated. Figure 4-8 provides a qualitative comparison between RANS and LES simulation approaches.

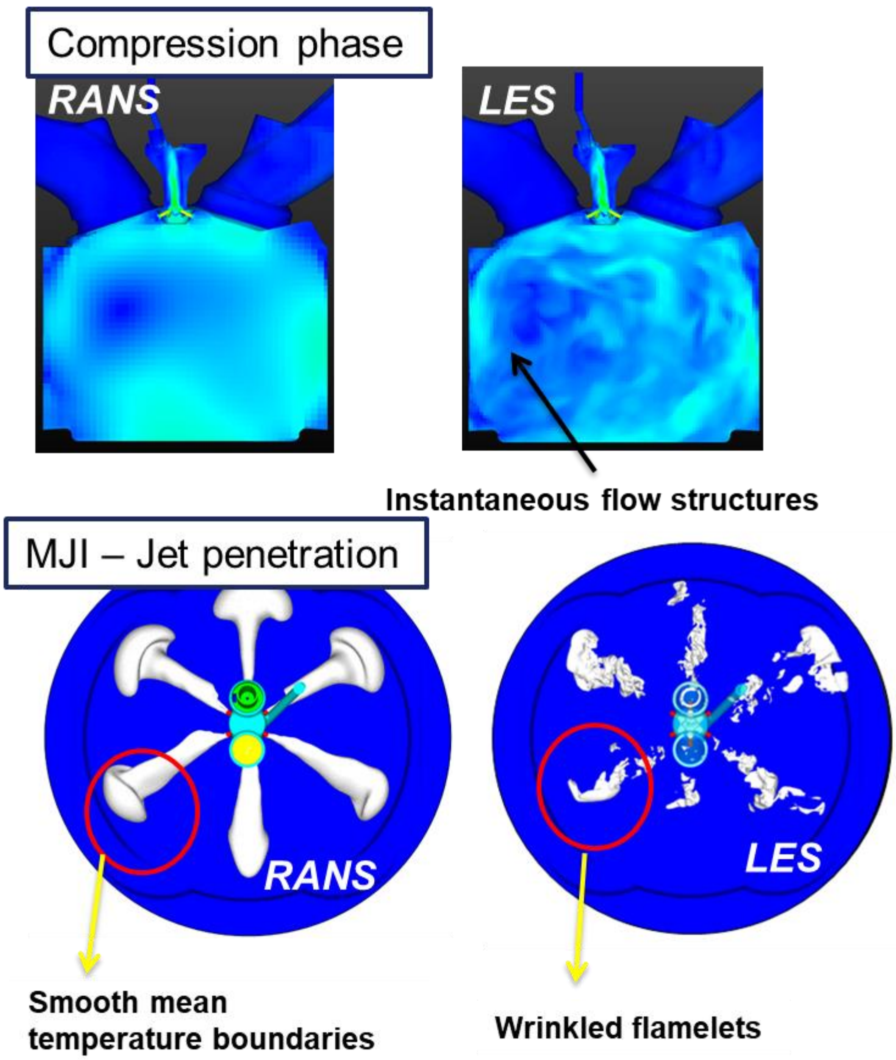

Figure 4-8: Qualitative comparison of RANS and LES simulation approaches to in-cylinder flow structure (top) and jet expulsion (bottom); white color in the bottom represents an iso-surface temperature of 1800K.

4.2.3 Grid Convergence

Grid size was determined through a grid convergence study. The AMR function of the code allows for increased grid resolution within areas of interest. AMR also allows increased resolution in flow fields with elevated temperature, pressure, or specific species. A relatively coarse base grid can therefore be used in order to reduce computational intensity of the simulation.

The model platform used in this study has been used in numerous other studies, so there was some precedence for the grid and AMR sizes chosen. The inducement of increased levels of charge motion in these simulations, and the importance of tracking motion within both chambers led to a refinement of the grid size selection approach. A high speed, high load condition was chosen in order to generate an in-cylinder environment with complex, fast-moving flow fields.

Figure 4-9 shows a qualitative comparison of grid resolution within the combustion chamber of the two selected grid resolution levels: a coarse grid consisting of 4mm base grid size with a minimum AMR grid size of 1 mm tracking temperature gradients in the main chamber, and a fine grid consisting of a 4mm base grid size with a minimum AMR grid size of 0.5 mm tracking temperature gradients in the main chamber. Comparing against experimental data in Fig. 4-10 it is apparent that the finer grid resolution level is a superior match with the experimental in-cylinder average pressure trace than is the coarser grid resolution level. Comparative mass in the cylinder is shown in Fig. 4-11, and it is again evident that the finer grid resolution level proved a better match to the experimental data than in the coarser grid case. As a result, the finer grid resolution was chosen for this study, as an adequate balance between accuracy and computational time.

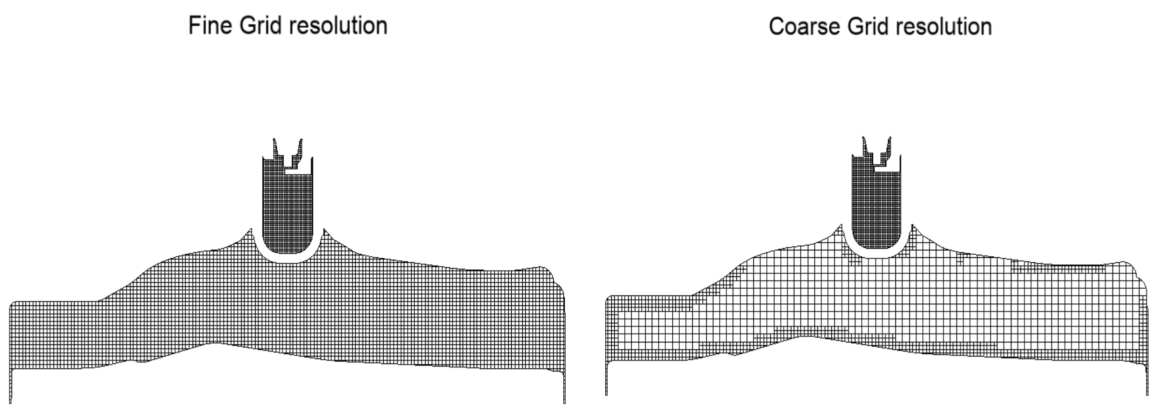

Figure 4-9: Qualitative comparison of grid resolution in the two cases considered in this study.

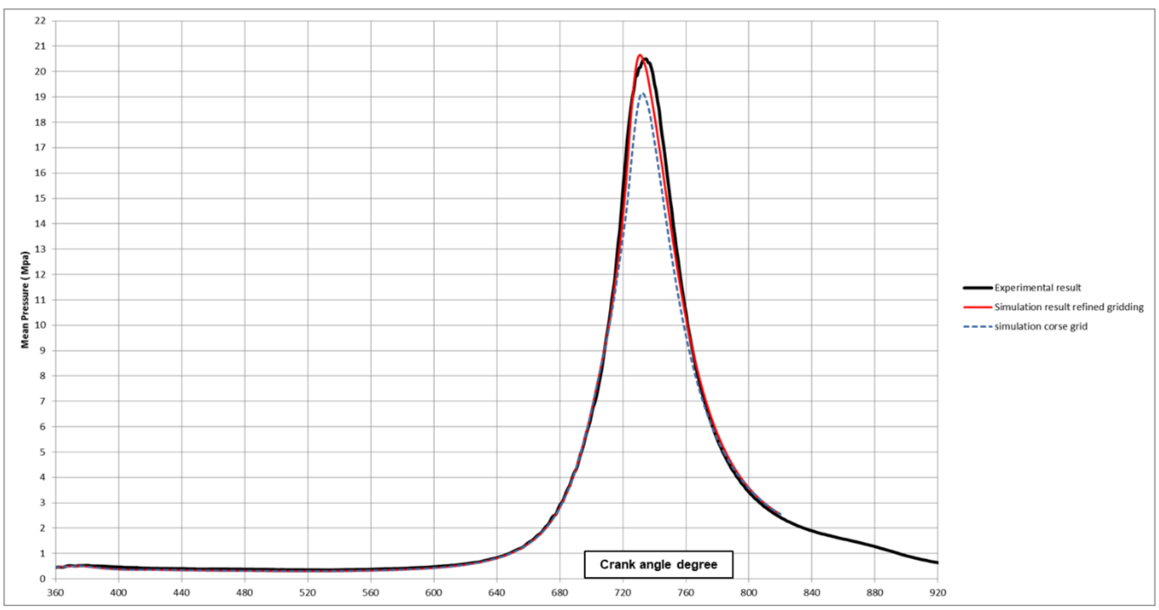

Figure 4-10: Main chamber pressure comparison amongst experimental data and the two grid resolution cases considered in this study.

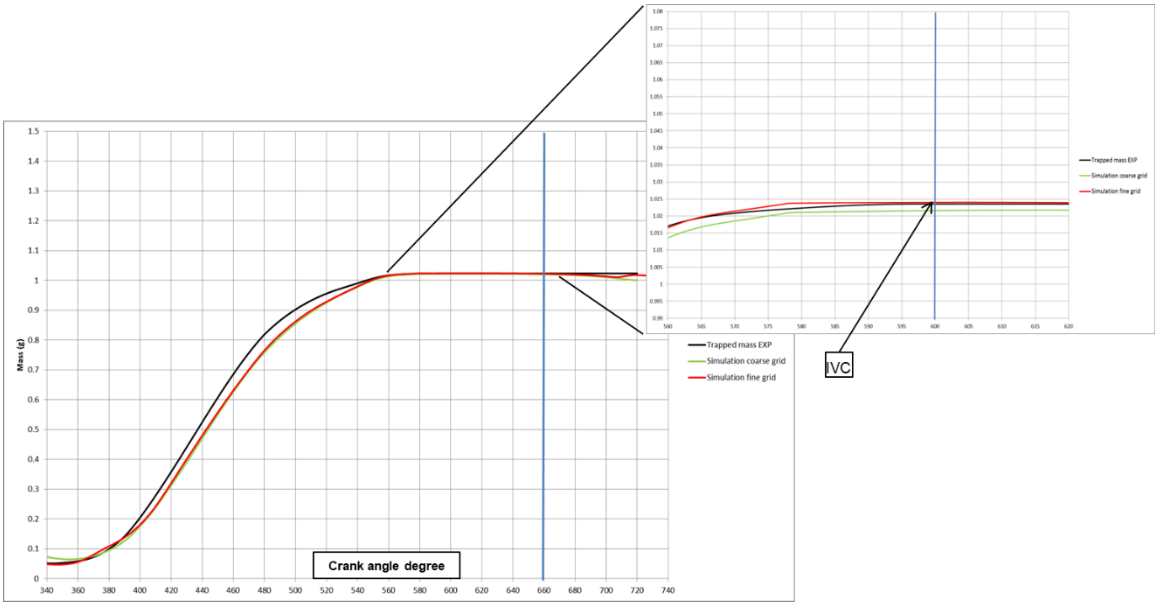

Figure 4-11: In-cylinder mass comparison amongst experimental data and the two grid resolution cases considered in this study.

4.3 Model Usage

The model was used to simulate engine performance with each charge motion variant at the 4000 rpm, 8 bar BMEP operating condition present in the test plan for the MJI DI3 engine. A λ of 1.7 was selected. It was assumed that this lean, relatively high speed condition would produce the greatest discrepancy in engine performance amongst the charge motion variants. Charge motion, especially TKE, is known to influence flame speed. This influence is more pronounced under lean conditions where the lean flame speed is relatively slow compared to the flame speed under stoichiometric conditions. At high engine speed conditions, relatively slow flame speeds and long burn durations can result in a high degree of incomplete combustion, as the encroaching flame front attempts to consume charge in an environment that is expanding at a faster rate than is typical at other locations in the engine map. The rapid volume expansion leads to rapid decrease in unburned charge temperature, potentially arresting combustion. Due to this effect, it was assumed that the variations in charge motion would produce more prominent disparities in combustion efficiency and late burning (CA50-90). Because of the fidelity of the CFD simulations used in this study and the directional nature of the expected results, conditions that produce large performance discrepancies in the experimental data that may then propagate to the simulations are ideal. If the experimental data for a given condition showed only subtle differences in engine performance, regardless of the significance of these parameters, the simulation would likely not be able to track these differences with sufficient resolution, leading to inaccurate assumptions of causal relations.

As will be shown in Chapter 6, the 4000 rpm condition did in fact display the most prominent differences in experimental engine performance amongst the charge motion variants. As predicted, late burn durations especially at lean conditions exhibited notable separation amongst the variants. This confirms the validity of selecting the 4000 rpm condition for simulation development. The selected λ of 1.7 ensured sufficiently lean operation to maximize the differences amongst the variants while also maintaining strong combustion stability. Data at leaner conditions would have displayed combustion stability near the limit of acceptability for the engine. Simulating engine performance at a condition that is relatively unstable would have led to a high likelihood of the simulation tracking a snapshot of this instability rather than reflecting the average result.

A simple macro parameter correlation approach was used in this study. The primary focus for correlation is on matching the experimental pressure traces with the simulated pressure trace result. In the experimental engine, burn parameters are calculated from the main chamber high speed pressure trace. In CFD, however, the simulation resolves the chemical reaction kinetics in each grid, combines them to characterize the full combustion process, and then calculates the in-cylinder pressure rise from this characterization. The pressure trace is therefore a good candidate for evaluating macro level correlation since it is a measured parameter in the experiment and a fundamental parameter that the simulation resolves. Engine performance, even in the case of the pre-chamber engine, is dictated by main chamber combustion so the pressure trace of particular interest for the simulation is the main chamber trace.

There are key in-cylinder events that are reflected in the pressure trace that are used to define the validity of the match. These are illustrated in Fig. 4-12. The first key event is IVC. In-cylinder pressure at IVC is indicative of the total trapped charge mass in the cylinder. Coupling this result with air-fuel ratio in the case of SI engines provides an understanding of fuel mass trapped in the cylinder. Subsequent heat release results are highly sensitive to this figure, as the fuel energy is a fundamental parameter determining energy release during the combustion process. This makes it imperative to match pressure at IVC between the two pressure traces in question. Other important parameters that influence this result include fundamental engine geometry such as CR, and boundary conditions such as intake and exhaust temperature and pressure.

The second key event is the angle of introduction of the ignition source. In SI engines this is the spark timing. For the MJI DI3 engine, this is also the spark timing, despite the fact that the spark plug is segregated in the pre-chamber. Spark kernel formation and other aspects of early combustion are sensitive to the background pressure in the cylinder at spark timing. Spark kernel formation is in turn heavily influenced by species mass fraction within the cylinder and the wall heat transfer model, so this event presents another check of model initialization. Despite the fact that the spark plug in this study is located in the pre-chamber, pressure at spark timing remains an important parameter; at this crank angle, pre-chamber and main chamber pressure are essentially identical.

The third key parameter for the pressure trace correlation is the start of heat release. This is when pressure due to the combustion event increases sufficiently so as to begin to generate energy. This would be the angle at which combustion pressure first deviates detectably from motored non-firing pressure. In SI engines there is typically a short ignition delay between Points 2 and 3. The angular location of this event in the simulation is influenced by fuel injection and mixing and liquid fuel evaporation. In the case of the pre-chamber engine this point typically corresponds to the first emergence of reactive jets from the pre-chamber. Though it is arguable that combustion has not yet occurred in the main chamber at this point, the pressure rise in the pre-chamber due to pre-chamber combustion cause jets, initially non-reactive, to enter the main chamber at high velocity, contributing to a small but detectable rise in main chamber pressure. This pressure event is then quickly superseded by the subsequent jet-induced main chamber combustion. This event therefore provides an indication of the validity of the simulated pre-chamber combustion event, and all of the associated inputs such as pre-chamber fuel injection timing, quantity, spray pattern, and vaporization rate.

The fourth key parameter is the peak heat release. This is evaluated by the angle at which the rate of heat release reaches its peak. This angle is typically near the angle of peak cylinder pressure. The value and angle of this event in simulation are influenced by both initialized parameters and model resolved results. The former includes the lower heating value and other properties of the simulated surrogate fuel, injector spray targeting, and mesh resolution. The latter includes mixing dynamics and compressed charge temperature. A mismatch in angular position between experimental data and simulation results indicates the simulated combustion proceeding in a manner inconsistent with that of the experimental data, and it is highly likely that all subsequent pressure results will not match the experimental result.

The final parameter for evaluating cylinder pressure matching is not tied to a specific event but typically occurs approximately midway in the expansion stroke. This post-combustion parameter captures late combustion behavior. It is a parameter that is highly sensitive to the preceding 4 key pressure events. It is also influenced by real-time temperatures throughout the grid. Lower than expected temperatures in this part of the cycle can arrest reaction kinetics, resulting in poor combustion efficiency and a pressure discrepancy between simulation and experimental results. A mismatch in this parameter also portends incorrect cylinder pressure at EVO, which would lead to incorrect species concentration remaining in the cylinder in the subsequent cycle, leading to propagating inaccuracies.

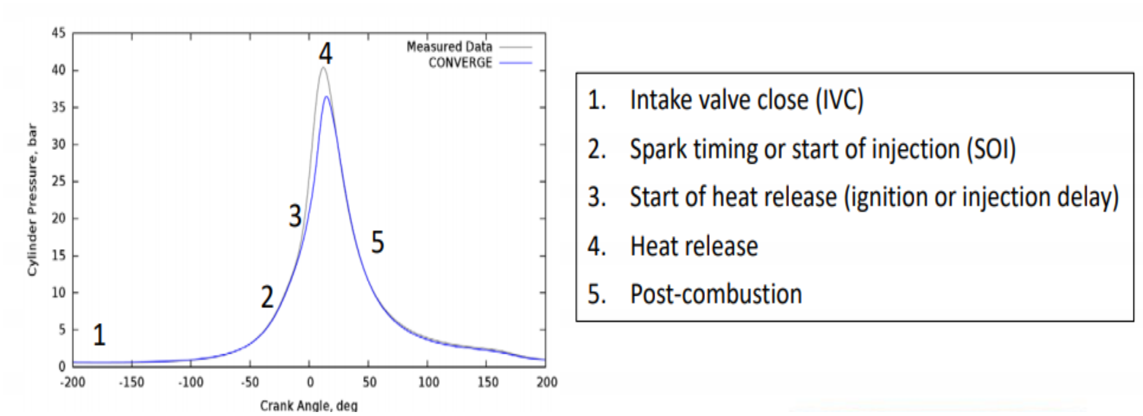

Figure 4-12: Key engine events reflected in the main chamber pressure trace and their approximate angular locations.

In order to accurately reflect experimental engine behavior, the initialized simulation parameters were iterated until the simulated pressure trace achieved an acceptable match with the experimental pressure trace. This exercise was carried out for each charge motion variant. All iterated parameters were held constant across all four charge motion variant simulations. This helped to ensure that the correlation strategy was consistent and captured universal behavior, rather than tracking experimental noise or other non-universal effects. Only initialized parameters that did not have a direct high fidelity experimental measured value were iterated. Commanded inputs such as spark timing and fuel injection parameters were not iterated. Data was input and pressure was matched against a single cycle of the experimental result. The single cycle was selected due to its reflection of the 300-cycle average pressure result. Figure 4-13 shows a typical qualitative match between experimental pressure trace and simulated pressure trace. Figure 4-14 shows the match within the area of interest.

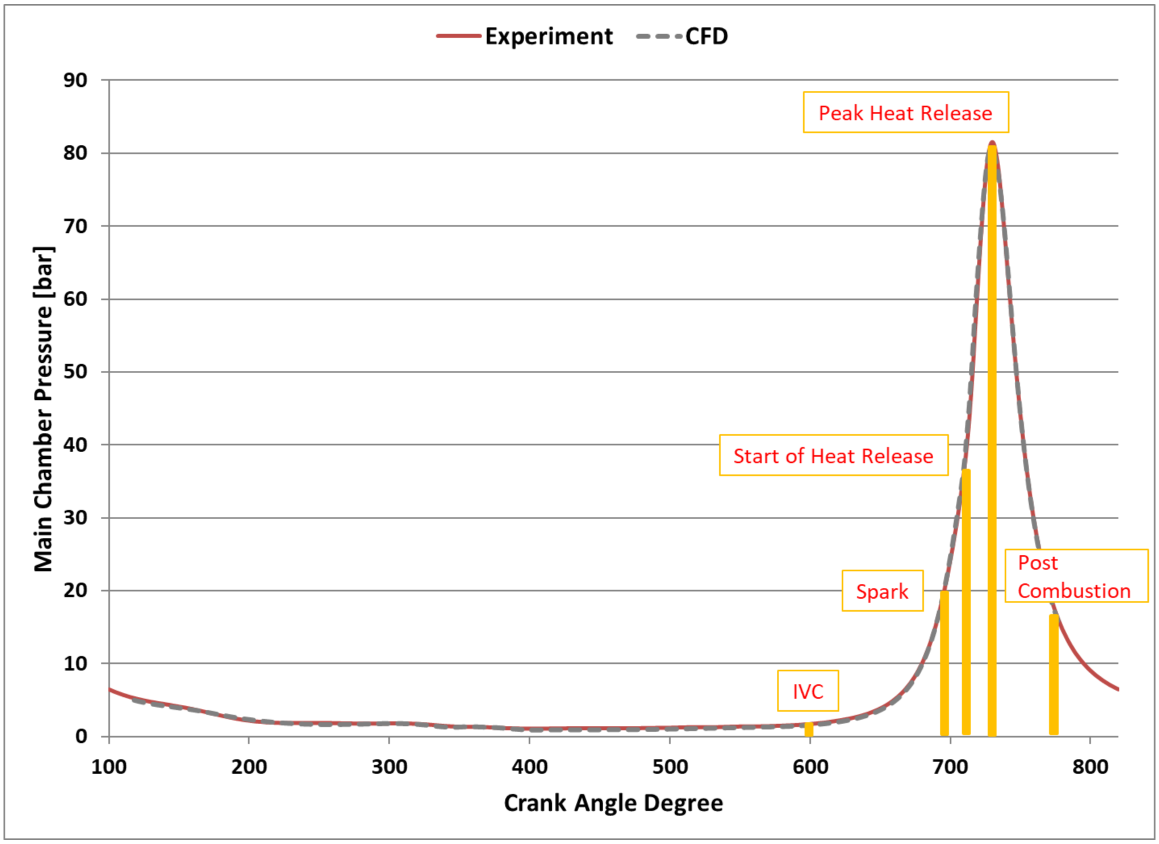

Figure 4-13: Key engine events reflected in the main chamber pressure trace, and qualitative match between simulation and experimental results.

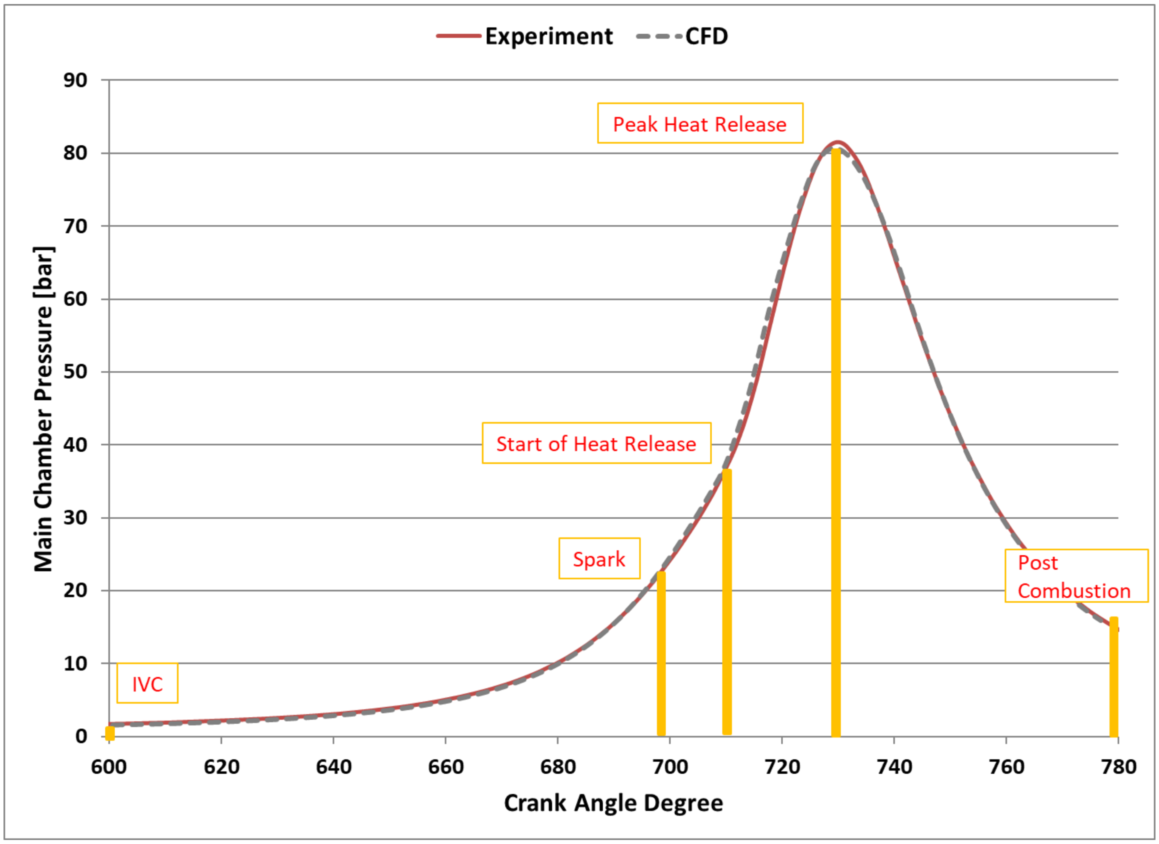

Figure 4-14: Key engine events reflected in the main chamber pressure trace, and qualitative match between simulation and experimental results – area of interest.

The maximum allowable discrepancies between the experimental and simulated main chamber pressure traces are shown in Table 4-1. Pressure at the key events described above and angular position of these events are the main criteria for evaluation. The largest allowable discrepancy on either pressure or angular position is 5% from the experimental result. These larger allowable discrepancies mainly apply to the events well downstream of the initialized parameters, such as peak heat release and post combustion. Most of the parameters have an allowable discrepancy of 2% or less from the experimental result. These relatively tight maximum allowable discrepancies help to ensure that combustion behavior and especially burn durations in the simulated result closely reflect the experimental result.

The simulation results should be considered relatively accurate with a good degree of confidence. Due to the nature of this macro correlation focused exclusively on main chamber pressure, the simulation results are indicative in nature. The magnitude of the result can be treated with less confidence due to the lack of correlation applied directly to the pre-chamber pressure trace, but the relative magnitude of the results amongst the four charge motion variants can be considered with a high degree of confidence.

Table 4-1: Maximum allowable discrepancies between experimental main chamber pressure trace and simulated main chamber pressure trace in order to achieve correlation.

		Maximum Discrepancy
Pressure	IVC	5%
	Spark/SOI	1%
	Start of Heat release (Ignition or Ignition delay)	2%
	Heat release	5%
	Post combustion	5%
Trapped mass		1%
Intake mass flow rate		2%
Location of Pressure value	IVC	5%
	Spark/SOI	1%
	Start of Heat release (Ignition or Ignition delay)	2%
	Heat release	5%
	Post combustion	5%

4.4 Summary

While experimental engine results are critical to evaluating relative performance differences amongst the charge motion variants, high fidelity CFD simulation is needed to uncover causal relationships that are shielded from observation through experimental methods. Key in-cylinder processes that prove difficult to experimentally observe but are critical to understanding pre-chamber engine sensitivity to charge motion include in-pre-chamber mixture preparation and pre-chamber combustion.

In this chapter the modeling methodology and its efficacy were described. A methodology for macro correlation with the main chamber experimental pressure trace was also described in detail. Because of the correlation approach used in this study, the results can be interpreted as indicative of real-world behavior, and the relative magnitudes of the results amongst the four charge motion variants will be discussed in the results chapters. Correlation criteria were listed in Table 4-1; adherence to these criteria constitutes a high quality match between experimental and simulation data.

Chapter 6 will explore the degree of correlation achieved between the simulation and the experimental results for the four charge motion cases. With correlation established, the simulation results will be harmonized with the experimental results to help explain underlying causes for the results observed. This will include an examination of pre-chamber charge motion sensitivities as well as main chamber sensitivities.

Chapter 5

Jet Ignition Engine Operation Under Low Load Conditions

5.1 Introduction

5.1.1 Applicability of Jet Ignition Across the Engine Map

Modern SI engine maps span numerous regions that each possess their own distinct primary efficiency loss pathways and operational challenges. This modern engine versatility requirement has historically proven difficult to overcome for advanced combustion technologies. While technologies such as HCCI or corona ignition can be well optimized for a given part load condition, the applicability of these technologies across the engine map can be limited. For example, HCCI tends to produce excessive Rmax under high load conditions and corona ignition sensitivity to breakdown voltage requires careful tuning of the power electronics to accommodate minute shifts in background cylinder pressure. The applicability of any new combustion technology, jet ignition included, across the full engine map must therefore be interrogated as part of a larger assessment of commercialization potential.

Through the author's research, and through a review of jet ignition research, one main topic has been identified that needs to be addressed in order to ensure applicability of jet ignition to the demands of modern SI engine maps [157,158]. This is performance under low load conditions, particularly catalyst heating operation. Low load performance limitations are the main impediment to developing a jet ignition concept that can effectively span the entire engine operating map.

This low load challenge manifests in two distinct ways; poor combustion stability under heavily throttled low load (less than approximately 2 bar BMEP) and limited spark retard capability at idle and catalyst heating, or CSSR conditions [159,160]. The well documented efficiency benefits of jet ignition at part load and high load [3,4,161] cannot be practically translated to non- and mild hybrid engine applications unless a solution to the low load pre-chamber limitation is identified.

Poor combustion stability under low load conditions translates to sharper than typical thermal efficiency and combustion efficiency deterioration under these conditions. This includes some operating residency points in vehicle drive cycles, especially those cycles that skew towards lower load operation, thereby impacting cycle fuel consumption and possibly even tailpipe emissions. The low load stability challenge also has implications for the likelihood of achieving successful combustion in the first few cycles upon cold start.

The most impactful challenge posed by the low load spark retard limitation concerns the ability to heat the aftertreatment catalysts upon cold start. The tailpipe emissions produced by vehicles are more significant during the startup phase prior to catalyst light-off than they are at any other point in a legislated vehicle drive cycle. Catalysts require heat input to operate effectively. Prior to achieving a high temperature light-off condition and catalyst activation temperature a large proportion of the engine-out emissions pass through un-catalyzed or uncaptured to the tailpipe. Aggressive warm up of the catalysts is therefore critical to ensuring that the vehicle can meet legislated emissions requirements. The common solution to ensure rapid heat input to the catalyst is to retard spark timing to such a degree that combustion occurs exclusively during the expansion stroke. The much later burning process results in both increased exhaust temperature and increased exhaust flow. The latter results from the non-optimal combustion phasing requiring de-throttling to compensate for the load deficit that occurs as a result of the poor thermal efficiency. This poor thermal efficiency is purposeful since a large proportion of the combustion process has minimal contribution to torque and instead is used largely to generate heat. Spark retard, and its ability to generate high exhaust enthalpy, therefore is an essential element of CSSR operation, which makes pre-chambers' nominal lack thereof a major impediment to the applicability of the technology to modern SI engines.

Several theories have been proposed as to the cause of the low load limitation for jet ignition concepts. The most popular hypothesis is that the heavy throttling associated with low load operation impedes the pre-chamber purging process. In this process, residual gas from the previous cycle's combustion event is replaced with intake air and fuel. As will be described in the next section, this process is highly pressure driven, and the low pressure intake process caused by heavy throttling prevents adequate gas exchange. This assumption is widely held, and many commercialized active heavy duty (HD) natural gas (NG) engines employ a pilot injection event in the pre-chamber, as early as the start of the intake stroke, in order to facilitate the purging of residual gases [162,163]. This pilot injection event can be the sole pre-chamber injection event or can be supplementary to a secondary injection event later in the cycle prior to spark timing. Regardless of its place in the larger pre-chamber injection strategy, the primary purpose of the early pilot injection event is to purge residual gas from the pre-chamber. Figure 5-1 illustrates this process, with the pilot injection event occurring early in the intake stroke for the express purpose of purging pre-chamber residuals.

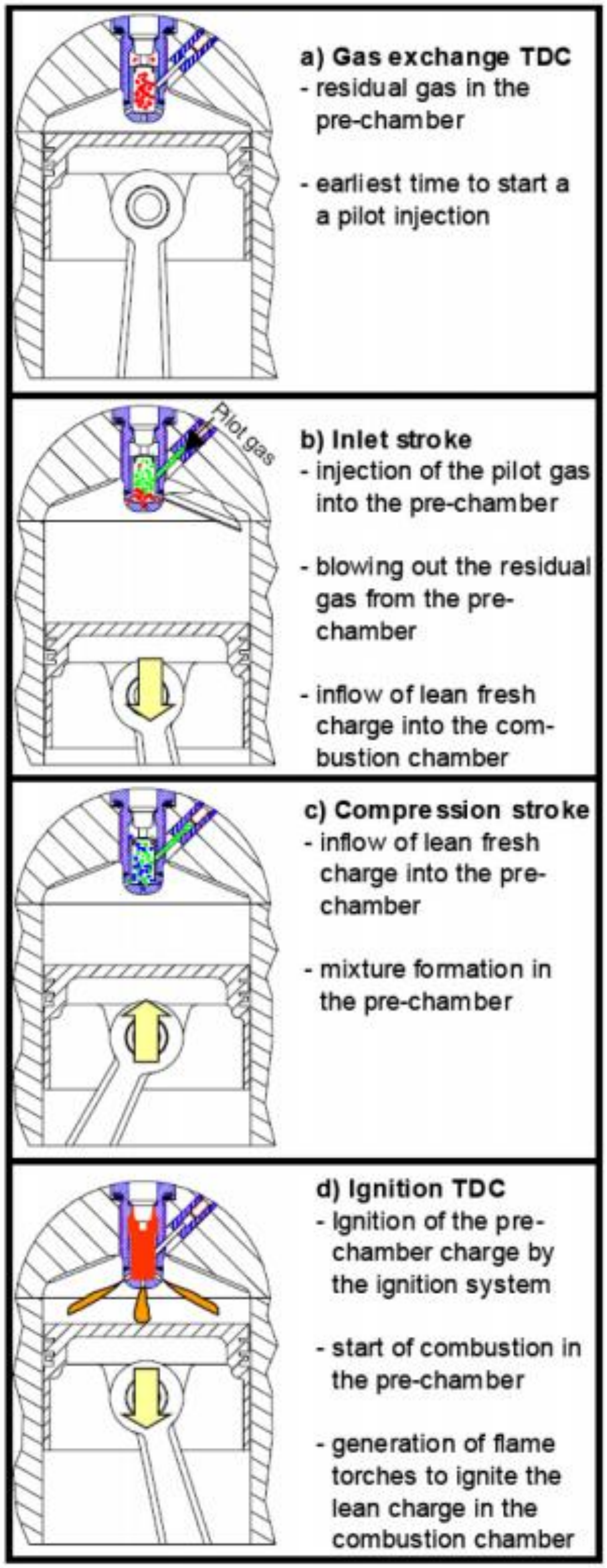

Figure 5-1: Principle of pilot injection in the pre-chamber [163].

While this hypothesis has some validity, as will be confirmed in subsequent sections, it does not adequately explain the spark retard limitation under CSSR conditions. In this case, the engine must be gradually de-throttled as spark timing is retarded in order to account for the decreased thermal efficiency of the engine as combustion is phased later in the expansion stroke. If throttling-induced purging issues were the sole driver of the apparent spark retard limitation, then combustion stability should exhibit a relatively flat slope of degradation as spark timing is retarded due to the proportional de-throttling. Additionally, should the pre-chamber contain a significantly higher percentage of residuals than the main chamber, the incoming main chamber charge should “dilute” this residual fraction with air and fuel, and the two chambers’ residual fraction delta should decrease with later spark timing, reaching a minimum when spark timing occurs at TDC of the compression stroke. Therefore, retarded spark timing should allow for *reduced* in-pre-chamber residual fraction. While the hypothetical positive stability trend that takes these two effects into account would be partially offset by the general negative stability trend associated with later combustion phasing, the net stability trend should exhibit a less severe deterioration with spark retard compared to conventional SI engines if the residual gas hypothesis is solely responsible for the limitation. In reality, retarding spark timing in jet ignition engines produces significantly steeper deterioration in stability versus conventional SI engines, exceeding stability limits at much earlier spark timings than is observed in SI engines. Therefore, while the residual gas hypothesis undoubtedly accounts for some, likely most, of the poor low load performance of jet ignition engines, it cannot be the sole contributor to the poor spark retard authority in particular.

Another emerging hypothesis of the cause of the low load combustion challenges of jet ignition engines is the low charge density at these conditions. Jet ignition is believed to rely to a high degree on the concept of re-ignition in the main chamber. As was established, pre-chamber combustion processes are partially or fully arrested as the burning contents are forced through the nozzle orifices and the combustion flame is partially or fully quenched. Chemical, thermal, and turbulent effects then cause the reactive jets to induce combustion in the main chamber in the form of distinct auto-ignition sites within the volume of the jets. While the jets induce these auto-ignition sites, their formation is also influenced by the background cylinder temperature and pressure, as are conventional auto-ignition processes in ICEs. Under low load conditions, the background pressure and temperature in the cylinder are well below the auto-ignition temperature of gasoline and therefore the ability of the jets to induce auto-ignition site formation under these conditions is limited.

Additionally, jet reactivity and velocity rely totally on the quality of the pre-chamber combustion event. This pre-chamber combustion event requires a certain degree of charge density in order for the combustion event to induce sufficient jet velocity. If the charge density is too low, the pre-chamber combustion event does not generate sufficient pressure to force the contents to exit the pre-chamber while these contents are still reactive. Instead, the slow or weak burning process results in excessive heat loss to the pre-chamber walls or through the orifice walls as the jets exit, with a larger percentage of fuel energy lost to heat transfer than at higher charge density conditions. If any significant flow is generated from the pre-chamber to the main chamber in this case, the emerging contents will therefore have low or no reactivity because chemical-kinetic activation temperatures have not been maintained. Under spark retard conditions, this slow burning pre-chamber effect is compounded by the fact that combustion is occurring non-ideally during the expansion stroke, where charge density during the bulk of the combustion event reduces further.

In optical engines, this effect has manifested as a complete loss of visible light spectrum jet luminescence at low loads, indicating a severe reduction in jet reactivity. Figure 5-2, taken from a study by Sens *et al* [157] compares this effect for two pre-chamber geometry variants under low load conditions. In this case the engine load of 2 bar BMEP is slightly higher than a typical CSSR load but is comparable for the purpose of this analysis. With pre-chamber variant A, luminous jets are partially visible with a CA50 of 8 dATDC. When combustion phasing is retarded to 46 dATDC, no luminosity is apparent in the jets, if indeed any reactive or non-reactive jets are formed at all, and combustion does not occur. Pre-chamber variant B contains a central hole with a significantly increased orifice diameter which in theory reduces the degree of flame quenching as jets exit. Luminous jets are again visible at a CA50 of 8 dATDC. Notably, at a CA50 of 46 dATDC only the central jet is luminous. Sens *et al* therefore declare variant B to possess superior spark retard capability. Inferring from the presented results, the reduced degree of flame quenching of the larger central orifice in variant B more readily promotes main chamber combustion at highly retarded combustion phasings, and overly quenching nozzle orifices reduce jet reactivity, inhibiting auto-ignition site formation. Reduced flame quenching of the jets partially or fully transitions the engine from a jet ignition mode to a torch ignition mode under these conditions, with the structural integrity of a flame front somewhat preserved as contents transfer from the pre-chamber to the main chamber. This is evident from the results in Fig. 5-2. It is hypothesized that the lack of luminous jets from the side orifices under heavily retarded conditions, even in variant B, are due to excessive heat losses through the orifice walls, coupled with a clear jet bias to the largest orifice. The latter effect is qualitatively apparent at a CA50 of 8 dATDC and would become more dominant as spark timing is retarded and charge density for the bulk of the combustion event reduces.

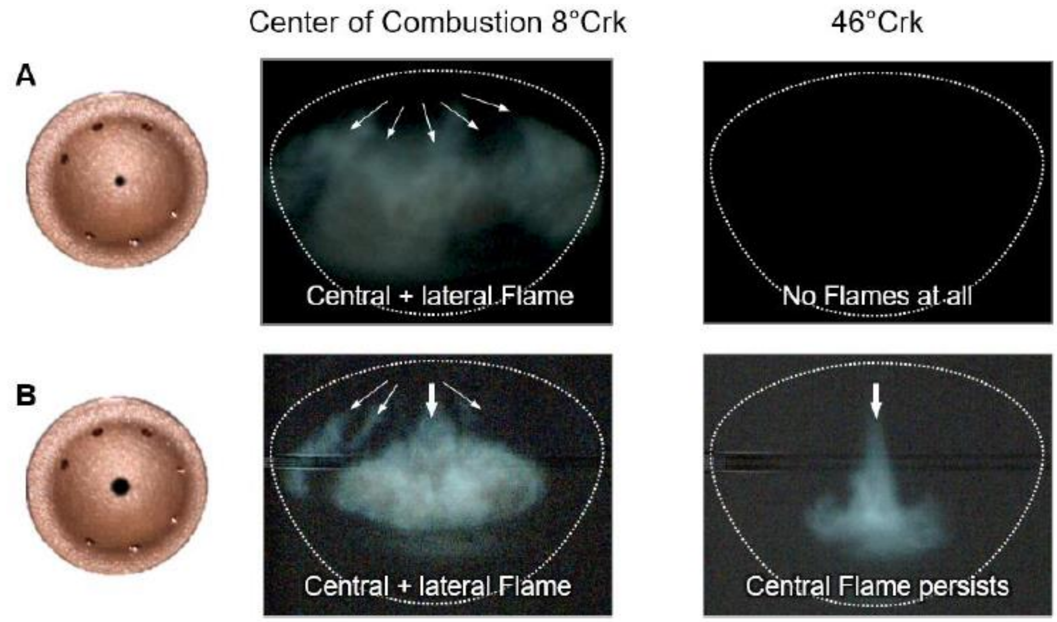

Figure 5-2: High speed camera images from a single-cylinder engine showing emitted visible light from combustion at 1250 rpm / 2 bar BMEP for two pre-chamber variants at base and very late center of combustion [157].

Based on the above result, the study authors provided an assessment of the applicability of a common pre-chamber geometry across the engine map, shown in Fig. 5-3. Critically, the authors described the Variant B pre-chamber as exhibiting poor knock mitigation properties at high load conditions. This is certainly due to the fact that jet velocity increases proportionally with charge density, so high charge density operation produces a central orifice jet so fast that it impinges on the piston crown, creating a localized temperature and pressure spike that contributes directly to increased knock.

Figure 5-3 illustrates the central point of this section clearly. Historically, and especially in the case of the referenced study, pre-chamber geometries and strategies that provide high load knock mitigation or part load lean limit extension or optimal thermal efficiency have provided poor low load performance and limited spark retard capability. Quantifying and understanding the low load limitation can lead to the identification of a “compromise” pre-chamber geometry, but to truly decouple the inversely related high load and low load performance trends, jet ignition operating strategy is key. Active pre-chambers, with their ability to operate in a wide λ band provide an added degree of flexibility to help address this issue.

Additionally, MJI and similar concepts provide precise control over pre-chamber fuel injection parameters, offering further flexibility.

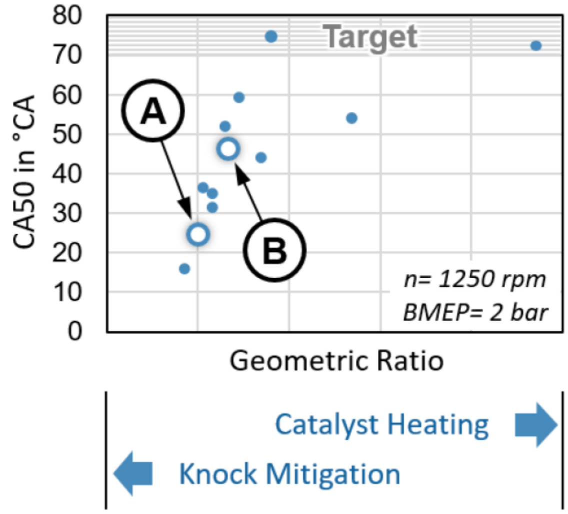

Figure 5-3: Latest possible CA50 across the pre-chamber specific geometric ratio for different pre-chamber layouts at 1250 rpm / 2 bar BMEP [157].

The subsequent sections in this chapter quantify the combustion stability and spark retard challenges of the MJI engine used in this study relative to the baseline SI engine performance. Optimization pathways that can mitigate these challenges are presented and discussed.

5.1.2 Intra-Chamber Gas Exchange

In order to evaluate the potential influence of inadequate purging of pre-chamber residual gas under heavily throttled conditions, it was important to first establish an understanding of the fluid communication between pre-chamber and main chamber. Most jet ignition concepts, including MJI, do not include any direct introduction of oxygen in the pre-chamber, instead relying on induced gas exchange between the pre-chamber and main chamber to provide sufficient oxygen for combustion. This gas exchange process is driven by pressure differential amongst the intake and exhaust ports, the pre-chamber and the main chamber throughout the 4-stroke engine cycle. Figure 5-4 depicts the gas exchange process as described by a CFD simulation of a representative lean part load operating condition.

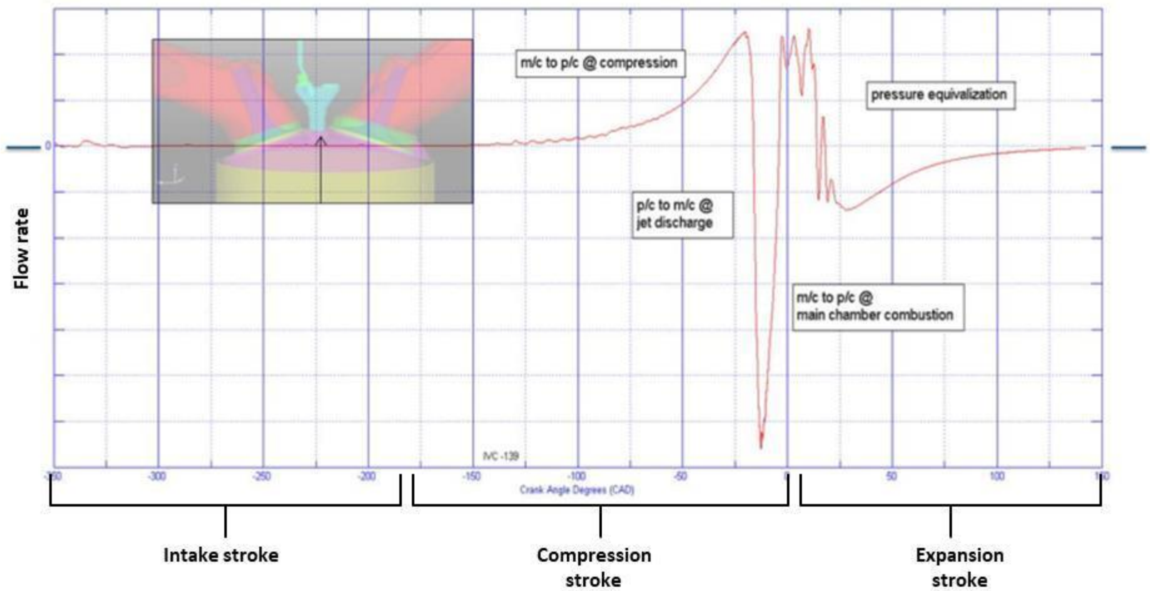

Figure 5-4: Example mass flow between pre-chamber and main chamber; 1500 rpm, 5.5 bar BMEP, λ = 1.

In Fig. 5-4, positive flow rate indicates flow from the main chamber into the pre-chamber. During the compression stroke, air and fuel charge in the main chamber is forced into the pre-chamber at a rate of acceleration proportional to the pressure increase in the cylinder due to the upward movement of the piston. This positive flow is disrupted when the pre-chamber contents are ignited and pressure in the pre-chamber exceeds that of the main chamber prior to the piston reaching TDC. As the pre-chamber is open to the main chamber, the chambers will seek to rapidly equalize their pressures subsequent to this event. This manifests as a sudden reversal in flow direction from the pre-chamber to the main chamber as high velocity jets penetrate into the main chamber. These jets are a mixture of unburned fuel and air initially, followed by partially and fully combusted species that constitute the reactive portion of the jets. The duration and peak flowrate of this jet expulsion phase is dictated by multiple factors including background pressure, fuel quantity, fuel placement, pre-chamber volume and nozzle geometry. The jet process is short-lived, and once main chamber combustion is initiated and pre-chamber combustion fully dissipates, flow reverses again and the main chamber combusted products are forced into the pre-chamber. As main chamber combustion pressure dissipates during the expansion stroke, now fully burned contents in the pre-chamber are extracted due to the downward motion of the piston.

Figure 5-5 displays the CFD simulated O_2 and CO_2 mass fractions inside the pre-chamber for a representative part load cycle. The intake valve opening event is when O_2 is introduced into the system. The O_2 fraction then rises in the pre-chamber despite the downward motion of the piston during this phase. The discontinuities apparent in the O_2 mass fraction trace correspond to events during the intake process, such as valve fully open and start of valve ramp down, indicating that valve position has a substantial influence on O_2 filling of the pre-chamber during this phase. It should be noted that there is an increase in O_2 mass in the pre-chamber during the intake stroke and prior to Bottom-Dead Center (BDC) being reached.

With the intake valve closed and piston motion upward during the compression stroke, the remainder of the O_2 filling process occurs, which in turn dilutes the CO_2 mass fraction in the pre-chamber. With sufficient O_2 present, fuel can then be separately added to ensure a pre-chamber λ within the ignitability limits of the spark plug.

In the representative part load condition depicted in Fig. 5-5, approximately 50% of the mass fraction of O_2 enters the pre-chamber during the intake stroke. This result indicates a complex charge interaction between pre-chamber and main chamber during this period that is driven by micro-pressure dynamics within the combustion chamber. Any inhibitions during this period, such as reduced intake pressure due to heavy throttling, will negatively impact pre-chamber O_2 filling during the intake stroke, which in turn reduces the rate of replacement of residual gas with intake air. Therefore, under low load conditions that require heavy throttling, inadequate purging of the pre-chamber results in higher residual fraction in the pre-chamber versus the main chamber at time of spark, with progressively larger offset between pre-chamber and main chamber residual fraction at time of spark as load decreases. This higher residual fraction negatively impacts the pre-chamber combustion event, increasing the burn duration or, if residuals are present in sufficiently high quantity, leading to misfires inside the pre-chamber. Poor pre-chamber combustion performance, including misfires, will propagate to the main chamber.

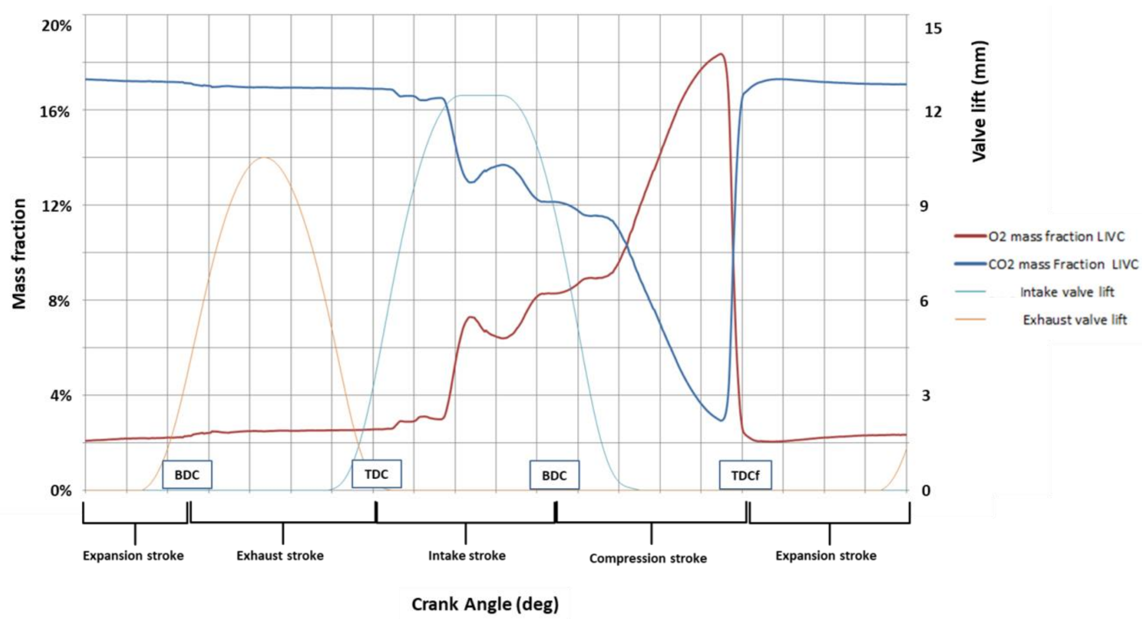

Figure 5-5: Example of O_2 and CO_2 mass fraction evolution in the pre-chamber; 1500 rpm, 5.5 bar BMEP, λ = 1.

In order to confirm this residual behavior and to identify levers to mitigate its effect, a series of sample gas measurements were made directly from the pre-chamber. A fast CO_2 analyzer was used to sample gas continuously from the pre-chamber through a small capillary tube that was designed to allow the minimum required flowrate to reach the analyzer without completely evacuating the contents of the pre-chamber. Measurements were taken on a crank angle basis, but due to the large variation in pressure experienced by the analyzer during sampling, only data acquired under high pressure conditions, i.e. near TDC were considered accurate. From the CO_2 measurement, residual fraction was calculated. Figure 5-6 displays the experimental results of the fast CO_2 sampling of contents in the pre-chamber during fired engine operation. There was a discernable step in the CO_2 trace that occurs between the measurement of the pre-combustion CO_2 mass fraction and the post-combustion CO_2 mass fraction (immediately after the minimum CO_2 value was reached, accounting for measurement transport delay) that possibly indicated CO_2 mass fraction resulting from the initial pre-chamber combustion event. Subsequent to this intermediate step, the CO_2 value achieved a maximum before gradually returning to a nominal value. The maximum CO_2 value, occurring out of phase with the combustion pressure peak due to transport delay, corresponded to the CO_2 generated during main chamber combustion after these contents were transported to the pre-chamber.

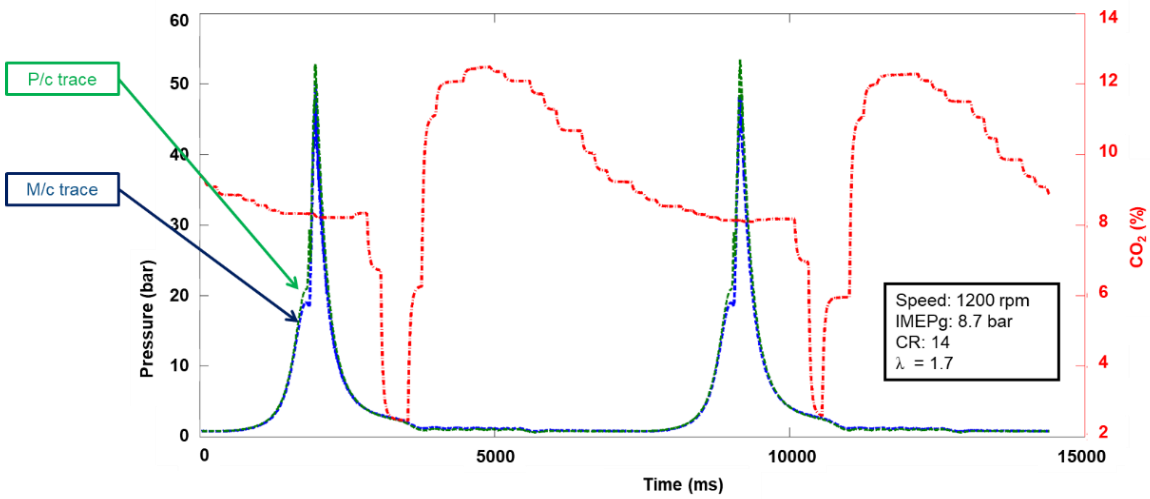

Figure 5-6: CO_2 evolution in the engine as measured through the pre-chamber sample port; 1200 rpm, 8.7 bar IMEP, λ = 1.7.

In order to evaluate the influence of pre-chamber fuel injection parameters on pre-chamber residual gas fraction, the engine was operated at a λ value of 1.4, a stable condition regardless of whether fuel is being injected directly into the pre-chamber. As is shown in Fig. 5-7, residual fraction decreased appreciably when fuel was injected directly into the pre-chamber. The residual fraction continued to decrease as the injected fuel quantity was increased. Figure 5-8 includes a contour graph showing residual fraction trends with pre-chamber fuel injection angle and quantity. While there appears to be little sensitivity to the timing of the injection event, the sensitivity to quantity of fuel injection is apparent. It is likely that the addition of the fuel mass either displaces a portion of the residual content at the time of injection, or has a more a complex impact on the completeness of pre-chamber combustion in a given cycle that cannot be detected using this experimental apparatus. This data suggests that the addition of pre-chamber fuel, even at a constant main chamber λ, is an effective means by which to reduce the potentially negative impact of residual fraction on pre-chamber combustion.

There are two key points about this conclusion that should be noted. Firstly, the fuel quantity being injected in these experiments was injected late in the compression stroke and was therefore used for pre-chamber combustion; it was not used purely as a purging mechanism as it is in some HD NG pre-chamber engine applications. Low pressure injection of liquid gasoline during the start of the intake stroke would likely result in significant wetting of the pre-chamber walls, thereby increasing HC and soot emissions. Secondly, there is a limit to the use of this strategy with all other engine conditions remaining constant. As in typical SI combustion chambers, λ conditions in the pre-chamber must be carefully managed to ensure an ignitable mixture at time of spark. Overly rich combustion in the pre-chamber can slow pre-chamber burn rates just as it slows burn rates in SI engines. Additionally, because of the short length scales in the pre-chamber, over-injection in the pre-chamber may result in a substantial quantity of liquid fuel at time of spark, potentially resulting in flooding of the plug. Therefore, in order to effectively use this combustion fuel purging strategy, the increased fuel quantity must be coupled with de-throttling to allow adequate O_2 in the pre-chamber.

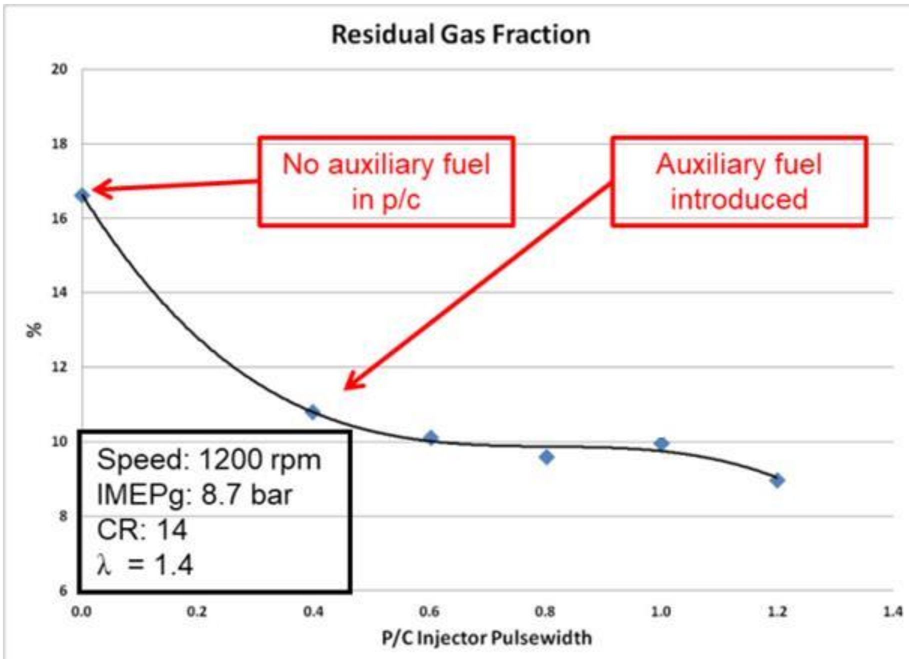

Figure 5-7: Residual fraction trends with pre-chamber fuel quantity at a representative condition; 1200 rpm, 8.7 bar IMEP, λ = 1.4.

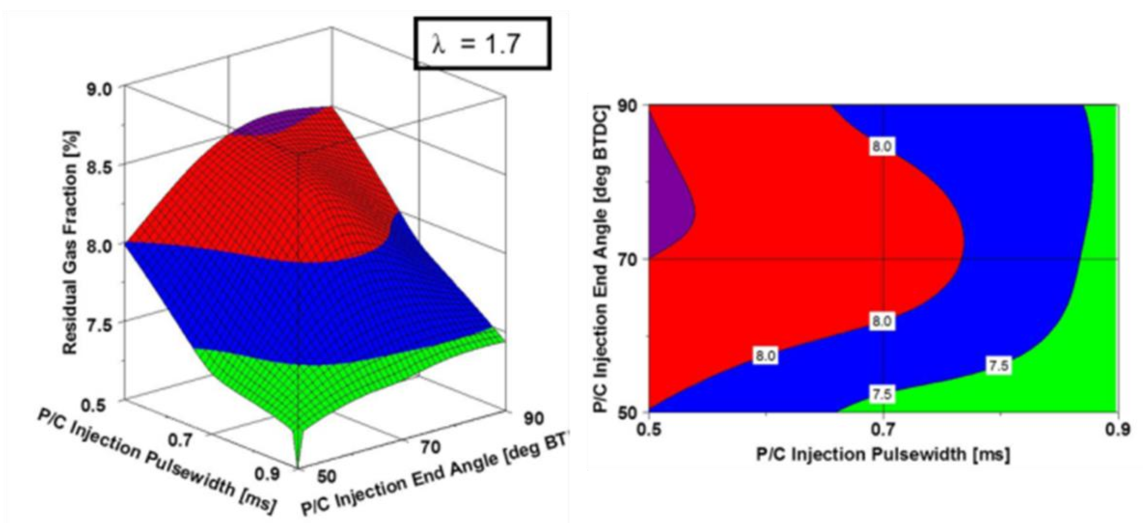

Figure 5-8: Residual fraction trends with pre-chamber fuel quantity and end of injection angle at a representative condition; 1200 rpm, 8.7 bar IMEP, λ = 1.7.

5.2 Low Load Operation

Active pre-chambers have the flexibility to both operate lean in the main chamber and to introduce fuel directly in the pre-chamber. Lean operation provides excess O_2 in the main chamber, increasing the O_2 mass transferred to the pre-chamber during the intake and compression strokes. To account for this dilution, fuel is then injected directly into the pre-chamber. Data from the measured residual fraction experiment discussed in the previous section suggests that direct fuel injection in the pre-chamber provides an added advantage that can be exploited at low load conditions: the physical displacement of residuals through the introduction of high pressure fuel.

Figure 5-9 shows LNV, COV, and combustion efficiency trends for various λ conditions in the DI3 MJI engine as engine load was decreased (towards the left side of the x-axis) at a constant speed of 850 rpm. This engine condition approximated an idle load (approximately 1 bar BMEP). At this condition, an LNV limit of 60% indicates excessive misfires (depicted by the orange dashed line in Fig. 5-9). A standard deviation of IMEPg limit is typically more appropriate than COV at loads below 2 bar BMEP, so the COV trends are indicative of combustion stability but do not have a relevant limit. The λ = 1 variant displayed rapid deterioration in COV and LNV below 1.4 bar BMEP engine load. Between the data points acquired at 1.5 bar and 1.2 bar BMEP the LNV reduced from > 90% to < 60%, indicating a sudden onset of misfires. Two lean λ variants were also tested, both with fuel injected directly into the pre-chamber: λ = 1.5 and λ = 1.7. Both variants demonstrated stable low load extension below 0.8 bar BMEP. Aside from an obvious misfire with the λ = 1.7 variant at 1.5 bar BMEP, both variants produced similar LNV trends. Combustion efficiency was reduced by approximately 2 percentage points with the λ = 1.7 variant, but notably the λ = 1 and λ = 1.5 variants displayed nearly identical combustion efficiency trends.

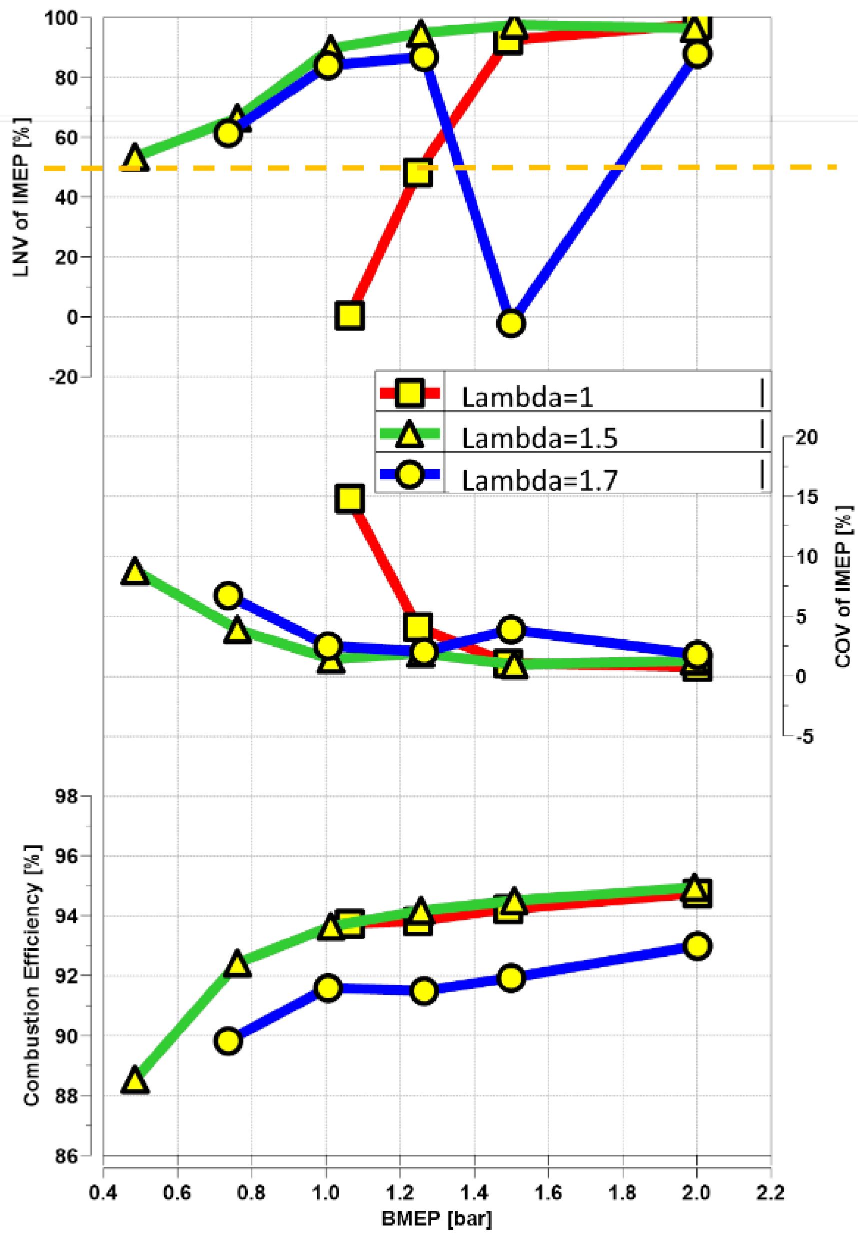

Figure 5-9: Stability and combustion efficiency trends at steady state 850rpm low load operation.

Figure 5-10 shows burn duration segment trends with engine load. The challenge associated with burning a lean mixture in a low charge density environment was reflected in increased CA10-50 as load is decreased. The lean variants exhibited faster CA0-10 values than the λ = 1 variant, with the discrepancy increasing as load was decreased. CA0-10 is a burn duration segment that typically encompasses the entirety of the pre-chamber combustion event. Here it was used as a simplified metric for pre-chamber combustion duration. With the λ = 1 variant, where no auxiliary fuel was added to the pre-chamber, pre-chamber combustion was influenced solely by static engine conditions. With the lean λ variants, injected fuel quantity was held constant across the load sweep. Notably, the late burning (CA50-90) results showed relative parity amongst the variants. Lean combustion produces colder combustion temperatures which should negatively impact the burning process. Combustion was most sensitive to this temperature effect during late burning when the increasing combustion chamber volume naturally helped to depress bulk temperatures. However, under this low load condition this effect appeared to be negligible.

The results strongly indicated that residual gas fraction in the pre-chamber continued to increase to unacceptable levels in the $\lambda = 1$ variant as load was decreased and the engine became more heavily throttled. In the lean variants, the engine was de-throttled and enleaned in order to allow more fresh charge to displace residual gas during the intake stroke, and the addition of direct fuel injection provided a residual displacement effect as well. Therefore, lean fueled pre-chamber operation is an effective operating strategy to mitigate the steady state low load challenge of jet ignition.

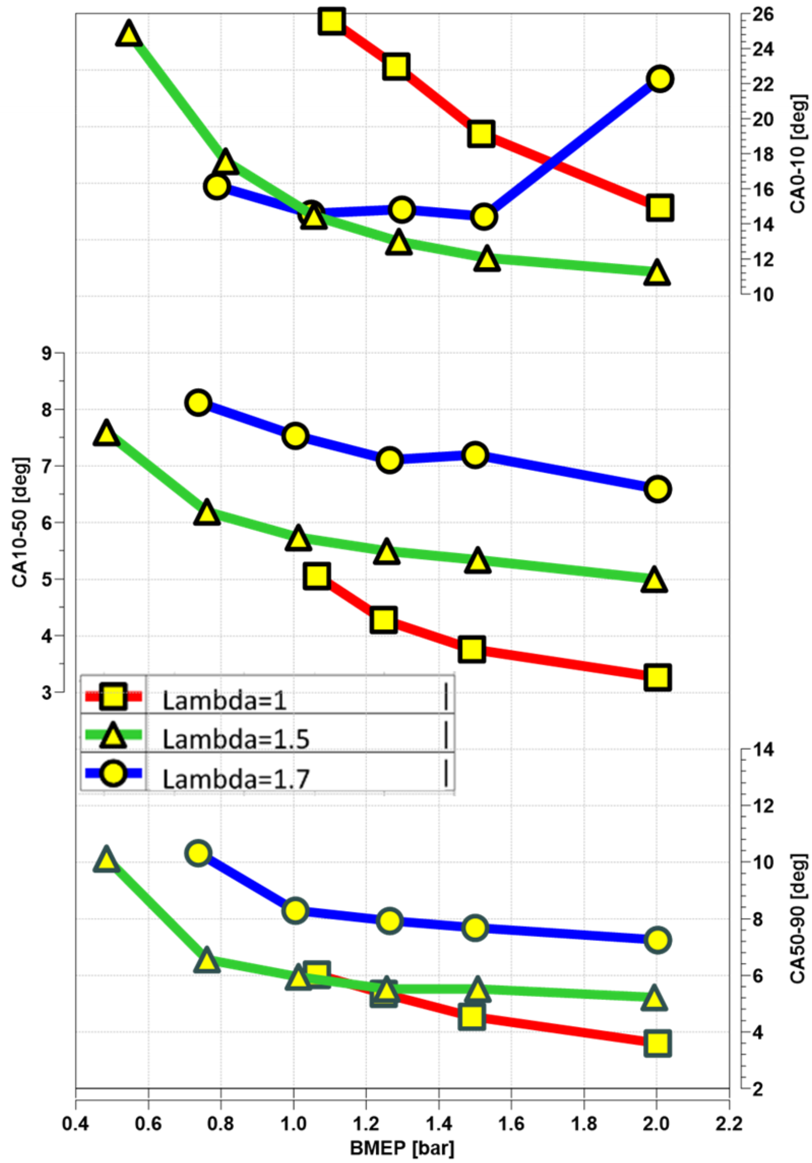

Figure 5-10: Burn duration trends at steady state 850rpm low load operation.

The lean variants exhibited superior low load extension compared to the λ = 1 variant. The λ = 1.5 variant displayed a flatter standard deviation of IMEPg curve across the load sweep compared to the λ = 1.7 variant (Fig. 5-11). This metric is more commonly used for combustion stability under low loads than is COV. A limit of 0.10 is used at this condition. The comparative lean results presented in Figs. 5-9 and 5-10 indicate that there is an optimal lean λ for this condition that balances O_2 filling requirements with combustion stability and efficiency. This λ value is likely in the λ = 1.3 to λ = 1.6 region based on the presented results. This optimal λ value is richer than the lean limit at this low speed / low load condition but still beyond typical λ capability for the SI engine at this condition.

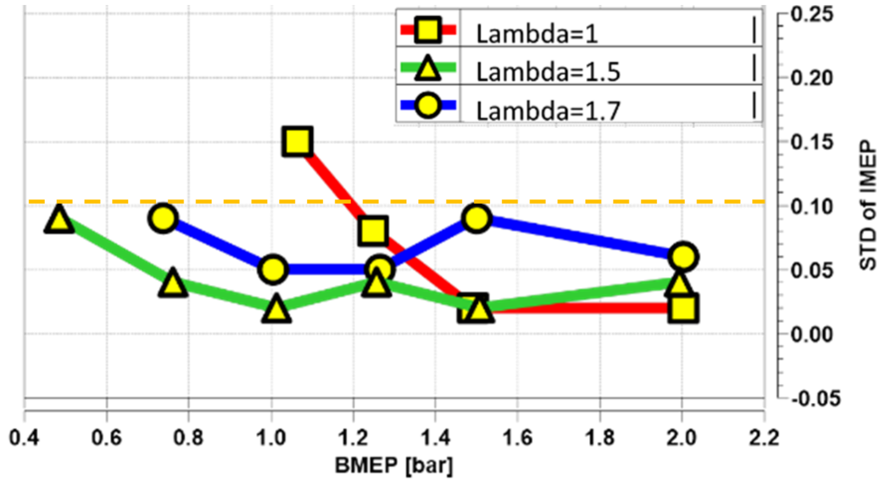

Figure 5-11: Combustion stability trend at steady state 850rpm low load operation.

The engine-out brake specific emissions results presented in Fig. 5-12 demonstrated that there was a net emissions benefit achieved when the engine was operated lean in this load sweep. Given the lean λ values specified, the brake specific NO_x ($BSNO_x$) result showing significant reductions across the load sweep compared to the λ = 1 variant were expected. Also obvious was the similar brake specific CO (BSCO) result showing significant reductions when the engine was operated lean. More unexpected was the brake specific HC (BSHC) result. HC emissions typically remained flat across a λ = 1 to λ > 2.0 range with jet ignition under part load and wide open throttle conditions. Under low load steady state conditions, jet ignition engines typically produced increases in HC emissions across the same λ range. Additionally, brake specific emissions are normalized by exhaust flow which is higher for lean conditions when the engine is de-throttled. This should then compound the HC emissions challenge, producing BSHC emissions under the lean conditions considered here double or more those at stoichiometric conditions. But as the result in Fig. 5-11 shows, BSHC were nearly identical for the λ = 1 and λ = 1.5 variants, with the λ = 1.7 variant demonstrating only minor increases across the load sweep. This is most likely due to the fact that the late burn (CA50-90) durations, a major indicator of HC and CO emissions, were roughly comparable amongst the variants at this condition. This, coupled with the substantial reduction in early burn (CA0-10) duration, produced an overall reduction in CA0-90 burn duration with the λ = 1.5 variant versus the λ = 1 variant, providing a possible explanation for the parity observed in engine-out BSHC.

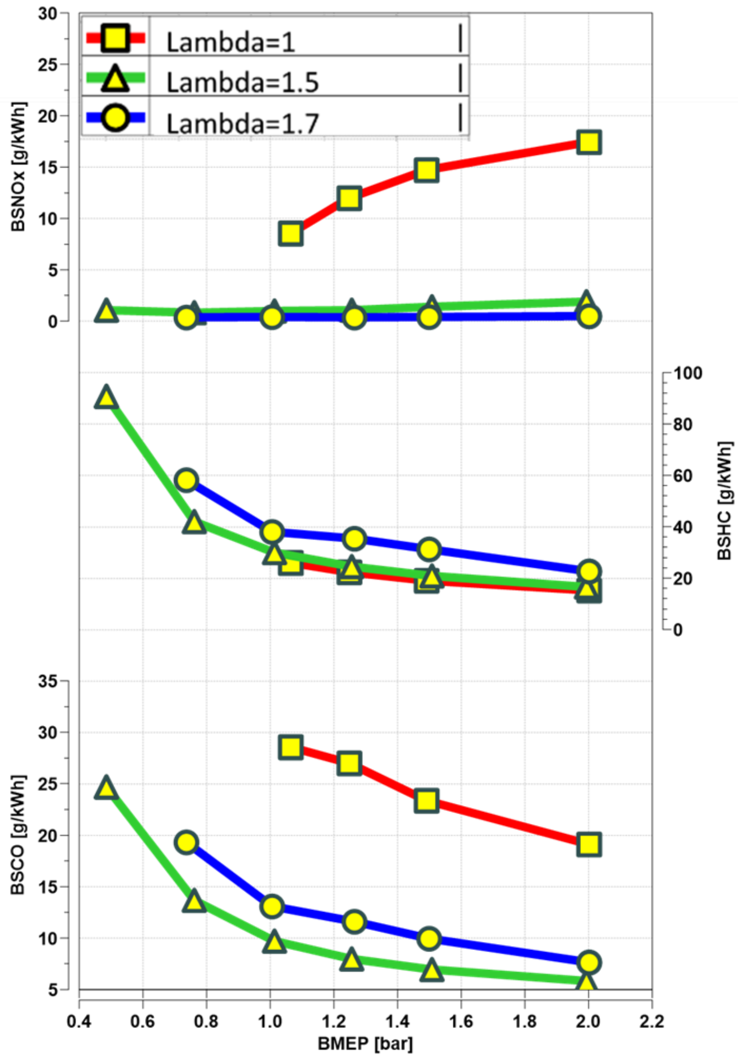

Figure 5-12: Engine-out brake specific emissions trends at steady state 850rpm low load operation.

5.3 Idle Operation

Idle operation is performed at low engine speed (< 1000 rpm) and low or net zero load, where the engine generates just enough load to spin itself and power the ancillary devices. A requirement for idle is retarded spark timing. At an idle condition there is an anticipation of sudden torque demand from the operator. The most rapid means by which to increase torque at this condition is to advance spark timing from a retarded location to a location in advance of TDC. This is due to the engine controller’s ability to adjust spark timing on a cycle-by-cycle basis. Few other engine parameters can respond on such a short time basis. This rapid advancement in spark timing corresponds to a proportional increase in torque.

In order to propose mitigation measures for the poor spark retard capability of jet ignition engines, the spark retard limitation was first quantified in the DI3 MJI engine. The acknowledged pre-chamber spark retard limitation did manifest in the DI3 MJI engine, as is shown in Fig. 5-13. At an engine speed of 1500 rpm and the jet ignition engine operating at $\lambda = 1$ with no auxiliary fuel in the pre-chamber, the engine retained full spark authority in the part load region. At a load of 6 bar BMEP, acceptable standard deviation of IMEP was maintained out to a spark timing of 30 dATDC, near the limit of spark retard capability in a PFI SI engine. However, as engine load was reduced this spark retard capability progressively decreased. At 5 bar BMEP, spark retard capability reduced by about 5 crank angle degrees. At 4 bar BMEP, spark retard capability reduced by a further 13 crank angle degrees. At 2 bar BMEP, the engine lost the capability to retard spark to TDC. This spark retard limitation was dictated by deterioration in COV and LNV. The LNV trend in particular showed no evidence of misfires in the spark timing sweep down to a load of 5 bar BMEP, but all lower loads exhibited surprisingly rapid transitions into a frequent misfire condition. In the 2 bar BMEP case, the engine simply ceased to combust before spark timing could be retarded to 5 dBTDC.

The results demonstrated the severe deterioration in spark retard capability with decreasing engine load, to the extent that at 2 bar BMEP, the engine was incapable of retarding spark timing beyond TDC. This level of spark retard provided only minimal torque reserve when applied to an idle condition. As was established in the previous sections, the misfires in the pre-chamber were likely the result of increased residual gas fraction in the pre-chamber and increased residual gas fraction delta between the pre-chamber and main chamber as the engine was progressively throttled, i.e. as load was decreased. The residual gas fraction inside the pre-chamber exceeded the flammability limit of the air-fuel mixture. The misfire or partial burn event in the pre-chamber propagated to the main chamber, producing a similar result in the main chamber. Hybrid engine applications where the electric motor accommodates most low load requirements provide some mitigation for this low load spark retard deficiency. However, hybridized powertrains typically utilize engines that also serve as prime movers in non-hybrid applications, emphasizing the need for combustion-related mitigations.

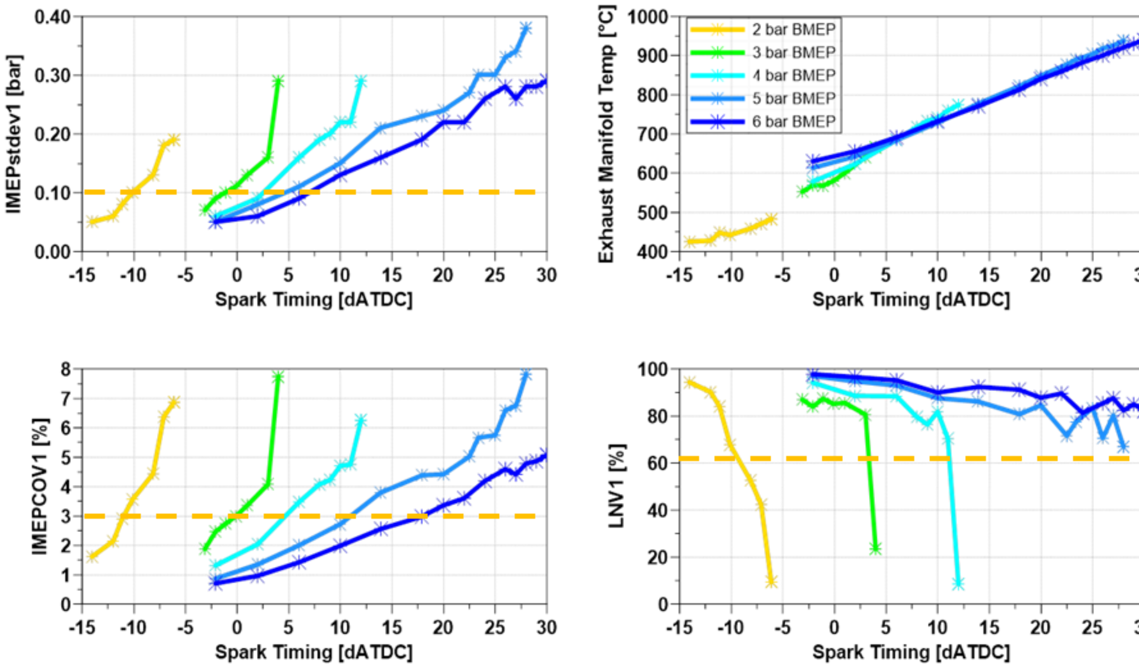

Figure 5-13: Spark retard trends with load at 1500rpm, λ = 1, warm engine conditions.

Figure 5-14 uses data from the set presented in Figs. 5-9 through 5-12. In this figure, engine performance was evaluated in a spark timing sweep at a load of 1 bar BMEP. Two conclusions are apparent from the results in this figure. Firstly, and consistent with the results in Fig. 5-9, the engine was incapable of being operated at stoichiometric or near-lean λs at a load of 1 bar BMEP. The engine must be operated lean in order to achieve acceptable combustion stability at this condition. Secondly, operating the engine lean did not in and of itself increase the spark retard capability of the jet ignition engine. A CA50 limit of 30 dATDC at this condition is consistent with a spark timing limit of near or advanced of TDC.

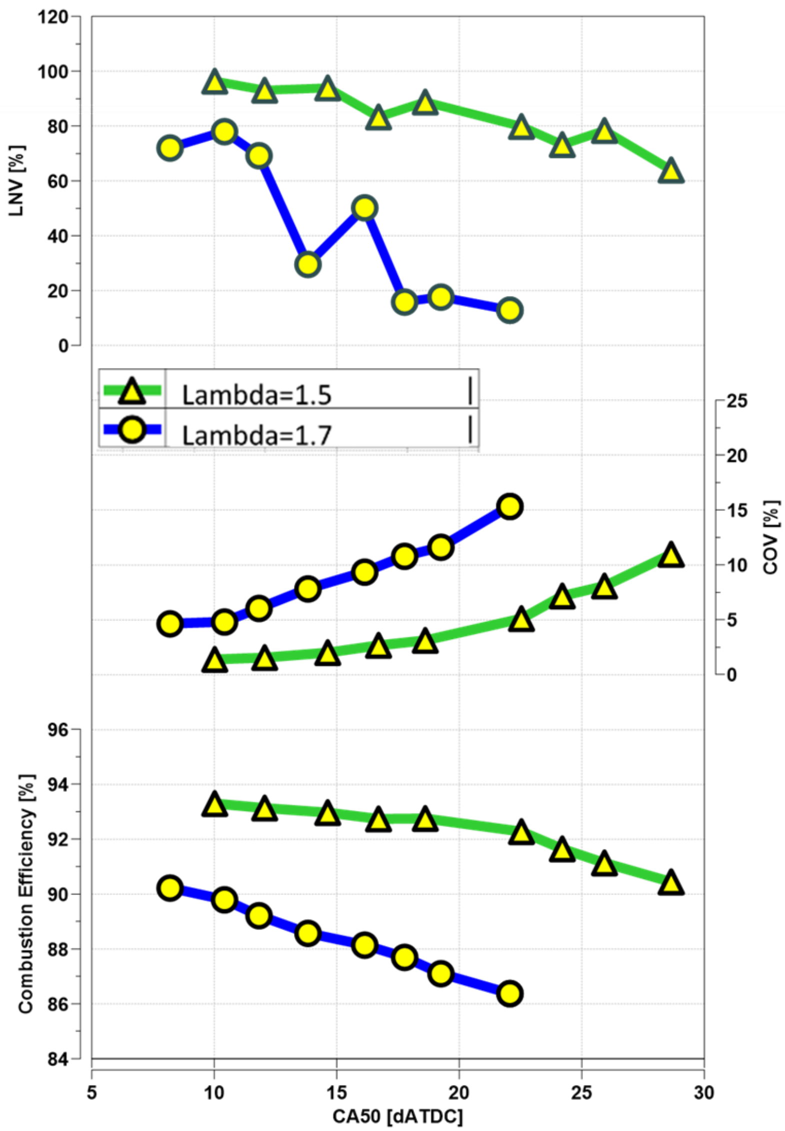

Figure 5-14: Combustion stability and efficiency trends with CA50 at a load = 1 bar BMEP at 1500 rpm.

As in the case of low load steady state operation, the active system carries the flexibility of operating at a relatively wide range of λ values at the idle condition (though not, as was established, at a stoichiometric or near-lean λ). This capability does provide an advantage for idle operation despite the fact that it does not increase spark retard capability directly. Fuel injection quantity, like spark timing, can be adjusted by the engine controller on a cycle-by-cycle basis. However, throttle position cannot be adjusted on a cycle-by-cycle basis and throttle commands can produce a hysteresis that is impactful in this heavily throttled environment, so it is not feasible to adjust throttle and fuel quantity simultaneously to accommodate rapid torque demand and this is not attempted in production applications. However, because the active system can operate at a range of stable λ values at the speed and load necessary for idle, λ tolerance can be coupled with the existing minimal spark retard capability at these λ values to provide ample torque reserve (Fig. 5-15). Sudden torque demand would therefore instigate both a rapid advancement of spark timing within the limited stable spark timing window and, simultaneously, a rapid increase in fuel quantity injected. The latter strategy results in rapid shifts in lean λ values.

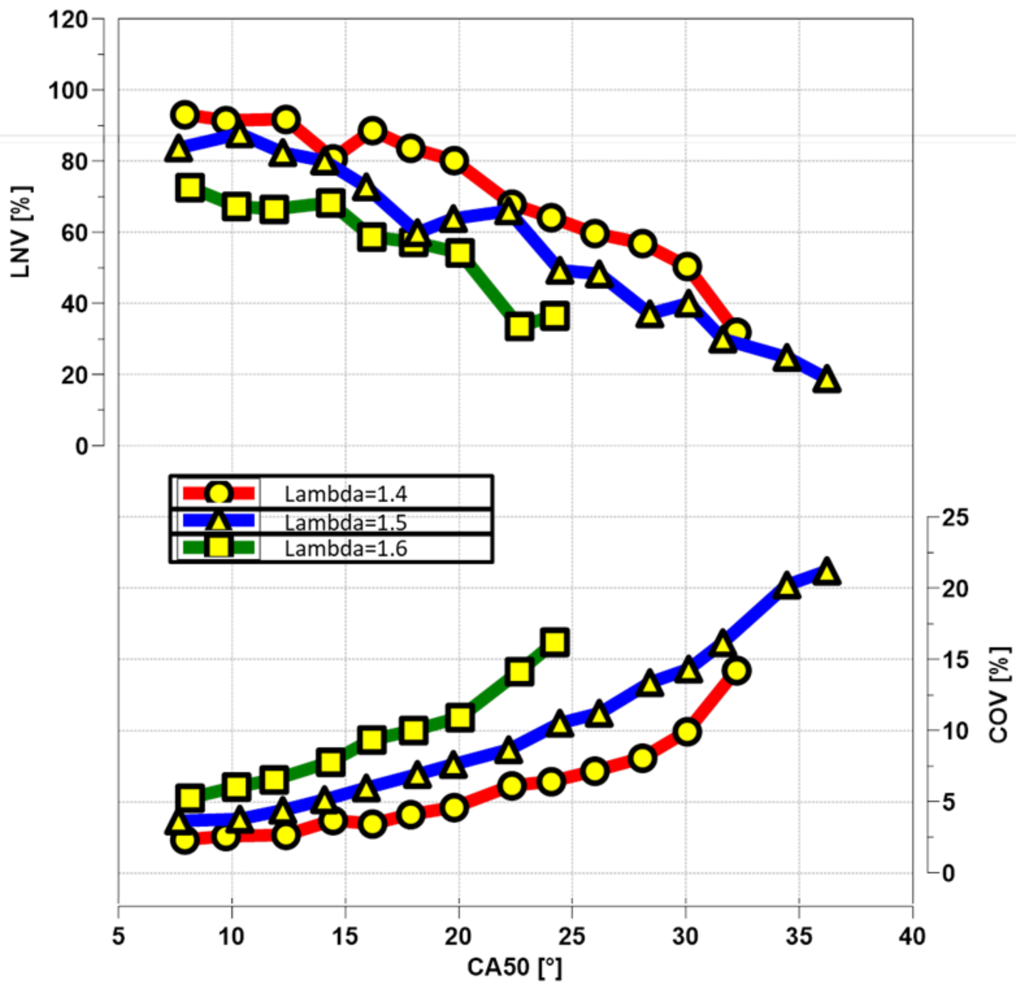

Figure 5-15: CA50 trends with load at 850rpm, 1 bar BMEP with a range of lean λ values.

Figures 5-16 and 5-17 demonstrate the adequacy of this combined spark/fuel approach to generating the torque reserve required of an idle condition. Figure 5-16 demonstrates the relationship of BMEP to CA50 retard at a constant λ of 1.5 in the DI3 MJI engine. Required air flow to achieve 1 bar BMEP is determined for the λ=1 condition at a maximum brake torque CA50 phasing of 10 dATDC. With air flow held constant, i.e. constant throttle position, combustion phasing was retarded until a misfire limit was reached and a prescribed CA50 could not be stably maintained. Due to the reduction in thermal efficiency as phasing was retarded, BMEP reduced as CA50 was retarded beyond the maximum brake torque phasing of 8-10 dATDC. The 20 crank angle degree range considered in these results produced a 40% reduction in BMEP.

Figure 5-17 demonstrates the relationship of BMEP to enleanment at a constant air flow and a constant CA50 of 8 dATDC. In this test, a constant throttle position maintained air flow and fuel flow was reduced in order to achieve the target λ. The air flow condition corresponded to the required air flow to achieve 5 bar BMEP at an engine speed of 850 rpm and a stoichiometric λ. From this starting condition fuel flow was gradually reduced in order to enlean the λ until the lean limit was achieved. Consequently, BMEP reduced with enleanment. Over the λ range considered here, λ = 1-1.8, BMEP reduced by 60%.

Both the constant λ, constant air flow BMEP vs. CA50 trend and the constant phasing, constant air flow BMEP vs. λ trend could be adequately described by linear relationships.

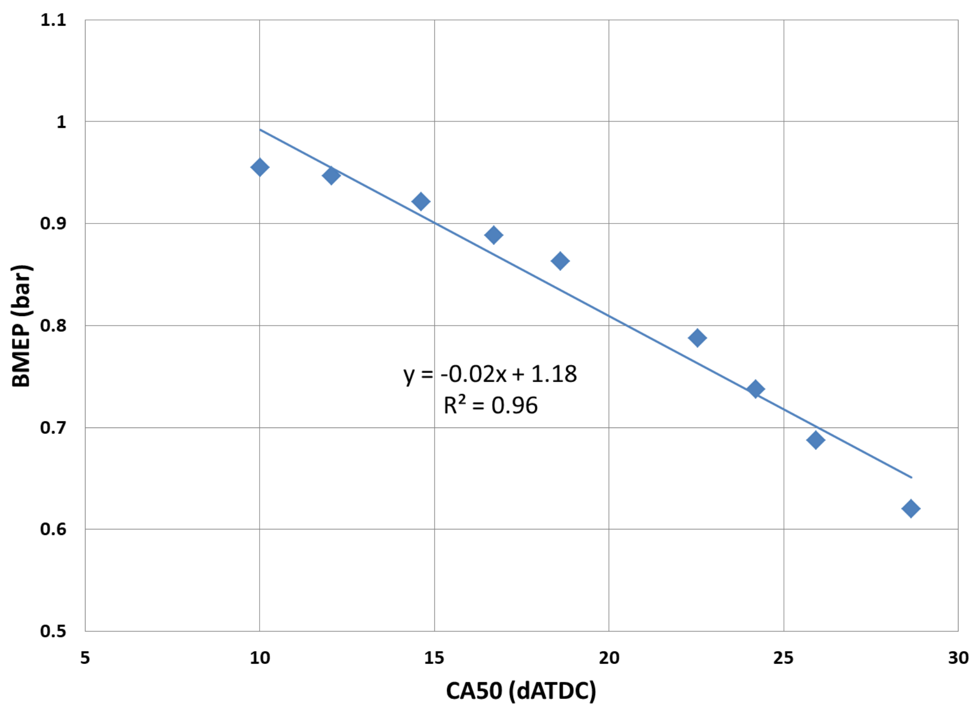

Figure 5-16: Change in BMEP with retarding CA50 at 850 rpm, λ = 1.5, constant air flow.

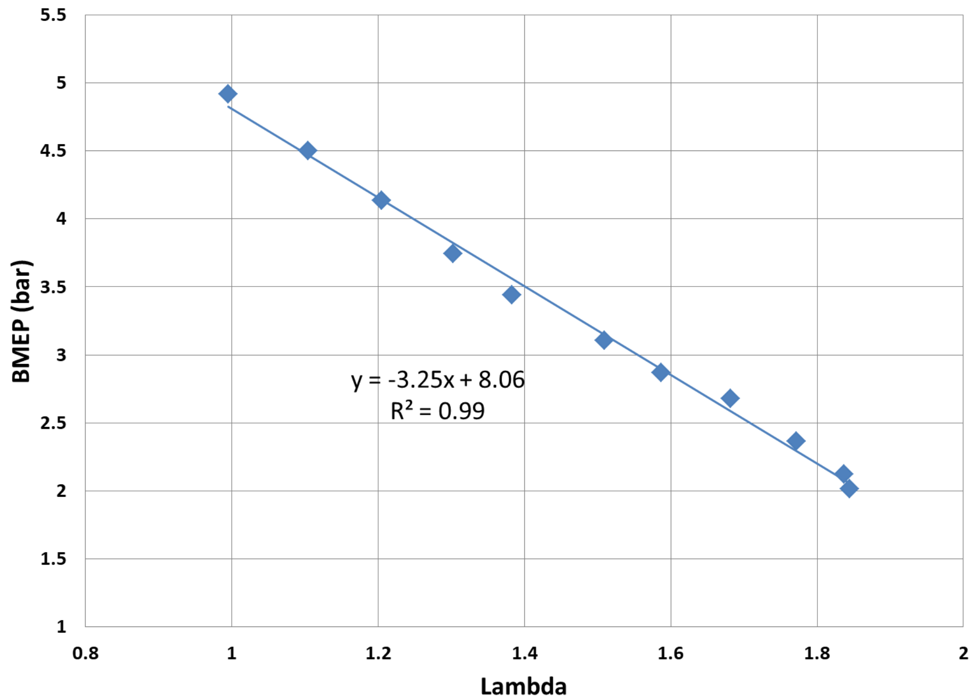

Figure 5-17: Change in BMEP with enleanment at 850 rpm, CA50 = 8 dATDC, constant air flow.

Torque reserve requirements of modern SI engines translate to approximately a 20 crank angle degree window of CA50 retard while maintaining an LNV above 70% [164]. The CA50 window for idle torque reserve is usually 10-30 dATDC. The LNV limit ensures that there are no misfires within this spark retard window. Applying this 20 crank angle degree requirement to the trend presented in Fig. 5-16, this CA50 window corresponds to a delta of 0.4 bar BMEP, assuming the torque demand function is held to a constant engine speed. While constant engine speed may not be an accurate assumption, it is immaterial to the results presented here since the trends are easily extrapolated across any engine speed changes that would occur in a production engine idle calibration. Therefore, the total torque reserve equates to 0.4 bar and the maximum “instantaneous” or cycle-resolved BMEP that can be added as a result of pedal demand at an idle condition is 0.4 bar.

Considering only the data presented in Fig. 5-15 and using 70% as a lower limit on LNV, the CA50 retard authority present in the combined λ = 1.4-1.6 test range is 29 crank angle degrees. This corresponds to an available BMEP range of 0.58 bar considering the linear relationship between BMEP and CA50 detailed in Fig. 5-16. This mechanism alone provides torque reserve in excess of the requirement at idle, however the ability of active jet ignition to operate stably across a λ range at the idle load provides a further mechanism for achieving adequate torque reserve. For the relatively narrow λ range considered in Fig. 5-15, λ = 1.4-1.6, the linear relationship described in Fig. 5-17 provides an additional 0.65 bar of BMEP range. Combining the two mechanisms provides a total of 1.23 bar BMEP range, well in excess of the required 0.4 bar. These results are detailed in Table 5-1.

Table 5-1: Change in BMEP provided by spark retard and λ authority at 850 rpm, 1 bar BMEP.

λ	**Maximum CA50**	**Range of CA50 retard**	**Change in BMEP**	
-	**dATDC**	**deg**	**bar**	Using linear equation y=-0.02x+1.18
1.4	22	14	-0.28	
1.5	16	8	-0.16	
1.6	15	7	-0.14	
			-0.58	**BMEP range using spark retard (bar)**
Min λ	**Max λ**	**λ range**	**Change in BMEP**	
-	**-**	**-**	**bar**	Using linear equation y=-3.25x+8.06
1.4	1.6	0.2	**-0.65**	**BMEP range using λ (bar)**
			-1.23	**Total BMEP range available (bar)**

Active jet ignition therefore can overcome the spark retard limitation by using λ tolerance in conjunction with limited spark retard to accommodate stable idle operation and required torque reserve, with potentially superior performance to modern SI engines. Widening the λ range considered in this dataset can increase torque reserve further, but spikes in engine-out NO_x in the near-lean region may negate this further widening to λ values richer than approximately 1.3.

5.4 CSSR Operation

5.4.1 Spark Retard Limitation

The most impactful challenge posed by the low load spark retard limitation concerns the ability to heat the aftertreatment catalyst upon cold start. Data in Fig. 5-13 was shown at warm oil and coolant temperatures which are not representative of the CSSR condition. CSSR is an operation that occurs immediately upon cold starting of the engine, so the engine fluids and catalyst are far from fully warmed up. Generally, SI engine performance and capability are compromised when fluid temperatures are at cold or ambient conditions. Figure 5-18 demonstrates the further degradation in spark retard capability with jet ignition at both part load and low load conditions when engine fluid temperatures were at ambient conditions (~20˚C) consistent with CSSR operation. Note that the previously observed full spark retard authority at 6 bar BMEP degraded by 20-25 crank angle degrees with cold fluids. The already severely limited spark retard capability at 2 bar BMEP degraded by 5-10 crank angle degrees, placing the spark retard limit at this condition well advanced of TDC. In fact, this limit is at a crank angle that is likely within the realm of required nominal operation. Notably, and consistent with previously presented data, the spark retard limitation at the part load condition was exclusively defined by combustion stability, whereas the spark retard limitation at the low load 2 bar BMEP condition was exclusively defined by the onset of misfires. This result indicates that misfire onset was sudden and, because it was not apparently predicted by main chamber combustion stability trends, likely originated in the pre-chamber or was a direct product of a compromised pre-chamber combustion event.

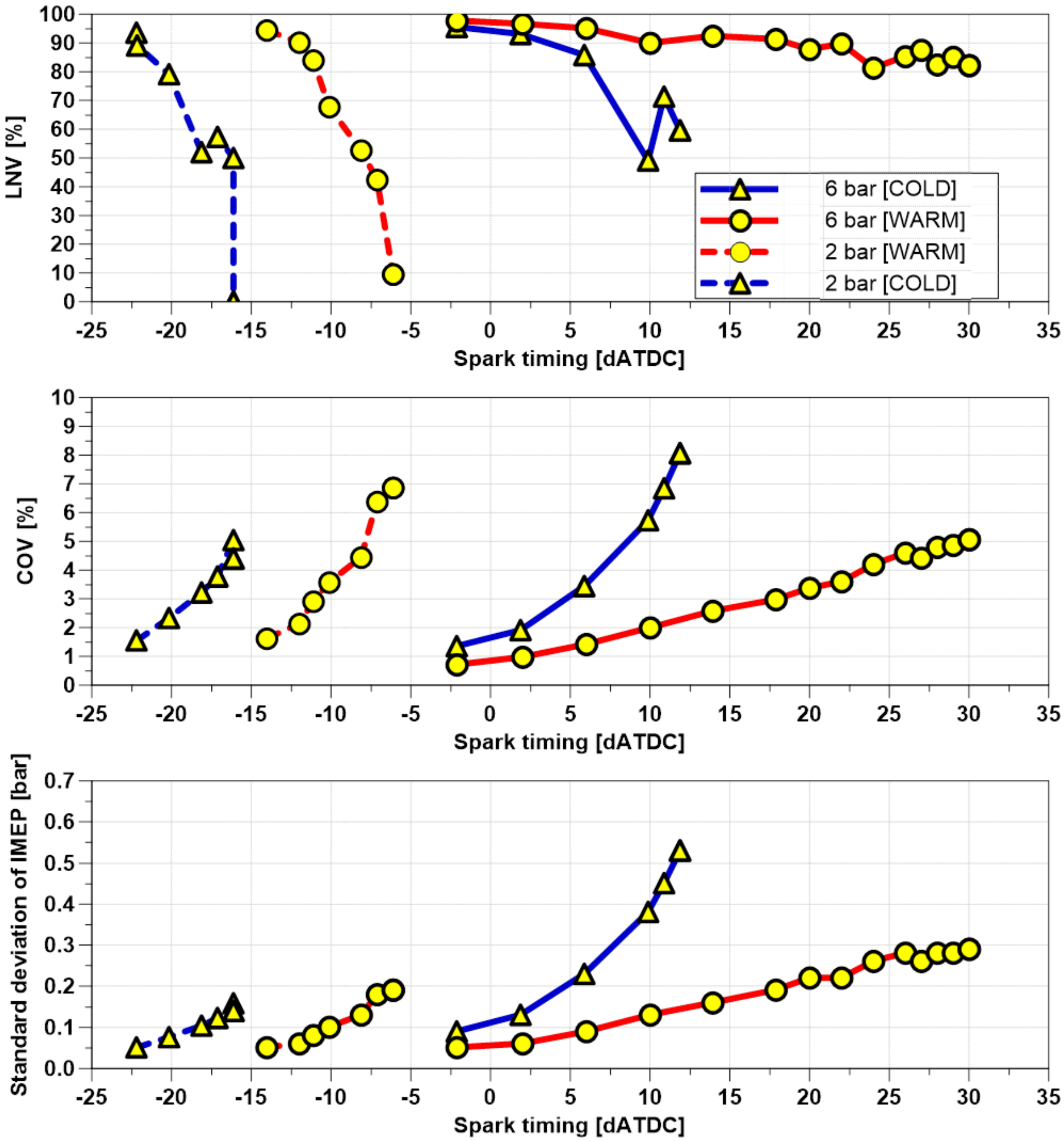

Figure 5-18: Combustion stability trends with spark retard at warm (approximately 70-90˚C) and cold (approximately 20˚C) fluid conditions for various loads at 1200 rpm, λ = 1.

5.4.2 Strategy Optimization

To properly address this severe cold fluid spark retard limitation at the CSSR condition, an examination of the failure mode was necessary. An understanding of the combustion process as described by distinct burn duration segments is instructive. With jet ignition engines, different segments of the burn curve provide distinct information about combustion progress:

- Early burning, captured in the CA0-10 duration, encompasses the pre-chamber combustion process from spark through time of at least initial radical jet introduction into the main chamber. This duration occasionally captures the initial ignition process in the main chamber, depending on pre-chamber volume and fuel quantity present [165].

- Mid-burning, reflected in the CA10-50 duration, encompasses the full jet-induced ignition process in the main chamber and therefore is the burn duration segment most influenced by jet characteristics such as velocity and reactivity.

- Late burning, CA50-90, occurs long after the jet ignition process has concluded, when the distinct flame fronts combine to form a single flame front. Therefore, this phase is largely uninfluenced by characteristics of pre-chamber combustion or the resulting jets.

Figure 5-19 illustrates a typical jet ignition combustion phase. Key points are identified: when mass transfer initially reverses direction due to pressure build up during the pre-chamber combustion event, and the first emergence of reactive jets. Figure 5-20 illustrates combustion behavior at CA10, CA50, and CA90. From this particular case study, it is clear that CA10 corresponds to the angle at which reactive jets first emerge from the pre-chamber. Therefore, the CA0-10 duration in this case corresponds to the pre-chamber combustion event from time of spark to emergence of reactive jets. At CA50, jets have emerged, the jet ignition process completed, and the ignition sites have created distinct flame fronts. CA10-50 describes the full jet process from reactive jet emergence to distinct flame front formation. At CA90, there is only a single flame front and nearly all fuel has been consumed. CA50-90 therefore encompasses the combination of the distinct flame fronts to form a single flame front to consume the remainder of the fuel. This latter process exhibits no significant influence of jet characteristics or the jetting process.

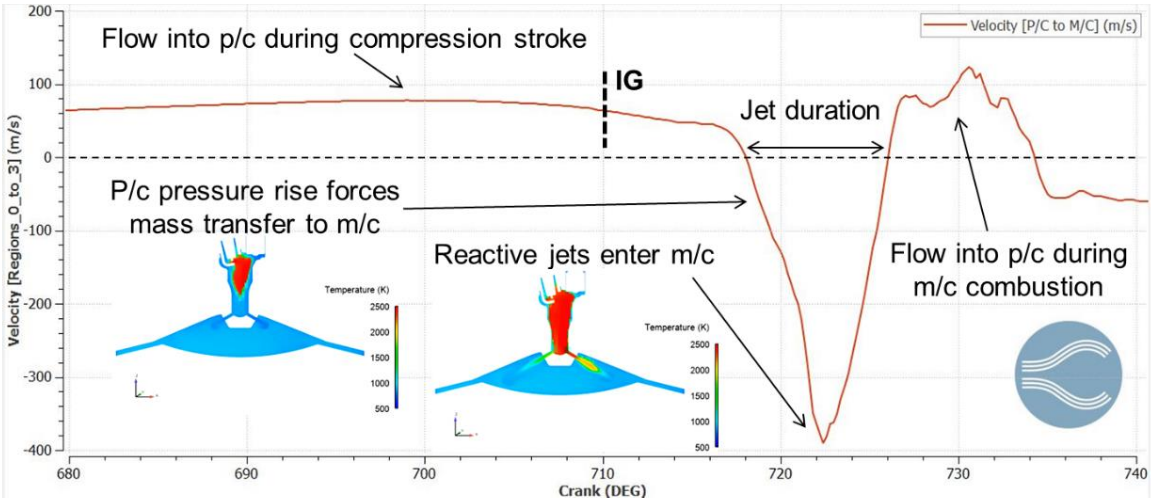

Figure 5-19: Example mass transfer between pre-chamber and main chamber during the combustion phase, with key events identified. 2400 rpm, 10 bar BMEP, λ = 1.8.

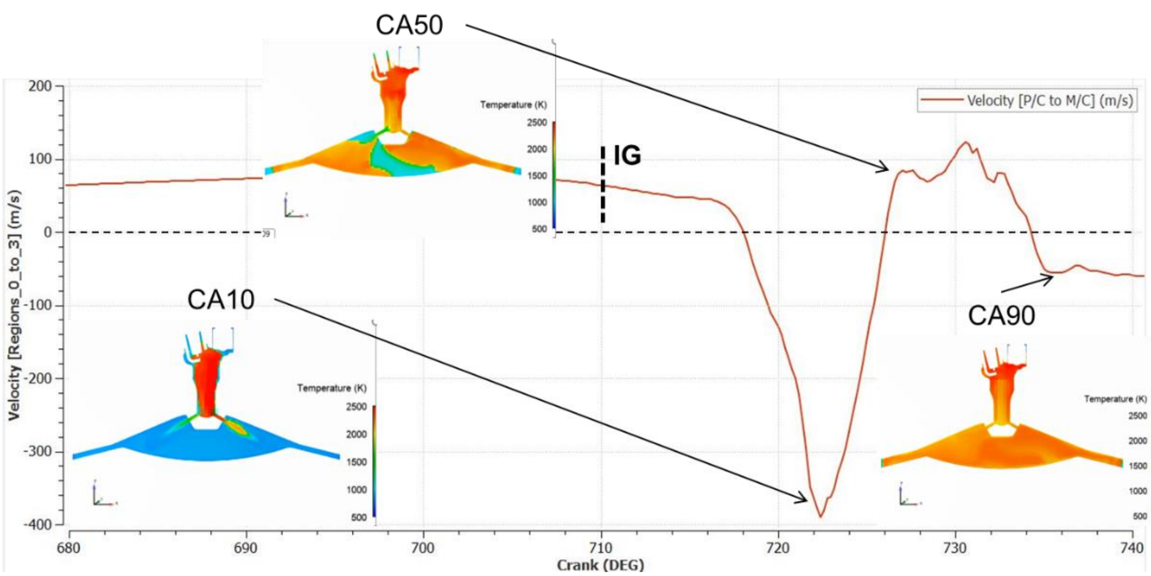

Figure 5-20: Example mass transfer between pre-chamber and main chamber during the combustion phase, with CA10, CA50, and CA90 events identified. 2400 rpm, 10 bar BMEP, λ = 1.8.

Returning to the CSSR condition, an examination of the different burn duration segments (Fig. 5-21) showed linear trends observed in burn duration versus spark timing. These durations were shorter with MJI at λ=1 compared to SI, which was counterintuitive to the spark retard limitation result, as reduced burn duration at common conditions should indicate available headroom to continue retarding spark timing. The 300-cycle average burn duration (left column in Fig. 5-21) provided no indication of instability. In the cycle average burn duration segments, the burn duration trends with spark timing remained linear, with no apparent degradation even at the spark retard limit. However, inspection of the standard deviation of these burn duration segments indicated an increasing instability in the burn durations themselves with MJI at λ = 1 as spark timing was retarded. The instability was present in all three burn duration segments, including CA0-10. The presence of the instability in the early burn duration metric while the cycle averaged burn durations remain relatively short, implied that the pre-chamber combustion event was experiencing infrequent misfires or partial burns which caused the main chamber to misfire.

Pre-chamber combustion instability can have several causes including variable mixture preparation conditions or variable heat transfer. Here the ability of the active system to operate with fuel injected directly into the pre-chamber was again exploited. Auxiliary fuel injection provides direct control over both the fuel quantity and its relative location at time of spark, thereby mitigating some variability in mixture preparation. In order to prevent over-fueling in an auxiliary fueled scenario, the engine is operated lean.

Once the MJI engine was operated at λ = 1.4 with auxiliary fuel added to the pre-chamber, the early on-set instability in the burn duration segments present at λ = 1 was eliminated. Auxiliary fueled λ = 1.4 operation produced CA0-10 durations faster than both SI and MJI at λ = 1, and the CA10-50 and CA50-90 burn durations were similar to or slightly faster than those of SI at λ = 1. The sudden deterioration in burn duration stability as spark timing approached TDC with MJI λ = 1 operation was no longer present, allowing auxiliary fueled λ = 1.4 operation to proceed to later spark timings, consistent with the spark retard limit of SI operation.

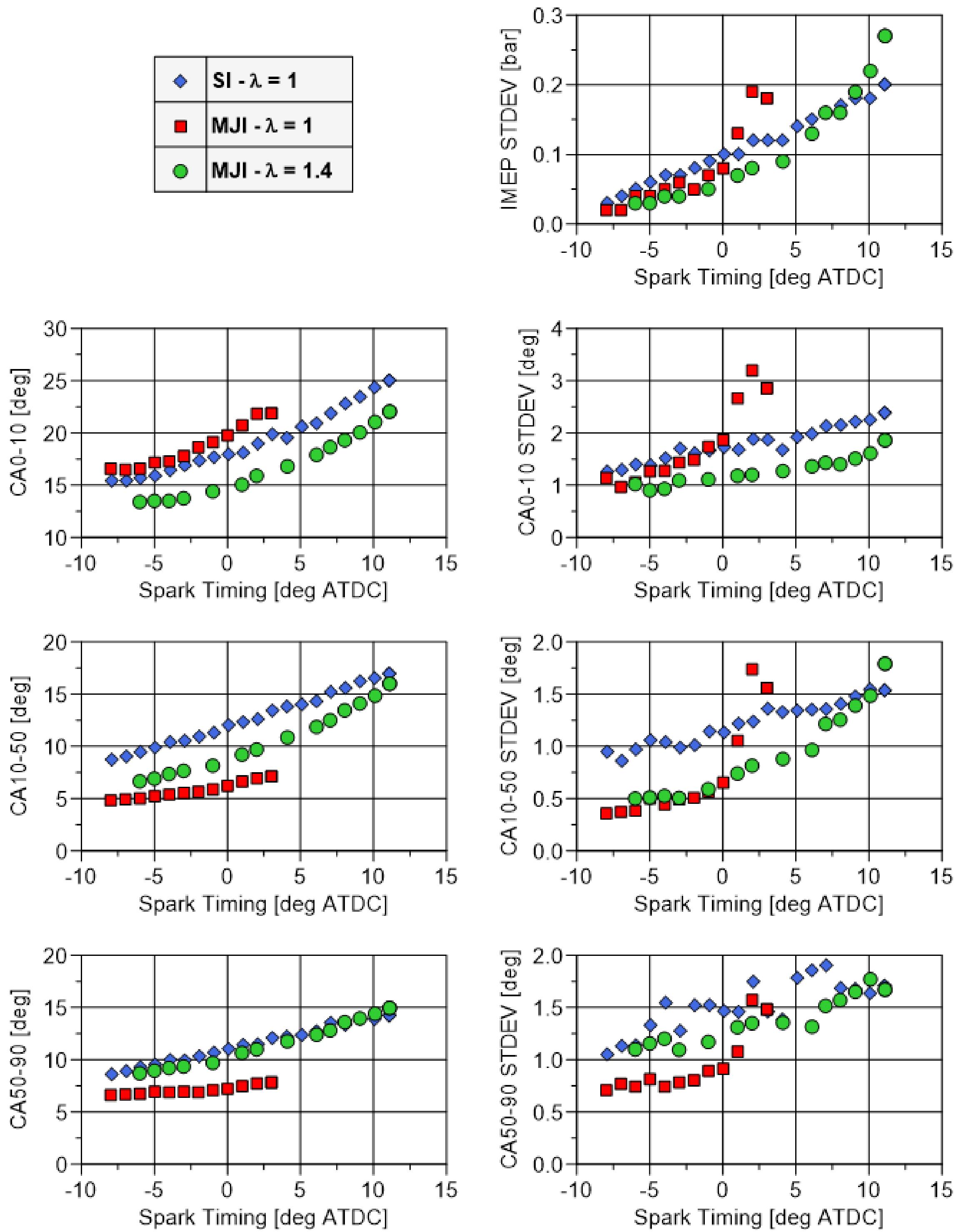

Figure 5-21: Spark retard trends at 1500rpm, 2 bar net mean effective pressure (NMEP), 20˚C fluid temperature.

Partial lean auxiliary fueled MJI operation was consequently established as an effective strategy for expanding MJI spark retard authority at the CSSR condition.

Figure 5-22 illustrates the benefit that this strategy provided. SI engine spark retard authority was contrasted with that of the baseline MJI strategy, which was non-auxiliary fueled $\lambda = 1$ operation. At the CSSR condition for this engine, the PFI SI engine achieved a stable CA50=60 dATDC, exceeding the specific exhaust enthalpy target of 5.5 kW/L without any detectable misfires. This exhaust enthalpy target was based on MAHLE Powertrain's database of modern SI engine performance tables, including CSSR operation. By contrast, the MJI baseline strategy experienced excessively frequent misfires beyond a CA50 = 20 dATDC, a remarkable loss of 40 crank angle degrees of spark retard authority. This produced a maximum specific exhaust enthalpy of just over 2 kW/L, < 40% of the target. Additionally, a calculated 10 second cumulative HC and NO_x result was nearly 3 times the total of the SI case at the respective spark retard limits. The optimized MJI operating strategy achieved a nearly identical spark retard limit as the SI engine. This strategy also produced identical specific exhaust enthalpy and emissions results to the SI case over the full spark retard range.

It should be noted that the exhaust enthalpy and emissions targets identified in Fig. 5-22 are most applicable to production SI engines that operate at or near stoichiometric at the CSSR condition and use 3-way catalysts for emissions control. These targets were chosen because of their widespread availability in literature and within MAHLE Powertrain's database. Lean SI engines have employed multiple aftertreatment strategies and target exhaust enthalpy and engine-out emissions are not widely cited. An active MJI engine that operates lean for the majority of the engine map would have a lean aftertreatment solution. Lean aftertreatment generally is meant to operate at nominally lower temperatures than those of stoichiometric engines. Additionally, lean aftertreatment packages typically contain storage catalysts that would theoretically be able to tolerate higher NO_x emissions than 3-way catalysts because uncatalyzed NO_x could be stored. Therefore, maintaining the same specific exhaust enthalpy and emissions targets is considered a conservative approach for lean MJI; an optimized aftertreatment solution would likely have reduced specific exhaust enthalpy and perhaps even higher maximum engine-out emissions targets.

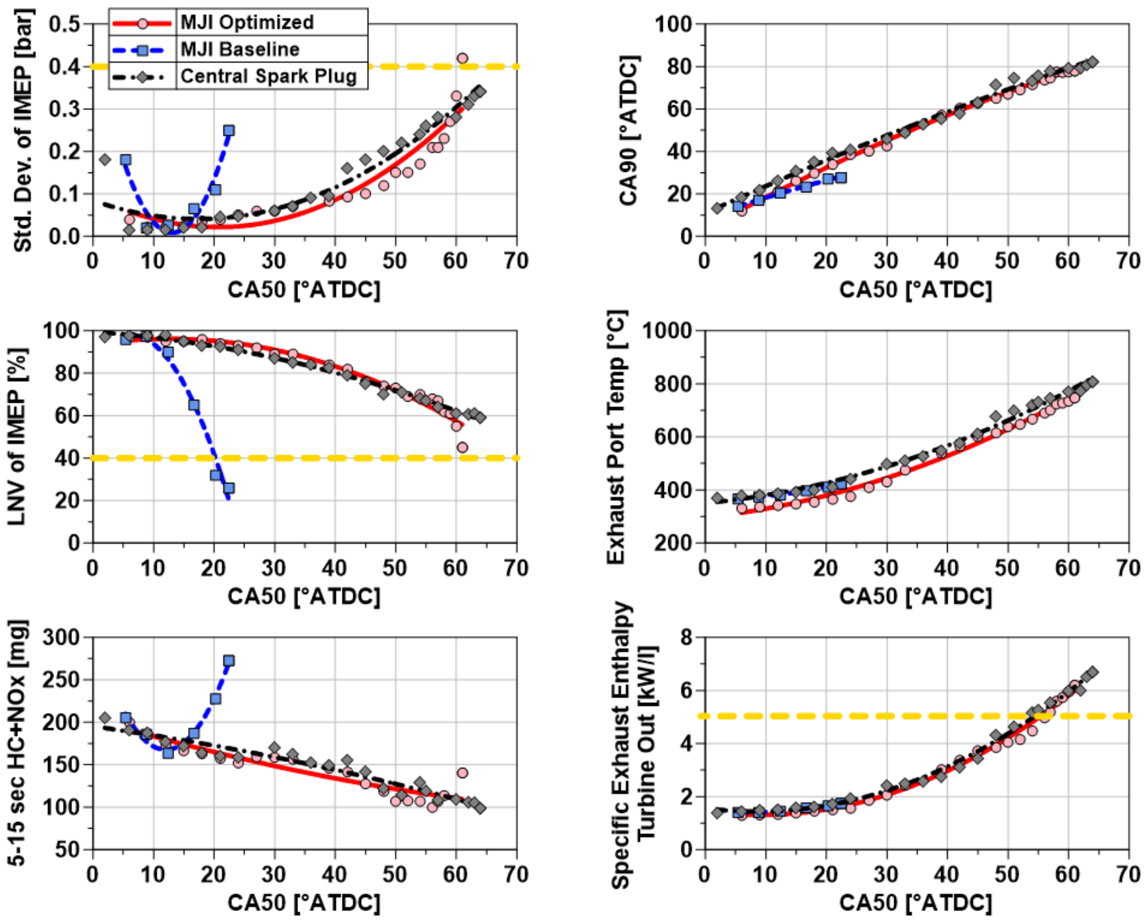

Figure 5-22: Comparison of relevant catalyst heating trends with CA50 at 1500rpm, 2 bar NMEP, 20°C fluid temperature for baseline SI engine, non-optimized MJI engine at λ = 1 with no auxiliary fueling, and optimized MJI engine at λ = 1.15 with auxiliary fueling.

The ability to adjust λ in the MJI engine was used to minimize engine-out emissions during spark retard at the CSSR condition. A calculated 10 second cumulative mass of HC and NO_x emissions is presented in Fig. 5-23. Enleanment produced counter HC and NO_x trends, as is evident in Fig. 5-23. Beyond the λ = 1.2 condition, NO_x emissions reduced with enleanment due to the reduction in combustion temperatures with increased dilution. Conversely, HC emissions increased substantially beyond λ = 1.2 at this speed and load. The steep increase in HC emissions was exacerbated by the retarded CA50 of approximately 50 dATDC leading to a high degree of incomplete combustion. The minimum cumulative mass was clearly evident in the near-lean region, at approximately λ = 1.15, with auxiliary fuel still required.

These emissions trends are sensitive to several factors, including fuel quantity injected into the pre-chamber and pre-chamber volume. Therefore, a comprehensive analysis of all sensitivities at the CSSR condition is necessary in order to identify the true optimal λ.

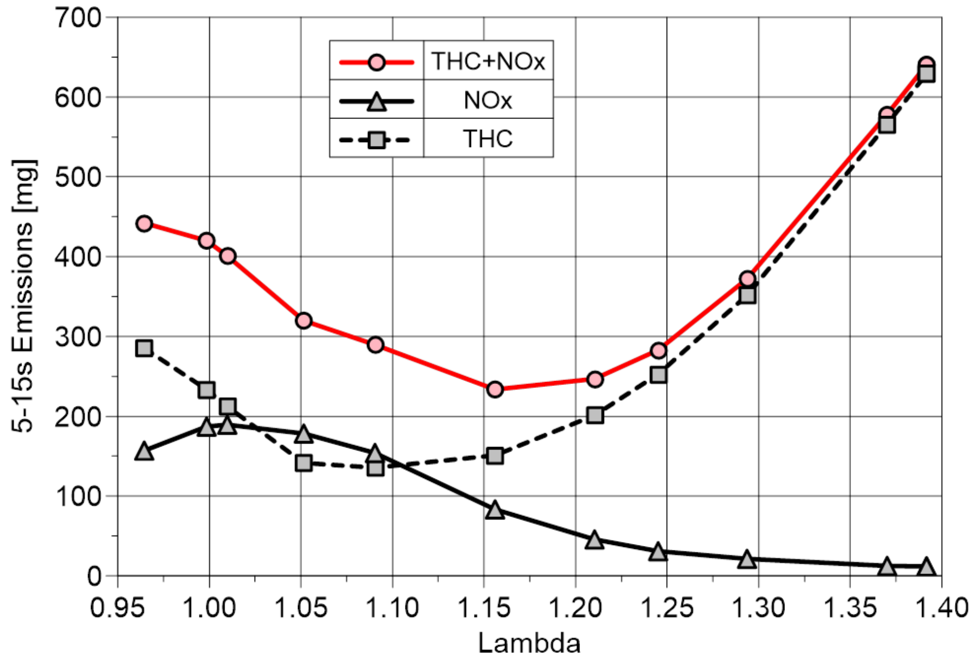

Figure 5-23: Emissions trends with λ at 1500rpm, 2 bar NMEP, CA50 = 50 dATDC, 20°C fluid temperature.

5.4.3 Sensitivity to Charge Motion

The effect of charge motion on jet ignition performance is not well understood, particularly its impact at retarded spark timing. For these experiments, the four charge motion variants were evaluated at the CSSR condition at the optimal emissions λ of 1.15 identified in the previous section. The charge motion variants were evaluated across the full range of spark retard authority. Figure 5-24 shows good agreement amongst the baseline, tumble, and swirl variants across multiple combustion stability metrics. The “swumble” variant exhibited a spark retard limit 10 crank angle degrees advanced from those of the other variants. This represents a significant reduction in spark retard capability for the swumble variant. The COV and standard deviation of NMEP trends mirrored the LNV trend with the swumble variant, indicating that swumble produced a higher degree of partial burn events that eventually transition to full misfires, and that this constituted the failure mode.

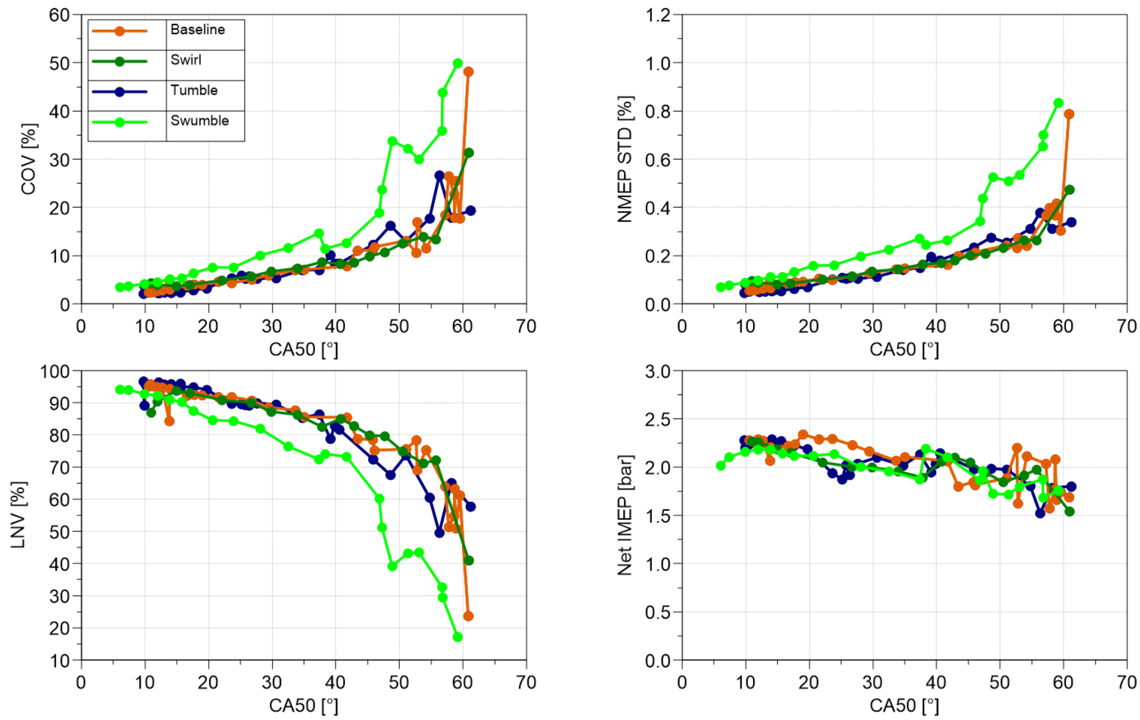

Figure 5-24: Various combustion stability metrics vs. CA50 at 1500rpm, 2 bar NMEP, λ = 1.15.

An examination of brake and gross indicated thermal efficiency and fuel consumption in Fig. 5-25 reveals similar values amongst all four charge variants. While efficiency is not a major criterion used for CSSR calibration development, it is interesting to note that charge motion has minimal impact on thermal efficiency across a spark retard sweep, even at the stability limit of the sweep. This is in contrast to the part load and high load results in λ sweeps presented in the next chapter, where differing levels of charge motion do produce differences in both gross indicated and brake thermal efficiencies, with the tumble variant producing ITE increases of 1 percentage point over the baseline and the swirl variant producing ITE deficits in excess of 1 percentage point versus the baseline at lean λ values.

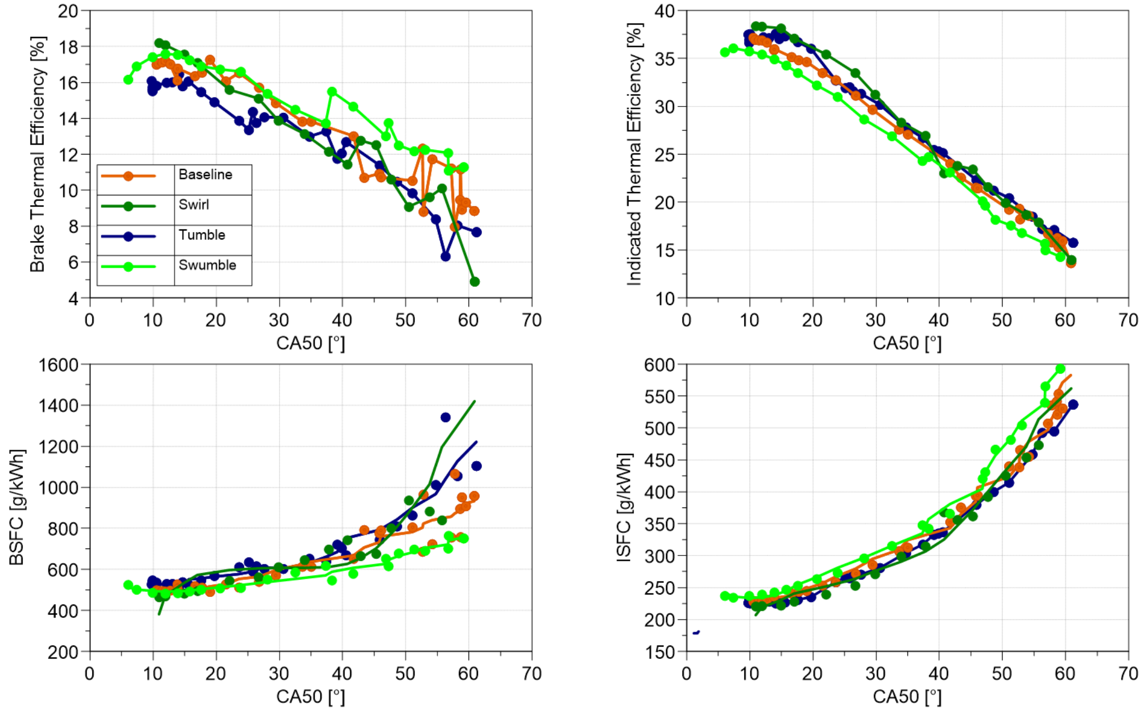

Figure 5-25: Efficiency and fuel consumption metrics vs. CA50 at 1500rpm, 2 bar NMEP, λ = 1.15.

The CA10-90 results are presented in Fig. 5-26, with tumble showing consistently faster burn durations and swumble showing consistently slower burn durations versus the ensemble average (approximately 10% faster and 10% slower, respectively). The burn duration segment that is driving this result is the late burning stage, CA50-90. The separation in burn durations was most apparent in this analysis, with swumble again displaying the slowest late burn duration. This result provides an indication of the cause of the reduced spark retard authority observed in Fig. 5-24. The elongated late burning stage implies the presence of partial burning cycles in the 300 cycle average.

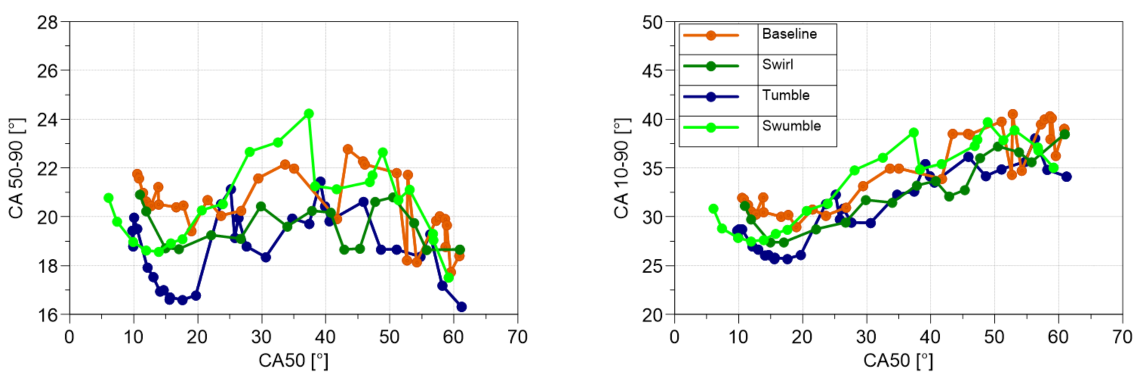

Figure 5-26: Burn duration vs. CA50 at 1500rpm, 2 bar NMEP, λ = 1.15.

The engine-out emissions results in Fig. 5-27 also demonstrated the superior performance of the tumble variant. The separation of the baseline, tumble, and swirl variants was more prominent in these results than it was in the efficiency results, however. The tumble variant displayed consistently lower engine-out HC emissions than the other variants (approximately 40% below the ensemble average), and, along with the baseline variant, the lowest CO values (approximately 30% below the ensemble average). Combustion efficiency takes both of these emissions species into account, and consequently the tumble variant produced a combustion efficiency 0.5-1 percentage points higher than the next nearest variant (baseline), and 2 percentage points higher than the swumble variant. The swumble variant produced the highest CO, HC, and, notably, NO_x emissions (approximately 50% higher than the ensemble average under heavy spark retard conditions) of all the variants. This result implies that combustion with the swumble variant is simultaneously hotter and less complete than the other variants. The optimum points overlaid in Fig. 5-27 demonstrate that the tumble variant produces the most consistently optimal results.

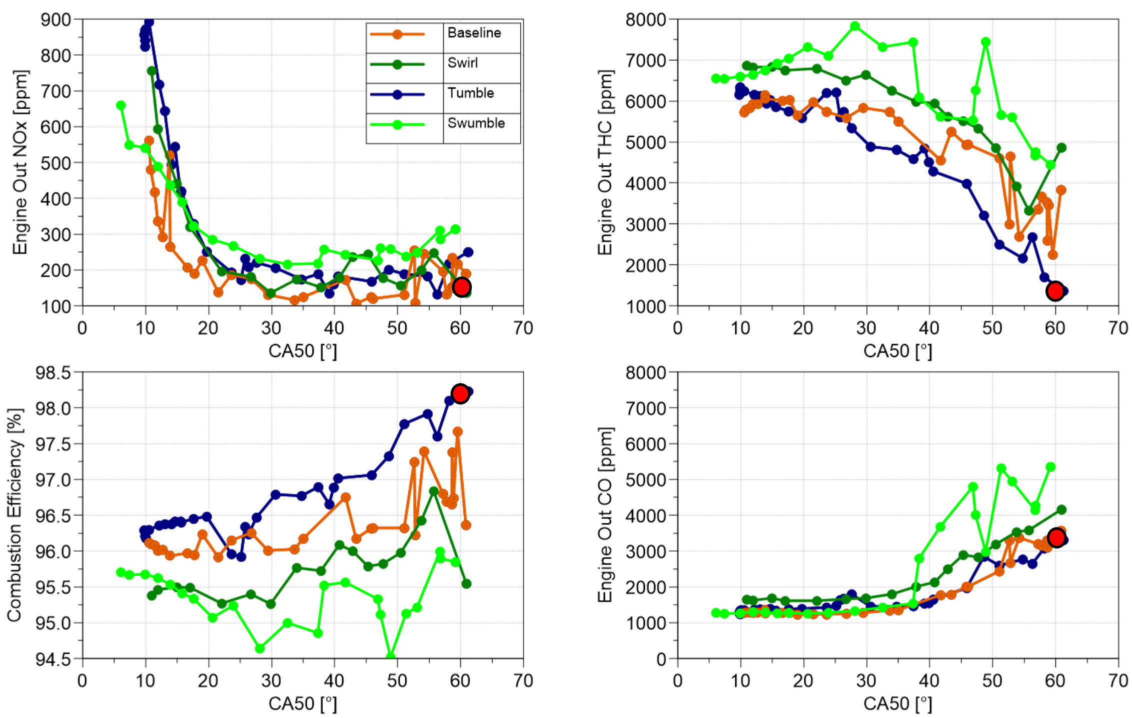

Figure 5-27: Engine-out emissions and combustion efficiency vs. CA50 at 1500rpm, 2 bar NMEP, λ = 1.15.

Any combustion temperature difference with swumble versus the other variants was not significant enough to manifest in noticeably different exhaust enthalpy. Figure 5-28 shows all charge motion variants achieved roughly the same peak specific exhaust enthalpy, without any major separation across the full spark retard range. However, with the higher measured engine-out NO_x and HC, the two key emissions levels monitored at the CSSR condition, swumble produced substantially higher cumulative NO_x+HC emissions than the other charge variants, approximately 50% higher than the ensemble average. Therefore, while charge motion generally does not have much of an impact on spark retard authority or thermal efficiency at a common λ at the CSSR condition, the introduction of combined swirl and tumble does have the potential to reduce spark retard authority and produce higher engine-out HC and NO_x emissions without producing any higher specific exhaust enthalpy. This makes swumble the clearly inferior charge motion type for this condition. Conversely, a moderate increase in engine tumble over the baseline, in this case an increase of 13%, can significantly impact combustion efficiency and emissions under heavy spark retard conditions. As seen in Fig. 5-28, the tumble variant produces a combined NO_x+HC value 50% lower than the ensemble average under heavy spark retard conditions.

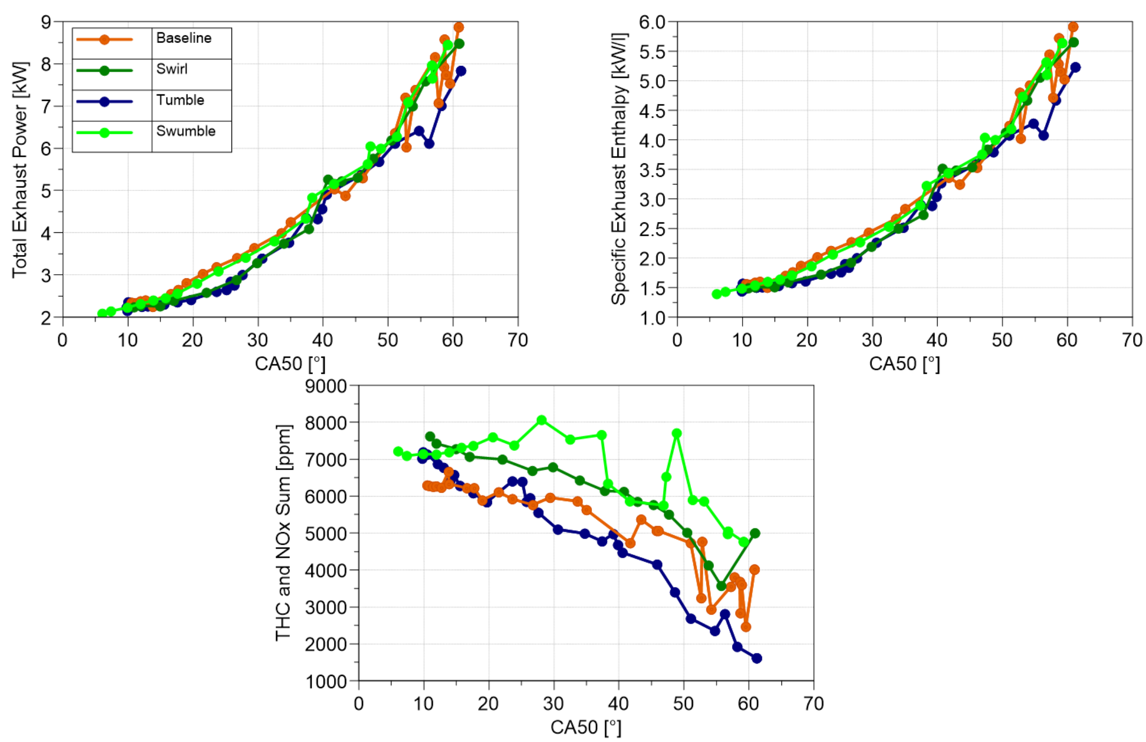

Figure 5-28: Exhaust enthalpy and emissions vs. CA50 at 1500rpm, 2 bar NMEP, λ = 1.15.

5.5 Summary

Modern production SI engines are required to be exceptionally versatile in their ability to operate across a wide range of engine speeds and loads, with many distinct speed/load regions having their own set of highly specific operating requirements. This requirement for engine versatility has inhibited the application of advanced combustion strategies and technologies. Typically, advanced combustion technologies are conducive to high efficiency operation in singular regions of the engine map. For instance, successful operation of many advanced compression ignition concepts is highly temperature dependent. While not as sensitive to external factors as some of these advanced concepts, jet ignition has historically demonstrated poor performance under low load conditions. The three key operating regimes that fall under this umbrella are: steady state low load operation, idle, and CSSR.

There are several theories as to the underlying cause of this low load limitation. Arguably the most popular theory is that the gas exchange process between pre-chamber and main chamber is arrested when the engine is heavily throttled, causing an unacceptably high mass fraction of residual gas to remain trapped in the pre-chamber at time of spark. A combination of CFD simulations and direct gas sampling from the pre-chamber have shown that the gas exchange process during the intake stroke in particular provides a significant percentage of O_2 to the pre-chamber, and that heavy throttling can disrupt this portion of the gas exchange process, rendering it ineffective.

Another theory is that background cylinder pressure and temperature under low load conditions are not conducive to jet formation of auto-ignition sites in the main chamber. Similarly, the low charge density at these conditions may lead to weak or slow pre-chamber combustion causing a greater percentage of fuel energy to be lost to pre-chamber wall heat transfer, effectively reducing the reactivity of the jets. Synthesizing the results presented in this chapter with those from literature, it appears likely that a combination of these two theories is responsible for the observed limitations with jet ignition.

Data from the direct pre-chamber gas sampling experiment demonstrated that injecting fuel in the pre-chamber using the auxiliary fuel injector was effective at reducing in-pre-chamber residual gas fraction, either through direct displacement or changed intra-chamber pressure dynamics. This provided the genesis of a potential strategy for stable low load operation.

Under steady state conditions, it was demonstrated that auxiliary fueling extended the load limit downward by 0.8 bar, or a 2/3rd reduction. In order to prevent overly rich conditions in the pre-chamber, the engine was simultaneously de-throttled to increase the main chamber and background pre-chamber λ. This mild de-throttling provided the additional advantage of allowing more O_2 mass to enter the pre-chamber during the intake stroke. The results showed that moderate enleanment provided the most stable low load extension, and the optimal λ for this operation is likely between 1.3 and 1.6. Despite the moderate enleanment, all major emissions including engine-out HC reduced with λ = 1.5 operation versus λ = 1 operation. This provides confidence that the change in operating strategy will not overly burden the aftertreatment system.

Idle and CSSR operation with jet ignition both suffer from a severe nominal spark retard limitation. Spark retard is necessary at idle and CSSR to ensure adequate torque reserve and exhaust enthalpy, respectively. To address the idle torque reserve issue, it was shown that operating the jet ignition engine with a combination of limited spark retard authority and a range of λ values provides a level of torque reserve that far exceeds typical SI engine requirements. Because spark timing and fuel injection pulsewidth can be adjusted on a cycle-by-cycle basis, this λ and spark retard strategy meets the timescale requirements for pedal torque demand.

The limited spark retard authority is most impactful at the CSSR condition, which has a disproportionately large influence on cumulative drive cycle tailpipe emissions levels. An examination of burn duration segments and the 300-cycle standard deviation of the duration of these segments revealed that an instability was present at the spark retard limit that was not being reflected in the average burn duration segment trends. This discrepancy, coupled with the appearance of the instability in all burn duration segments starting with the segment that describes the pre-chamber combustion event, indicates that the pre-chamber combustion event experiences infrequent partial burns and misfires which in turn propagate to poor main chamber combustion performance and that this effect was the cause of the spark retard limitation. Once again, the addition of auxiliary pre-chamber fuel added consistency to the pre-chamber mixture preparation and combustion phases, eliminating the instability and extending the spark retard window all the way to that of the base SI engine. A sweep of λ demonstrated an ideal near-lean λ that minimized the critical emissions species during CSSR operation, HC and NO_x.

Various levels and types of charge motion were introduced to examine whether they induced any performance differences at the CSSR condition. The baseline, tumble, and swirl variants demonstrated identical spark retard performance, but the swumble variant exhibited noticeably worse performance. Additionally, the swumble variant produced higher engine-out NO_x (30%), HC, and CO (50%) across the spark retard sweep versus the ensemble average with no noticeable increase in exhaust enthalpy, making swumble motion distinctly unsuited for jet ignition CSSR operation. Tumble motion, however, showed reductions in engine-out emissions across the spark retard sweep, with a 50% reduction in engine-out

NO_x+HC emissions and a 1.5 percentage point increase in combustion efficiency versus the ensemble average under heavy spark retard conditions.

Addressing these low load challenges is critical to ensuring the applicability of the jet ignition technology to modern SI engines. The well documented part load and high load efficiency results are only relevant if the jet ignition engine can accommodate the full suite of engine operating requirements, especially those that are customer-facing and those that impact emissions legislation.

Chapter 6

Influence of Charge Motion on Jet Ignition Engine Operation

6.1 Introduction

In the previous chapter, the need for optimization of the active pre-chamber engine to encompass operation over the whole engine map was established. While active pre-chamber engines have historically exhibited limitations when operating under low load conditions, they also introduce new parameters and degrees of freedom that can be manipulated to mitigate these challenges. Results shown in the previous chapter indicate relative changes in degree of sensitivity to certain parameters when the active pre-chamber operates lean versus at stoichiometric conditions. Of most relevance to the present chapter is the change in engine response to charge motion as engine operation becomes regressively ignitable.

At the CSSR condition, the charge motion variants considered in this study produced essentially no changes in engine performance at conventional spark timings, but the separation in certain parameters grew as spark retard increased and combustion stability deteriorated. Tumble motion produced advantages in NO_x emissions, combustion efficiency, and stability versus the other charge motion variants, and these advantages became more pronounced as spark retard increased. The results indicate that optimized charge motion becomes more impactful as engine conditions become regressively ignitable.

In this chapter, the concept of charge motion influence on combustion under difficult-to-ignite engine conditions is explored in greater detail. Specifically, the changes in combustion sensitivity to charge motion as the engine is enleaned and as the load becomes knock limited are analyzed. While sub-optimal charge motion might not present significant operational limitations as it did at the CSSR condition, it can have a significant impact on thermal efficiency, combustion efficiency and engine-out emissions. In this chapter, the potential of optimized charge motion to improve engine performance under part load and full load conditions is evaluated. Analysis of high speed in-pre-chamber pressure data provides insight into how induced differences in pre-chamber conditions can have a cascading impact on main chamber combustion. Application of CFD reveals the mechanics of charge motion translation from main chamber to pre-chamber and how charge motion affects both mixture dynamics and the pre-chamber combustion event itself.

Harmonizing these three distinct streams of data (overall experimental engine performance, in-pre-chamber experimental data and simulation) provides both a fundamental understanding of the effect of charge motion and a roadmap for charge motion optimization for jet ignition engines.

6.2 Non-Knock Limited Operation

6.2.1 Overall Engine

Jet ignition engine sensitivity to charge motion is first examined at Condition 1, a non-knock limited part load condition (1500 rpm, 6 bar BMEP). Results are presented across a sweep of λ, from 1 to the lean limit of the engine at this condition. Knock is not prevalent for any of the charge motion variants except at the λ values closest to 1. Figure 6-1 shows the two relevant combustion stability metrics, COV and LNV of IMEPg. Modern production ICEs typically hold to a COV of IMEPg limit ≤ 3%, which was adopted for this test. An LNV value < 88% indicates a high likelihood that a partial burn event has occurred, whereby a significant portion of the fuel present in the cylinder is not consumed by the combustion flame in multiple intermittent cycles. These limits are depicted by the red dashed lines in Fig. 6-1. It should be noted that the test plan required continued engine operation beyond these limits in the context of the λ sweep, with data collection ending when misfires became too severe to maintain engine load or when the boost system was no longer capable of providing sufficient boost to maintain constant load.

In Fig. 6-1, it is evident that the tumble variant maintains acceptable stability throughout the range of λ from 1.0 to 2.0, without any partial burn events. The baseline variant performs similarly but with increased instability from λ = 1.5 and a stability limit from λ = 1.9. There is also more pronounced deterioration in LNV in this lean λ range. The swirl and swumble variants perform measurably poorer, with stability limits reached between λ = 1.3 and 1.6.

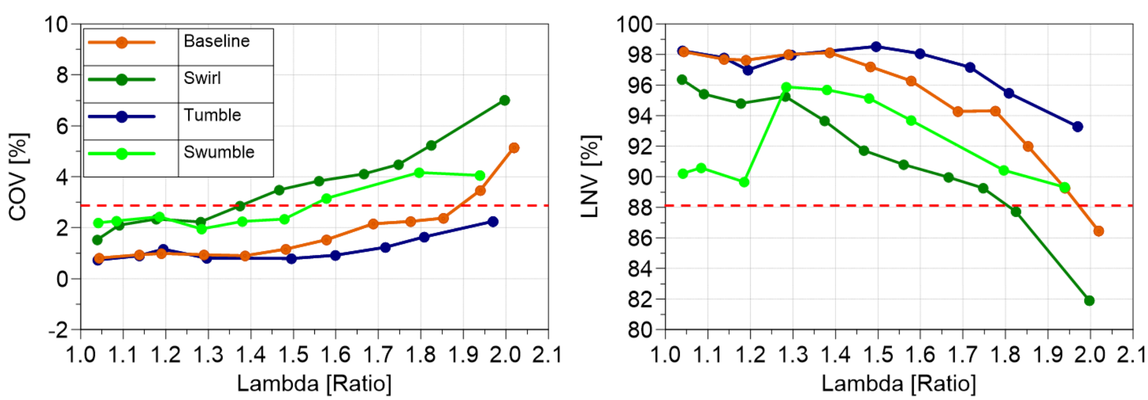

Figure 6-1: Combustion stability metrics vs. λ; 1500 rpm, 6 bar BMEP, CA50 = 8 degrees after TDC.

As was described in Chapter 3, pre-chamber fuel injection quantity was held constant among the charge motion variants wherever possible. The baseline charge motion variant largely dictated pre-chamber fuel injection relationship to λ, with the other variants approximately adhering to this relationship. Pre-chamber fuel quantity is a variable with a significant influence over main chamber combustion stability. Typically, it must increase with main chamber λ in order to maintain a consistent pre-chamber λ, as the background (passively provided) λ in the pre-chamber enleans with that of the main chamber. In this study, the process for determining pre-chamber injection quantity for the baseline variant involved increasing injection pulsewidth to allow the minimum quantity of fuel required to maintain main chamber COV of IMEPg ≤ 3%. This combustion stability requirement was used as the primary criterion for determining pre-chamber injection quantity, with adherence to the baseline variant's fuel flow-λ relationship as the secondary criterion. As can be witnessed in Fig. 6-2, this resulted in relatively consistent quantity-λ relationships amongst the baseline, tumble, and swumble charge motion variants at this speed-load condition. The swirl variant, however, required approximately twice the pre-chamber fuel quantity that the other variants required. The swirl variant also required pre-chamber auxiliary fuel injection to begin at an earlier λ value in the sweep (beginning at 1.2 versus 1.4 for the other variants). Despite this increased quantity requirement, the swirl variant consistently demonstrated inferior combustion stability behavior to the other variants across the full sweep of λ values. This indicates both a high level of instability in the system induced by swirl motion and that the instability originates in mixture preparation in the pre-chamber, or at least it cannot be adequately mitigated through the traditional means of increasing pre-chamber fuel injection quantity.

The poor stability results of the swirl charge motion variant propagate to other metrics as well, including burn durations and efficiency as will be demonstrated. CFD simulations, discussed later in this chapter, provide an insight into the in-pre-chamber mixture dynamics and how the swirl motion affects these dynamics.

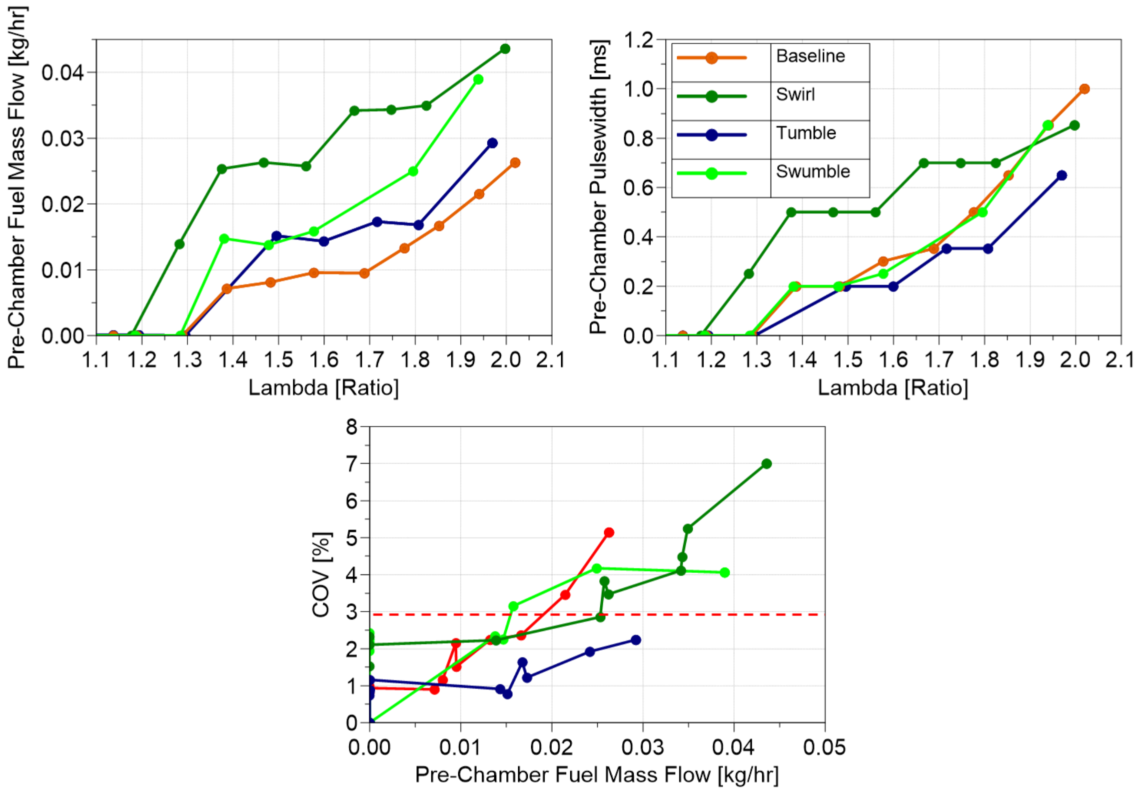

Figure 6-2: Pre-chamber fuel injection parameters; 1500 rpm, 6 bar BMEP, CA50 = 8 degrees after TDC.

Fig. 6-3 shows the CA50 for the charge motion variants, confirming that light knock may be present near λ = 1 but is absent for all variants from λ = 1.2. The instability in CA50 in the near-lean region (λ = 1.0-1.3) is due to cylinder-to-cylinder variation that manifests under lean conditions but is mitigated by the addition of pre-chamber auxiliary fuel starting at λ = 1.4 for most variants. An examination of the burn duration segments shows that the two variants that include increased tumble motion (tumble and swumble variants) produce faster overall combustion duration. The difference in burn duration amongst the variants becomes prominent under lean conditions, with minimal separation at λ = 1. This result is consistent with the CSSR results, showing the influence of charge motion on burn duration is most prominent under poor-ignitability conditions. Under lean conditions, the swirl variant exhibits consistently slower late burning (CA50-90) than the other variants. This results in an overall longer CA10-90 burn duration with the swirl variant under lean conditions.

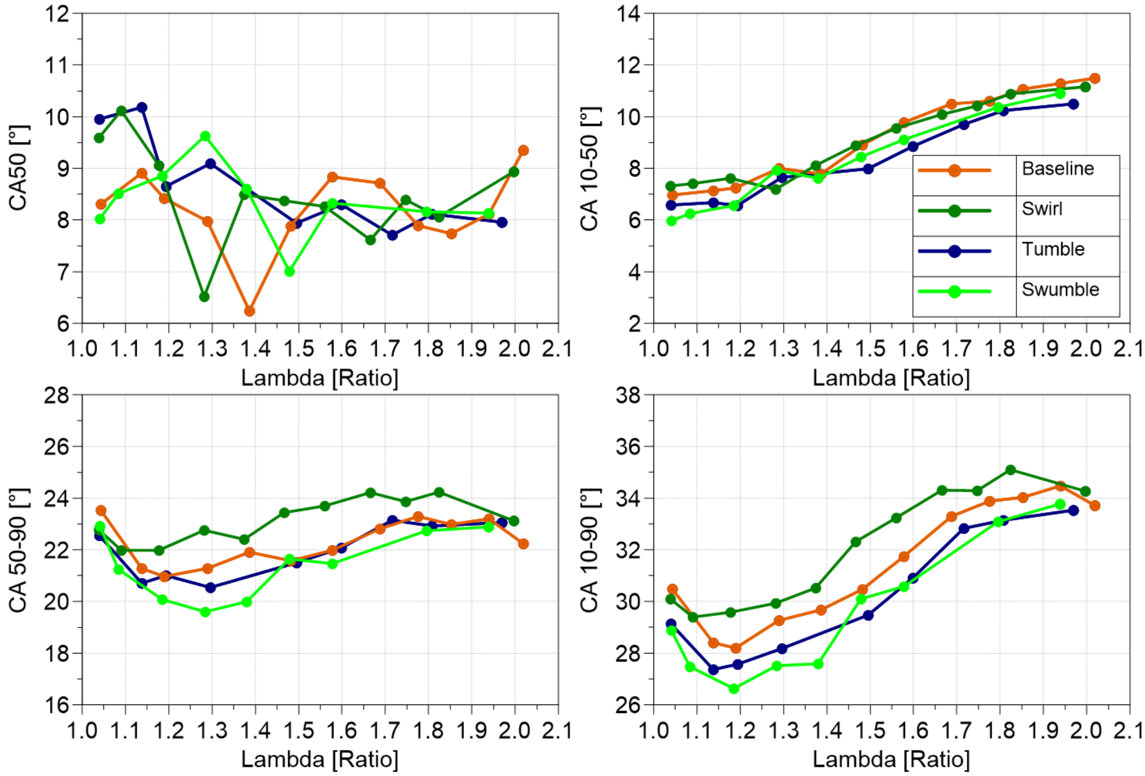

Figure 6-3: Burn duration metrics vs. λ; 1500 rpm, 6 bar BMEP.

IMEPg and BMEP trends with λ are depicted in Fig. 6-4. These results confirm the validity of the constant BMEP testing approach at this condition. As is observed, PMEP is not prominent at this condition, despite the added intake manifold and port restriction introduced by the charge motion inserts. Therefore, brake results provide the most accurate comparison amongst the charge motion variants at this condition.

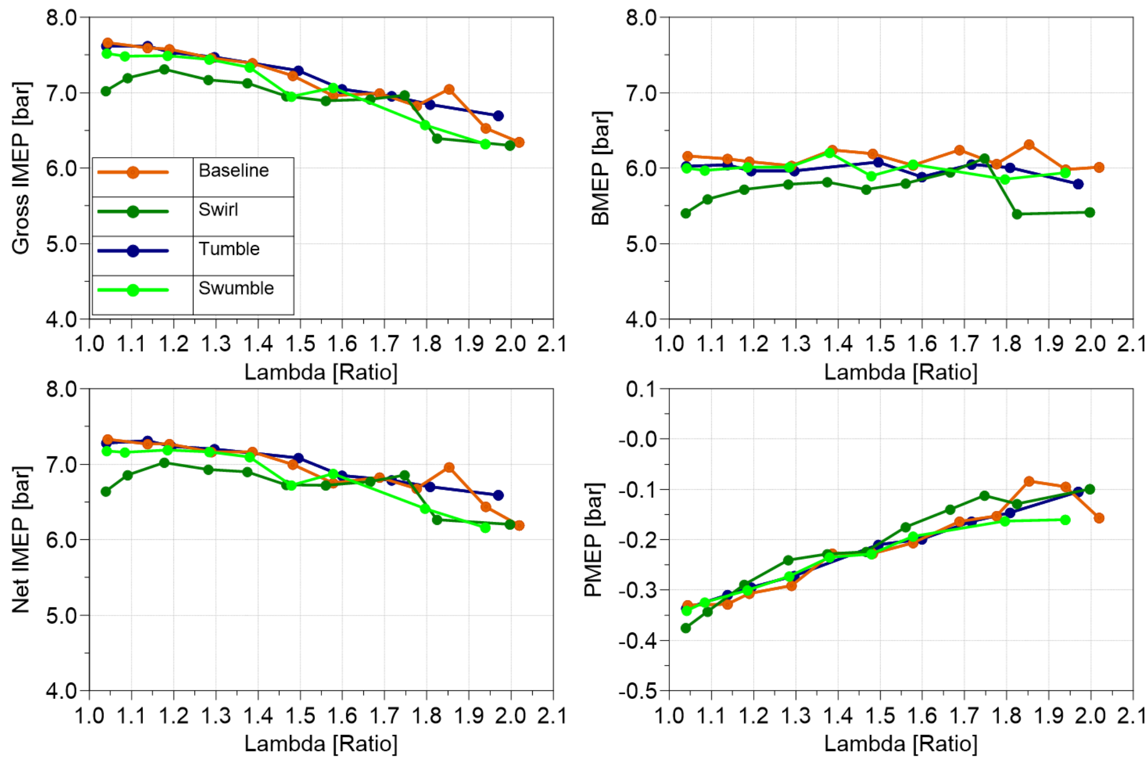

Figure 6-4: Mean effective pressure metrics vs. λ; 1500 rpm, 6 bar BMEP, CA50 = 8 degrees after TDC.

The competing efficiency pathways of reduced in-cylinder heat losses and increased incomplete combustion losses with enleanment result in a λ that corresponds to peak thermal efficiency occurring at a richer λ than the lean limit. This effect is observed in Fig. 6-5, with the peak BTE λ occurring approximately between λ = 1.6 and 1.7 for most variants. Because BMEP was held constant amongst the charge motion variants at this speed / load condition, BTE provides the most accurate comparison. Here the results largely mirror the stability and burn duration trends, with the tumble variant producing the highest BTE, followed by the baseline, swumble, and swirl variants, with the latter exhibiting rapid deterioration in BTE beyond the lean stability limit. ITE, which does not consider the relative pumping losses encountered across the λ sweep at this condition and also decreases across the sweep, exhibits similar trends but with differing peak efficiency λ values.

It is not known why the swirl variant outperforms the swumble variant in both BTE and ITE in the range of λ = 1.4-1.7 despite this trend not being reflected in either the burn duration or combustion efficiency metrics. This could be due to minor discrepancies in BMEP amongst the variants in this range. It should be noted that the swirl results display poor combustion stability, above the 3% limit, in this range.

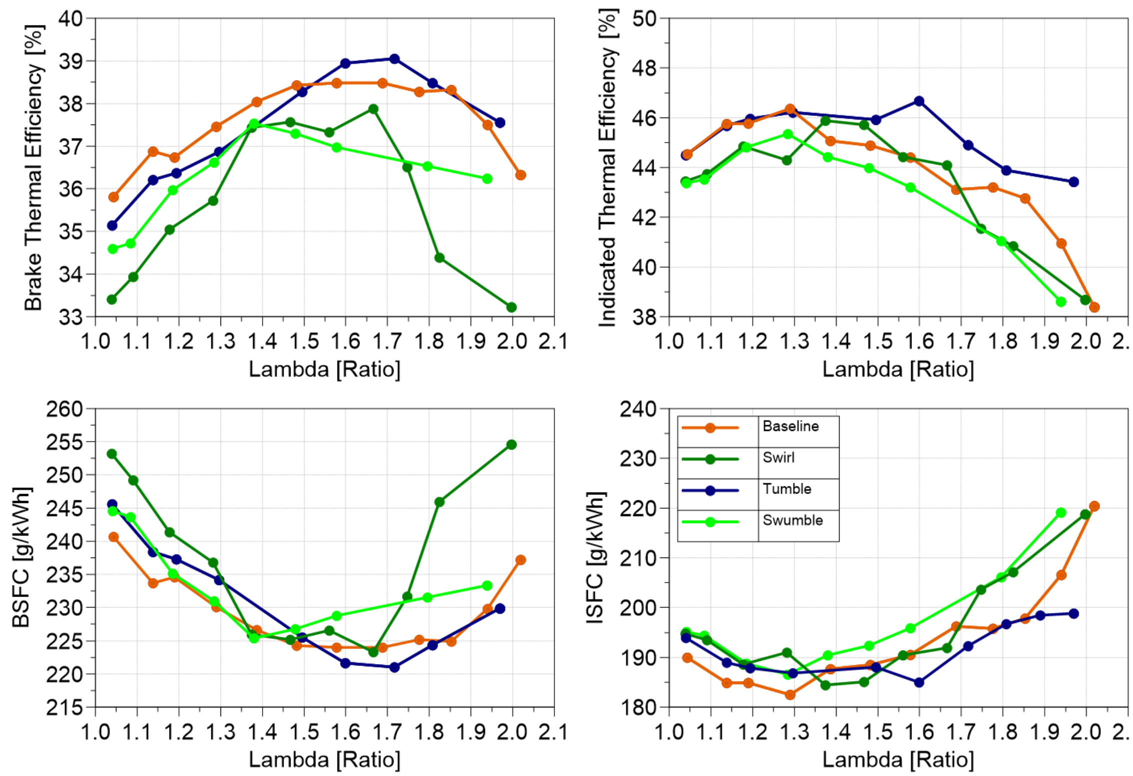

Figure 6-5: Efficiency and fuel consumption metrics vs. λ; 1500 rpm, 6 bar BMEP, CA50 = approximately 8 degrees after TDC.

Analysis of NO_x emissions trends versus λ in Fig. 6-6 show relative parity amongst the charge motion variants from λ = 1-1.6. The erratic trends in the range beyond λ = 1.6 do not appear to mirror any other major parameter's trend, and are likely the result of increasingly unstable combustion in this region, particularly in the swirl and swumble variant data. Therefore, it does not appear that charge motion has any noticeable impact on NO_x formation at this condition. However, the comparison of Figs. 6-1 and 6-6 demonstrates the benefit of enhanced combustion stability in the ultra-lean region, namely the ability to further reduce NO_x emissions by operating at stably leaner λ values.

An examination of the CO emissions trend shows a significant drop in emissions from λ = 1 to the near-lean region. CO then slowly increases with further enleanment. THC emissions decrease slightly in the near-lean region but then increase with enleanment, severely in the case of poor stability variants such as swirl.

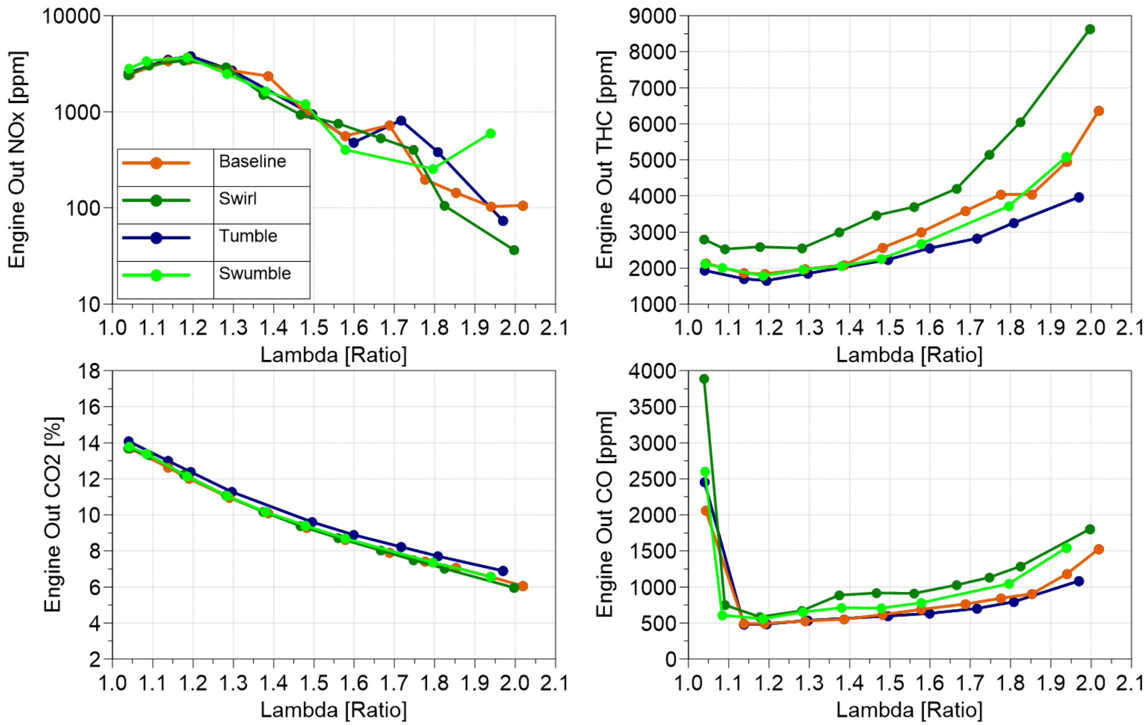

Figure 6-6: Engine-out emissions vs. λ; 1500 rpm, 6 bar BMEP, CA50 = approximately 8 degrees after TDC.

The CO and THC results translate well to the combustion efficiency trend depicted in Fig. 6-7. While combustion efficiency reduces with increasing enleanment, the swirl variant produces depressed combustion efficiency versus the other charge motion variants across the λ range starting from λ = 1.2. With late burning performance having a prominent impact on combustion efficiency, this swirl variant performance is expected. Conversely, the tumble variant produces the highest relative combustion efficiencies under lean conditions. Note that the combustion efficiencies depicted in Fig. 6-7, especially under lean conditions, are lower than would be expected for this type of combustion system. This is due to the relatively high CR for an SI engine coupled with the homogeneous mixture leading to a relatively greater crevice volume fuel percentage of total fuel than would be found in production engines. Also note that the piston and ring combination used for this study are not production-intent and are not based on any existing production designs, and are therefore not optimized for the purposes of this combustion system.

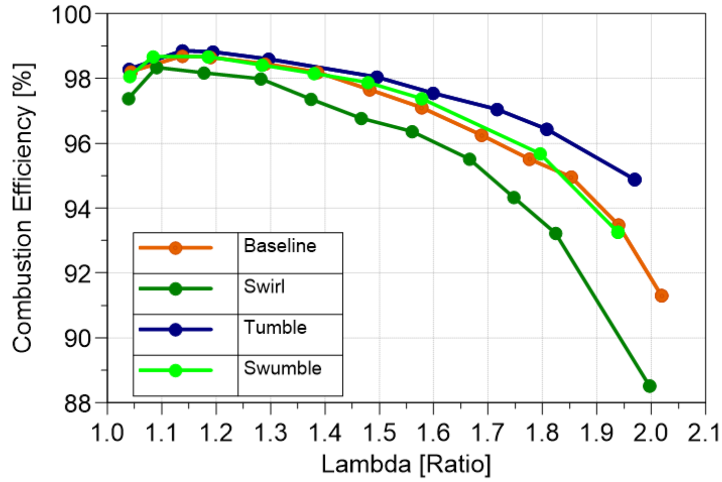

Figure 6-7: Combustion efficiency vs. λ; 1500 rpm, 6 bar BMEP, CA50 = approximately 8 degrees after TDC.

The results presented so far demonstrate clearly superior performance when additional tumble is introduced in the engine, and clearly inferior performance when swirl is introduced. While there is parity in the results at stoichiometric conditions, the relative difference amongst the variants grows as the engine is enleaned. The engine is therefore most sensitive to charge motion under lean conditions as the engine approaches its stability limit. While these trends grow in prominence with enleanment, they remain relatively consistent across the full λ range. The following analysis highlights peak performance of the variants within the context of the λ sweeps at this condition. These peak values can be considered as starting points for engine calibration, both demonstrating approximately how an engine with each specific level and type of charge motion might be operated, and indicating the relative robustness of an engine calibration that would be based on these results.

In determining optimal conditions for a combustion system capable of significant dilution tolerance, it is important to consider the λ at which the engine would operate under steady state conditions. For the purposes of this study, a λ corresponding to peak BTE within the λ sweep was assumed to be a likely primary input for determining steady state λ in an eventual engine calibration. Figure 6-8 shows the peak BTE for each of the four charge motion variants at this part load condition. Note that for the swirl variant, peak BTE occurred in a λ region where COV of IMEPg exceeded the 3% limit. Consistent with the data presented previously, tumble and baseline variants exhibited superior BTE to the swirl and swumble variants. Figure 6-8 also shows the λ at which the peak BTE values occur. The baseline and tumble variants have peak BTE λ values of 1.7. Peak BTE for the swumble variant occurs at a much richer λ of 1.4. Again, the swirl results are unstable. A measure of BTE robustness is shown in Fig. 6-9. Results here correspond to λ range within which the BTE drops to less than 1 percentage point below that of the peak value. Wider λ range results in this figure indicate a relatively wide and flat high efficiency λ range. With this result an engine calibrator would be able to optimize λ for a range of secondary criteria including emissions without incurring a significant BTE penalty by choosing a λ other than the peak BTE λ. In this figure it can be seen that each of the charge motion variants produced relatively flat BTE results across relatively wide λ ranges of at least 0.4 λ. For example, this result would dictate that there is relatively minor change in BTE with a charge motion variant across the λ range of 1.6 to 2.0. Within this range, for example, emissions profiles and exhaust temperatures vary substantially, offering much headroom for optimization of non-BTE parameters.

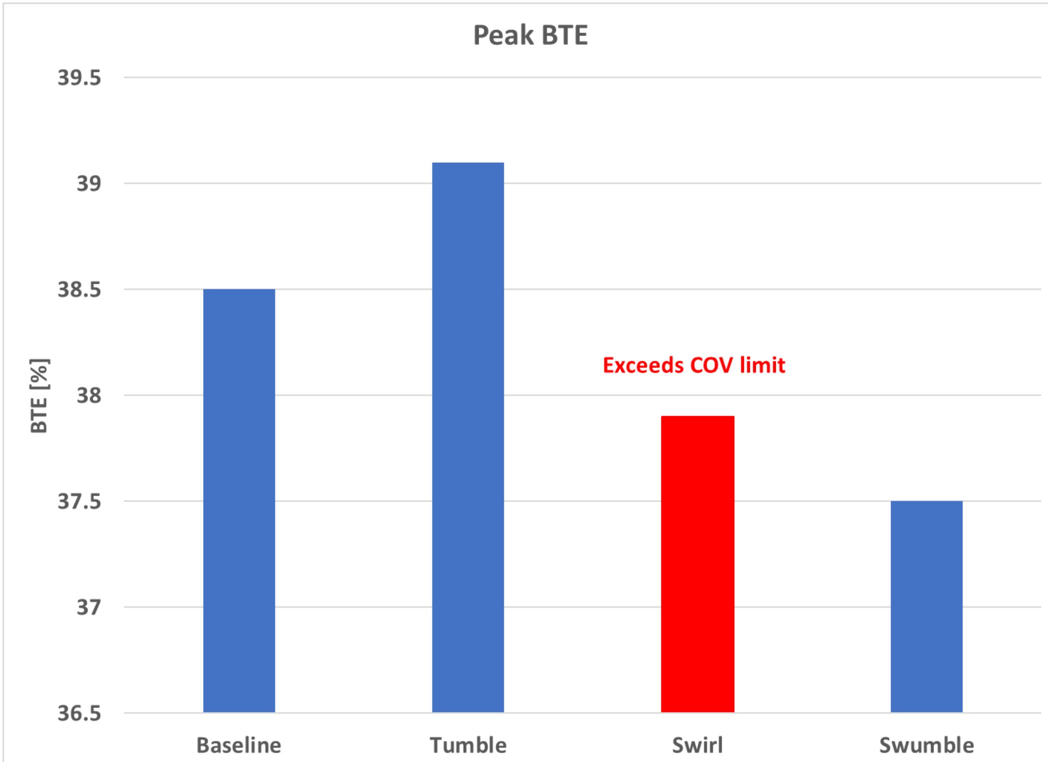

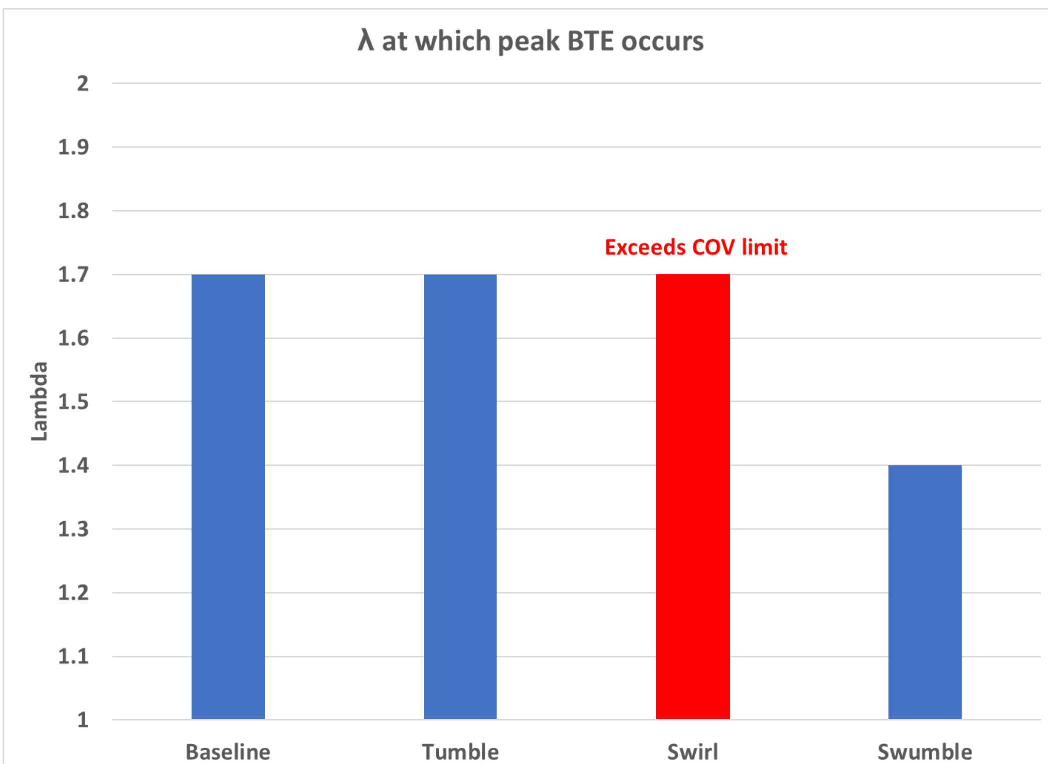

Figure 6-8: Peak BTE (top) and λ at which Peak BTE occurs (bottom) within a λ sweep from 1 to the lean limit; 1500 rpm, 6 bar BMEP, CA50 = approximately 8 degrees after TDC.

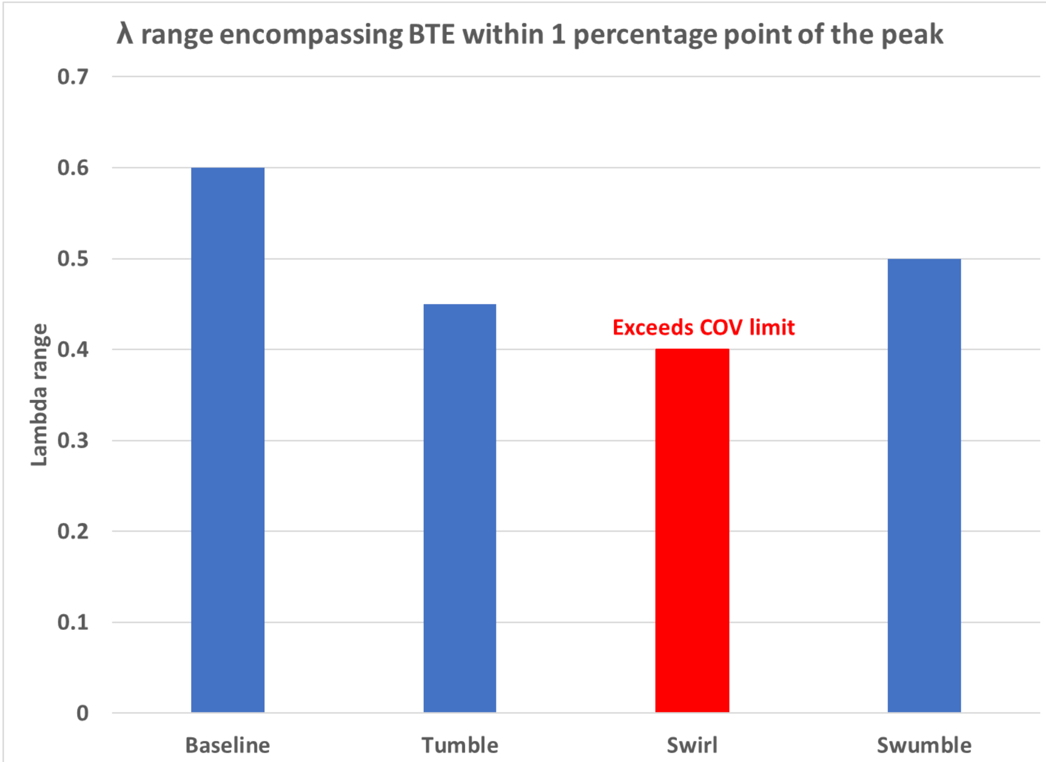

Figure 6-9: λ range encompassing BTE within 1 percentage point of the peak BTE value within a λ sweep from 1 to the lean limit; 1500 rpm, 6 bar BMEP, CA50 = approximately 8 degrees after TDC.

Leaner peak BTE λ values can be beneficial from an emissions control perspective. Engine-out NO_x concentration decreases significantly at λ values leaner than approximately 1.2. A peak BTE occurring 0.1 λ leaner can mean a reduction of several hundred ppm of NO_x. Figure 6-10 shows engine-out NO_x levels at the peak BTE λ values for each of the four charge motion variants. The swumble variant, with a peak BTE λ occurring 0.3 λ richer than the tumble and baseline variants, has a NO_x level approximately double those of the other variants. Despite the higher exhaust temperature associated with the richer peak BTE λ, the higher NO_x level likely puts a strain on the lean NO_x storage catalyst.

Similar to the emissions implications of peak BTE λ, the lean stability limit also has a bearing on aftertreatment effectiveness. Charge motion variants with extended lean stability limits enable engine operation in a low NO_x region, which can be leveraged as a part of a NO_x storage optimization strategy to extend lean operating times for higher cycle efficiencies or to reduce fluid consumption for urea-based aftertreatment systems. Figure 6-11 quantifies the λ limit at which COV of IMEPg exceeds 3%, LNV drops below 88%, or the experimental engine is incapable of holding constant BMEP at this part load condition. The tumble variant displays the highest lean stability limit extension, slightly higher than that of the baseline variant. The swirl and swumble variants displayed noticeably inferior lean stability limits. Figure 6-11 also shows the engine-out NO_x levels at the lean stability limits. The baseline and tumble variants both have NO_x levels below 100 ppm, an approximately 85% reduction from even the levels at the peak BTE λ values for the respective variants. Also notable is the wide gulf in NO_x levels between the swirl and swumble variants, with lean stability limits only 0.15 λ apart. This 1000 ppm gulf illustrates the extreme sensitivity of NO_x to λ in this region, slightly lean of the near-lean region. From this analysis it is evident that charge motion variants with wide dilution tolerance that have both peak BTE and lean stability limit occur at λ values well into the ultra-lean region offer significant advantages in terms of engine performance and emissions but also degree of calibration flexibility. Such combustion systems allow robust high efficiency operation with headroom to allow for precise targeting of emissions profiles, or flexibility to accept a certain amount of λ uncertainty during transient operation while still maintaining acceptable engine-out emissions. The tumble and baseline charge motion variants have the highest BTE at the leanest λ values with superior lean limit extension to the swirl and swumble variants.

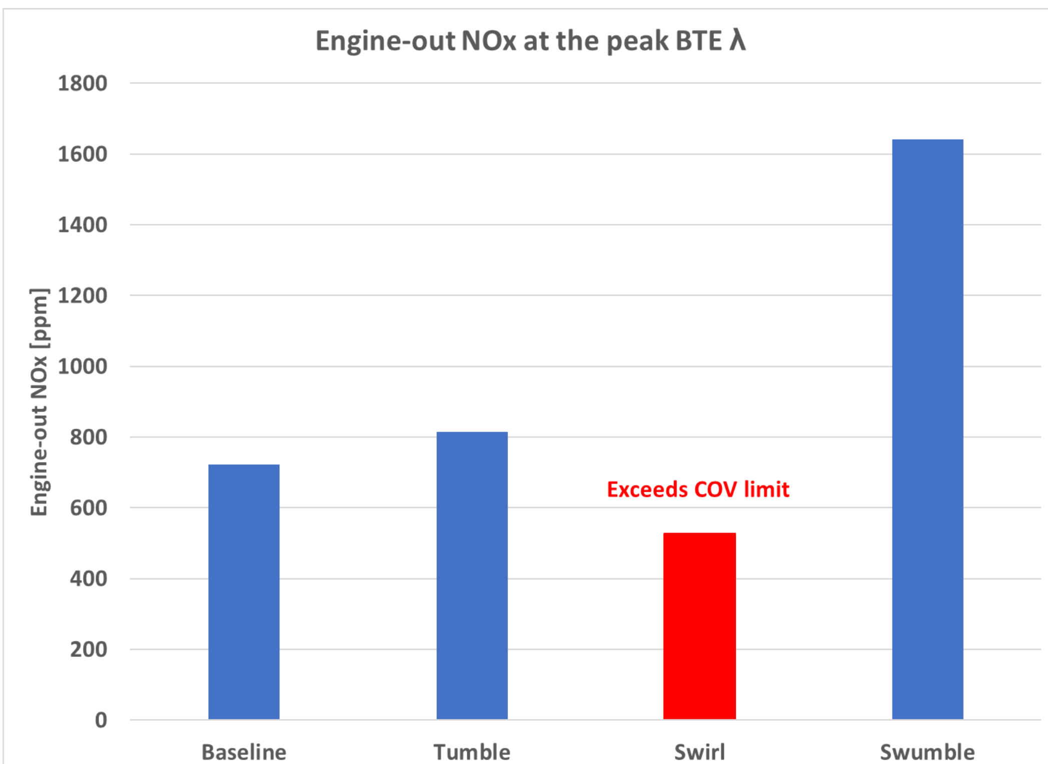

Figure 6-10: Engine-out NO_x at the peak BTE λ within a λ sweep from 1 to the lean limit; 1500 rpm, 6 bar BMEP, CA50 = approximately 8 degrees after TDC.

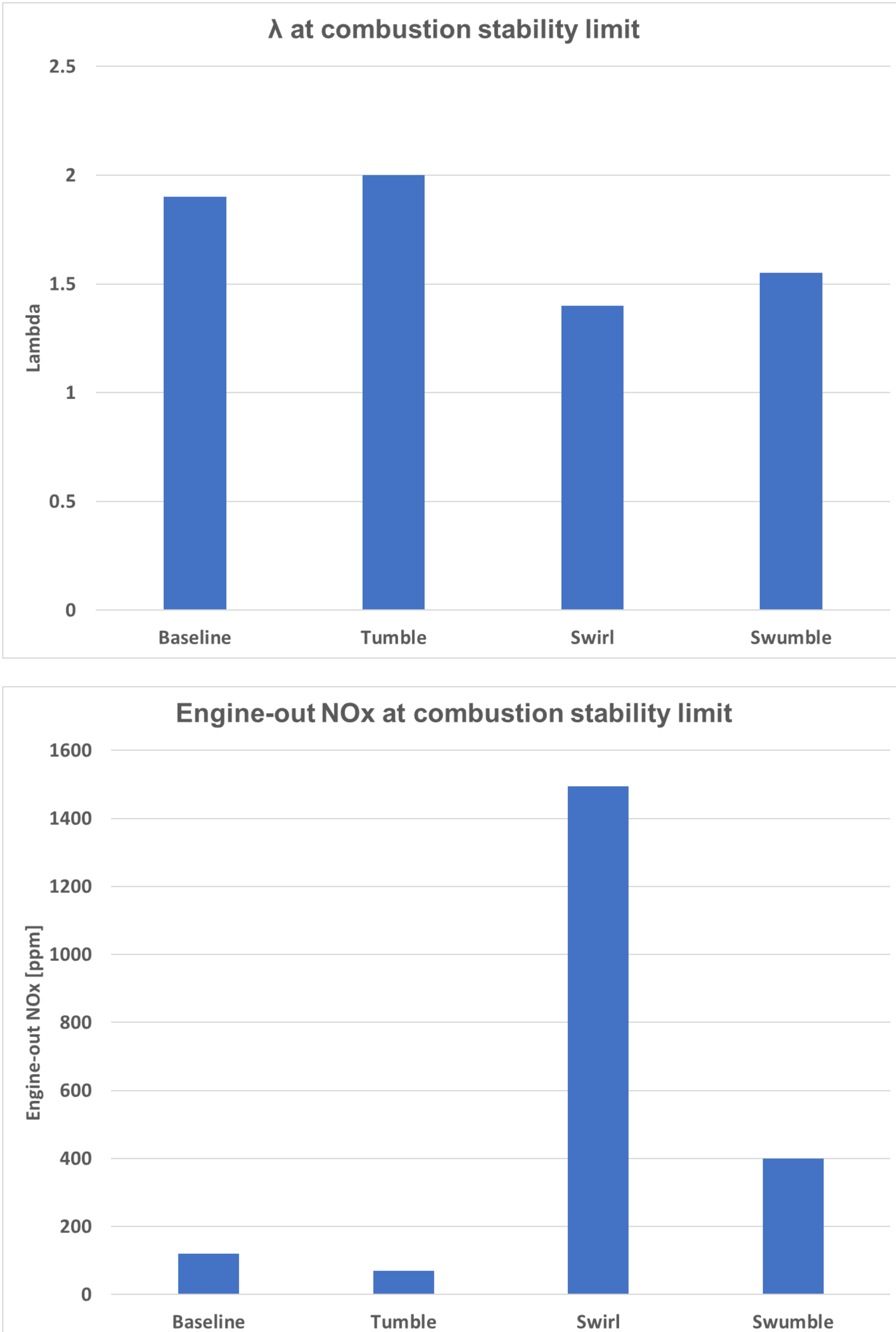

Figure 6-11: λ (top) and engine-out NO_x (right) at the combustion stability limit within a λ sweep from 1 to the lean limit; 1500 rpm, 6 bar BMEP, CA50 = approximately 8 degrees after TDC.

As was stated in Chapter 2, increased charge motion present in the cylinder can accelerate heat transfer from the combustion gases to the cylinder walls. An efficiency loss analysis was performed at stoichiometric and ultra-lean (λ 1.8) conditions to quantify in-cylinder heat transfer losses from the charge motion variants (Fig. 6-12). At the λ = 1 condition, pumping work was corrected to account for the restriction of the plate inserts in the charge motion variants; such a correction was not needed at the λ = 1.8 condition due to reduced relative significance of pump work. At both λ values, the tumble variant displayed slightly increased in-cylinder heat loss compared with the baseline. This higher in-cylinder heat loss is overcompensated at the λ = 1.8 condition by the lower incomplete combustion losses compared to the baseline variant. This result is consistent with the previously presented data showing the tumble variant having a higher combustion efficiency than the baseline variant, with this difference becoming increasingly prominent as the engine is enleaned. The swirl and swumble variants exhibit the highest in-cylinder heat loss at both λ conditions. The results at λ = 1 indicate that swirl motion is especially conducive to high in-cylinder heat transfer losses, moreso than is tumble motion. This effect is consistent with conclusions drawn from literature on the topic of heat loss induced by swirl motion in lean burn engines [143-145]. Also, notably at both λ conditions the swirl variant produces the highest incomplete combustion loss, consistent with the CA50-90 trends.

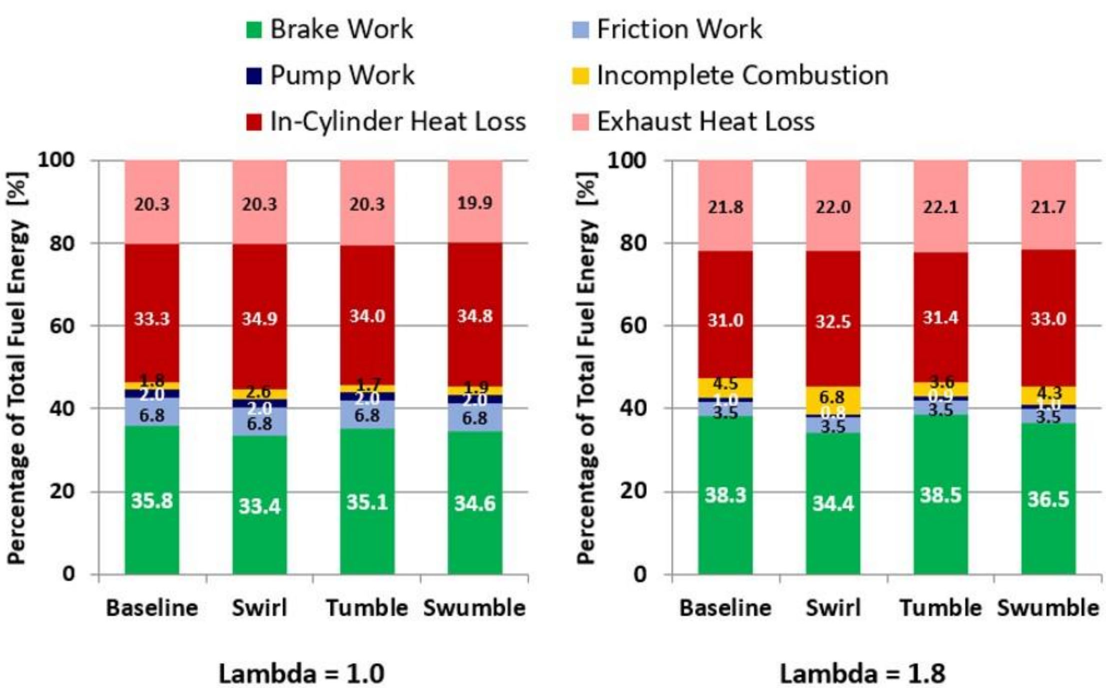

Figure 6-12: Efficiency loss analysis as a percentage of total fuel energy; 1500 rpm, 6 bar BMEP, λ = 1.0 (left) and λ = 1.8 (right).

6.2.2 Pre-Chamber Combustion

The late burning and combustion efficiency results indicate that the differing levels and types of charge motion investigated in this study have an influence on main chamber combustion, especially in the late burning period. However, these results may be both a cause and a symptom of the differing combustion stability behavior amongst the variants. Charge motion plays a role not just in late main chamber burning processes but also in front-end processes such as pre-chamber combustion. The analysis presented in this section will seek to explain main chamber combustion stability differences as functions of pre-chamber combustion stability differences. Demonstrating a correlation between pre-chamber and main chamber combustion stability would confirm that 1) charge motion induced in the intake and developed in the main chamber also has an impact on in-pre-chamber processes, and 2) that main chamber combustion performance is determined in large part by the pre-chamber combustion event, and main chamber COV of IMEPg is dictated by the stability of pre-chamber combustion. Pre-chamber combustion stability can be manipulated via active pre-chamber fuel injection strategy, which could potentially be used to correct for negative charge motion influence in the pre-chamber mixing or combustion processes.

Analysis was performed on the 300-cycle average pre-chamber high speed pressure trace. Examination of pre-chamber behavior is confined to the portion of the pre-chamber pressure trace where pre-chamber pressure rises measurably higher than main chamber pressure. This portion of the trace corresponds with the pre-chamber combustion event and expulsion of combustion products as reactive jets. Pre-chamber combustion behavior is described using the metrics detailed in Chapter 3, the most prominent being ΔP, which describes the largest measured difference between pre-chamber and main chamber pressure. This difference is maximized during the pre-chamber combustion event, approximately midway through the pressure rise event in the pre-chamber. Research [170] has shown that this point generally corresponds with the angle at which reactive jets first emerge from the pre-chamber.

While the magnitude of chamber ΔP does vary somewhat amongst the four charge motion variants at common λ values, the standard deviation of chamber ΔP provides the most robust indication of pre-chamber combustion stability [171]. In this analysis, standard deviation of ΔP was the only parameter that produced significant correlation with main chamber COV of IMEPg. Data for all four charge motion variants was analyzed at three λ values: 1, 1.4, and 1.8. Figure 6-13 shows this correlation between the standard deviation of chamber ΔP and main chamber COV of IMEPg for all charge motion variants. Most of the variation in this trend observed in Fig. 6-13 corresponds to performance at $\lambda = 1$ operation. Notably, these data points are the only ones where auxiliary pre-chamber fuel is not being added, and the pre-chamber relies solely on main chamber fuel delivered passively during the compression stroke. It is therefore possible that pre-chamber combustion is influenced to a larger degree by inconsistent cycle-to-cycle fuel delivery to the main chamber or passive fuel delivery from the main chamber to the pre-chamber, or to cycle-to-cycle charge motion variation as experienced by the pre-chamber. The correlation becomes increasingly robust at the lean, auxiliary-fueled conditions where pre-chamber fuel quantity is much more controllable, as evidenced by Fig. 6-14. Practically, this means that the variation in the peak pressure generated in the pre-chamber by the pre-chamber combustion event induces variation in main chamber combustion performance. It also means that main chamber COV of IMEPg, across the full λ range but especially under lean conditions, is primarily influenced by the degree of variation in the pre-chamber combustion event.

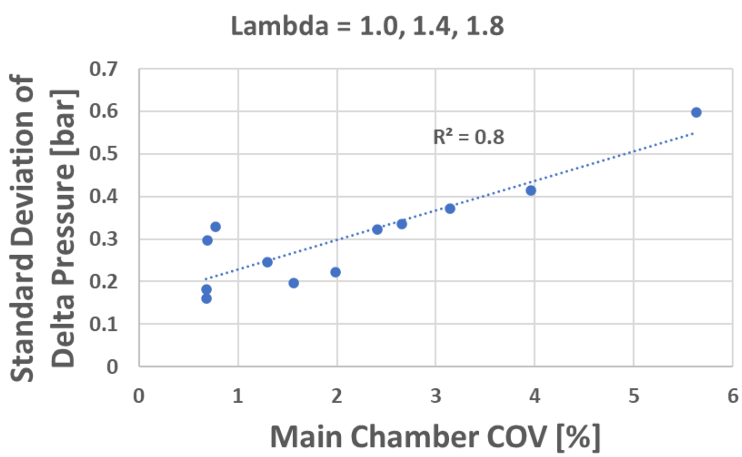

Figure 6-13: Main chamber COV of IMEPg as a function of the standard deviation of chamber ΔP at λ = 1, 1.4, and 1.8 for all charge motion variants; 1500 rpm, 6 bar BMEP.

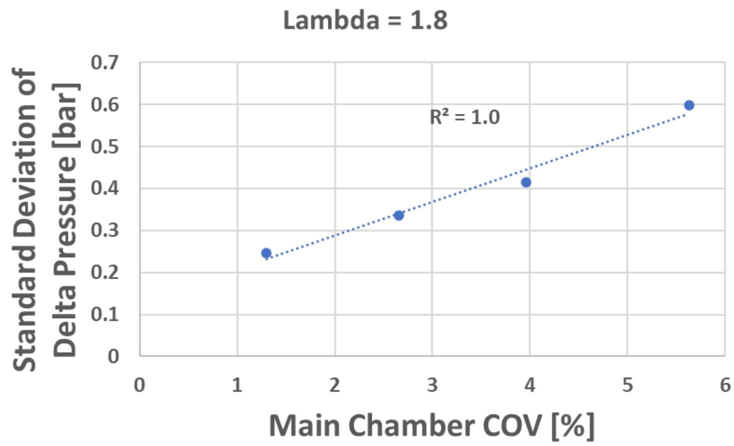

Figure 6-14: Main chamber COV of IMEPg as a function of the standard deviation of chamber ΔP at λ = 1.8 only for all charge motion variants; 1500 rpm, 6 bar BMEP.

Figure 6-15 shows the difference in standard deviation of chamber ΔP amongst the charge motion variants. Notably, these results mirror both the main chamber COV of IMEPg and combustion efficiency trends discussed previously, with parity at the λ = 1 condition and an ever increasing disparity as the engine is enleaned. As was observed in Fig. 6-2, auxiliary pre-chamber fueling quantity was increased with increasing λ. While this does not guarantee that a constant λ is maintained in the pre-chamber across the main chamber λ sweep, it does imply that the pre-chamber is not significantly enleaned, and therefore the stability results presented here are unlikely to be a result of enleanment occurring in the pre-chamber. At the leanest condition considered in this dataset, λ = 1.8, the tumble variant shows the least variation in chamber ΔP and therefore the lowest main chamber COV of IMEPg, followed closely by the baseline variant. The swumble and swirl variants exhibited the highest degree of variation in chamber delta pressure.

The tumble variant actually displays more pre-chamber combustion stability (reduced standard deviation of ΔP) at the λ = 1.8 condition versus the λ = 1.4 condition. This is likely due to differences in pre-chamber λ at the two conditions. At the λ = 1.4 condition, auxiliary fuel is first introduced into the pre-chamber due to engine COV of IMEPg requirements. Due to the minimum pulsewidth limitation of the pre-chamber fuel injectors, more fuel than desired is injected into the pre-chamber, creating a richer than desired pre-chamber. Further enleanment brings a greater degree of controllability over pre-chamber λ, as background λ becomes leaner and the auxiliary fuel injection pulsewidth must increase above its minimum in order to compensate. This means that pre-chamber λ at the 1.8 condition is more optimized (and more optimizable) than it is at the 1.4 condition, helping to explain why pre-chamber stability increases for the tumble variant. This effect is present in the other charge motion variants, so the worsening instability in these variants, particularly swirl and swumble, must be driven by other factors specific to the charge motion types and levels introduced, such as in-pre-chamber mixing dynamics. These factors are explored in greater detail in subsequent sections.

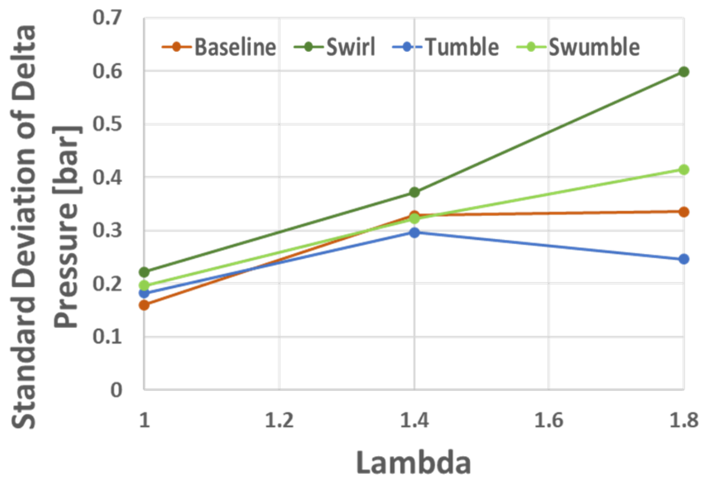

Figure 6-15: Standard deviation of ΔP vs. λ; 1500 rpm, 6 bar BMEP.

The relative stability of the pre-chamber combustion event influences the main chamber COV of IMEPg to a high degree [171], thereby impacting combustion efficiency at lean conditions and contributing to the peak BTE, the peak BTE λ, and the lean limit determinations. Figure 6-16 illustrates this point, with a linear correlation between standard deviation of chamber ΔP at the λ = 1.8 condition and main chamber lean stability limit for the four charge motion variants. The variants with most stable lean pre-chamber combustion events, specifically stable cycle-to-cycle ΔP values, produce the most extended main chamber lean stability limits.

This result is significant because it concentrates active pre-chamber system optimization to the pre-chamber combustion event itself. As has been demonstrated, active pre-chamber combustion systems generally maximize BTE when they are able to maximize the extension of the lean stability limit, thereby pushing peak BTE λ leaner. This also provides an engine-out emissions benefit. Depending on overall engine strategy, this leaner nominal operation can enable a higher CR than in engines with less dilution tolerance, further increasing both peak and cycle-average BTE. Results in this section prove that this ability to extend the lean limit and push peak BTE leaner is largely determined by the stability of the pre-chamber combustion event. Therefore, mechanisms to improve pre-chamber combustion stability are impactful optimization strategies for maximizing BTE. Charge motion has an influence over pre-chamber combustion stability. The most calibratable parameters with this influence, however, encompass pre-chamber auxiliary fueling strategy. The following sections evaluates whether pre-chamber auxiliary fueling strategy can be optimized to compensate for negative influence some of the charge motion variants have on pre-chamber combustion stability.

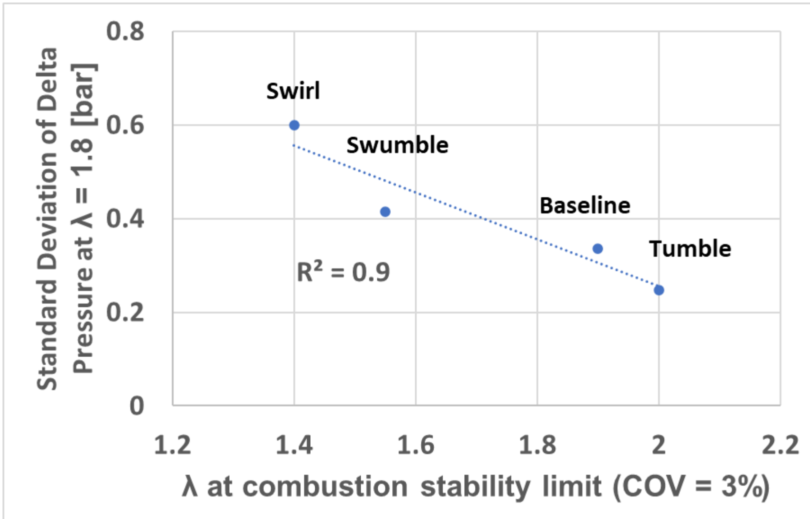

Figure 6-16: Main chamber lean stability limit as a function of standard deviation of chamber ΔP at λ = 1.8; 1500 rpm, 6 bar BMEP.

6.2.3 Pre-Chamber Fueling Parameters

The DI fuel injector used in the MJI pre-chamber enables scalable fuel injection with precise control over fuel quantity. Auxiliary fueling quantity increases proportionally with main chamber enleanment across a λ sweep. Similarly, pre-chamber fueling quantity is a primary lever that is commonly used to reduce main chamber COV of IMEPg under lean conditions. Figure 6-17 shows main chamber COV of IMEPg response to changes in pre-chamber fuel injection quantity and start of injection angle for the four charge motion variants at the λ = 1.7 condition. At retarded start of injection angles in close proximity to spark timing, combustion becomes highly unstable for most of the charge motion variants. At these angles the pre-chamber injection event ends after the spark has occurred, leading to a high probability of insufficient fuel in proximity to the spark plug at time of spark. Other than at these extreme late injection angles, however, start of injection timing does not have a prominent influence over main chamber COV of IMEPg.

Auxiliary fuel quantity has a stronger influence over main chamber COV than does injection timing. All charge motion variants display lower COVs of IMEPg as pre-chamber fuel mass flow increases, as is expected. However, for both the swirl and swumble variants, the enhanced stability induced by increased pre-chamber fuel quantity is still above the COV of IMEPg limit of 3%. In fact, these variants display slightly lower sensitivity to auxiliary fuel quantity than do the tumble and baseline variants.

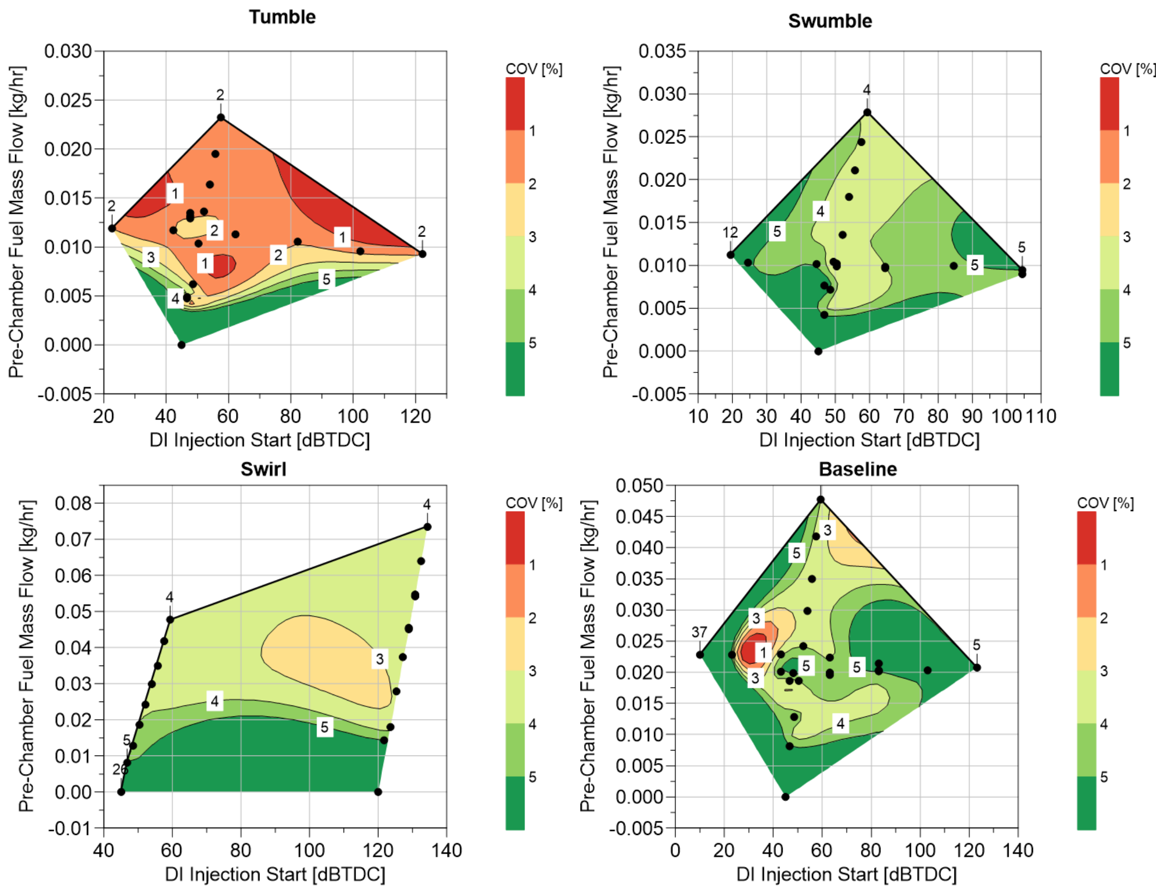

Figure 6-17: Main chamber COV of IMEPg as a function of pre-chamber fuel mass flowrate and start of injection angle at λ = 1.7; 1500 rpm, 6 bar BMEP.

Figures 6-18 and 6-19 show the change in engine-out NO_x and CO emissions, respectively, across the auxiliary fuel quantity and injection timing sweeps. Across the relatively narrow injection quantity band considered in this analysis, engine-out NO_x changes significantly, by at least 500 ppm in each variant. This indicates that changes in pre-chamber λ are occurring across the sweep, with increased quantity producing richer pre-chambers, resulting in less engine-out NO_x. The relative magnitude of the NO_x values and their sensitivity to fueling quantity also strongly indicates that the majority of NO_x is being formed in the pre-chamber by the pre-chamber combustion event, a common result for active pre-chambers under ultra-lean conditions.

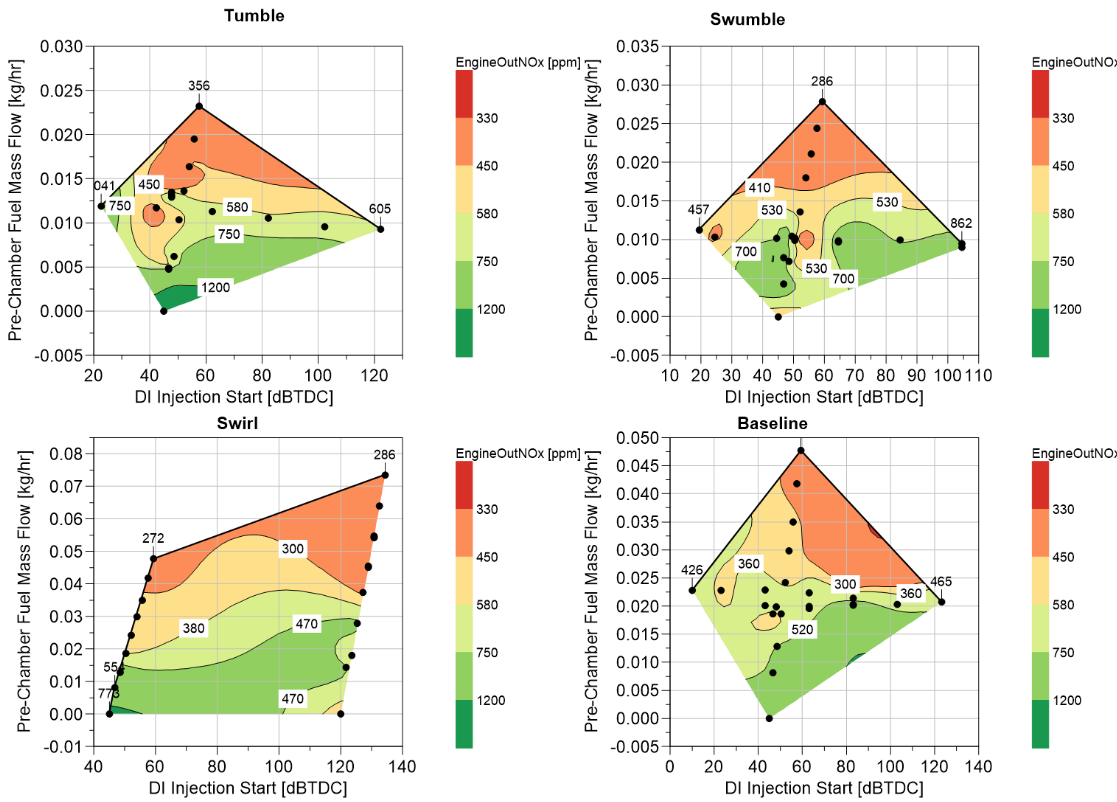

Figure 6-18: Engine-out NO_x as a function of pre-chamber fuel mass flowrate and start of injection angle at λ = 1.7; 1500 rpm, 6 bar BMEP.

The engine-out CO emissions demonstrate similar sensitivities to pre-chamber fueling quantity, with peak values occurring at the highest pre-chamber fuel flow rates. This also confirms a transition to richer λ values at the highest flow rates. A global pre-chamber λ determination, however, is not possible from this analysis given the highly stratified nature of the pre-chamber fueling event.

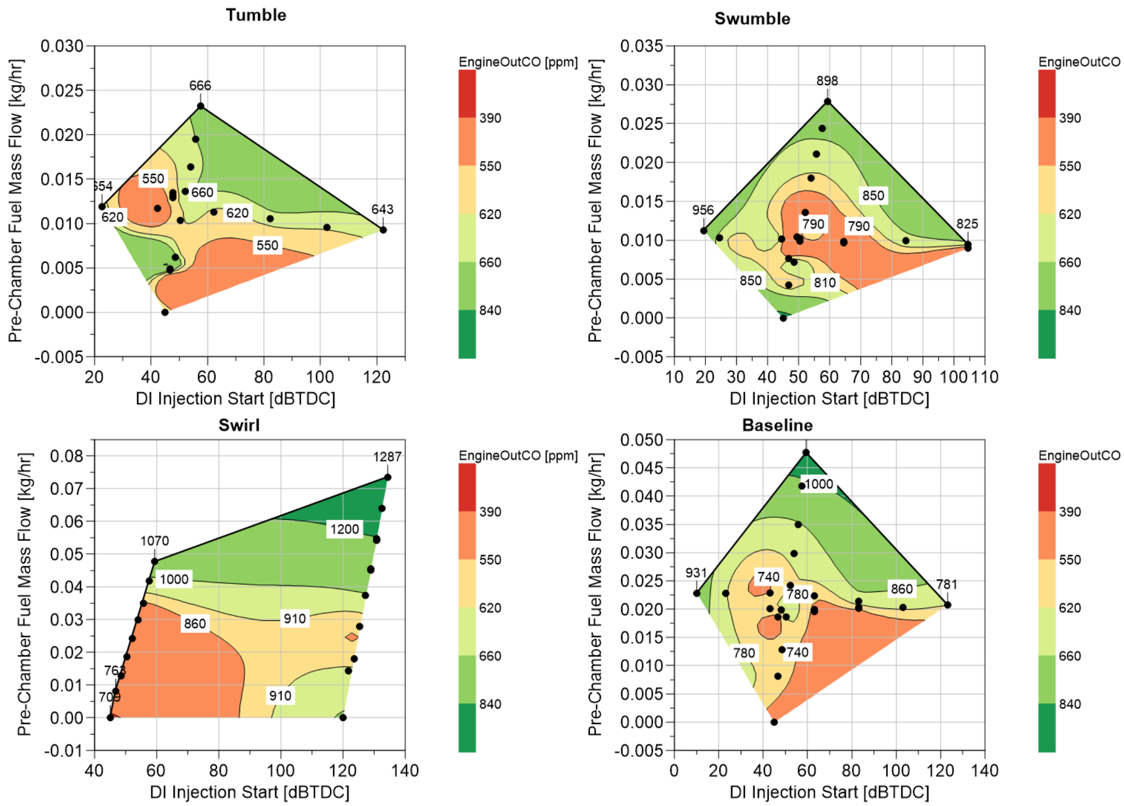

Figure 6-19: Engine-out CO as a function of pre-chamber fuel mass flowrate and start of injection angle at λ = 1.7; 1500 rpm, 6 bar BMEP.

The pre-chamber fueling quantity and injection angle results show that this common lever for increasing main chamber stability under lean conditions is not able to compensate for the negative stability pressure induced by the swirl and swumble variants. This proves that induced charge motion translates to the pre-chamber, and influences at least the pre-chamber combustion event and probably also pre-chamber mixing dynamics. The subsequent sections will first explore the consistency of these part load charge motion results across other engine operating conditions. The underlying effect of charge motion on in-pre-chamber processes will explored in more detail in the simulation results section.

6.3 Knock Limited Operation

With non-knock limited charge motion performance established, the engine was tested at condition 2 (3000 rpm, 13.5 bar IMEPg), where knock is encountered over a large portion of the λ sweep. IMEPg was selected as the constant load parameter in order to eliminate the influence of pumping losses at this highly boosted condition. Figure 6-20 illustrates the increased significance of pumping losses at this condition.

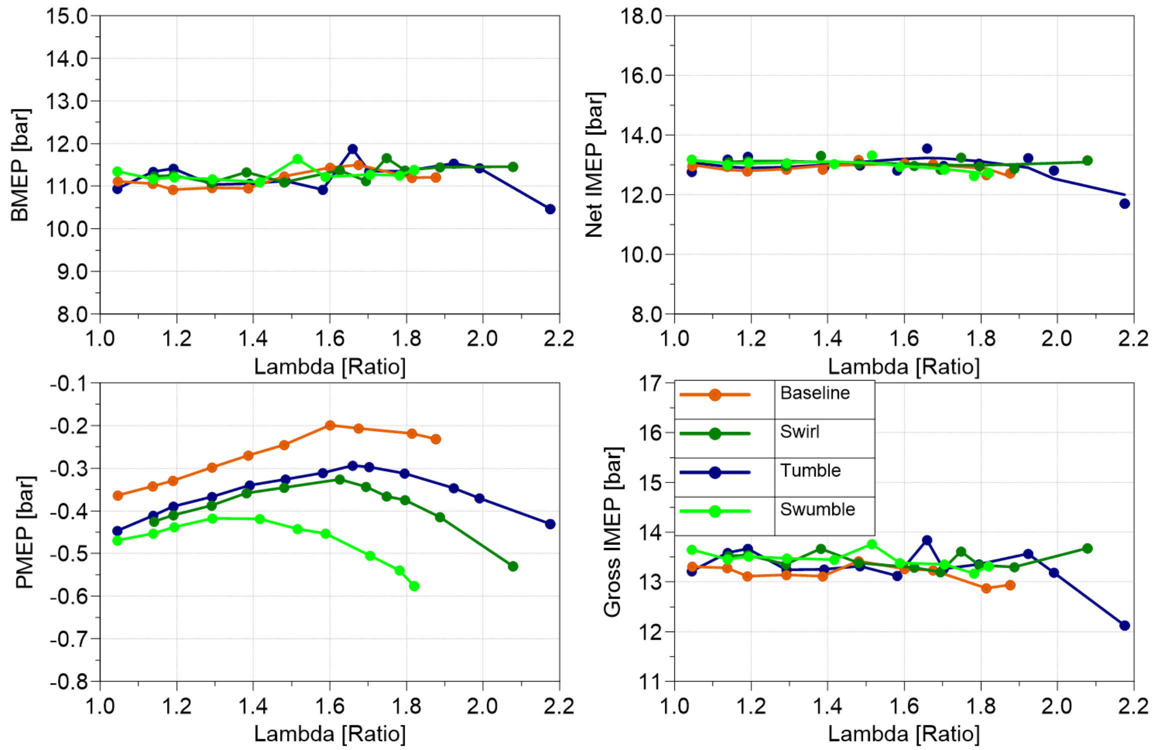

Figure 6-20: Mean effective pressure metrics vs. λ; 3000 rpm, 13.5 bar IMEPg.

Combustion stability follows similar trends to those observed at condition 1. At this knock limited condition 2, the tumble motion variant again displays superior combustion stability, with a lean limit at λ = 2, nearly identical to the result at condition 1 (Fig. 6-21). The swumble and baseline variants identical COV of IMEPg results, but the LNV results a slightly more robust resistance to partial burn cycles in the baseline variant. The swirl variant again exhibits the worst performance, with a lean stability limit of λ = 1.7, superior to its performance at condition 1 but inferior to the other charge motion variants' performance at condition 2. Once again, there appears to be effectively no stability differences amongst the variants at the λ = 1 condition, with the relative differences steadily increasing as the engine is enleaned.

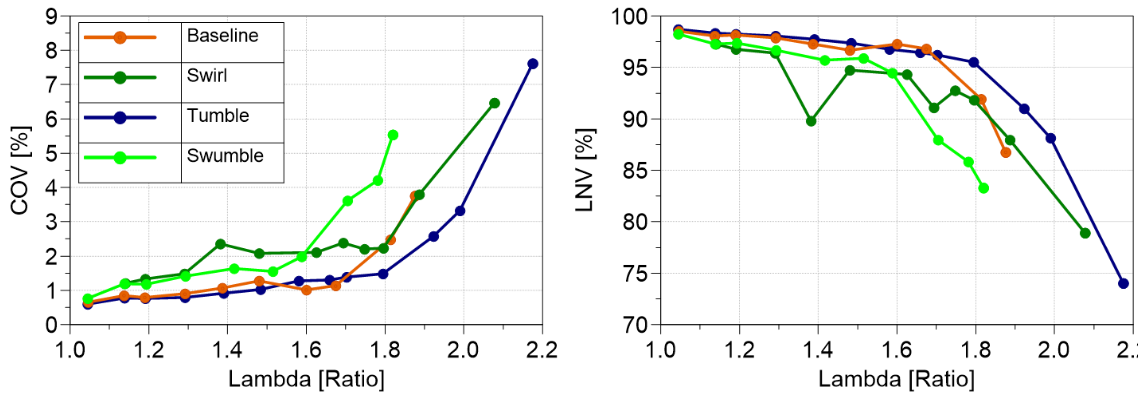

Figure 6-21: Combustion stability metrics vs. λ; 3000 rpm, 13.5 bar IMEPg.

As is observed in Fig. 6-22, pre-chamber auxiliary fueling quantity was increased as the engine was enleaned. At this condition 2, there is greater degree of parity amongst the fueling quantity vs. λ trends amongst the four charge motion variants than there was at condition 1.

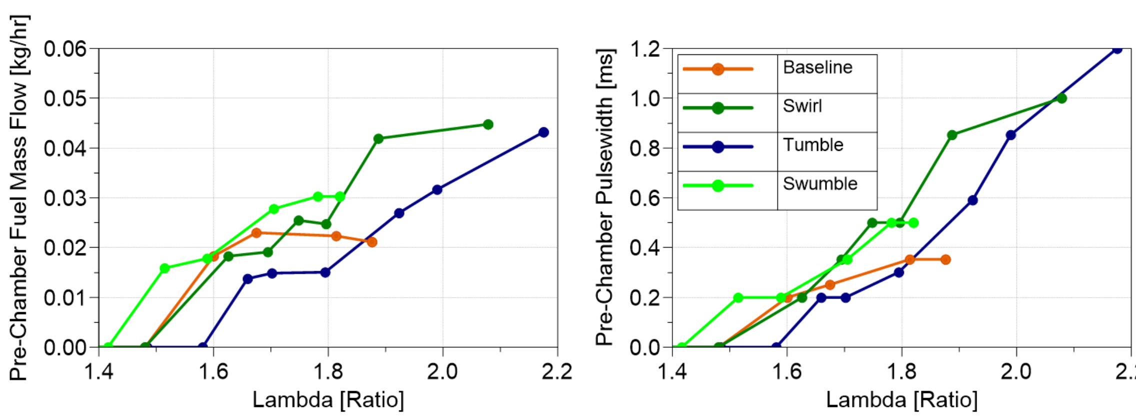

Figure 6-22: Pre-chamber fueling metrics vs. λ; 3000 rpm, 13.5 bar IMEPg.

The CA50 result in Fig. 6-23 shows that all charge motion variants require retarded combustion phasing to avoid knock over some portion of the λ sweep. The swirl and swumble variants are knock limited over the entirety of the λ sweep, while the baseline and tumble variants are fully free of knock at λ values from approximately 1.7. As a result of this variable knock performance amongst the charge motion variants, the burn duration trends across the λ sweep differ from the trends observed at the non-knock limited condition. At this condition, the largest discrepancy in burn duration occurs in the near-lean λ range of 1.2 to 1.4. The variants with the most retarded combustion phasing, swirl and swumble, exhibit the shortest late burning duration (CA50-90) in this near-lean range due to the lower background cylinder pressure associated with retarded phasing. This trend becomes less prominent at λ values beyond the near-lean region as bulk burn durations increase due to the engine's increasing performance sensitivity to λ. At these ultra-lean conditions (λ > 1.6) the tumble variant displays the fastest relative burn duration amongst the charge motion variants.

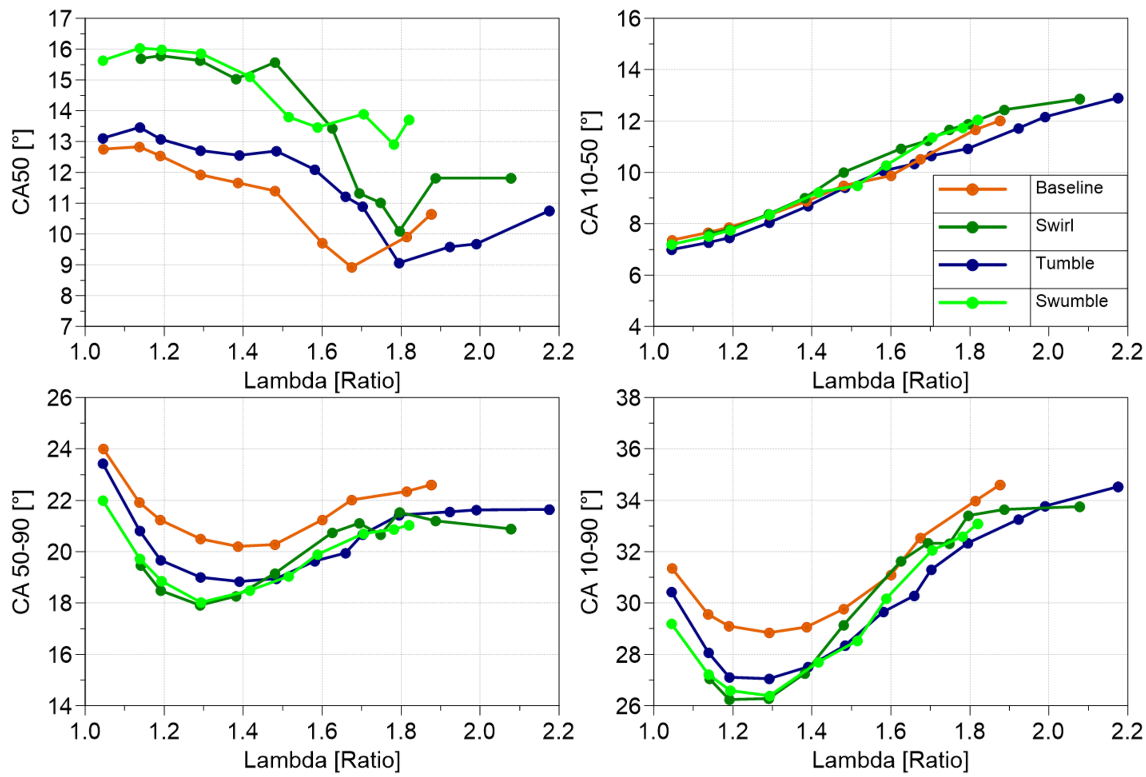

Figure 6-23: Burn duration metrics vs. λ; 3000 rpm, 13.5 bar IMEPg.

Due to the relatively high combustion efficiency in the near-lean region, the burn duration discrepancies in this region do not translate to any significant combustion efficiency disparities. Instead the trend appears similar to that of the non-knock limited condition 1, with the tumble variant producing clearly higher combustion efficiency in the ultra-lean region (Fig. 6-24). Of note is the inferior combustion efficiency of the baseline variant relative to the other variants. At condition 1, the baseline variant produced combustion efficiencies consistently higher than the swirl and swumble variants, but at this condition, there is parity amongst these three variants.

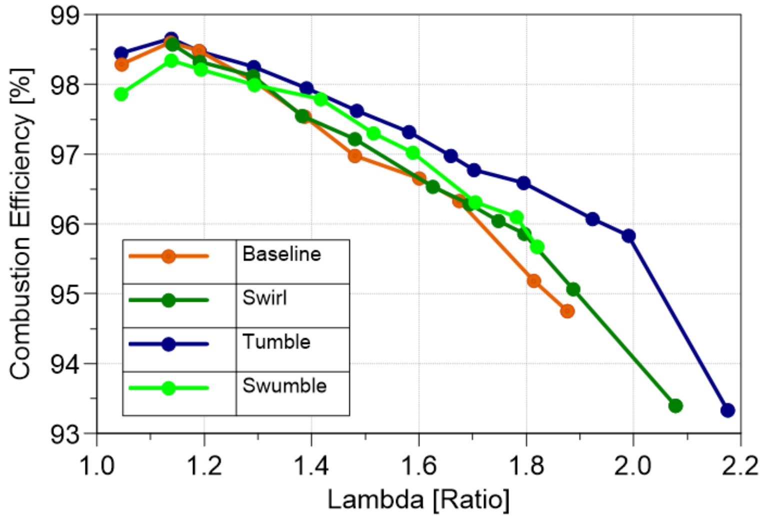

Figure 6-24: Combustion efficiency vs. λ; 3000 rpm, 13.5 bar IMEPg.

Efficiency and fuel consumption trends are shown in Fig. 6-25. ITE provides the more accurate comparison at this condition because IMEPg is held constant. The swirl and swumble variants exhibit an ITE deficit compared to the others across the full λ range that tracks well with the differences in CA50. The tumble variant displays superior peak ITE and high sustained ITE in the ultra-lean region compared to the other variants with an ITE value > 49.5%, an exceptionally high efficiency value representing a significant increase over those of production engines. Similarly, the ISFC value of 175 g/kWh is far below production engine ISFC values. A 49% minimum ITE value is maintained over a relatively wide λ range of 0.4, demonstrating the robustness of this efficiency improvement.

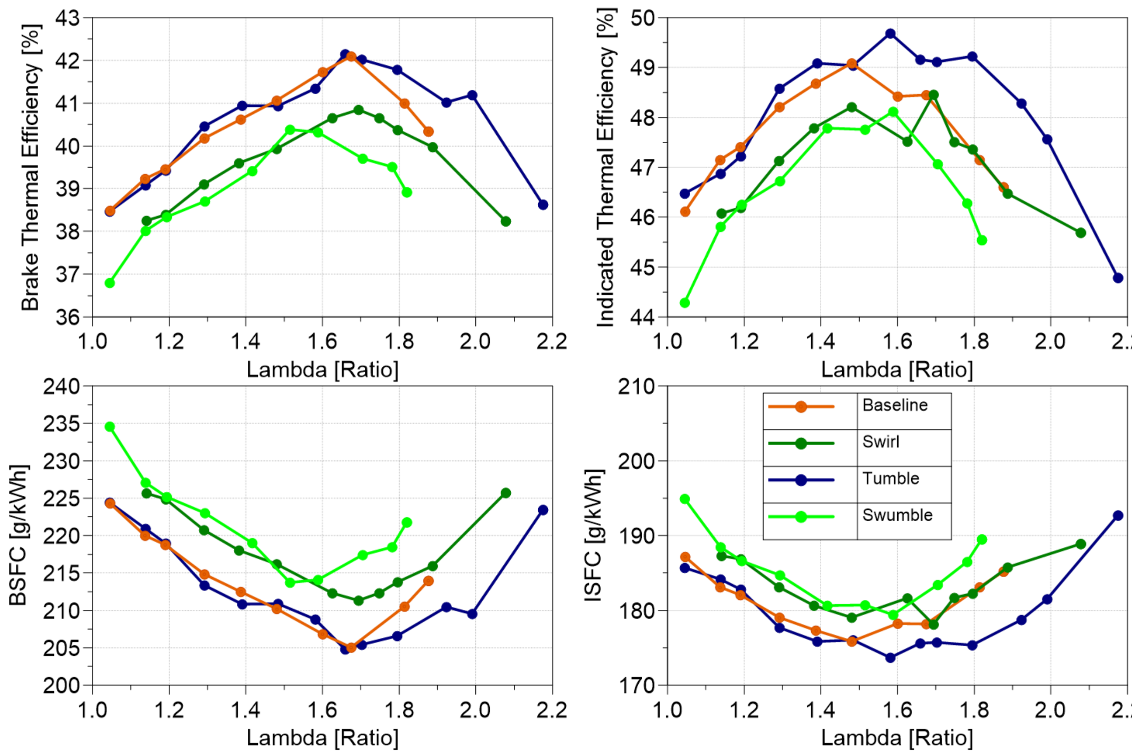

Figure 6-25: Efficiency and fuel consumption metrics vs. λ; 3000 rpm, 13.5 bar IMEPg.

Figure 6-26 shows engine-out emissions trends. The slightly lower NO_x emissions with the swirl and swumble variants from λ = 1 to at least λ = 1.6 are reflective of the retarded combustion phasing required with these variants over this λ range. Aside from the indirect effect of this knock sensitivity, it appears that charge motion itself does not have any significant impact on engine-out NO_x. Engine-out THC and CO emissions are consistently lower with the tumble variant in the lean region, a result consistent with the condition 1 results and the condition 2 combustion stability and efficiency results. Charge motion therefore does have an impact on THC and CO emissions, which are constituents that are indicative of late burning performance. Combining this result with the previous section's pre-chamber combustion stability result, it is clear that charge motion has an influence over critical combustion performance metrics comprehensively throughout the full pre-chamber and main chamber combustion process.

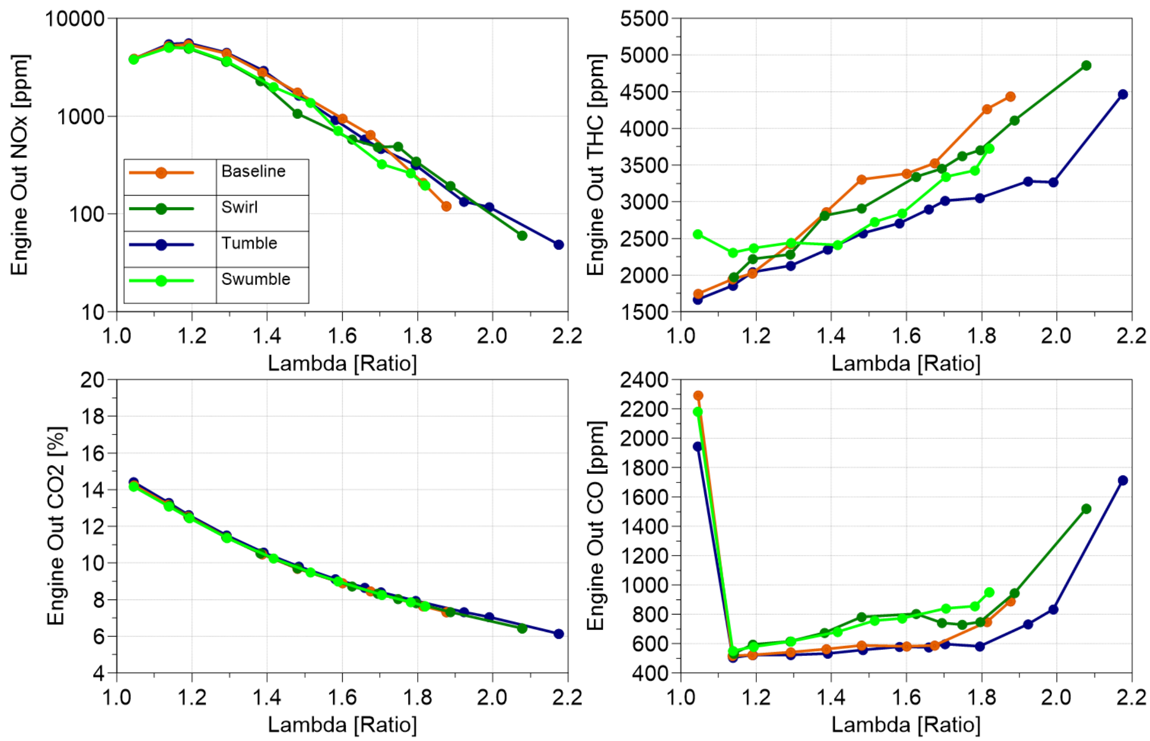

Figure 6-26: Engine-out emissions vs. λ; 3000 rpm, 13.5 bar IMEPg.

Figure 6-27 further demonstrates the advantage of the tumble variant, in this case across a sweep of load while λ is held at a constant value of 1.7 and speed is held to a constant 3000 rpm. Notably the charge motion variants exhibit a deterioration in COV of IMEPg as load reduces at this condition. All charge motion variants except the tumble variant produce COV of IMEPg values in excess of the stability limit at the lower loads in the sweep. Lean limit extension tends to erode as load and participating fuel quantity decrease in active pre-chamber engines due to the corresponding reduction in combustion temperatures. This shifts the lean limit to less lean λ values. This trend is mirrored somewhat in the combustion efficiency trend (Fig. 6-28). Here the superior performance of the tumble variant is evident as it maintains a 1-3 percentage point advantage in combustion efficiency across the load sweep.

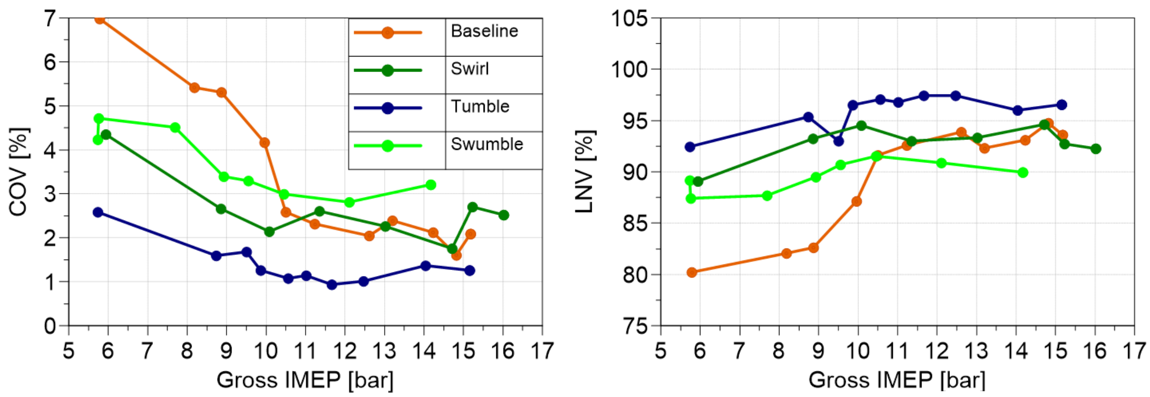

Figure 6-27: Combustion stability metrics vs. IMEPg; 3000 rpm, λ = 1.7.

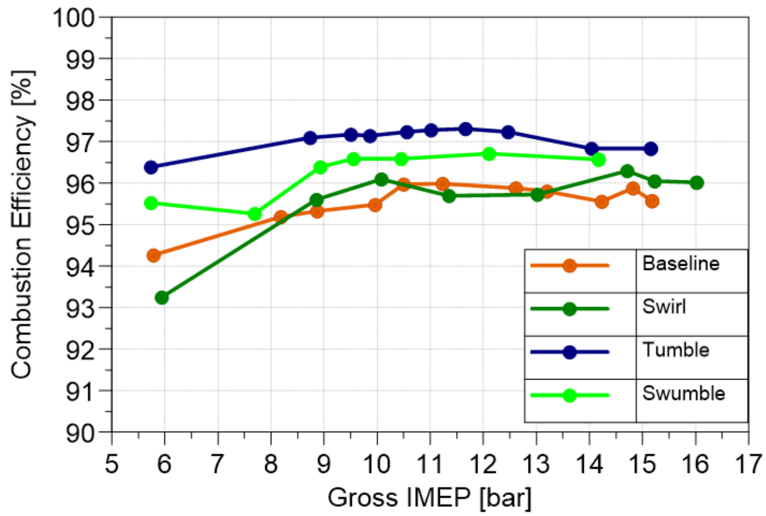

Figure 6-28: Combustion efficiency vs. IMEPg; 3000 rpm, λ = 1.7.

The superior combustion efficiency of the tumble variant helps contribute to higher ITE across the load sweep, achieving a peak of 49.5% (Fig. 6-29), an improvement of 1.5 percentage points over the peak baseline value. Here the discrepancy in ITE grows as load is decreased, i.e. as the main chamber conditions become regressively ignitable. Analysis of the emissions trends in Fig. 6-30 confirm a more complete combustion event in the tumble variant, producing lower CO and THC and higher NO_x emissions, with the differences between tumble and the other variants' emissions performance growing as load is decreased.

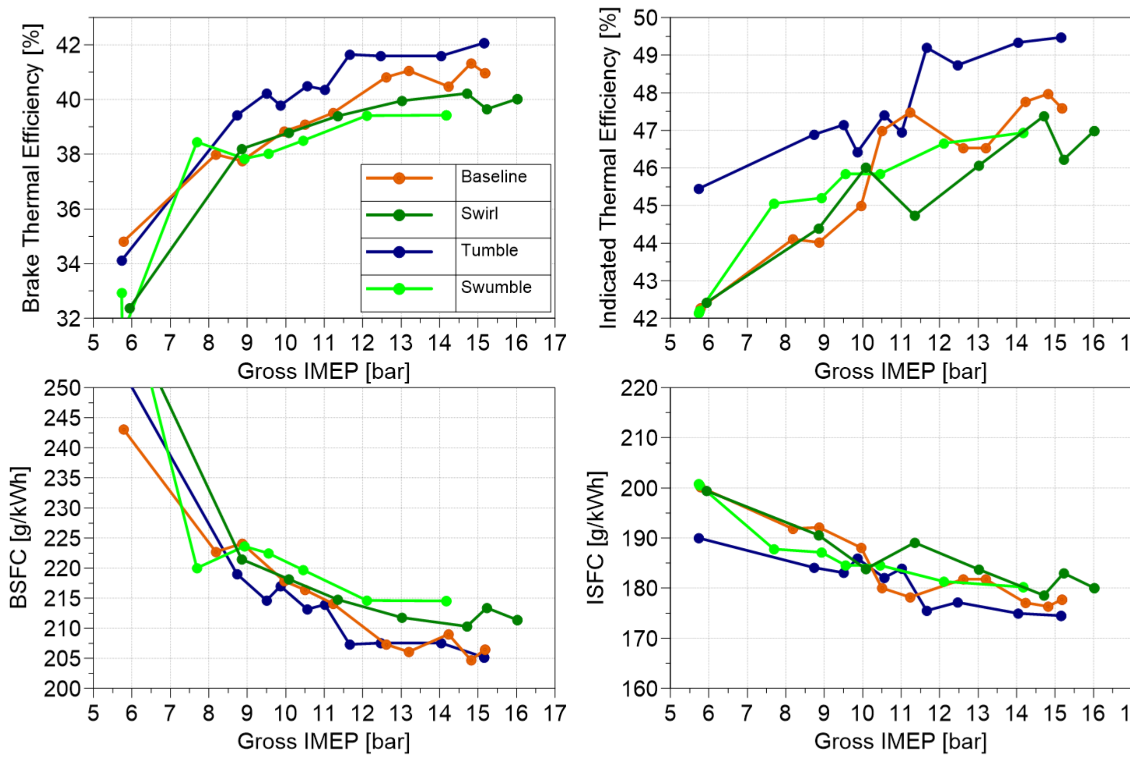

Figure 6-29: Efficiency metrics vs. IMEPg; 3000 rpm, λ = 1.7.

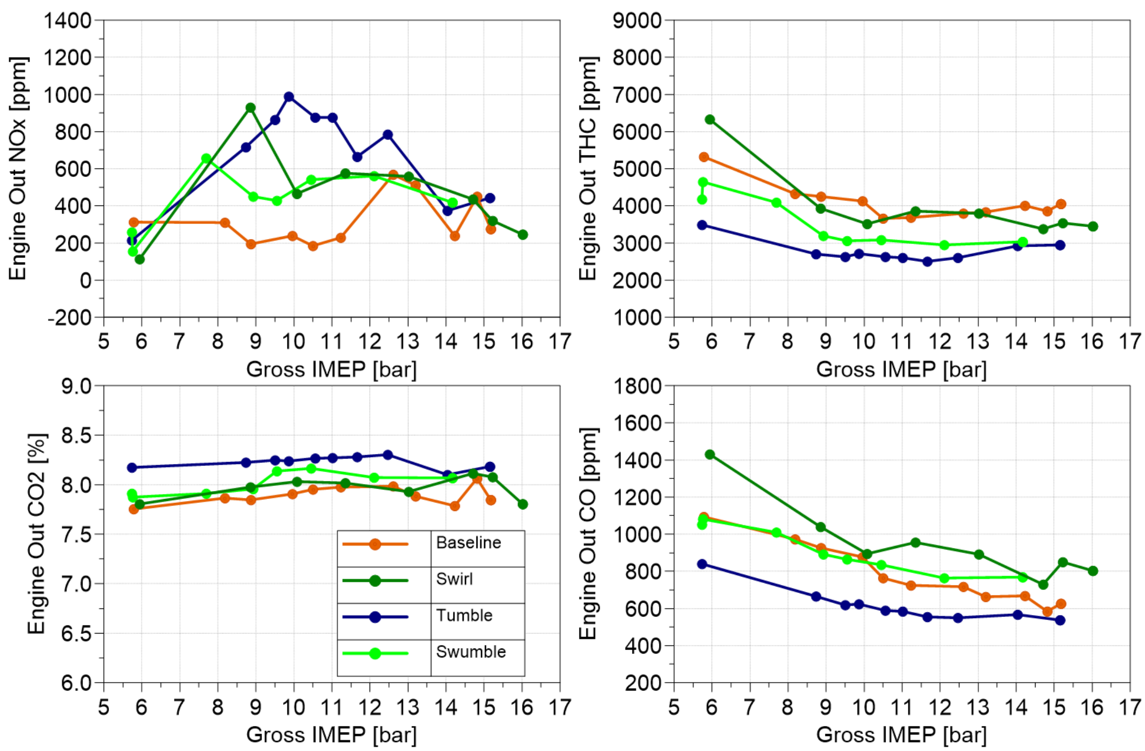

Figure 6-30: Emissions vs. IMEPg; 3000 rpm, λ = 1.7.

The engine performance and emissions trends across the charge motion variants are consistent at both knock and non-knock limited conditions. Higher engine speed operation introduces yet another sensitivity, as slow burn durations can contribute to more severe reductions in combustion efficiency as the engine is enleaned. These results are shown in the following section.

6.4 High Speed Operation

Engine results from the 4000 rpm 8 bar BMEP condition were evaluated. Here the IMEPg results appeared most constant, as differences in PMEP became prominent at the leanest λ values as the boost system engaged (Fig. 6-31). Therefore, indicated results provide the most accurate comparison amongst the charge motion variants.

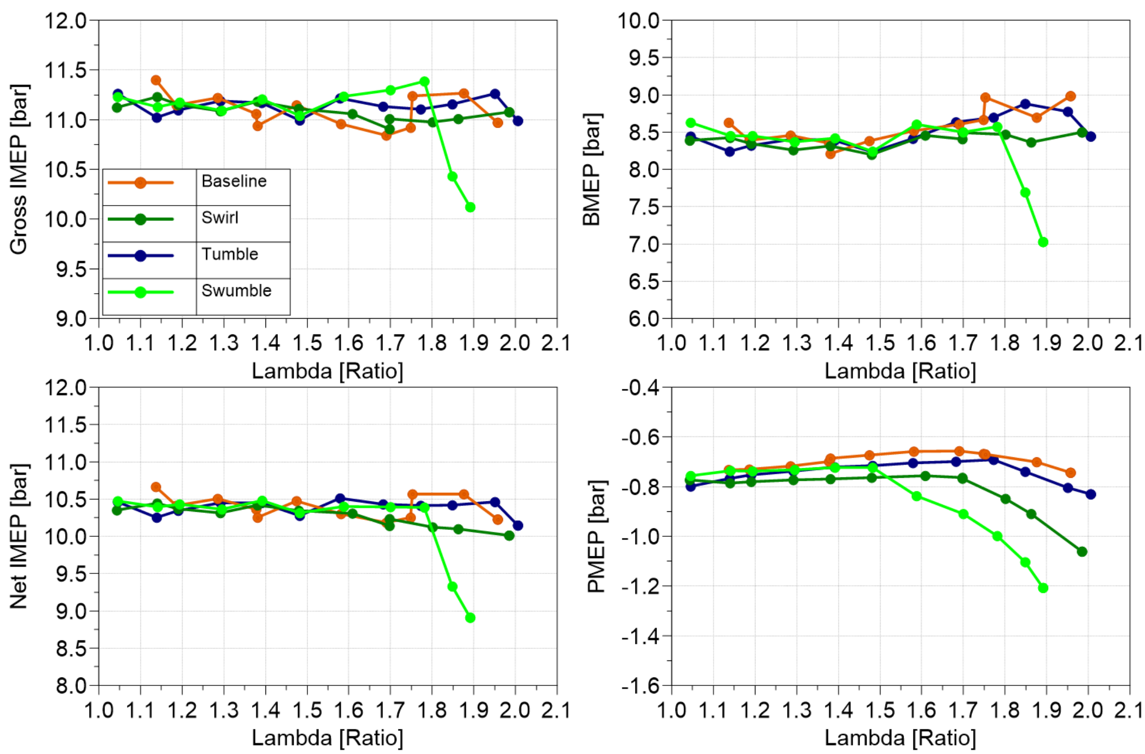

Figure 6-31: Mean effective pressure vs. λ; 4000 rpm, 8 bar BMEP.

Combustion stability trends are consistent with the results observed at the other conditions, with the tumble variant exhibiting superior stability (Fig. 6-32). Swirl and swumble variant combustion stability have generally been improved at this condition, with trends nearly identical to that of the baseline. In contrast to the results at the part load and full load conditions, each charge motion variant appears to enter a partial burn cycle regime at or near their lean stability limit. LNV values below 88% are encountered for all variants within the range λ = 1.8-2. This result illustrates the challenge of operating in regimes that produce slow burn durations at relatively high engine speeds, namely that the short timescale impedes the engine's ability to complete consume all of the fuel. Pre-chamber fueling trends with λ were generally consistent for all charge motion variants at this condition, as is shown in Fig. 6-33.

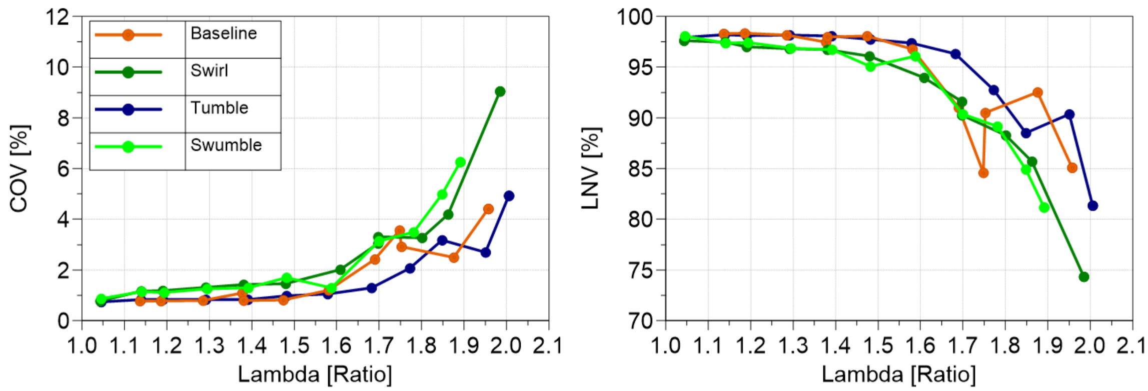

Figure 6-32: Combustion stability metrics vs. λ; 4000 rpm, 8 bar BMEP.

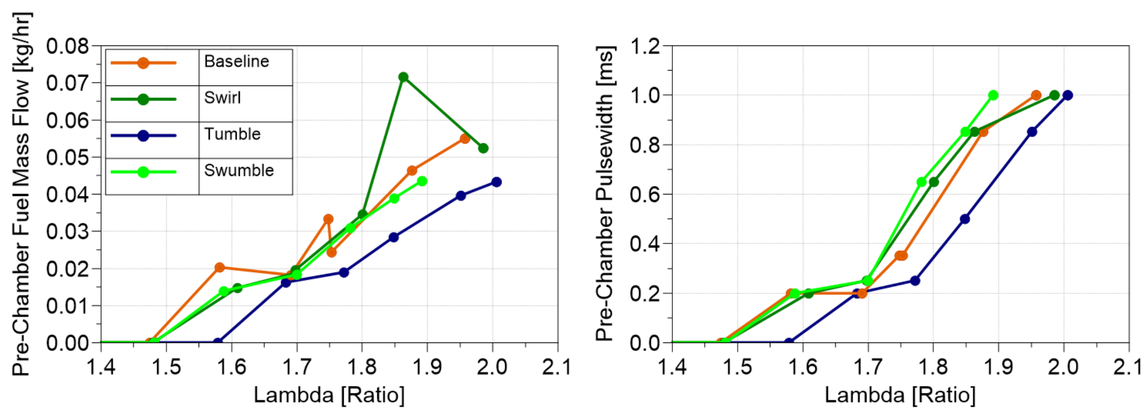

Figure 6-33: Pre-chamber fueling metrics vs. λ; 4000 rpm, 8 bar BMEP.

The CA50 results in Fig. 6-34 indicate mild knock encountered by all charge motion variants in the stoichiometric and near-lean regions, but little to no knock encountered beyond λ = 1.5. This slightly staggered knock performance produces discrepancies between the CA10-50 and CA5-90 results, but ultimately produces CA10-90 burn duration trends that show the tumble variant producing the shortest burn duration (approximately 1 CAD faster than the baseline) and the swirl and swumble variants producing the slowest burn durations (approximately 1 CAD slower than the baseline) under lean conditions.

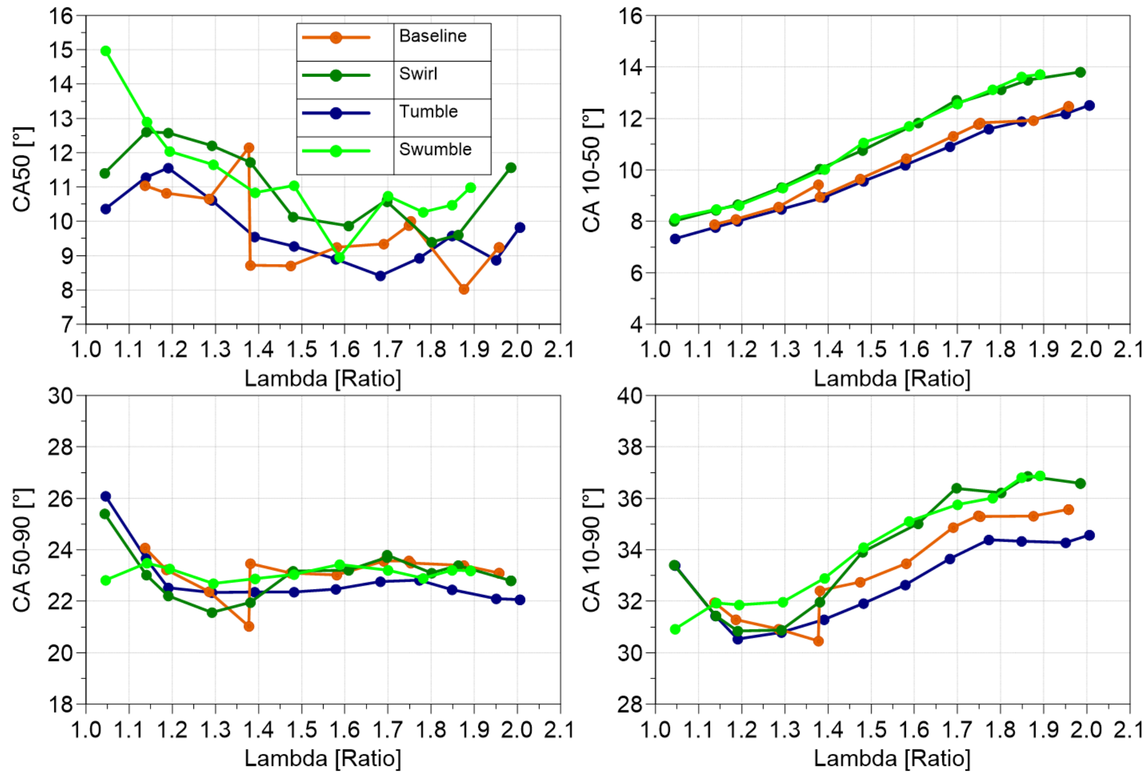

Figure 6-34: Burn duration metrics vs. λ; 4000 rpm, 8 bar BMEP.

The combustion duration results translate to higher ITE and BTE values for the tumble variant in the ultra-lean region, approximately 1 percentage point higher than the baseline variant beyond the λ = 1.7 condition (Fig. 6-35). Swirl and swumble BTE and BSFC results exhibit severe deterioration in the ultra-lean region, likely due to the increased pumping losses with enleanment, as this deterioration is absent from the ITE and ISFC results. The swirl and swumble variants do however show some degree of deterioration under lean conditions, approximately 1 percentage point lower ITE than the baseline. All charge motion variants achieved peak ITEs in excess of 50% with the tumble variant achieving nearly a 52% peak ITE.

Engine-out emissions trends are highly consistent with those at the other conditions, as can be seen in Fig. 6-36. Most notable at this condition is the steady rise in engine-out THC at all λ values lean of 1.2. The incomplete combustion effect is most accurately reflected in this substantial increase in THC, a 100% increase from λ = 1 to λ = 1.8. The combustion efficiency results shown in Fig. 6-37 mirror the trends at other conditions, but do so at generally lower combustion efficiency values than were observed at the other conditions.

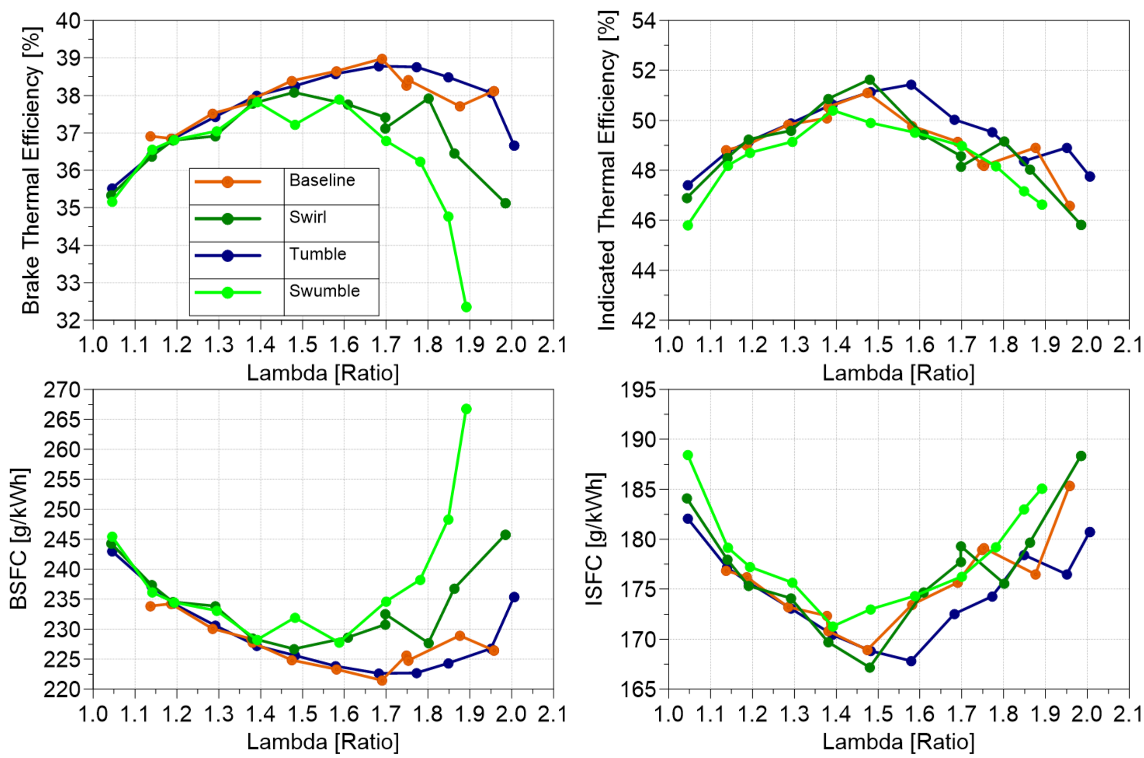

Figure 6-35: Efficiency and fuel consumption metrics vs. λ; 4000 rpm, 8 bar BMEP.

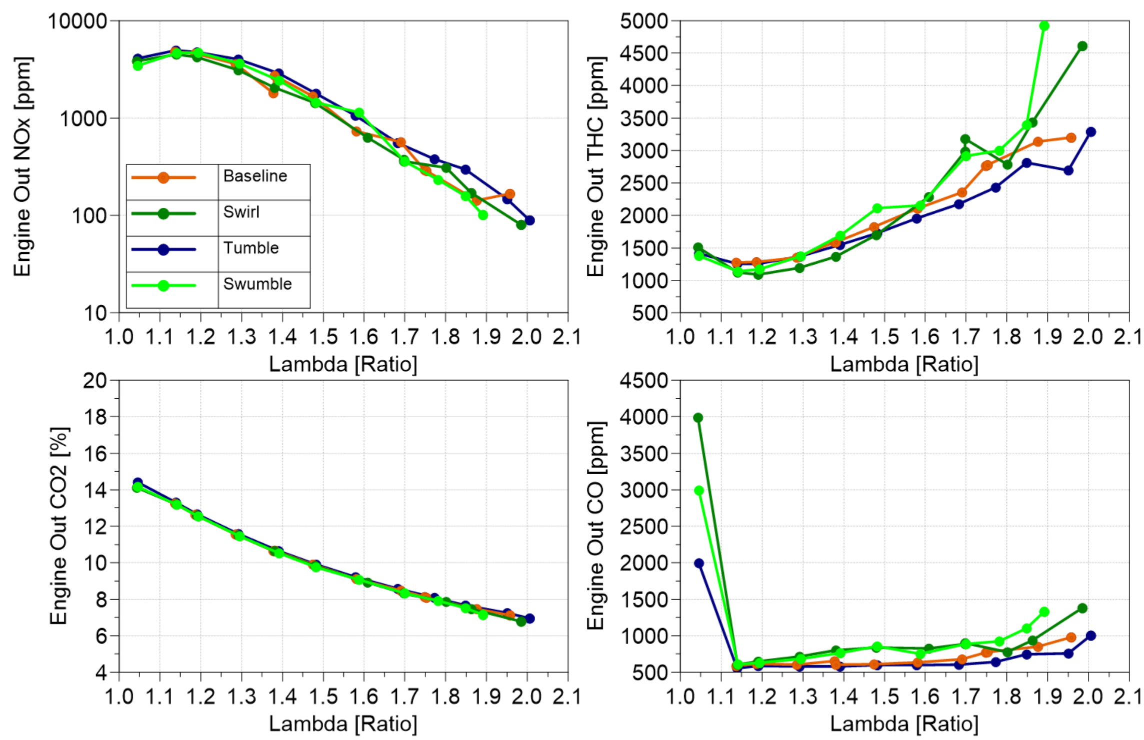

Figure 6-36: Engine-out emissions vs. λ; 4000 rpm, 8 bar BMEP.

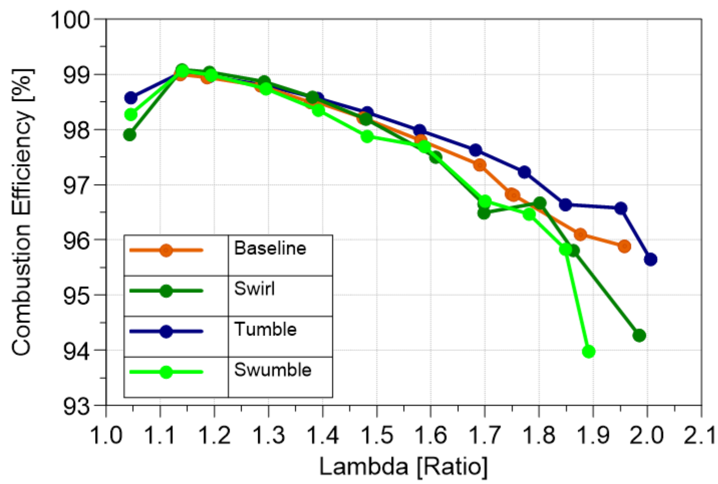

Figure 6-37: Combustion efficiency vs. λ; 4000 rpm, 8 bar BMEP.

The engine performance and emissions trends across λ and load sweeps with the charge motion variants are remarkably consistent across engine speed and load regimes. At each condition, disparities in stability, efficiency, and emissions were minor under stoichiometric operation but increased as the engine was enleaned. The tumble variant displayed consistently superior results in each key metric, while the swirl and swumble variants displayed inferior performance in the same metrics. While magnitudes naturally differed, the qualitative trends remained consistent. Therefore, it is hypothesized that simulation results should capture behavior that generally applies to operation across most of the engine map. The separation in both CA10-90 duration and combustion efficiency near the lean stability limit for this high speed condition, as well as the similar injected pre-chamber fueling quantities, made it an ideal candidate to simulate in CFD. Since performance result separation is most prominent under lean conditions, a λ of 1.7 was chosen for the simulations. Table 6-1 states the burn durations produced by the four charge motion variants at this high speed lean condition. This data is used for matching of the simulation results presented in the subsequent sections.

As was established in the discussion of the pre-chamber combustion results, charge motion influences in-pre-chamber processes significantly. The experimental data showed an influence over pre-chamber combustion but an influence over pre-chamber mixture dynamics could only be inferred. The CFD model is therefore a key tool to better understand how charge motion translates from the main chamber to the pre-chamber, and how this translation impacts pre-chamber and subsequently main chamber combustion to such an extent that it can generate a 0.5-1.5 percentage point improvement in ITE versus the baseline in the case of the tumble variant.

Table 6-1: Experimental burn duration results; λ = 1.7, 4000 rpm, 8 bar BMEP.

	CA0-10	CA10-50	CA50-90	CA10-90	CA0-90
Base Exp	20	11.3	23.5	34.8	54.8
Tumble Exp	20.5	11.2	22.7	33.9	54.4
Swirl Exp	26	12.6	24	36.6	62.6
Swumble Exp	22.2	12.6	23.2	35.8	58.0

6.5 Model Results

6.5.1 Correlation with Experimental Results

Before discussing the results of the CFD simulations, confidence in the ability of the CFD simulations to reflect experimental engine behavior must be established. The macro-level correlation process for establishing this degree of confidence was described in detail in Chapter 4. The results are presented in this section.

Figure 6-38 shows the correlation between experimental and CFD main chamber pressure traces for the baseline charge motion variant. This figure qualitatively shows a good match between experiment and simulation. This match is quantified in Tables 6-2 and 6-3, showing the discrepancy in pressure values at key engine cycle events and their locations, respectively. For this base variant all pressure values at the 5 key correlation locations are within the allowable discrepancy, and the events occur at consistent locations between the experimental and simulation results. This result confirms acceptable macro-level correlation for the baseline charge motion variant.

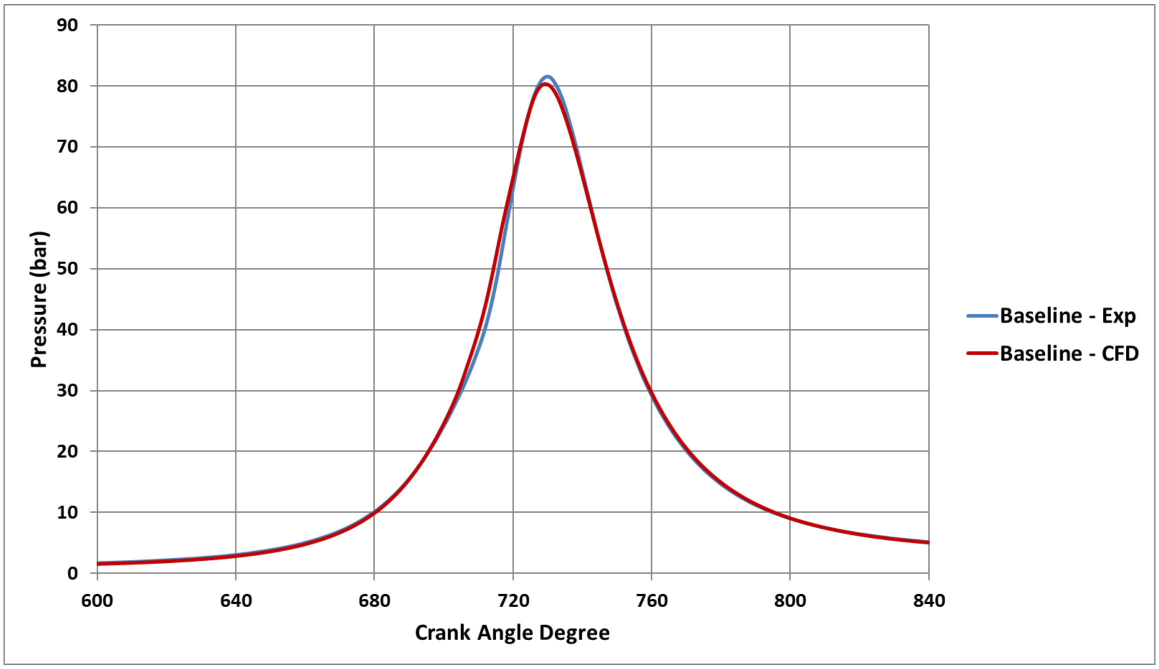

Figure 6-38: Comparison of experimental and simulation main chamber pressure for the baseline charge motion variant; 4000 rpm, 8 bar BMEP, λ = 1.7.

Table 6-2: Discrepancy between experimental and simulation pressure values at key engine cycle events for the baseline charge motion variant; 4000 rpm, 8 bar BMEP, λ = 1.7.

Base		
Points	**Acceptable Discrepancy**	**Current Discrepancy**
IVC	2%	0.18%
Spark	1%	0.28%
Heat Release	3%	1.80%
Peak	5%	1.23%
Post Combustion	3%	0.68%

Table 6-3: Discrepancy between experimental and simulation locations of key engine cycle pressure events for the baseline charge motion variant; 4000 rpm, 8 bar BMEP, λ = 1.7.

Base			
	Points	**Acceptable Discrepancy**	**Current Discrepancy**
Location of Pressure Value	IVC	0.20%	0.00%
	Spark	0.10%	0.05%
	Heat Release	0.20%	0.09%
	Peak	0.30%	0.30%
	Post Combustion	1.00%	0.10%

The match between experimental and simulation pre-chamber pressure traces in the area of interest for the baseline variant is shown in Fig. 6-39. As was discussed in Chapter 4, the pre-chamber pressure traces are not expected to provide as comprehensive of a match as do the main chamber pressure traces. Here the simulation predicts a higher degree of heat release during the pre-chamber combustion event as evidenced by the higher local pre-chamber pressure during this time. The simulation also predicts slightly earlier phasing of the pre-chamber combustion event.

A comparison of burn duration results is shown in Table 6-4. The simulation results predict similar early and mid-burning durations to the experimental results, with a slightly shorter late burning duration, producing a CA10-90 discrepancy of 3 CAD. This relatively good matching of the burn duration results confirms the validity of the macro-level pressure correlation approach used in this study.

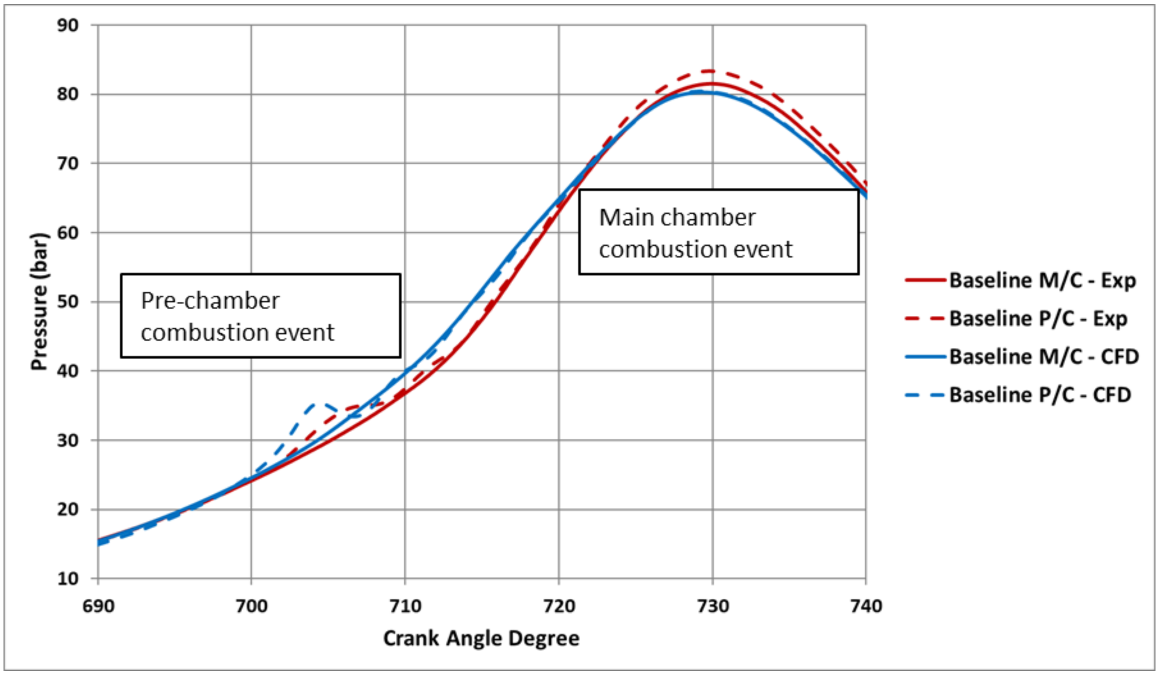

Figure 6-39: Comparison of experimental and simulation pre-chamber pressure for the baseline charge motion variant; 4000 rpm, 8 bar BMEP, λ = 1.7.

Table 6-4: Comparison of experimental and simulation burn duration metrics for the baseline charge motion variant; 4000 rpm, 8 bar BMEP, λ = 1.7.

	CA0-10	CA10-50	CA50-90	CA10-90
Base Exp	20	11.3	23.5	34.8
Base CFD	21.5	12.6	19	31.6

Similar analysis is shown for the tumble variant, with the main chamber pressure match in Fig. 6-40, the match of pressure values at the key locations in Table 6-5, and the match of key pressure locations in Table 6-6. Here the pressure at spark timing and time of initial heat release display a discrepancy between experiment and simulation that are slightly beyond the target threshold. However, the other pressure value metrics are within the threshold, as are the locations of each of the 5 key events. Therefore, the tumble variant simulation results are declared correlated to experimental results but with a lower degree of confidence than are the baseline variant results.

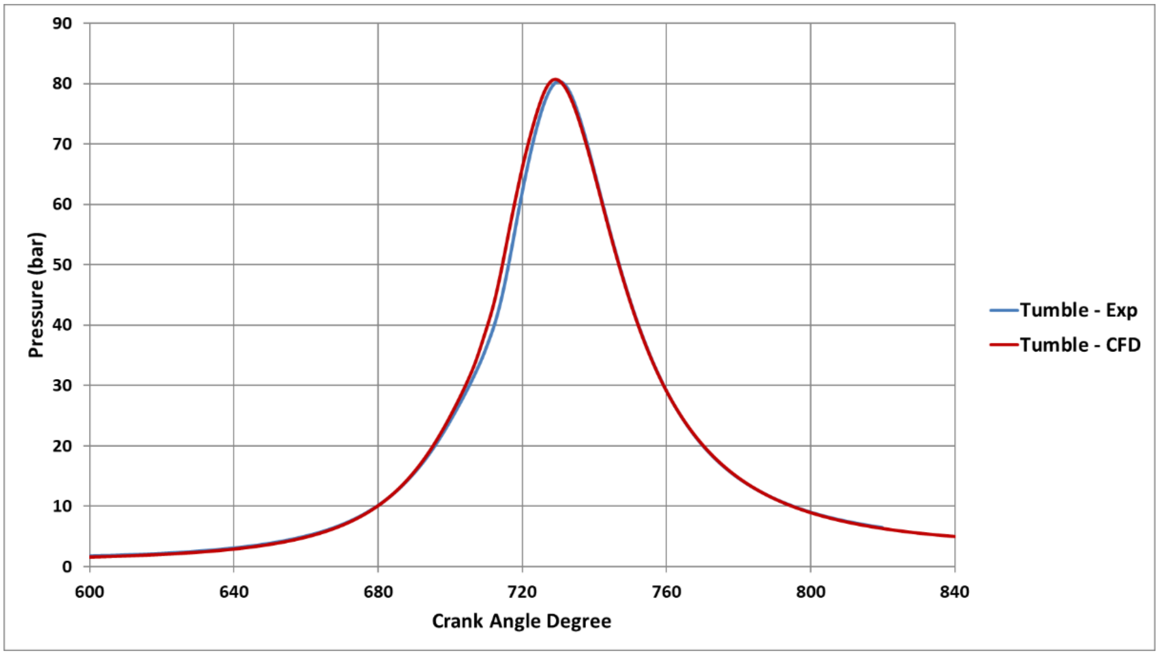

Figure 6-40: Comparison of experimental and simulation main chamber pressure for the tumble charge motion variant; 4000 rpm, 8 bar BMEP, λ = 1.7.

Table 6-5: Discrepancy between experimental and simulation pressure values at key engine cycle events for the tumble charge motion variant; 4000 rpm, 8 bar BMEP, λ = 1.7.

Tumble		
Points	**Acceptable Discrepancy**	**Current Discrepancy**
IVC	2%	0.40%
Spark	1%	1.50%
Heat Release	3%	3.33%
Peak	5%	0.25%
Post Combustion	3%	0.76%

Table 6-6: Discrepancy between experimental and simulation locations of key engine cycle pressure events for the tumble charge motion variant; 4000 rpm, 8 bar BMEP, λ = 1.7.

Tumble			
	Points	**Acceptable Discrepancy**	**Current Discrepancy**
Location of Pressure Value	IVC	0.20%	0.00%
	Spark	0.10%	0.00%
	Heat Release	0.20%	0.15%
	Peak	0.30%	0.13%
	Post Combustion	1.00%	0.10%

This minor discrepancy in two of the key pressure event matches can be examined qualitatively in the pre-chamber pressure trace comparison in Fig. 6-41. The simulation predicts a higher pressure pre-chamber combustion event that initiates main chamber heat release earlier than the experimental results indicate. There are several possible explanations for this behavior. Firstly, the Woschni heat transfer methodology used likely does not properly account for the impact of increased motion in the pre-chamber. As was shown previously, increased tumble and swirl motion contribute to higher heat losses in the main chamber. It is likely that this occurs in the pre-chamber as well. Secondly, the spray-wall interaction model used in the CFD simulation is not correlated to any physical behavior, as explained in Chapter 4. Therefore, the validity of this model, especially as it pertains to the rate of vaporization inside the pre-chamber, is unknown. Inability to capture rate of fuel vaporization as the fuel spray impinges on the pre-chamber wall could result in inaccurate quantities of vaporized fuel contributing to early burning during the pre-chamber combustion event. These inaccuracies strongly imply a need for an in-pre-chamber optical diagnostic to at least address the fuel vaporization rate question.

An examination of predicted burn durations in Table 6-7 show that the effects of this discrepancy are mostly confined to the early CA0-10 burn duration, and do not propagate in a detectable way to the CA10-90 burn duration, as there is only a 1.7 CAD discrepancy in CA10-90 between experiment and simulation with this tumble variant.

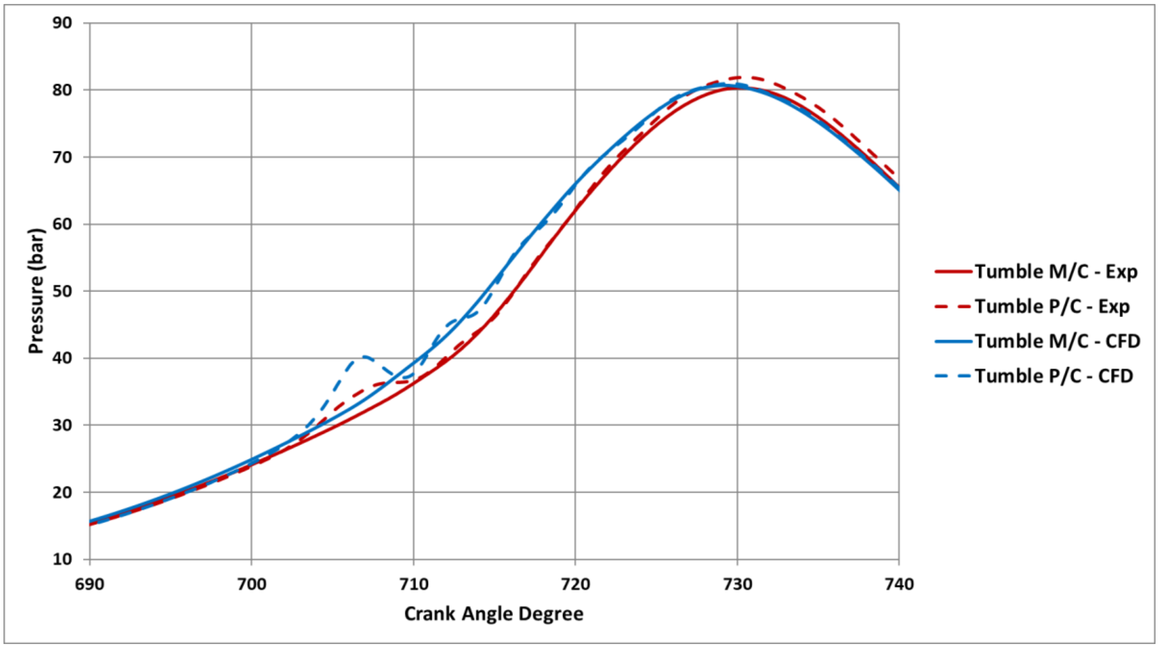

Figure 6-41: Comparison of experimental and simulation pre-chamber pressure for the tumble charge motion variant; 4000 rpm, 8 bar BMEP, λ = 1.7.

Table 6-7: Comparison of experimental and simulation burn duration metrics for the tumble charge motion variant; 4000 rpm, 8 bar BMEP, λ = 1.7.

	CA0-10	CA10-50	CA50-90	CA10-90
Tumble Exp	20.5	11.2	22.7	33.9
Tumble CFD	18	11.7	20.5	32.2

Correlation results for the swirl variant are shown in Fig. 6-42 (main chamber pressure match), Table 6-8 (match of pressure values at the key locations), and Table 6-9 (match of key pressure locations). With the swirl variant simulation, pressure at the 5 key locations are within the target threshold, as are all locations of pressure events with the exception of the post-combustion pressure location. Therefore, macro-level main chamber pressure correlation is established with a high degree of confidence for this charge motion variant.

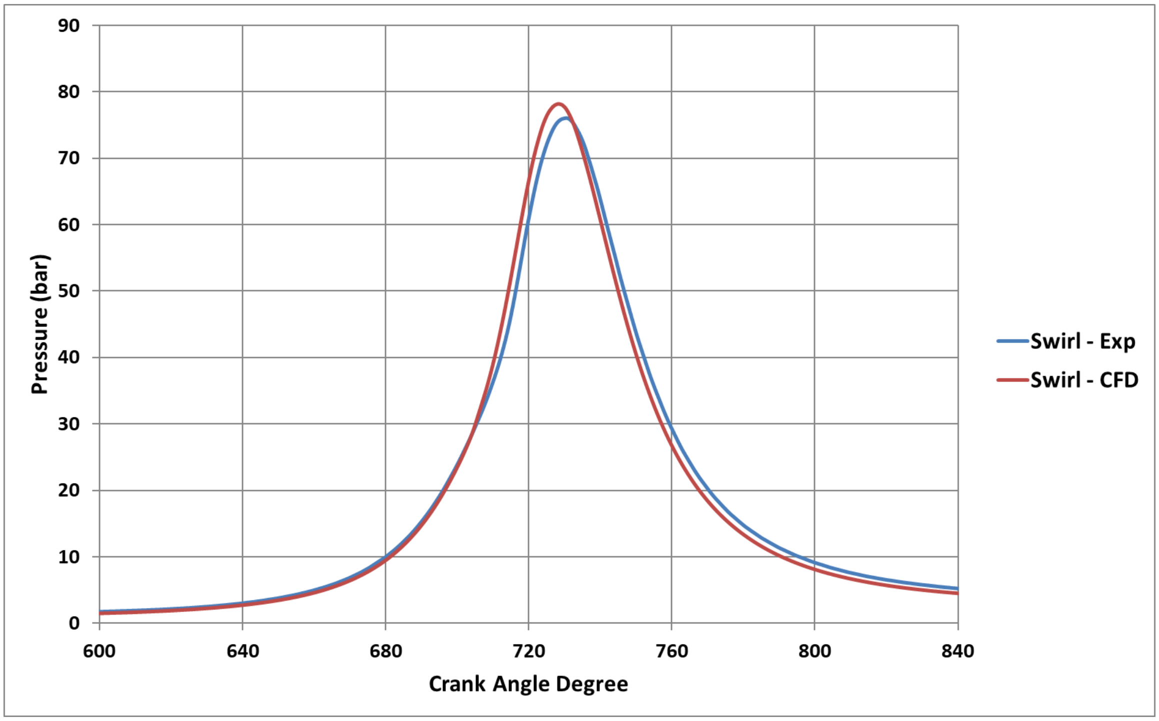

Figure 6-42: Comparison of experimental and simulation main chamber pressure for the swirl charge motion variant; 4000 rpm, 8 bar BMEP, λ = 1.7.

Table 6-8: Discrepancy between experimental and simulation pressure values at key engine cycle events for the swirl charge motion variant; 4000 rpm, 8 bar BMEP, λ = 1.7.

Swirl		
Points	**Acceptable Discrepancy**	**Current Discrepancy**
IVC	2%	0.38%
Spark	1%	0.63%
Heat Release	3%	0.34%
Peak	5%	2.85%
Post Combustion	3%	0.88%

Table 6-9: Discrepancy between experimental and simulation locations of key engine cycle pressure events for the swirl charge motion variant; 4000 rpm, 8 bar BMEP, λ = 1.7.

Swirl			
	Points	**Acceptable Discrepancy**	**Current Discrepancy**
Location of Pressure Value	IVC	0.20%	0.00%
	Spark	0.10%	0.00%
	Heat Release	0.20%	0.05%
	Peak	0.30%	0.28%
	Post Combustion	1.00%	1.70%

The pre-chamber pressure traces from the swirl variant experimental and simulation results are shown in Fig. 6-43. While the magnitude of the peak pre-chamber pressure appears consistent between experiment and simulation, the phasing differs by a few CAD, as it does with the other variants. This discrepancy is reflected in the early burning CA0-10 duration (Table 6-10) but does not propagate substantively to the CA10-90 burn duration. The CA10-90 discrepancy between experimental and simulation results is approximately 2 CAD.

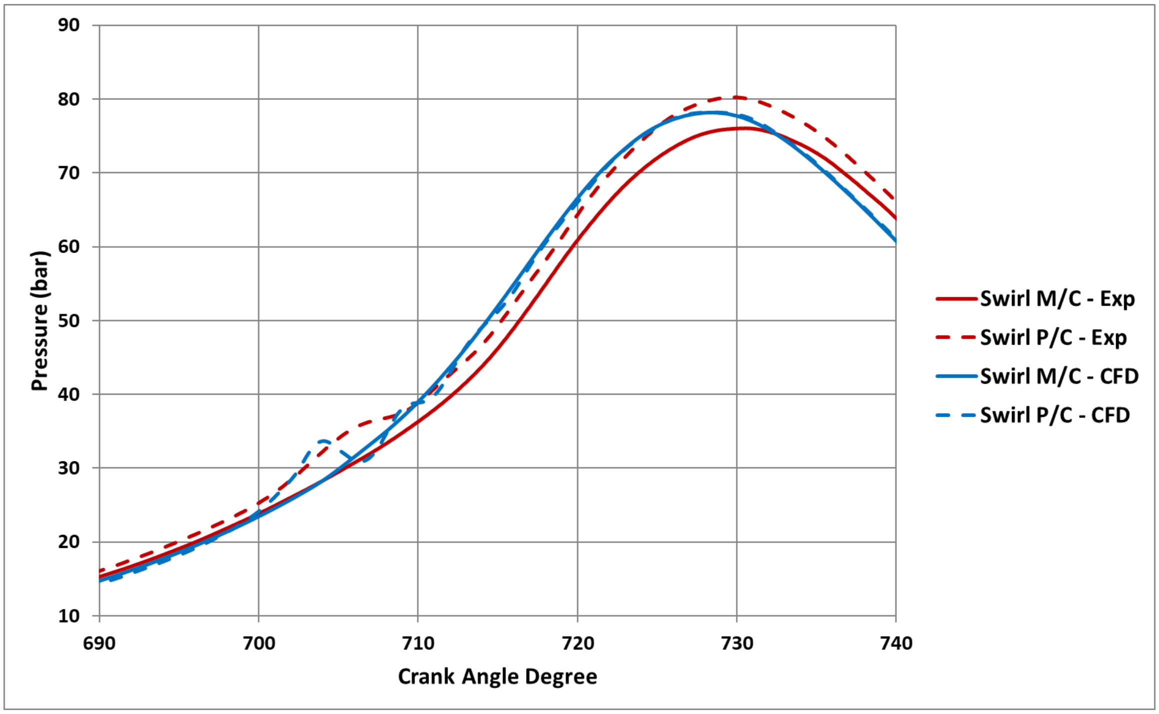

Figure 6-43: Comparison of experimental and simulation pre-chamber pressure for the swirl charge motion variant; 4000 rpm, 8 bar BMEP, λ = 1.7.

Table 6-10: Comparison of experimental and simulation burn duration metrics for the swirl charge motion variant; 4000 rpm, 8 bar BMEP, λ = 1.7.

	CA0-10	CA10-50	CA50-90	CA10-90
Swirl Exp	26	12.6	24	36.6
Swirl CFD	21.5	12.5	22	34.5

The swumble variant results shown in Fig. 6-44 seem to qualitatively indicate a poor match between experiment and simulation due to the visual disparity in peak pressure values, but an examination of the key pressure values (Table 6-11) indicate a relatively robust match, with the exception of main chamber pressure at spark timing. Despite the fact that pressure at IVC matches, the mismatch of pressure at spark timing implies that the simulation may not be accurately capturing the trapped mass of the experiment. An examination of the location of the 5 key pressure events (Table 6-12) indicates that only the post-combustion pressure event is out of phase of the target threshold. The swumble variant simulation therefore achieves a macro-level correlation with experimental results with a moderate degree of confidence.

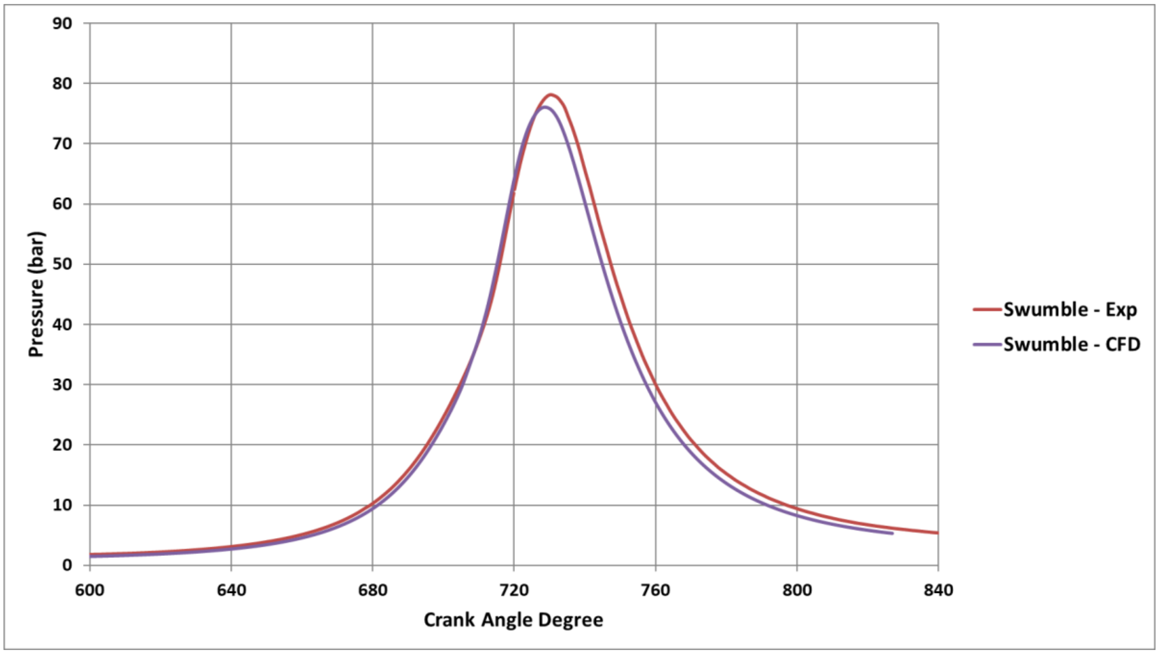

Figure 6-44: Comparison of experimental and simulation main chamber pressure for the swumble charge motion variant; 4000 rpm, 8 bar BMEP, λ = 1.7.

Table 6-11: Discrepancy between experimental and simulation pressure values at key engine cycle events for the swumble charge motion variant; 4000 rpm, 8 bar BMEP, λ = 1.7.

Swumble		
Points	**Acceptable Discrepancy**	**Current Discrepancy**
IVC	2%	0.33%
Spark	1%	1.52%
Heat Release	3%	1.88%
Peak	5%	2.70%
Post Combustion	3%	1.28%

Table 6-12: Discrepancy between experimental and simulation locations of key engine cycle pressure events for the swumble charge motion variant; 4000 rpm, 8 bar BMEP, λ = 1.7.

Swumble			
	Points	**Acceptable Discrepancy**	**Current Discrepancy**
Location of Pressure Value	IVC	0.20%	0.00%
	Spark	0.10%	0.00%
	Heat Release	0.20%	0.05%
	Peak	0.30%	0.25%
	Post Combustion	1.00%	1.20%

The pre-chamber pressure trace comparison in Fig. 6-45 shows the slight pressure offset between experiment and simulation in the region where spark timing occurs (693 CAD), likely explained by the inability of the simulation to completely capture the pressure restriction caused by the swumble insert in the intake. Despite this discrepancy, burn durations match relatively well between experiment and simulation (Table 6-13).

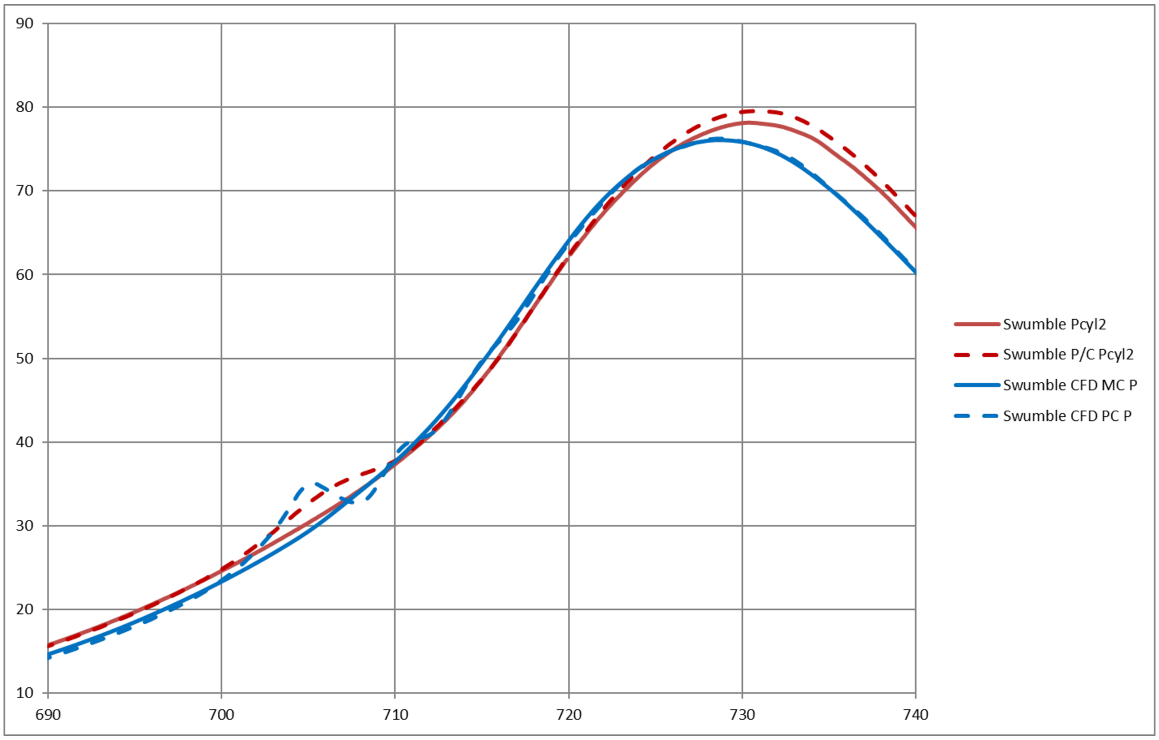

Figure 6-45: Comparison of experimental and simulation pre-chamber pressure for the swumble charge motion variant; 4000 rpm, 8 bar BMEP, λ = 1.7.

Table 6-13: Comparison of experimental and simulation burn duration metrics for the swumble charge motion variant; 4000 rpm, 8 bar BMEP, λ = 1.7.

	CA0-10	CA10-50	CA50-90	CA10-90
Swumble Exp	22.2	12.6	23.2	35.8
Swumble CFD	18.7	11.7	21.8	33.5

With macro-level main chamber pressure correlation confirmed, and this correlation translating to a robust matching of burn duration segments, a high degree of confidence in the simulation results' relative accuracy is established. The following section uses the insight provided by the simulation results to determine the influence of the induced charge motion on fuel-air mixture preparation in the pre-chamber prior to spark timing.

6.5.2 Pre-Chamber Mixture Preparation

In examining the influence of charge motion on in-pre-chamber mixture preparation, it is important to first establish how charge motion induced in the intake and manifested in the main chamber translates to the pre-chamber. To establish this translation, the evolution of tumble, swirl and TKE in the main chamber and pre-chamber are observed. Figure 6-46 shows the evolution of tumble ratio for all charge motion variants in one specific plane across an engine cycle. There is most separation in the tumble ratios of the charge motion variants as spark timing (690-700 CAD for all variants) is approached. As expected, the tumble variant achieves the highest tumble ratio (approximately 4.5) while the baseline variant achieves a peak tumble ratio of approximately 3 in this region. The swirl variant produces minimal tumble near spark timing. The swumble variant also produces minimal tumble near spark timing, likely a product of the 2D plane of observation chosen for this analysis.

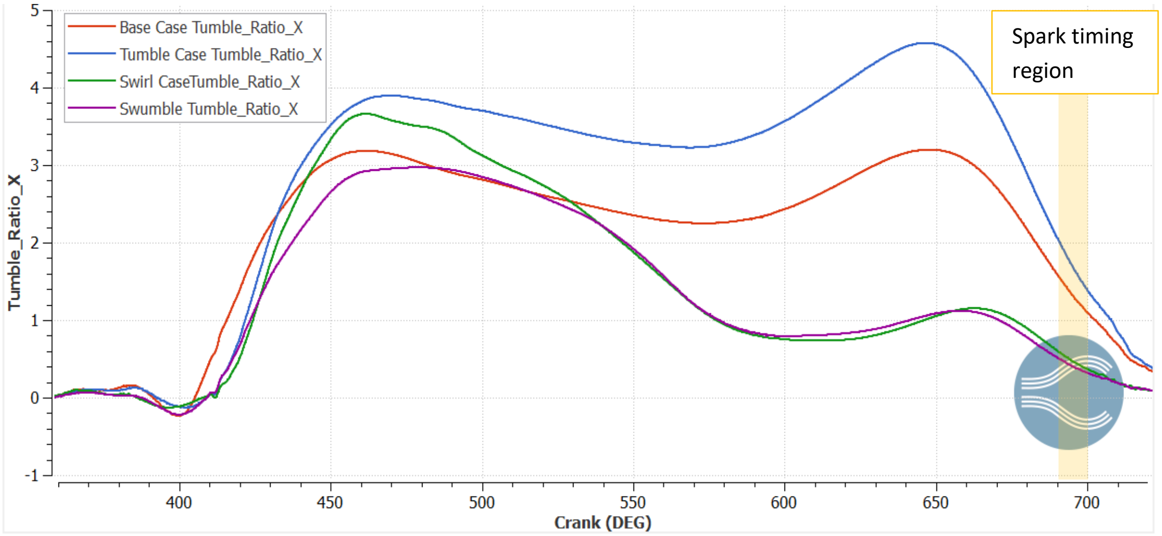

Figure 6-46: Comparison of simulation tumble ratio in the main chamber; 4000 rpm, 8 bar BMEP, λ = 1.7.

Comparing the main chamber tumble ratio result of Fig. 6-46 with that of the pre-chamber tumble ratio in Fig. 6-47 yields several interesting observations. Firstly, the tumble direction is reversed for each of the charge motion variants near spark timing. Main chamber tumble motion reverses direction as it enters the pre-chamber, likely as it ricochets off of the pre-chamber wall as it first enters. Despite this ricochet event, the tumble motion retains its magnitude as it reverses, with the tumble and baseline cases achieving tumble ratio absolute magnitudes similar to those achieved in the main chamber. Another interesting observation is that tumble motion in the main chamber achieves a peak approximately midway through the compression stroke (650 CAD) for all charge motion variants and reduces as the shrinking volume collapses the motion structure. In the pre-chamber, however, tumble motion appears to translate to the pre-chamber and increases in magnitude up until the pre-chamber combustion event dissolves it. This is true for all charge motion variants, with global maximum tumble ratios achieved in the region of spark timing.

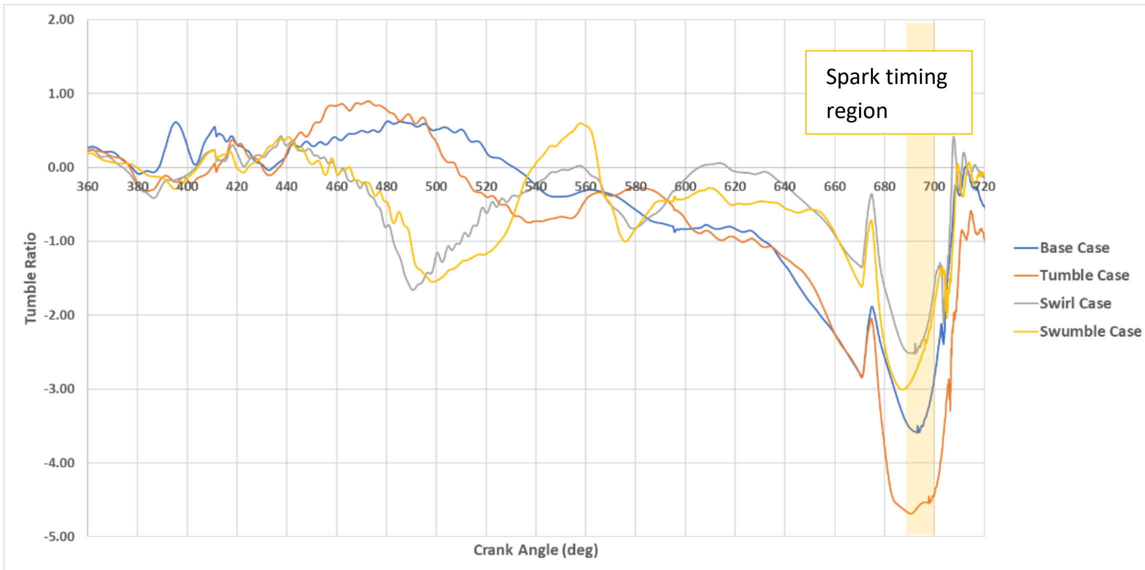

Figure 6-47: Comparison of simulation tumble ratio in the pre-chamber; 4000 rpm, 8 bar BMEP, λ = 1.7.

Main chamber swirl number results are shown in Fig. 6-48. The simulation predicts similar swirl number magnitude and evolution in the swirl and swumble variants. As expected, there is minimal swirl present in the baseline and tumble variants. Fig. 6-49 shows depressed translation of swirl from the main chamber to the pre-chamber, with the swirl and swumble variants showing some degree of swirl motion in the pre-chamber but at lower magnitudes than are present in the main chamber. The tumble variant swirl result in pre-chamber is believed to be erroneous since there is minimal swirl motion in the main chamber for this case. As with the tumble ratio results, swirl appears to translate to the pre-chamber in the cases of the swirl and swumble variants at a later phasing and in the opposite direction compared to its evolution in the main chamber.

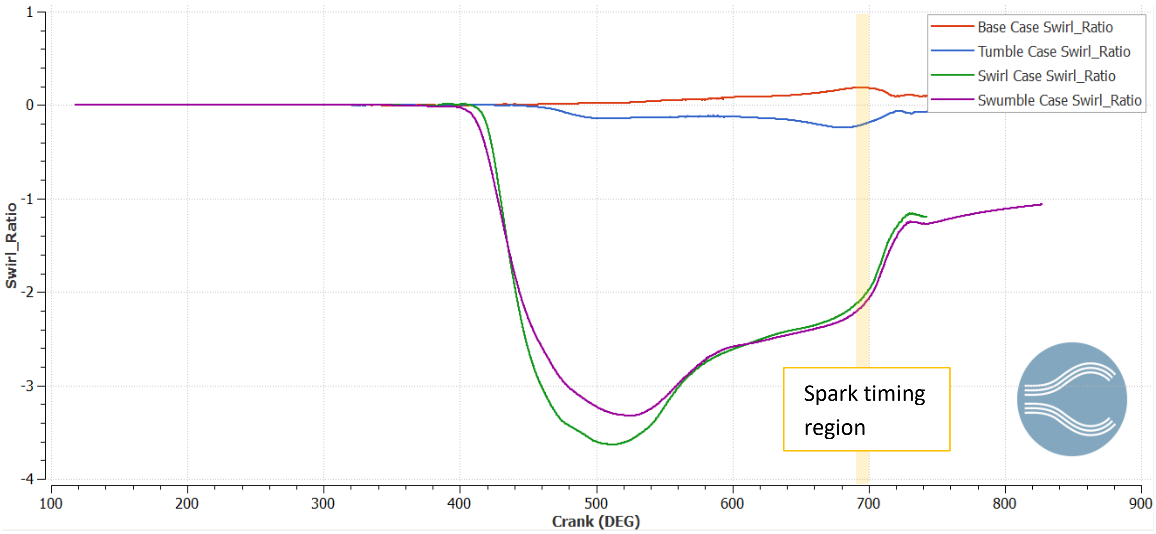

Figure 6-48: Comparison of simulation swirl number in the main chamber; 4000 rpm, 8 bar BMEP, λ = 1.7.

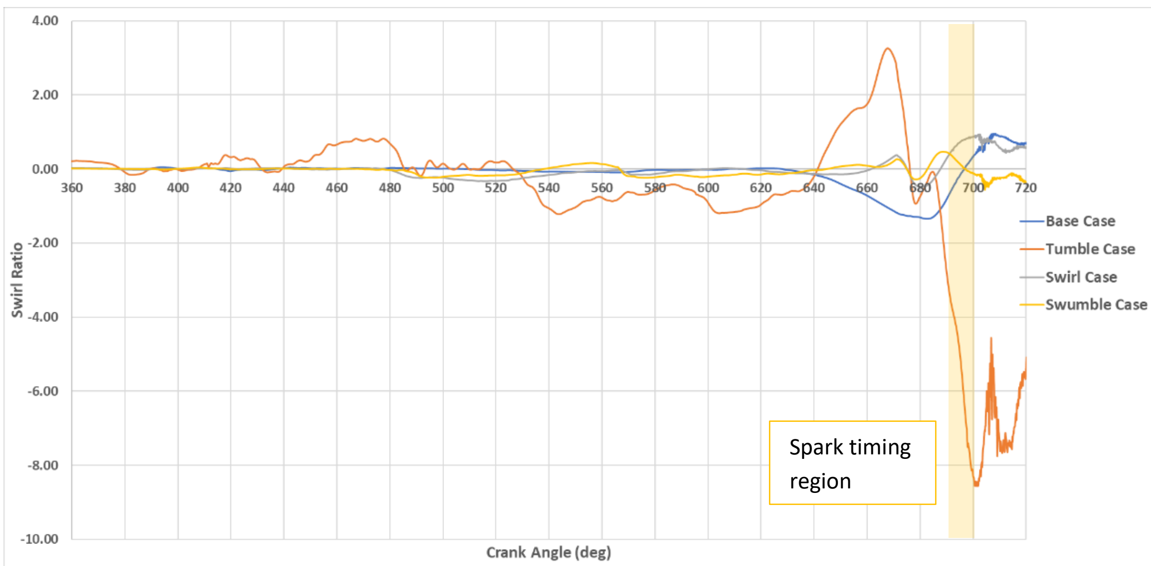

Figure 6-49: Comparison of simulation swirl number in the pre-chamber; 4000 rpm, 8 bar BMEP, λ = 1.7.

The main chamber TKE results shown in Fig. 6-50 are complementary to the main chamber tumble ratio results shown in Fig. 6-46. In the latter figure, tumble ratio peaks for the charge motion variants around 650 CAD and then decreases as the shrinking chamber volume causes tumble motion to collapse. Figure 6-50 shows that this tumble collapse event corresponds to a sharp increase in TKE for the tumble and baseline variants immediately prior to spark timing. TKE in the swirl and swumble variant cases continues to decline in this region.

In the pre-chamber, TKE increases for all charge motion variants throughout the compression stroke (Fig. 6-51). As expected, the tumble variant exhibits the highest level of TKE at spark timing, followed by the baseline variant. The swirl and swumble variants, despite decreasing TKE levels in the main chamber during the compression stroke, see increasing TKE levels in the pre-chamber during the compression stroke. The translation of tumble motion from the main chamber to the pre-chamber in these variants created a similar juxtaposition. Therefore, it is concluded that charge transfer from the main chamber to the pre-chamber during the compression stroke introduces both tumble motion and TKE into the pre-chamber regardless of the charge motion dynamic in the main chamber. Tumble motion in the main chamber increases the magnitude of both tumble and TKE in the pre-chamber in proportion to the main chamber tumble ratio magnitude.

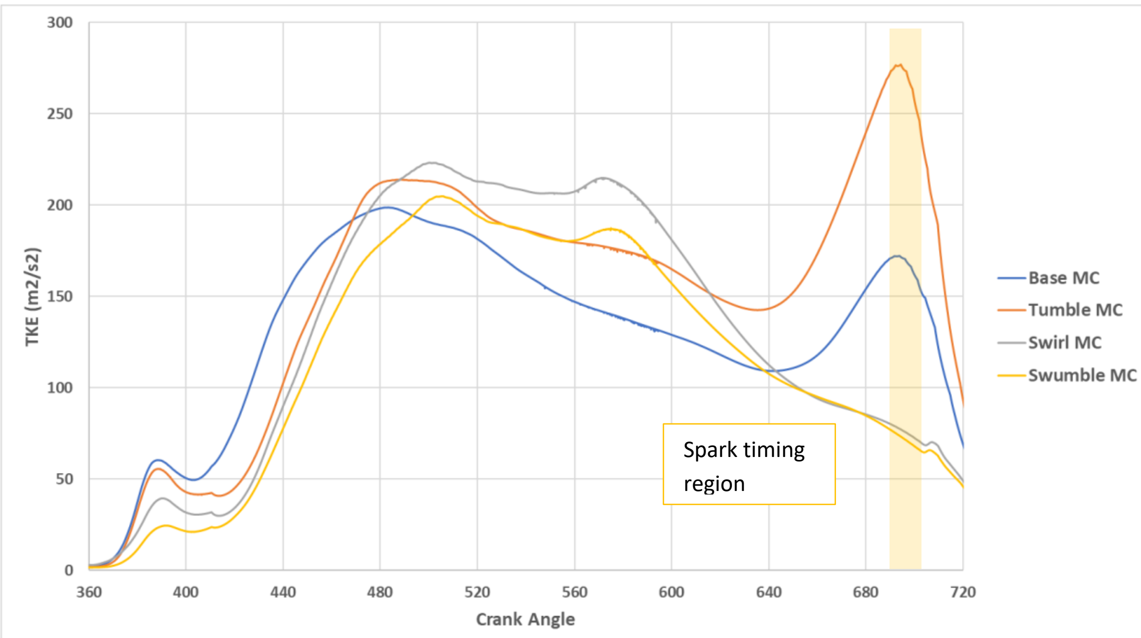

Figure 6-50: Comparison of simulation TKE in the main chamber; 4000 rpm, 8 bar BMEP, λ = 1.7.

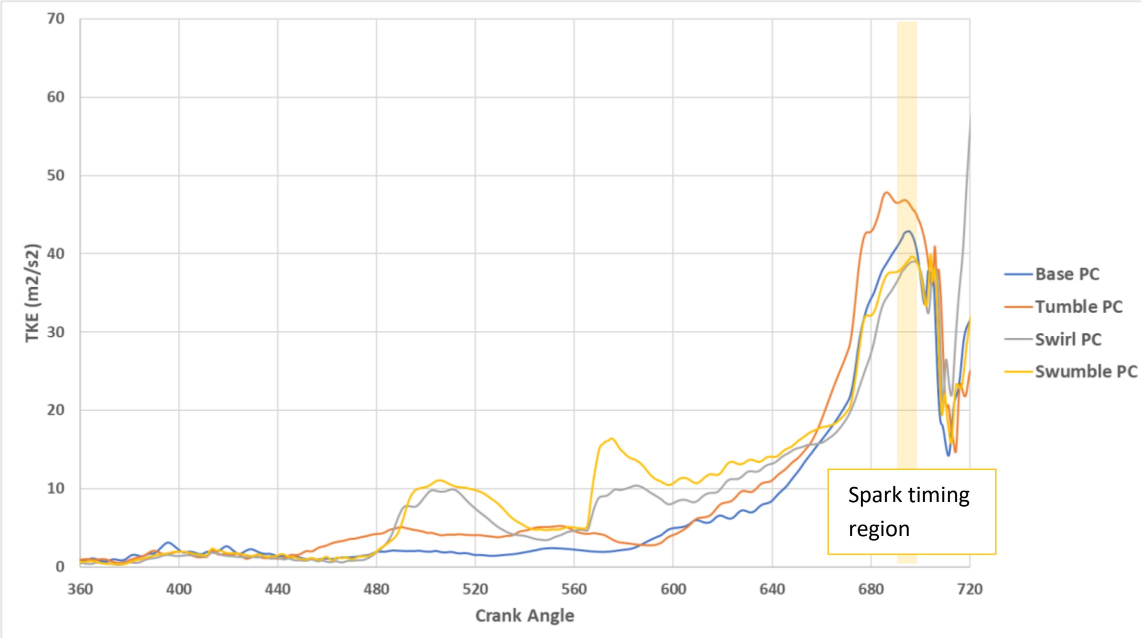

Figure 6-51: Comparison of simulation TKE in the pre-chamber; 4000 rpm, 8 bar BMEP, λ = 1.7.

With charge motion translation between chambers established, it is important to understand how in-pre-chamber charge motion influences mixing. Figure 6-52 displays the mean pre-chamber λ. During the injection event, λ swings rich and then enleans due to the entering lean charge from the main chamber. The swumble and swirl variants are slightly richer than the tumble and baseline variants, likely due to minor differences in auxiliary fuel quantities.

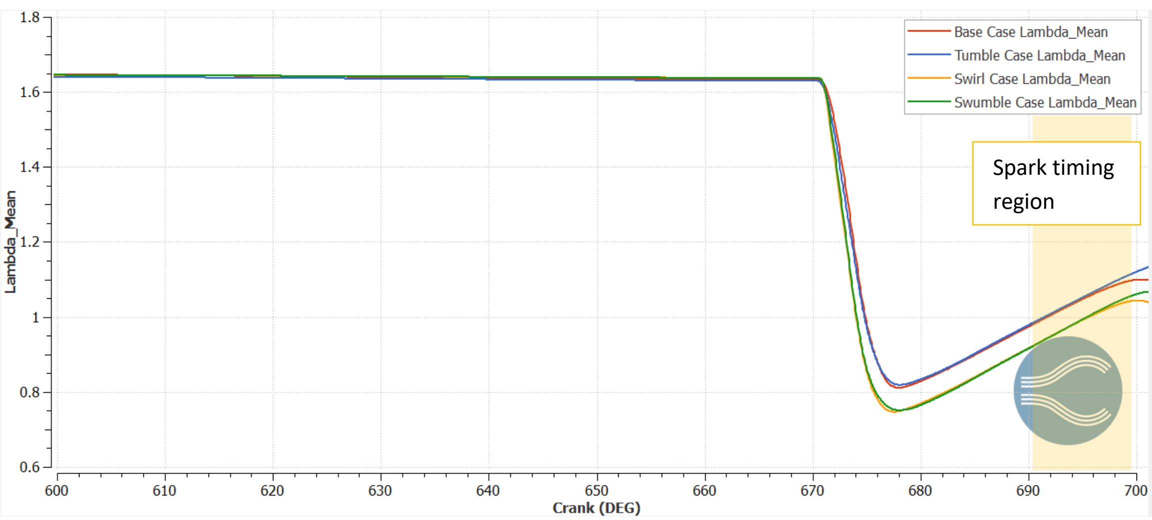

Figure 6-52: Comparison of simulation mean λ in the pre-chamber; 4000 rpm, 8 bar BMEP, λ = 1.7.

The standard deviation of λ in the pre-chamber is used as a metric for pre-chamber mixture stratification. Figure 6-53 shows the evolution of this parameter. In the spark timing region, both the swirl and swumble variants display slightly increased stratification than the tumble and baseline variants. This increased stratification tracks well with the richer λ evolution witnessed in Fig. 6-52, indicating that the differences amongst the charge motion variants are most likely due to slightly different auxiliary fuel quantities rather than being a product of in-pre-chamber charge motion.

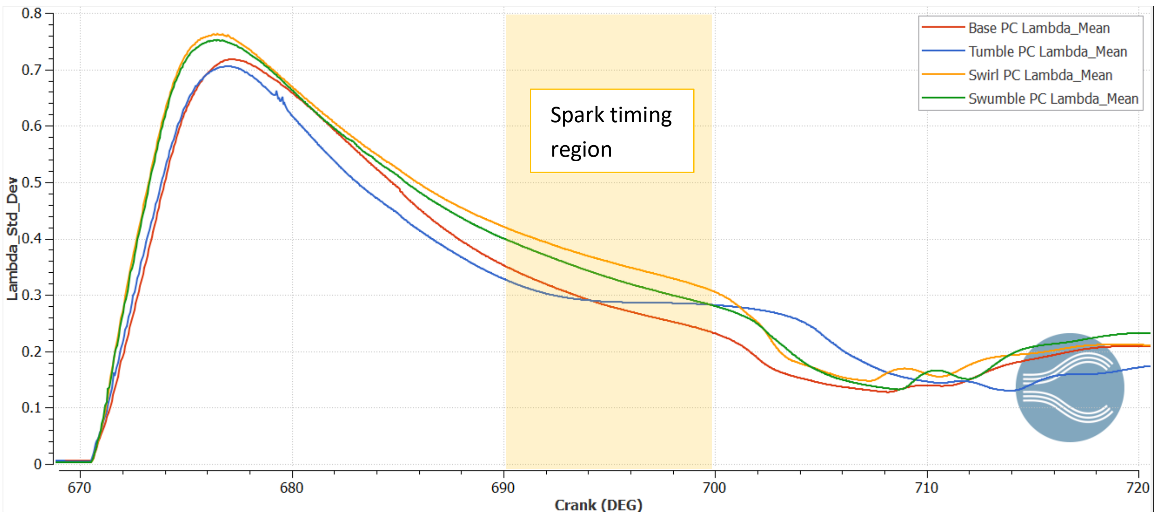

Figure 6-53: Comparison of simulation standard deviation of λ in the pre-chamber; 4000 rpm, 8 bar BMEP, λ = 1.7.

While global fuel-air mixing parameters appear largely unaffected by differing levels of charge motion, there is a charge motion influence on scavenging of residual gases from the pre-chamber. Figure 6-54 shows the evolution of O_2 mass percent and CO_2 mass percent in the pre-chamber, with O_2 as a stand-in for the air in fresh charge and CO_2 as a simplified stand-in for residual gases. This figure and the subsequent complementary figures are intended as a mostly qualitative evaluation of gas exchange differences amongst the charge motion variants. Prior to combustion, the combustion chamber must purge the residual gases from the previous cycle's combustion events out of the pre-chamber and replace them with fresh charge. The influence of the charge motion variants on this process is shown in greater detail in segments delineated by valve events. Evolution from EVO to IVO is shown in Fig. 6-55; evolution from IVO to exhaust valve closing (EVC) is shown in Fig. 6-56; evolution from EVC to IVC is shown in Fig. 6-57; and evolution from IVC to EVO is shown in Fig. 6-58.

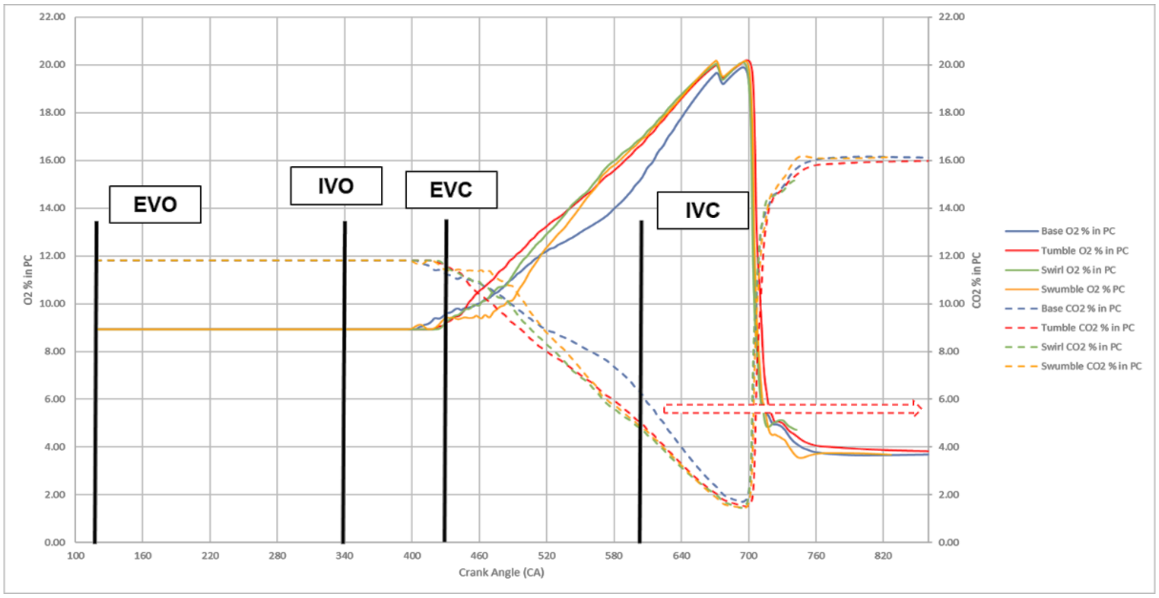

Figure 6-54: Comparison of O_2 and CO_2 mass % in the pre-chamber throughout the engine cycle; 4000 rpm, 8 bar BMEP, λ = 1.7.

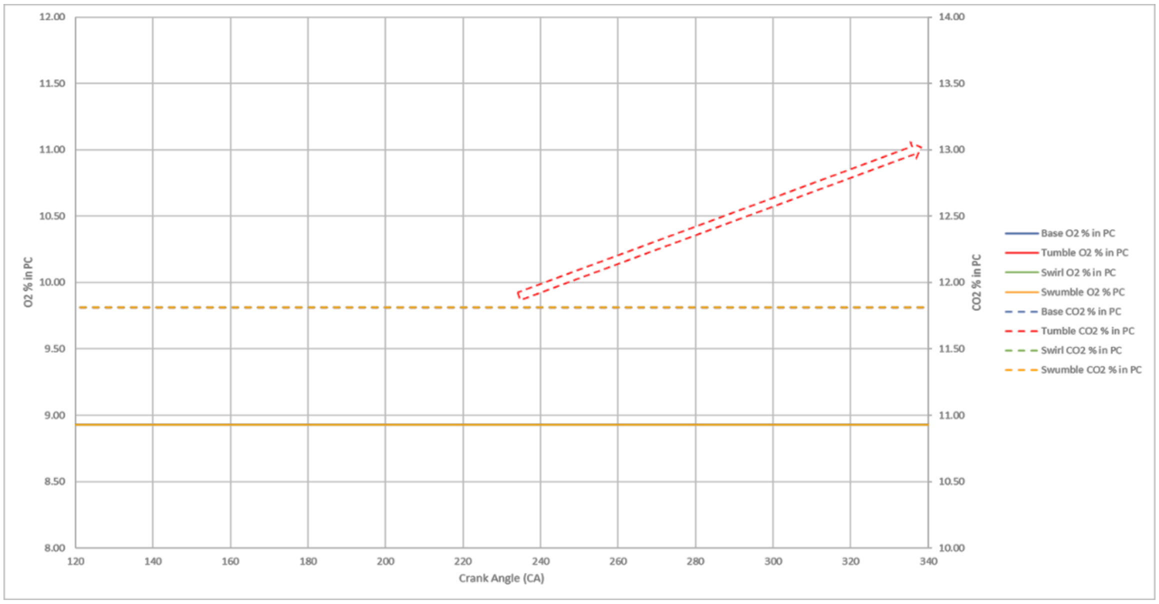

Figure 6-55: Comparison of O_2 and CO_2 mass % in the pre-chamber from EVO to IVO; 4000 rpm, 8 bar BMEP, λ = 1.7.

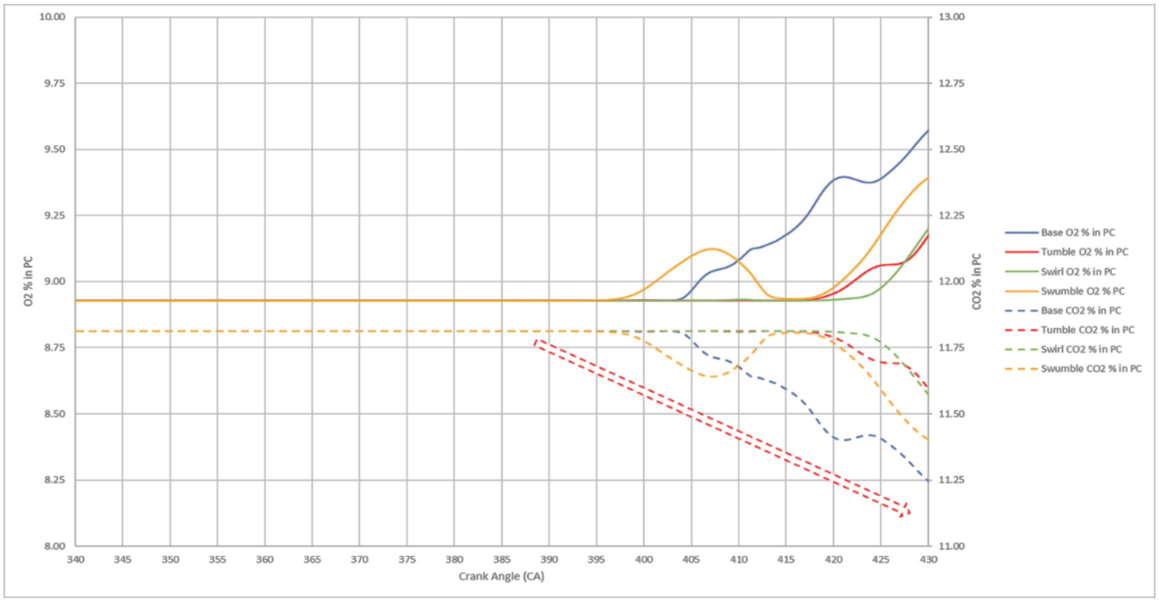

Figure 6-56: Comparison of O_2 and CO_2 mass % in the pre-chamber from IVO to EVC; 4000 rpm, 8 bar BMEP, λ = 1.7.

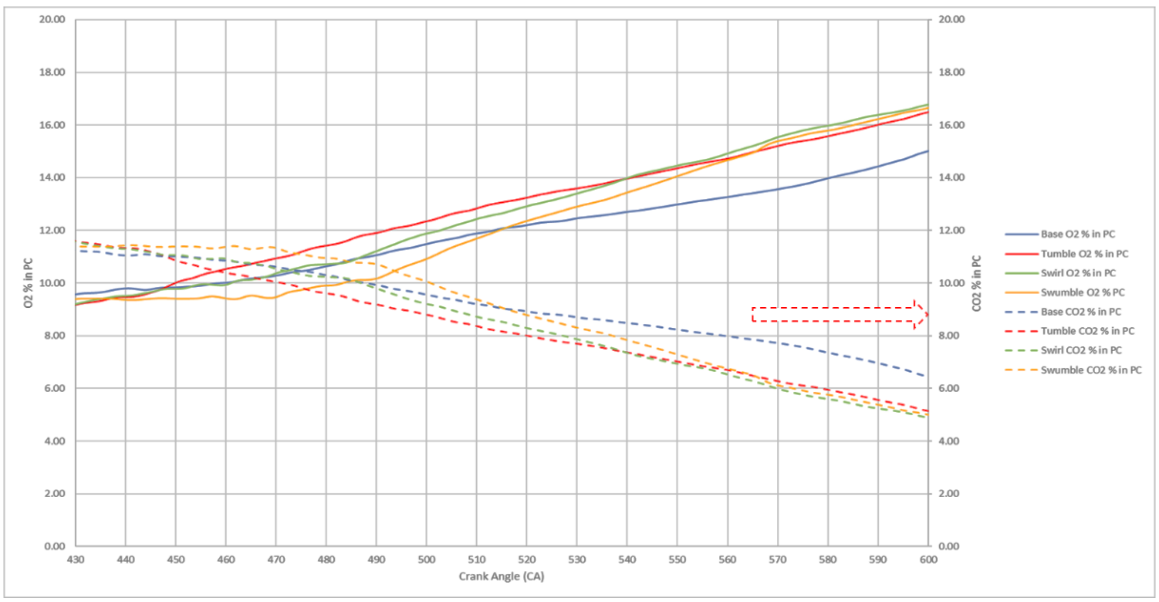

Figure 6-57: Comparison of O_2 and CO_2 mass % in the pre-chamber from EVC to IVC; 4000 rpm, 8 bar BMEP, λ = 1.7.

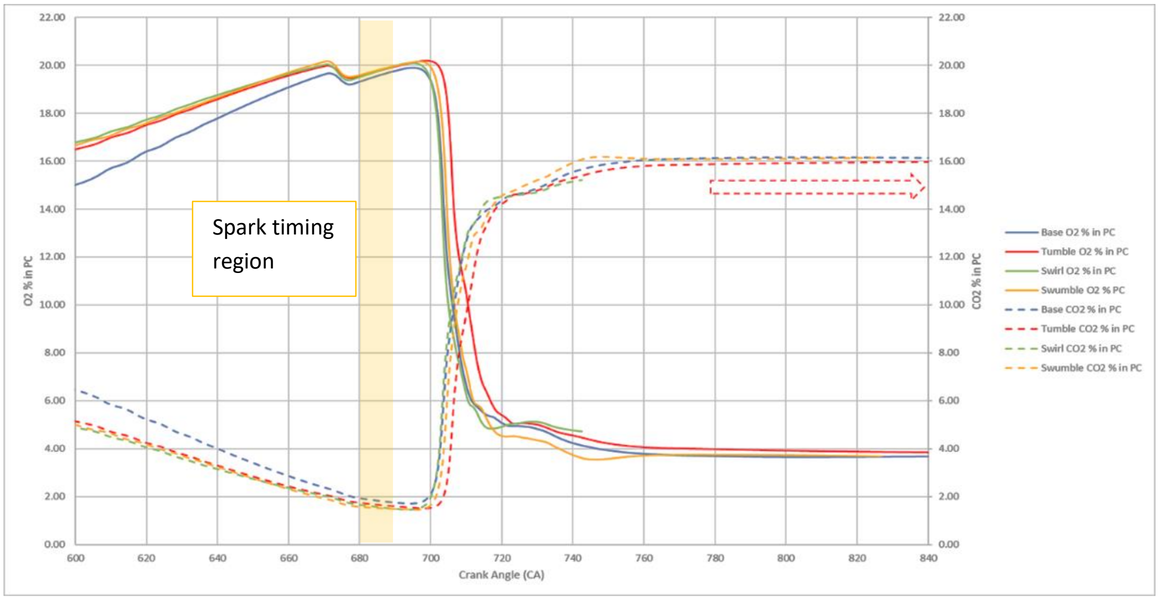

Figure 6-58: Comparison of O_2 and CO_2 mass % in the pre-chamber from IVC to EVO; 4000 rpm, 8 bar BMEP, λ = 1.7.

The charge motion variants induce different pre-chamber filling dynamics occurring midway through the period between IVO and EVC. In this period some fresh charge enters the pre-chamber to replace a portion of the residual gases that otherwise fill it completely. The baseline variant displays the highest degree of gas exchange amongst the charge motion variants in this period. However, this advantage is erased in the period between EVC and IVC, where the other three charge motion variants produce a higher rate of gas exchange in the pre-chamber, and O_2 mass fraction increases linearly throughout the rest of this period. After IVC and during the compression stroke, this advantage is maintained. The incoming lean charge of the contents transferred from the main chamber continue to add O_2 and displace or dilute residual gases in the pre-chamber. This general behavior can be leveraged to offer an advantage under certain conditions, where later spark timings enable higher O_2 mass fractions in the pre-chamber. From the results shown in Figs. 6-57 and 6-58, it is clear that introducing specific levels and types of charge motion can minutely impact pre-chamber scavenging, but the effect is not significant.

With the minor scavenging sensitivity to charge motion and relative parity amongst the pre-chamber fuel-air mixing global metrics understood, it is now prudent to examine how in-pre-chamber charge motion affects mixture stratification at spark timing in each of the charge motion variants. Figure 6-59 shows a cross-sectional plane of pre-chamber λ at spark timing on the left and velocity magnitude and direction on the right for the baseline variant. The counter-rotational tumble motion induced in the pre-chamber by the main chamber tumble motion is clearly visible in the velocity image, with a high velocity column carrying incoming charge up to the fuel injector face. The λ image mirrors this velocity image, with the incoming lean charge producing a lean mixture on the injector side of the pre-chamber, with minor enrichment of this column occurring near the injector phase as the incoming charge mixes with the recently injected pre-chamber auxiliary fuel. The tumble motion then carries this charge across the face of the spark plug to the opposite pre-chamber wall and then back down towards the pre-chamber nozzle.

This effect is much more prominent with the tumble variant, pictured in Fig. 6-60. In this case the velocity of the charge as it proceeds through its tumble motion structure is higher than in the baseline variant. Consequently, the barrier between the rich side of the pre-chamber and the lean side of the pre-chamber is much more pronounced than in the baseline variant. Figure 6-61 illustrates this tumble motion in the pre-chamber, as incoming charge ricochets off of the pre-chamber wall, creating tumble in the pre-chamber counter-rotational to that in the main chamber. The tumble motion carries charge up to the injector face as it mixes with the auxiliary fuel, and then carries this increasingly rich charge across the roof of the pre-chamber to the spark plug. In the case of the tumble variant, the spark plug resides in a distinctly rich λ pocket well segregated from the lean charge entering through the pre-chamber nozzle.

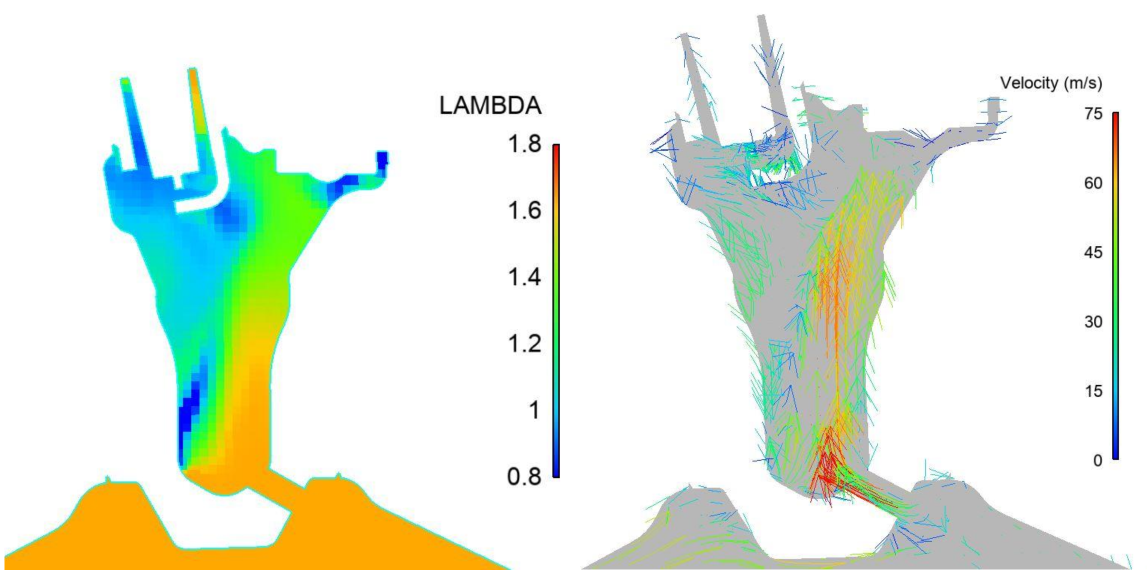

Figure 6-59: Cross-sectional view of λ (left) and velocity magnitude and direction (right) in the pre-chamber at time of spark (27 dBTDC) for the baseline variant; 4000 rpm, 8 bar BMEP, λ = 1.7.

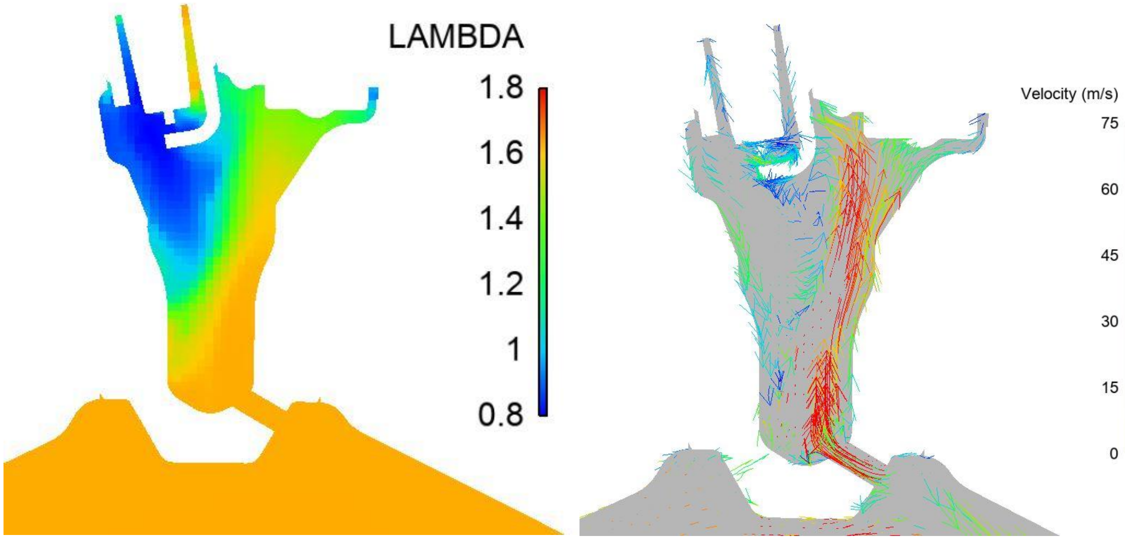

Figure 6-60: Cross-sectional view of λ (left) and velocity magnitude and direction (right) in the pre-chamber at time of spark (22 dBTDC) for the tumble variant; 4000 rpm, 8 bar BMEP, λ = 1.7.

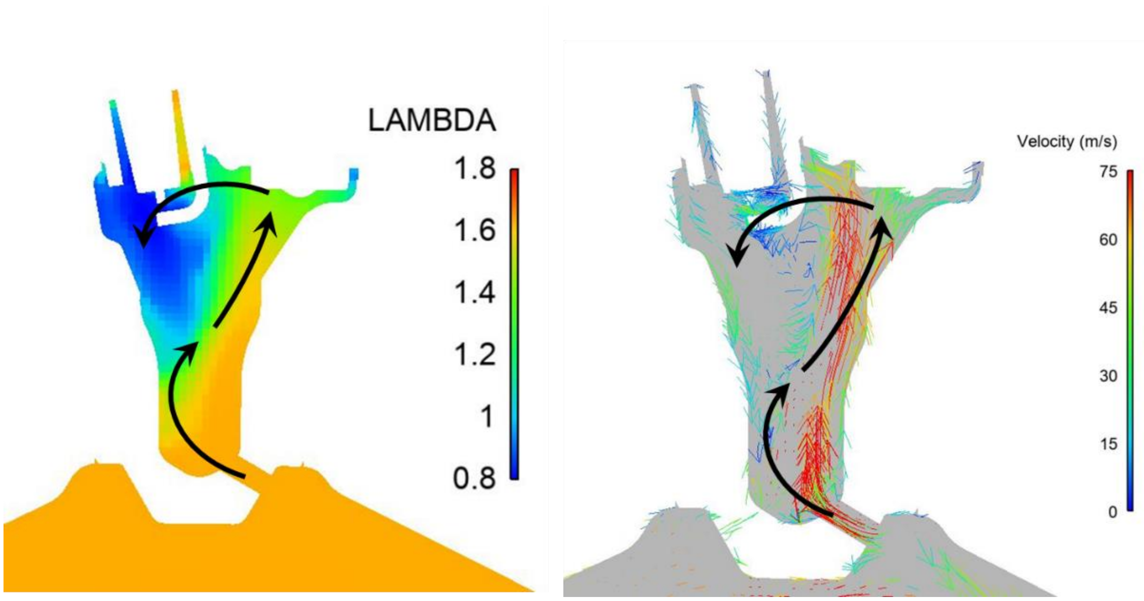

Figure 6-61: Cross-sectional view of λ (left) and velocity magnitude and direction (right) in the pre-chamber at time of spark (22 dBTDC) for the tumble variant with tumble motion annotated; 4000 rpm, 8 bar BMEP, λ = 1.7.

As was described, swirl motion in the main chamber translates to the pre-chamber in a counter-rotational direction, but the process of filling the pre-chamber during the compression stroke also induces comparatively low levels of tumble and TKE in the pre-chamber as flow is forced through the pre-chamber nozzle. Figure 6-62 demonstrates the effect that swirl and tumble motion have on λ stratification in the pre-chamber. Here the rich pocket near the spark plug witnessed in the case of the tumble variant is much more stratified, with the area near the spark plug achieving a λ value between 1.2 and 1.4 while a richer pocket sits below the spark plug near the pre-chamber nozzle. Figure 6-63 illustrates the direction of the ordered motion in the pre-chamber, with the same counter-rotational tumble motion framework as seen in the other cases, but with significantly weaker velocities. The combination of weak tumble and added swirl serves to create a mixing dynamic along the tumble-induced barrier separating the incoming lean charge from the existing rich charge. The additional of the swirl motion causes a portion of the lean charge to infiltrate the rich pocket near the spark plug. This effect is also observed in the swumble variant case in Fig. 6-64.

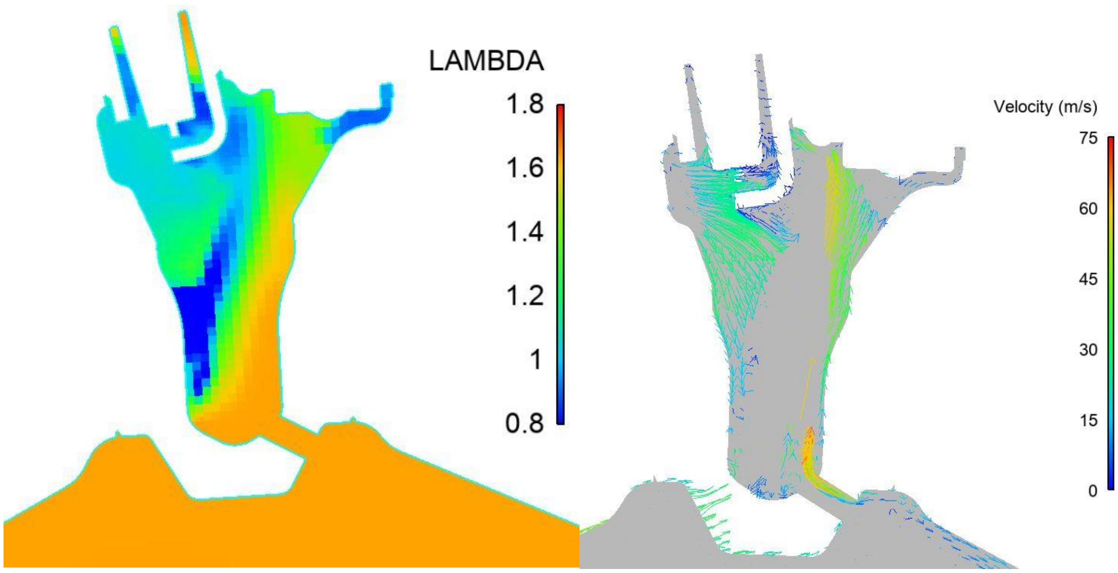

Figure 6-62: Cross-sectional view of λ (left) and velocity magnitude and direction (right) in the pre-chamber at time of spark (28 dBTDC) for the swirl variant; 4000 rpm, 8 bar BMEP, λ = 1.7.

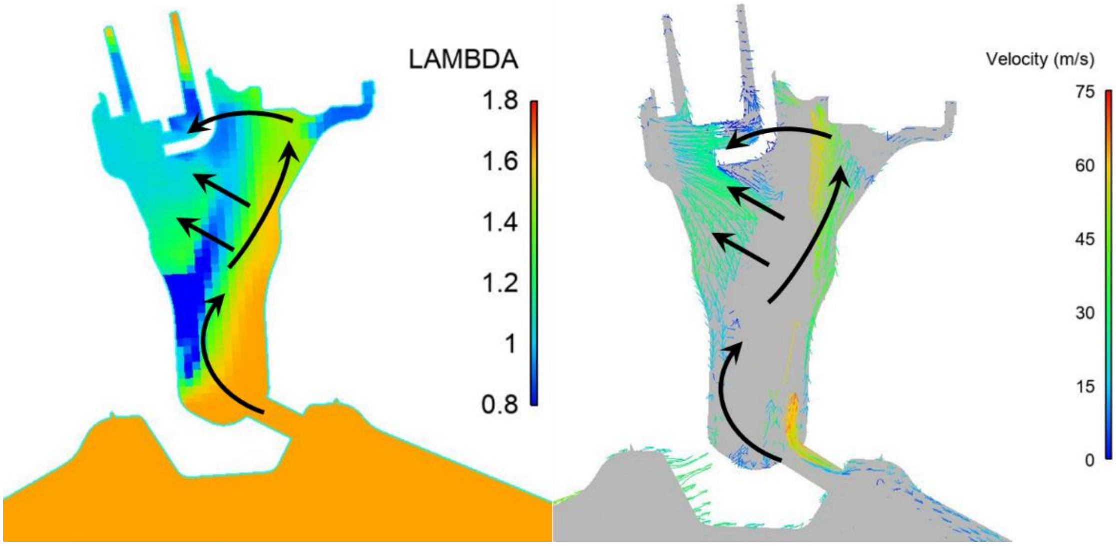

Figure 6-63: Cross-sectional view of λ (left) and velocity magnitude and direction (right) in the pre-chamber at time of spark (28 dBTDC) for the swirl variant with swirl motion annotated; 4000 rpm, 8 bar BMEP, λ = 1.7.

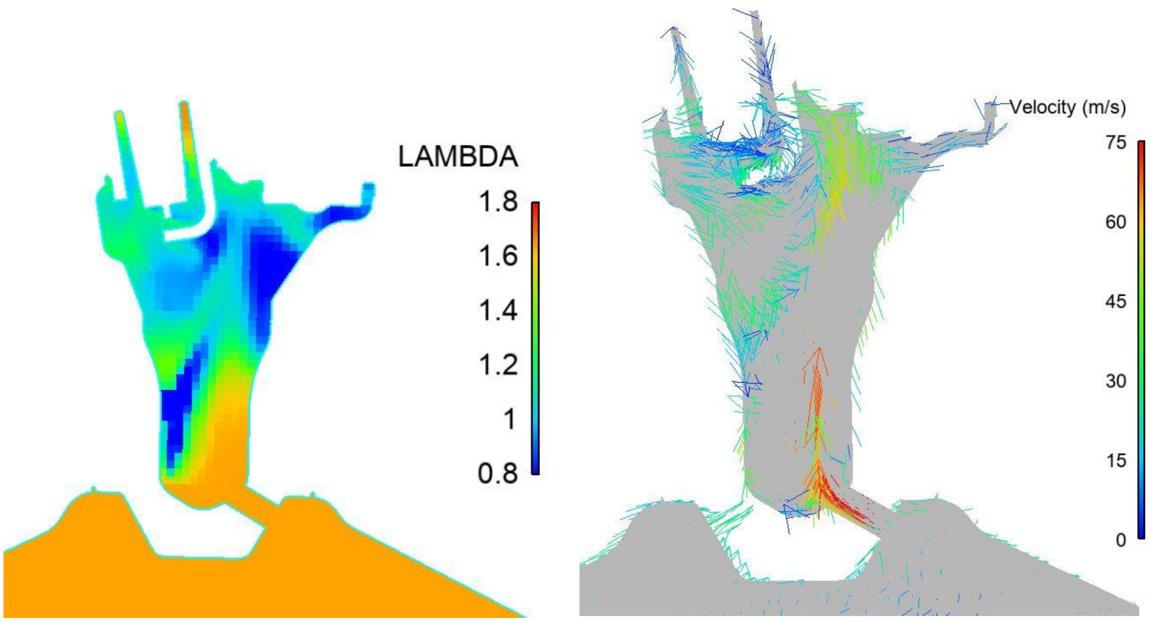

Figure 6-64: Cross-sectional view of λ (left) and velocity magnitude and direction (right) in the pre-chamber at time of spark (24 dBTDC) for the swumble variant; 4000 rpm, 8 bar BMEP, λ = 1.7.

Increasing the auxiliary fueling quantity in the pre-chamber in the swirl and swumble cases had limited effect on enriching this relatively lean pocket near the spark plug, as evidenced by the results in Fig. 6-17. The influence of the swirl motion on enleaning this fuel-air pocket near the spark plug is too dominant to compensate through pre-chamber injection strategy. Increased pre-chamber fueling quantity is also an inelegant solution to the problem as it causes significant increases in engine-out THC and CO emissions. By contrast, the tumble variant creating a relatively homogeneous λ pocket around the spark plug richer than the global pre-chamber λ enables the use of lower quantities of auxiliary fuel participating in the pre-chamber combustion event. This increases system BTE as less fuel must be sacrificed to ensure the stability of the pre-chamber combustion event. The impact of the various types of charge motion on in-pre-chamber mixture dynamics explains the pre-chamber combustion stability results as well.

The favorability of main chamber tumble motion demonstrated in this section is largely specific to the pre-chamber geometry and orientation used in this study. A 180° shift in pre-chamber indexing to the main chamber would likely result in notably inferior pre-chamber combustion stability and main chamber combustion performance, as the rich mixture created by the pre-chamber fuel injector on the opposite pre-chamber wall would be carried away by the tumble motion and transferred to the fuel injector face, leaving the spark plug to ignite a stratified near-lean mixture in the flow path of incoming lean charge. Therefore, the charge motion results presented here should be viewed in the context of complementary pre-chamber geometry and fuel injection parameters. Optimal main chamber charge motion translating to the pre-chamber will not produce optimal pre-chamber mixture preparation conditions in and of itself, but must be coupled with correct pre-chamber indexing and fuel injector spray targeting. The following section describes how the differing types of charge motion, and the mixture preparation conditions they created, contribute to the pre-chamber combustion event.

6.5.3 Pre-Chamber Combustion

Charge motion exerts an influence over the pre-chamber combustion events in two distinct ways. Firstly, the mixture preparation conditions at spark timing created by the charge motion to some extent dictate flame travel path from the spark plug to the pre-chamber nozzle. Combustion flames consume optimal proximal λ mixtures with ease while overly lean mixtures are consumed at a slower laminar burning velocity. The flame in each case therefore will likely consume the slightly rich pocket in close proximity to the spark plug first.

Secondly the charge motion itself will guide the flame travel path. Just as tumble motion in the pre-chamber creates a barrier between the incoming lean charge and the existing rich mixture, so too will the tumble motion inhibit the flame from crossing this barrier. Figure 6-65 shows a three dimensional view of the pre-chamber λ and velocity at spark timing for the baseline variant. Here the ricochet effect of the counter-rotational tumble motion in the pre-chamber is more evident than it is in the two dimensional cross-section.

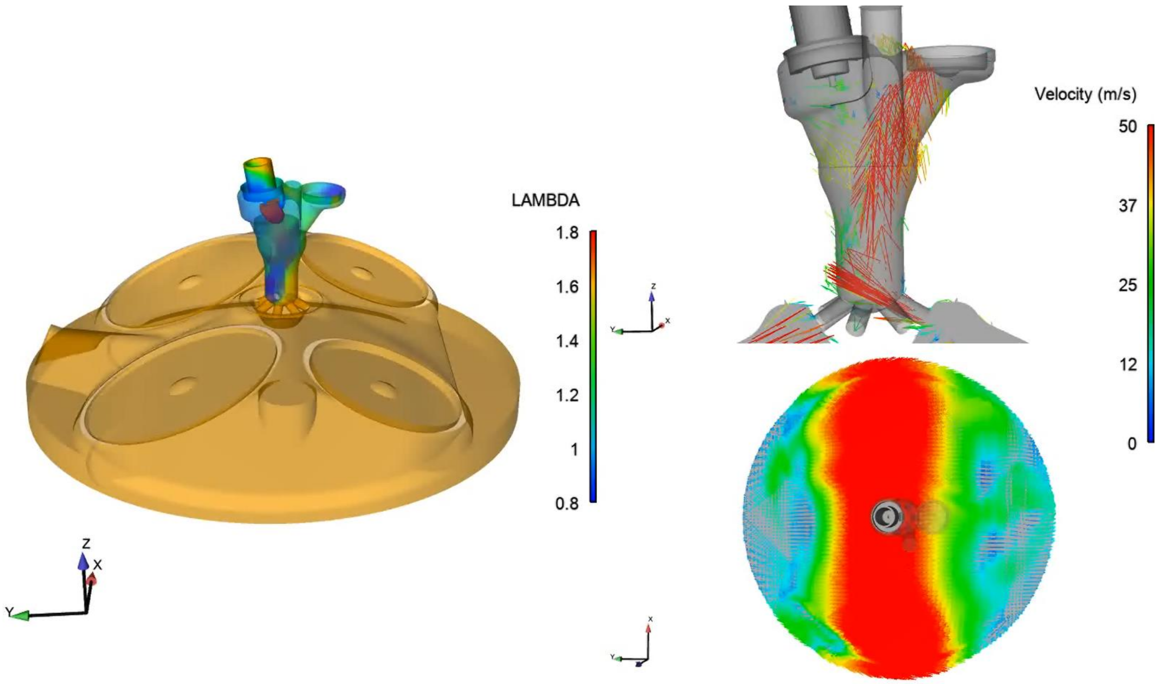

Figure 6-65: Three dimensional view of λ (left) and velocity magnitude and direction (upper right) in the pre-chamber and velocity magnitude in the main chamber (bottom right) at time of spark (27 dBTDC) for the baseline variant; 4000 rpm, 8 bar BMEP, λ = 1.7.

Similar analysis of the tumble variant (Fig. 6-66) shows the same twin effects present in the baseline variant, but in this case the rich λ pocket around the spark plug is much more defined and homogeneous, with a clear optimal λ path from the plug to the pre-chamber nozzle. The velocity magnitude of the tumble motion in the pre-chamber is also higher than it was with the baseline variant. Figure 6-67 shows the evolution of the flame in the pre-chamber 4 CAD after spark timing. The flame travel dictated both by λ and by tumble motion becomes clear, with the flame traveling down towards the pre-chamber nozzle along the “rich-side” wall, avoiding the high velocity column of lean charge moving up along the opposite wall.

Figures 6-68, 6-69, and 6-70 show continued evolution of the pre-chamber combustion flame 6, 7, and 8 CAD after spark timing, respectively. In Fig. 6-70, the flame has completed its path from the spark plug down to the pre-chamber nozzle. In this image, it is apparent that the flame has largely avoided consuming charge in the incoming lean column. Indeed the combusted mixture appears to cover the entrances to half of the pre-chamber nozzle orifices, while the other half continue to transport the lean charge from the main chamber into the pre-chamber. By the time the reactive jets emerge from the nozzle 2 CAD later (Fig. 6-71), however, jets emerge from all nozzle orifices. This is likely due to the pressure rise within the pre-chamber forcing flow through all available exits, overcoming the velocity magnitude of the incoming flow dictated only by compression pressure driven by the piston motion.

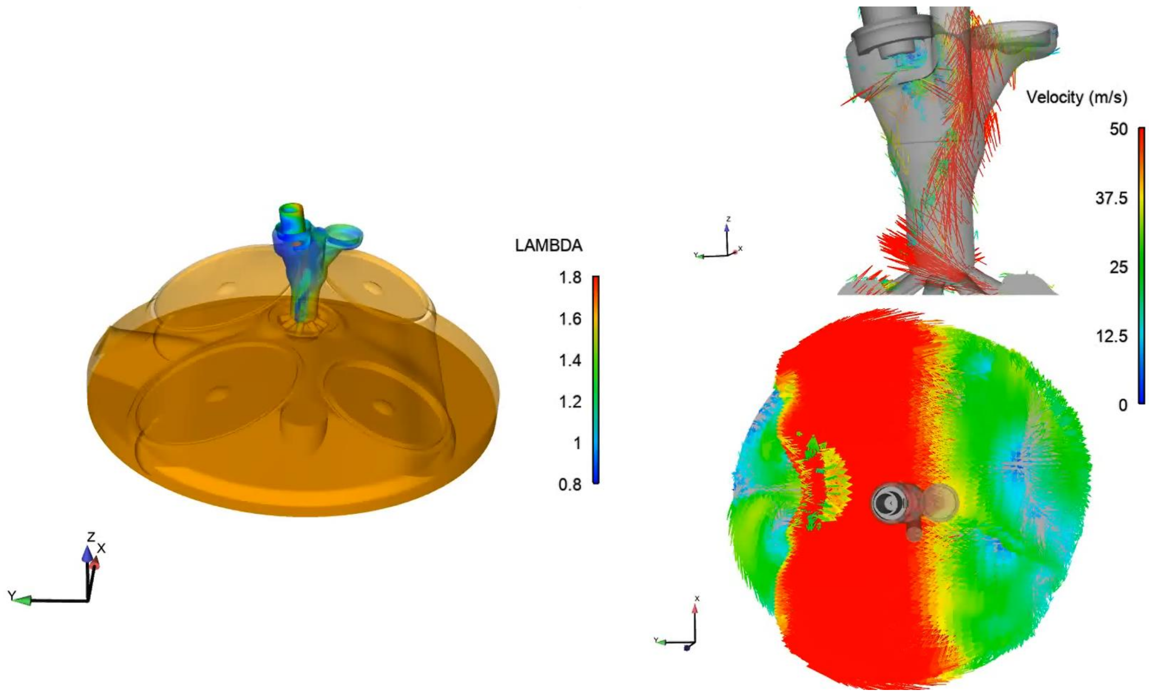

Figure 6-66: λ (left) and velocity magnitude and direction (upper right) and velocity magnitude in the main chamber (bottom right) at time of spark (22 dBTDC) for the tumble variant; 4000 rpm, 8 bar BMEP, λ = 1.7.

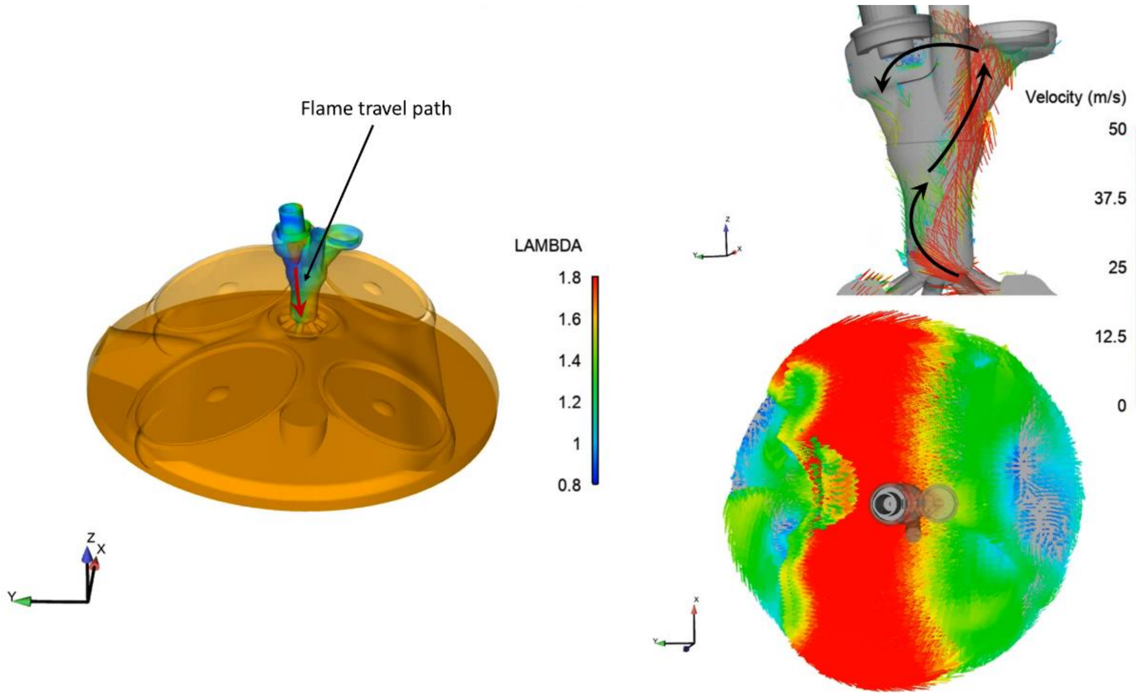

Figure 6-67: λ (left) and velocity magnitude and direction (upper right) and velocity magnitude in the main chamber (bottom right) at time of spark (18 dBTDC) for the tumble variant; 4000 rpm, 8 bar BMEP, λ = 1.7.

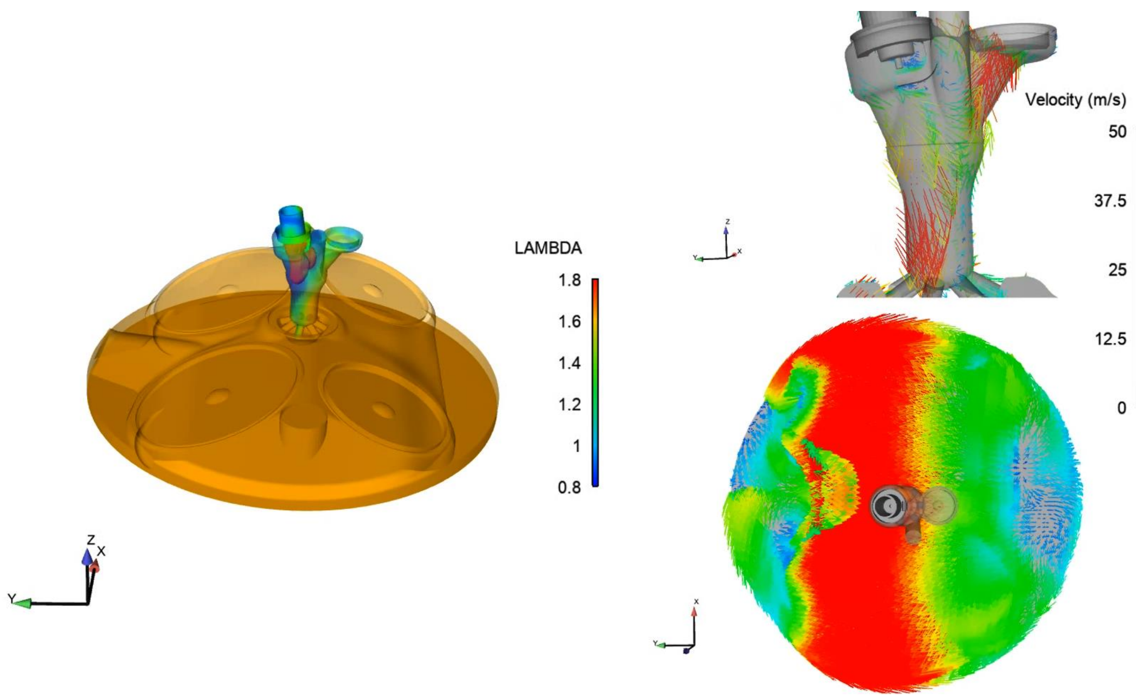

Figure 6-68: λ (left) and velocity magnitude and direction (upper right) and velocity magnitude in the main chamber (bottom right) at time of spark (16 dBTDC) for the tumble variant; 4000 rpm, 8 bar BMEP, λ = 1.7.

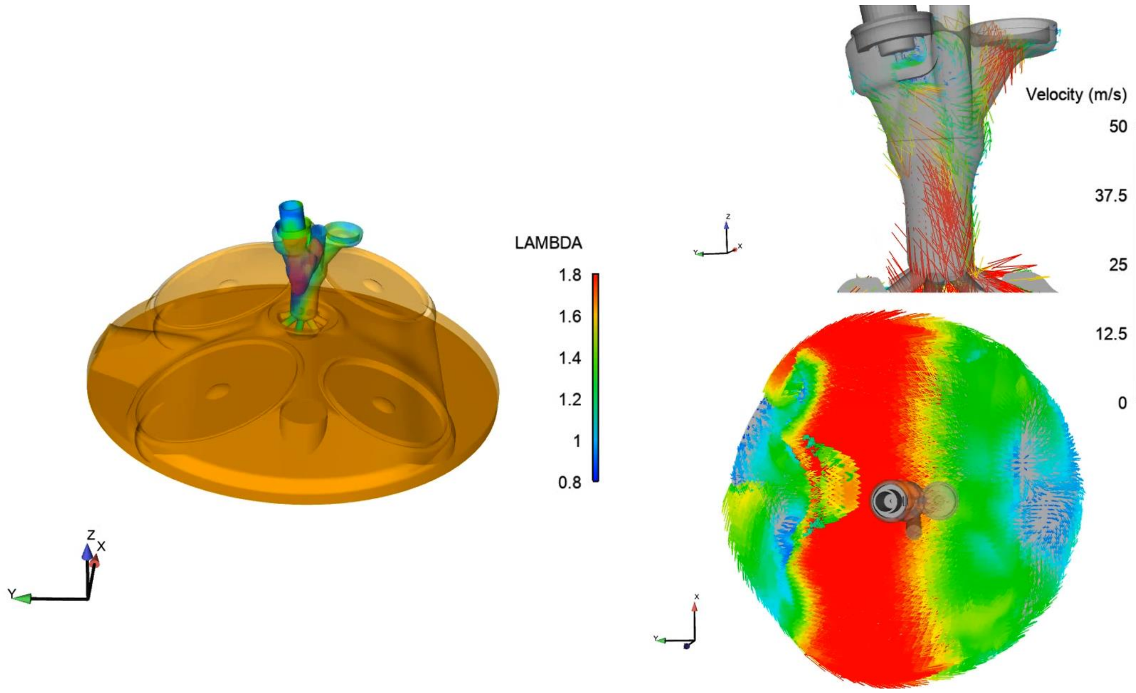

Figure 6-69: λ (left) and velocity magnitude and direction (upper right) and velocity magnitude in the main chamber (bottom right) at time of spark (15 dBTDC) for the tumble variant; 4000 rpm, 8 bar BMEP, λ = 1.7.

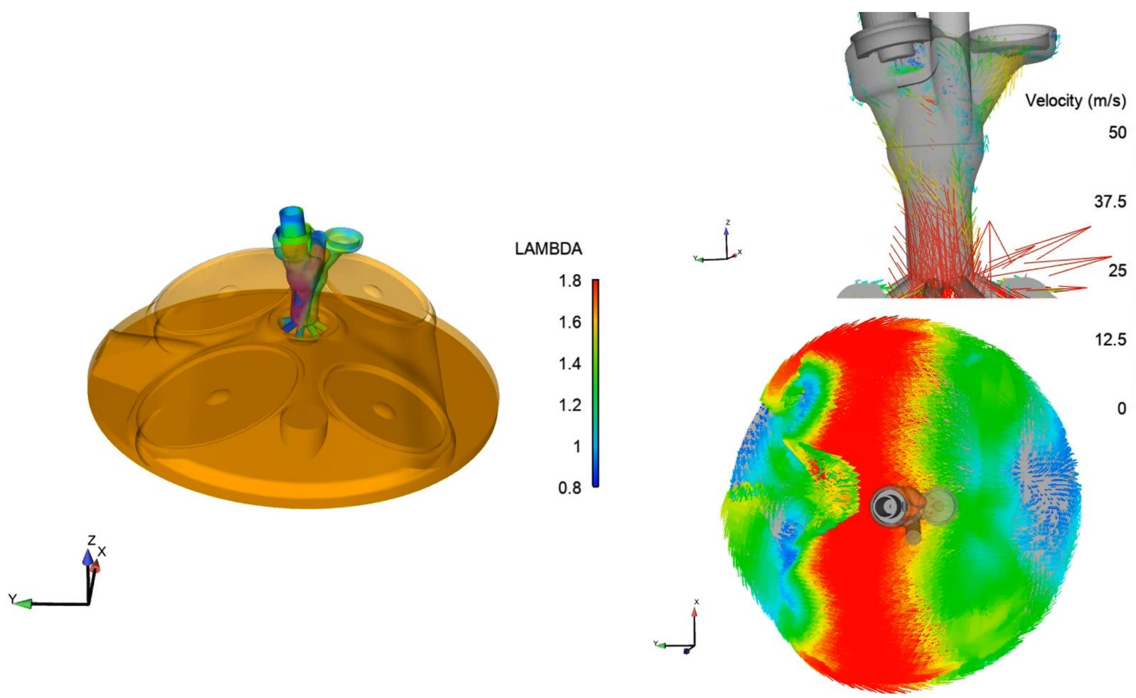

Figure 6-70: λ (left) and velocity magnitude and direction (upper right) and velocity magnitude in the main chamber (bottom right) at time of spark (14 dBTDC) for the tumble variant; 4000 rpm, 8 bar BMEP, λ = 1.7.

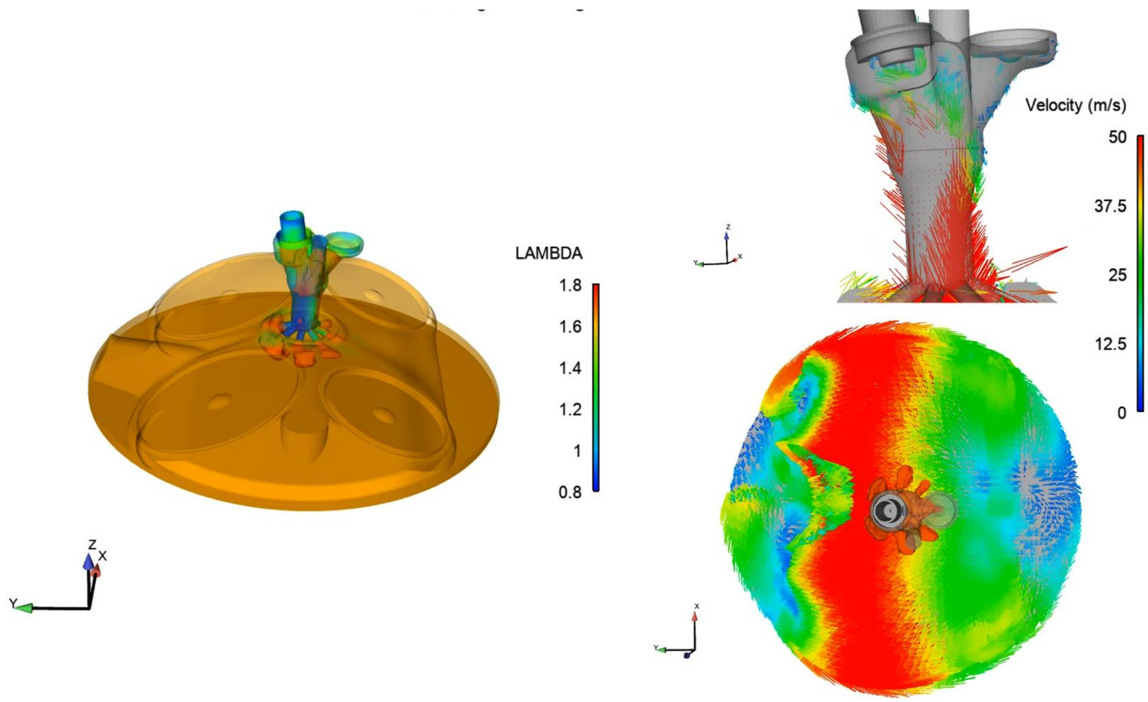

Figure 6-71: λ (left) and velocity magnitude and direction (upper right) and velocity magnitude in the main chamber (bottom right) at time of spark (12 dBTDC) for the tumble variant; 4000 rpm, 8 bar BMEP, λ = 1.7.

Figures 6-72 and 6-73 illustrate the mixture preparation and velocity conditions in the pre-chamber at spark timing for the swirl and swumble variants, respectively. As is confirmed here, the weak tumble motion and introduction of swirl in the pre-chamber reduce the integrity of the barrier between the incoming lean charge and the rich pocket near the spark plug.

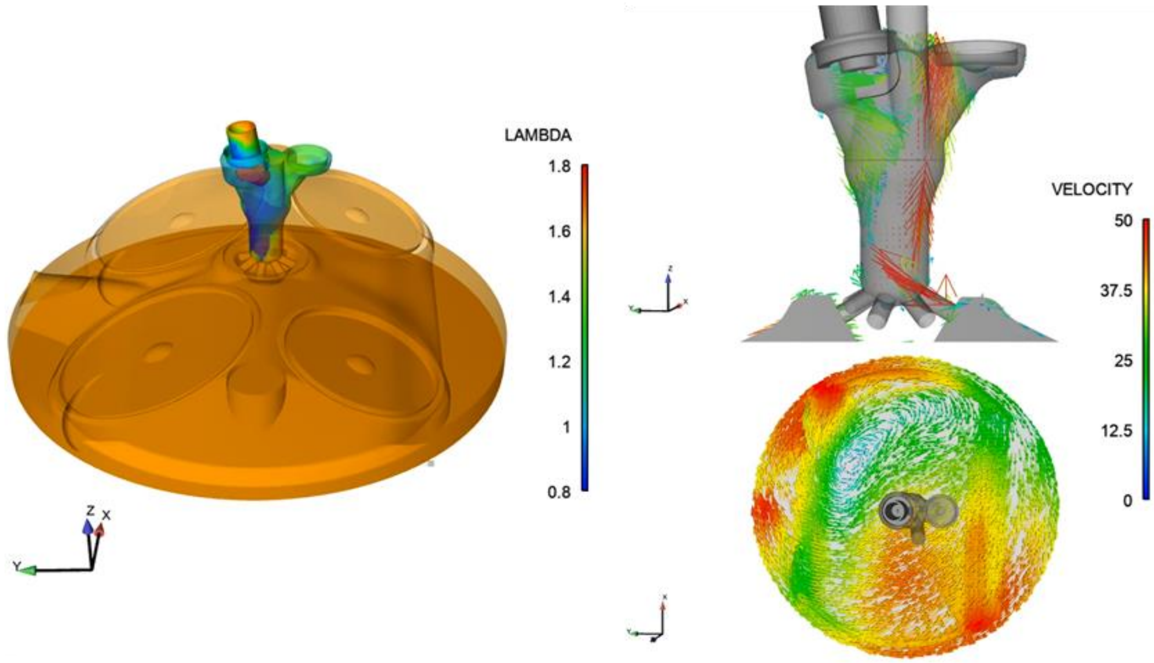

Figure 6-72: λ (left) and velocity magnitude and direction (upper right) and velocity magnitude in the main chamber (bottom right) at time of spark (28 dBTDC) for the swirl variant; 4000 rpm, 8 bar BMEP, λ = 1.7.

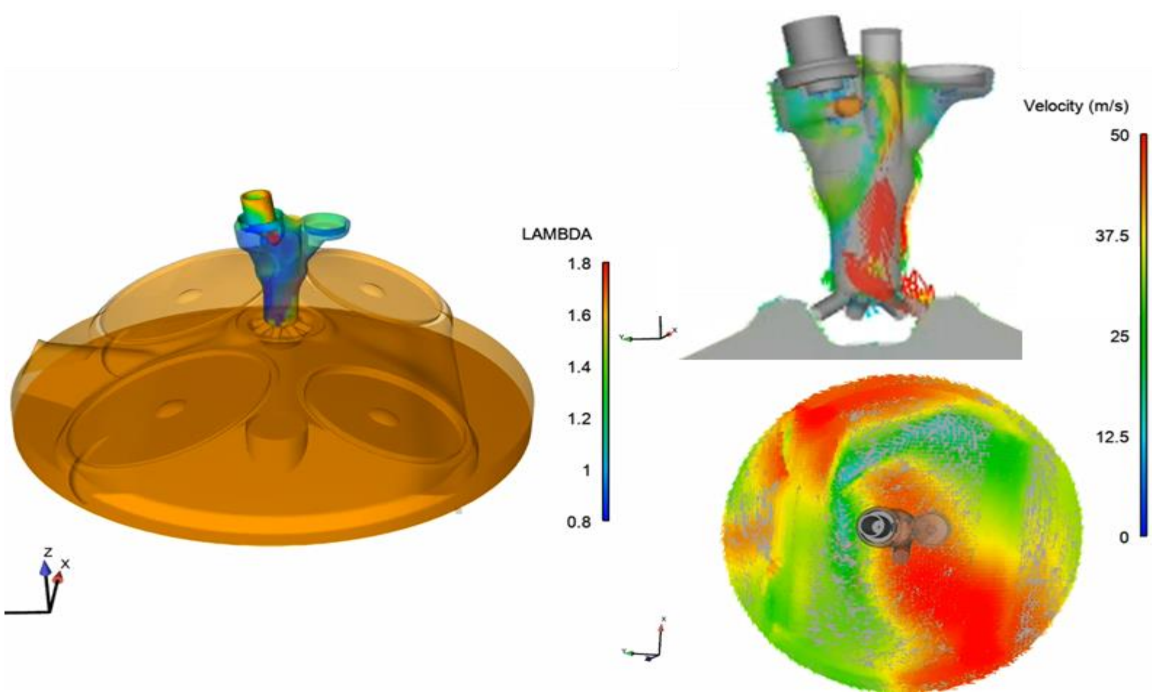

Figure 6-73: λ (left) and velocity magnitude and direction (upper right) and velocity magnitude in the main chamber (bottom right) at time of spark (24 dBTDC) for the swumble variant; 4000 rpm, 8 bar BMEP, λ = 1.7.

The spark timings for all four charge motion variants, determined by holding CA50 constant at 8 dATDC, give an indication of the practical effects of the flame travel path disparities. Figure 6-74 shows instantaneous heat release in the pre-chamber for the variants, with the tumble variant displaying a higher peak rate of heat release than the other variants despite the later phasing due to the later spark timing in this case. These results are mirrored in an examination of integrated pre-chamber heat release in Fig. 6-75. The tumble variant again demonstrates superior heat release to the other variants despite approximately the same quantity of fuel participating in the combustion event and similar global pre-chamber λ. The swirl variant exhibits the lowest integrated heat release, while the swumble variant has relatively slow heat release compared to the baseline and tumble variants.

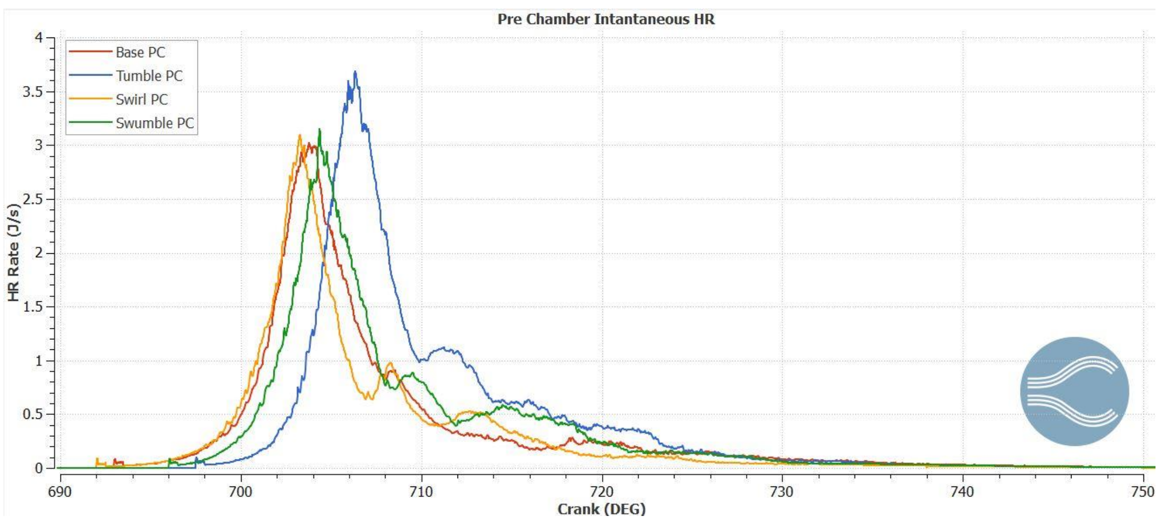

Figure 6-74: Comparison of simulation pre-chamber instantaneous heat release; 4000 rpm, 8 bar BMEP, λ = 1.7.

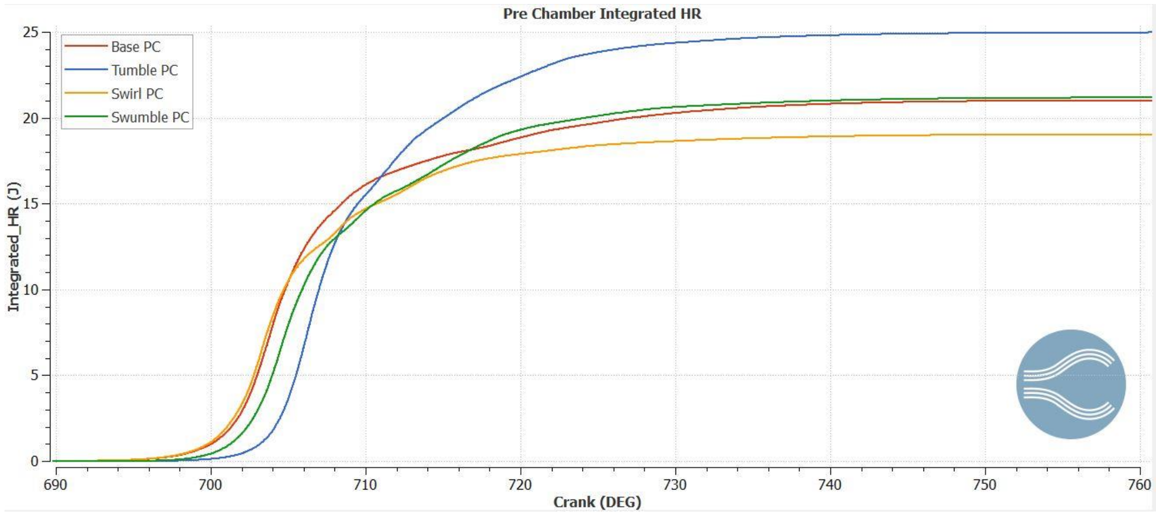

Figure 6-75: Comparison of simulation pre-chamber integrated heat release; 4000 rpm, 8 bar BMEP, λ = 1.7.

These results have implications for the reactive jet expulsion process. Figure 6-76 shows flow direction between the chambers. Positive velocity indicates flow from the main chamber into the pre-chamber, while negative velocity indicates reversal during the pre-chamber combustion process. The peak negative values represent peak average jet velocity. The duration of the negative flow is reflective of the momentum of the jet and, coupled with the velocity, is a representation of jet strength. The tumble variant displays the highest average jet velocity of 220 m/s, as was expected based on the heat release results. The baseline and swumble variants exhibit similar velocities of 200 m/s, while the swirl variant has the lowest.

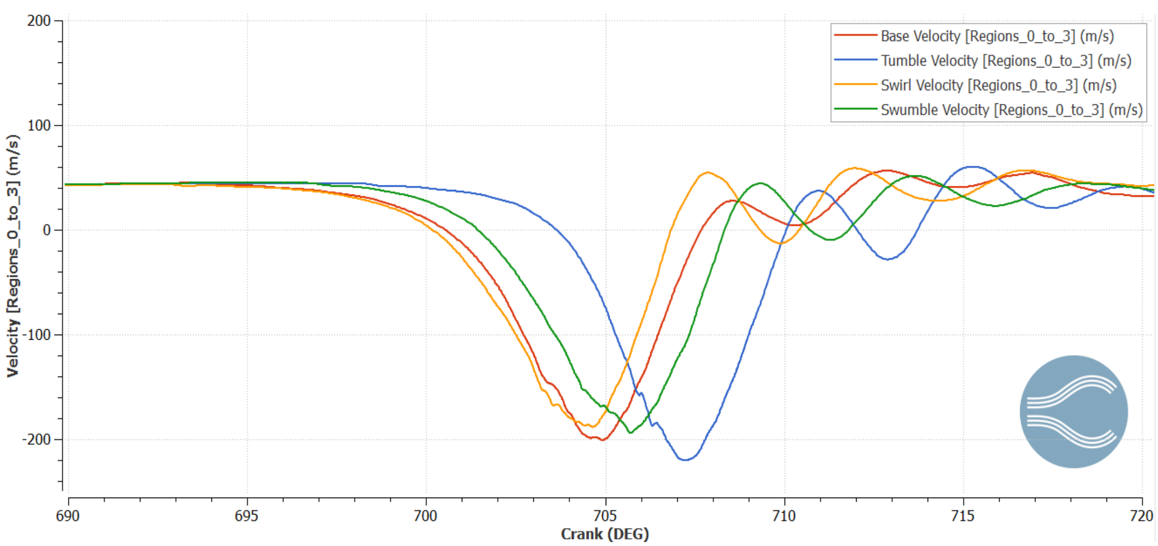

Figure 6-76: Comparison of simulation velocity of mass transfer from main chamber to pre-chamber; 4000 rpm, 8 bar BMEP, λ = 1.7.

The superior lean limit extension, pre-chamber combustion stability, combustion efficiency, and thermal efficiency of the tumble variant are explained here by an analysis of the charge motion influence on pre-chamber mixing dynamics and combustion. Even prior to understanding how the higher jet velocity impacts main chamber combustion, it is clear the tumble variant has a reduced pre-chamber fueling requirement and achieves a higher heat release with that lower fueling level than the other variants. This provides a minor BTE benefit in and of itself, as less system fuel is needed for the pre-chamber combustion event. The following section describes how these pre-chamber benefits translate to the main chamber.

6.5.4 Main Chamber Combustion

As was established in previous sections in this chapter, main chamber combustion is influenced by both pre-chamber combustion-initiated jet strength and by main chamber charge motion conditions subsequent to the jet ignition process. The latter is especially influential under ultra-lean conditions where flame speed is depressed. Figure 6-77 shows tumble in the main chamber after spark timing for each of the four charge motion variants. Tumble decreases in this region as the reducing combustion chamber volume collapses the length scales needed to maintain large scale tumble. The baseline and tumble variants have higher tumble in this region than do the swirl and swumble variants. Similarly, swirl motion reduces in this post-spark region (Fig. 6-78) but not to the same degree as does tumble. The swirl and swumble variants exhibit higher swirl number magnitudes than do the baseline and tumble variants.

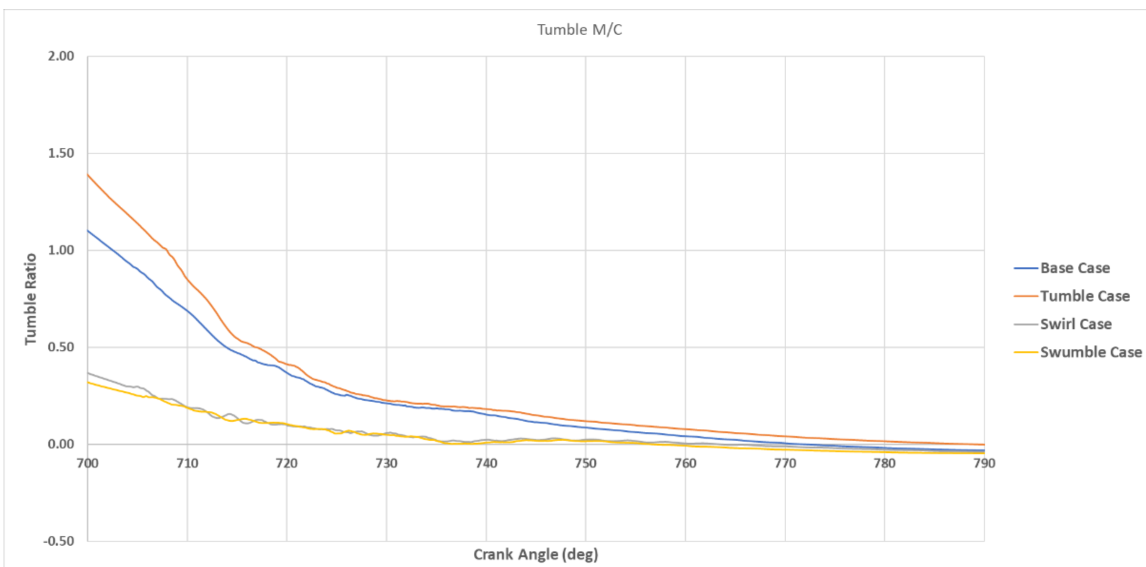

Figure 6-77: Comparison of simulation tumble ratio in the main chamber after spark timing; 4000 rpm, 8 bar BMEP, λ = 1.7.

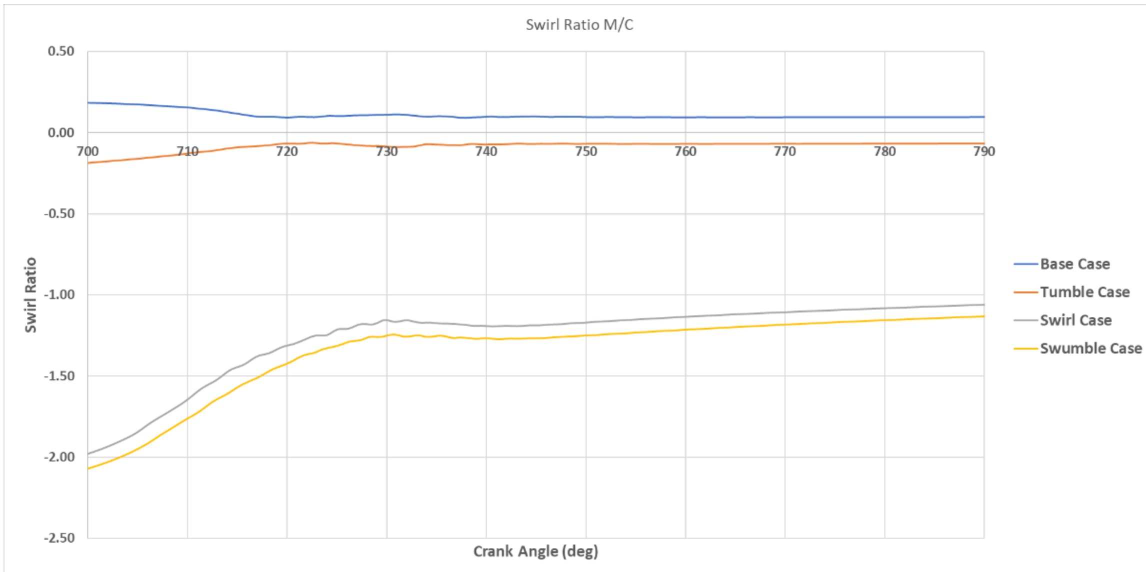

Figure 6-78: Comparison of simulation swirl number in the main chamber after spark timing; 4000 rpm, 8 bar BMEP, λ = 1.7.

TKE, shown in Fig. 6-79, reduces in the main chamber in this post-spark region. The tumble variant exhibits the highest TKE and tumble and lowest swirl in this region, a charge motion environment favorable to lean flame front propagation, especially during the late burning period.

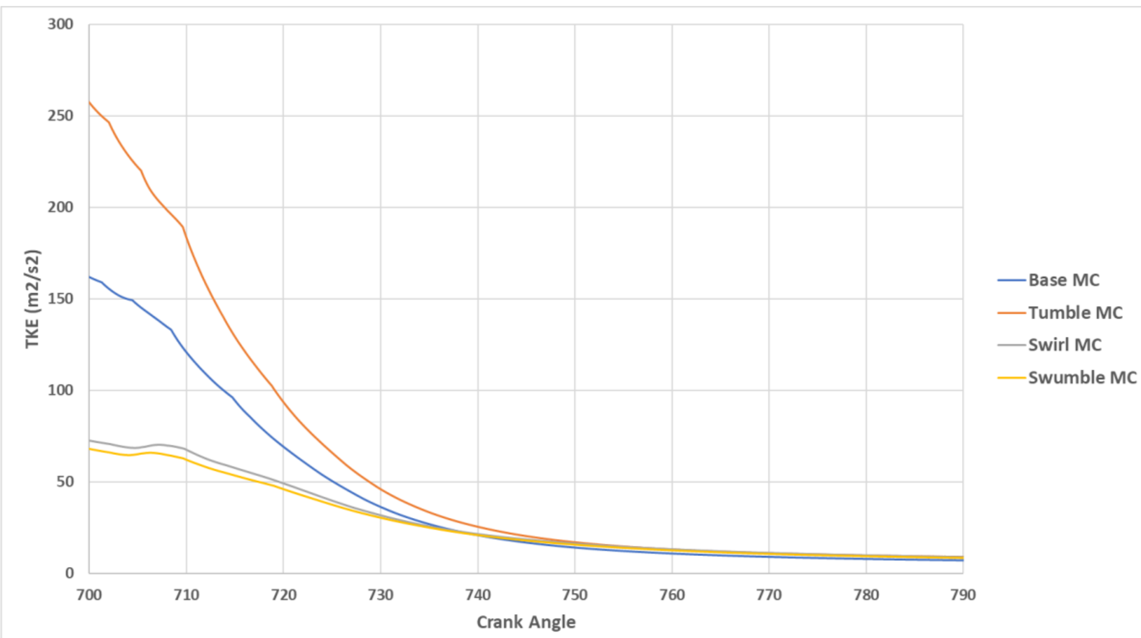

Figure 6-79: Comparison of simulation TKE in the main chamber after spark timing; 4000 rpm, 8 bar BMEP, λ = 1.7.

The instantaneous main chamber heat release results in Fig. 6-80 demonstrate a higher peak release rate with the tumble and baseline variants. In the region where baseline and tumble see spikes in heat release it is depressed for both the swirl and swumble variants. This result is reflected in the integrated heat release results (Fig. 6-81) which show a wide disparity in integrated heat release between the tumble and baseline variants and the swirl and swumble variants. Specifically, the swirl and swumble variants exhibit reduced heat release post-CA50. The tumble variant exhibits faster burning, even then the baseline variant in the period immediately preceding CA50. These qualitative results are confirmed by the burn duration comparison in Table 6-14. Simulation predicts the tumble variant to produce faster early burning (CA0-10) then the other variants. Tumble variant CA0-10 is about 15% faster than it is with the baseline variant. The tumble variant is again slightly faster than the baseline variant in the mid-burning period (CA10-50). The late burning (CA50-90) period shows an elongation with the swirl and swumble variants. Examining the full CA0-90 burn duration, simulation predicts tumble to produce the fastest burning with swirl producing the slowest. These main chamber combustion results match well with the experimental results.

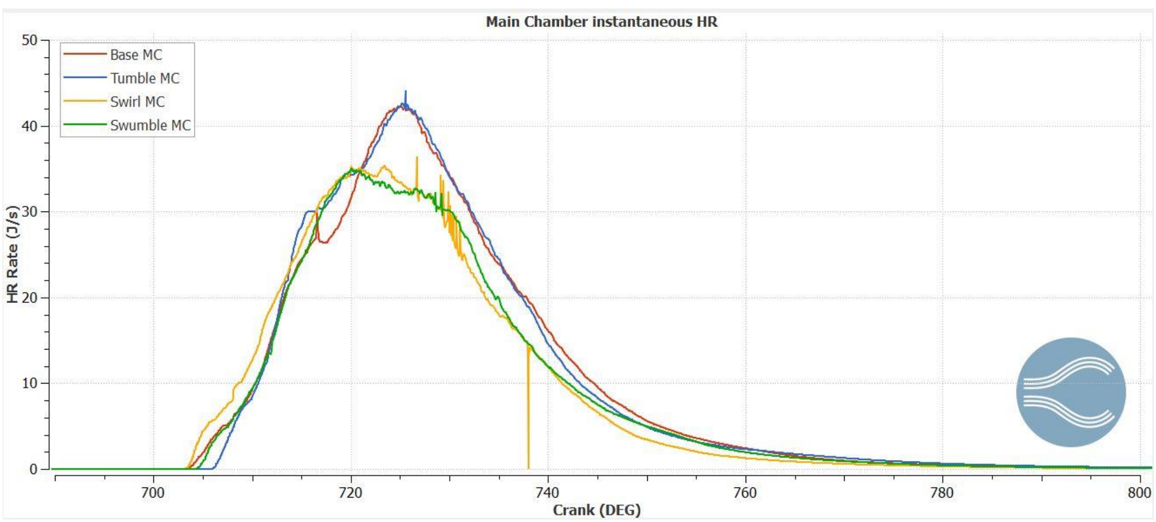

Figure 6-80: Comparison of simulation instantaneous heat release in the main chamber; 4000 rpm, 8 bar BMEP, λ = 1.7.

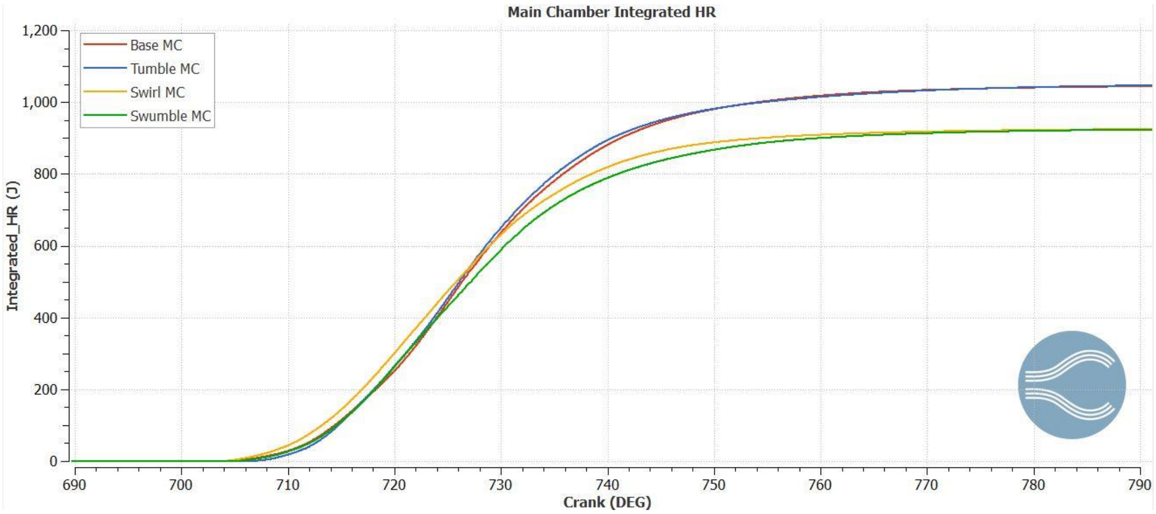

Figure 6-81: Comparison of simulation integrated heat release in the main chamber; 4000 rpm, 8 bar BMEP, λ = 1.7.

Table 6-14: Comparison of simulation burn durations; 4000 rpm, 8 bar BMEP, λ = 1.7.

	CA0-10	CA10-50	CA50-90	CA10-90	CA0-90
Base CFD	21.5	12.6	19	31.6	53.1
Tumble CFD	18	11.7	20.5	32.2	50.2
Swirl CFD	21.5	12.5	22	34.5	56
Swumble CFD	18.7	11.7	21.8	33.5	52.2

6.6 Summary

Chapter 5 demonstrated that charge motion can have an influence over engine system operation, and this influence grows as the fuel-air mixture in the main chamber becomes regressively ignitable. The data presented in Chapter 5 quantified this influence under heavily retarded spark timing conditions. This chapter focused on defining the influence of charge motion across a wide band of dilution levels in the main chamber. Experimental data was acquired at a part-load condition with no knock, a high load condition with knock limitations, a high speed condition, and a range of BMEP with the engine operating lean. The relative influence of the different charge motion types and levels was remarkably consistent across the full spectrum of experimental data. At each condition, the influence of charge motion became increasingly prominent as dilution was added to the engine and the lean stability limit of the engine was approached. The added tumble motion of the tumble variant produced superior lean limit extension, faster burn durations, and higher combustion efficiency in the ultra-lean region than the remaining charge motion variants. The ability to extend the lean limit also shifted the λ corresponding to the peak BTE or ITE leaner, depending on how the test was performed. In most cases this meant that the peak BTE or ITE was higher than with the charge motion variants whose peaks were at less lean λ values. Shifting nominal operating λ leaner enables the use of a higher CR in the engine, depending on operating strategy. Fully exploiting this benefit is beyond the scope of this study, but it does provide an opportunity to further increase BTE. Shifting the nominal operating λ leaner also reduced engine-out NO_x, providing a potential opportunity to reduce the cost and scope of the lean aftertreatment solution. While the addition of charge motion produced measurably increased in-cylinder heat losses, these were overcompensated by the reduced incomplete combustion losses with the tumble variant, proving that charge motion addition can have both a positive and negative influence over main chamber combustion.

Lean limit extension in the main chamber was correlated a metric for combustion stability in the pre-chamber during the pre-chamber combustion event. The stark differences in this stability amongst the charge motion variants proved that charge motion not only influences main chamber combustion directly, but also indirectly via influence over the pre-chamber combustion event. In order to gain insight into this influence, CFD simulation was used as an explanatory tool. Simulation results were compared to and matched with experimental results using a macro-level main chamber pressure-based correlation approach. This approach ensures acceptable matching of overall engine behavior while accommodating ill-defined complexities within the pre-chamber such as spray breakup and fuel-wall interaction that would require tremendous computational effort to properly resolve. The simulation results demonstrated a relatively robust correlation with experimental data that suited the purposes of this study.

Simulation results provided valuable insight into the dynamics of in-pre-chamber processes and how the different charge motion variants affected them. It was established that the pre-chamber itself generates weak tumble motion internally during the compression stroke even if the main chamber has little to no tumble motion. When the main chamber does have some tumble, this motion is transferred to the pre-chamber counter-rotationally. Swirl is also transferred from the main chamber to the pre-chamber, again counter-rotationally. The relative velocity of the tumble motion inside the pre-chamber has significant implications for mixture preparation. The pre-chamber experiences interaction between a rich λ pocket created by the pre-chamber injection event and the incoming ultra-lean charge from the main chamber. High velocity tumble motion inside the pre-chamber can effectively segregate these pockets and control the mixing that does occur between them. Weak tumble motion reduces the integrity of the barrier between them and swirl motion reduces it significantly further, promoting a high degree of mixing between the two regions that serves to enlean the λ pocket surrounding the spark plug.

The influence charge motion in the pre-chamber does not end with mixture preparation, but also influences pre-chamber combustion both directly and indirectly. The mixture preparation conditions driven by the in-pre-chamber charge motion to some extent dictate flame travel path and, as a result, relative flame speed as it consumes λ mixtures of varying degrees of enleanment. The motion itself also helps drive the flame from the spark plug down to the pre-chamber nozzle. The simulation results showed the flame travel path preference to avoid the incoming lean charge moving in the opposite direction. The strong tumble motion interior to the pre-chamber in the tumble variant helped produce higher heat release and faster peak average jet velocity than the other charge motion variants. The strong swirl component generated in the swirl variant created depressed pre-chamber heat release and jet velocity.

The jet strength initiated by the pre-chamber combustion event combined with the contribution of charge motion in the main chamber to combustion in the late burning period, creates a comprehensive depiction of the influence of charge motion in the active pre-chamber engine. Charge motion plays a role in pre-chamber mixture preparation, pre-chamber combustion, and main chamber combustion to varying degrees. Engines that generate relatively high levels of tumble can increase the heat release, efficiency, and stability of the pre-chamber combustion event, all of which have cascading positive effects on main chamber combustion. With the relatively modest increase in tumble presented in this study, ITE increased by 0.5-1.5 percentage points over the baseline, the lean stability limit was extended by 0-0.2 λ, combustion stability was improved, combustion efficiency was improved by 0.5-1 percentage points, and nominal λ operation was shifted leaner, all without increasing the CR and changing any other aspect of engine operation other than spark timing. These benefits have wide-ranging implications for the entire jet ignition engine system, including boost system specification and optimized CR.

The combined use of metal engine experimental data, statistical analysis of in-pre-chamber experimental data, and CFD provides insight into a comprehensive range of combustion phenomena. However, there are still elements of charge motion interaction with the jet ignition process that cannot be fully understood using this toolset. Future work in this area must utilize optical measurements from an optically-accessible engine. In particular, the tools used in this study cannot provide the fidelity needed to fully assess the impact of new different levels and types of charge motion on jet angle, degree of penetration, location of ignition site formation, main chamber flame propagation.

Chapter 7

Conclusions and Future Work

7.1 Conclusions

The primary motivation of this work was to define the influence that charge motion can have on mixing and combustion in a homogeneous highly dilute jet ignition engine. A comprehensive understanding of this influence enables selection of optimal charge motion for the jet ignition engine, leading to higher thermal efficiency and extended lean stability limit. The further extension of the lean stability limit typically provides a thermal efficiency benefit in and of itself, but also produces the potential for a further CR increase, thereby enabling further efficiency gain.

This study incorporated data from three separate but related sources. The primary source was performance and emissions data from a 1.5L 3-cylinder engine outfitted with an active jet ignition system and intake port inserts that generated differing levels and types of charge motion. A further source of data was high speed pressure measurement from the pre-chambers. This data was analyzed in order to develop a metric for pre-chamber combustion stability. The final data source was a CFD model of the 1.5L 3-cylinder active jet ignition engine, with simulation results correlated to experimental engine results. The data produced by these sources led to the following conclusions:

- Jet ignition engines generally and this study's engine specifically exhibit severe limitations for achieving adequate low load engine operation, manifesting as: misfires and high COV of IMEP under steady state low load conditions, misfire-limited spark retard capability for torque reserve at idle conditions, and misfire-limited spark retard capability for generating sufficient heat flux to warm the catalysts at CSSR conditions.
- These limitations can be addressed primarily through careful enleanment strategy.
- The introduction of increased tumble motion at the CSSR condition can increase combustion efficiency and reduce emissions by reducing late burn duration in the main chamber. The tumble motion variant produced a 1.5 percentage point improvement in combustion efficiency and a 50% reduction in engine-out NO_x+HC emissions versus the ensemble average under heavy spark retard conditions.

- The prominence of charge motion sensitivity under low-ignitability conditions translates across constant speed and constant load sweeps of λ.
- Across a wide spectrum of engine operation including part load non-knock limited, high load knock-limited, and high speed conditions, high levels of tumble consistently induced positive engine performance trends while the introduction swirl consistently induced negative performance trends. The tumble charge motion variant investigated in this study extended the lean stability limit by 0-0.2 λ versus the baseline, reduced COV over the full dilution range, improved combustion efficiency at the peak BTE λ by 0.5-1 percentage points, and increased ITE by 0.5-1.5 percentage points and BTE by at least 0.5 percentage points, all at common CR. The thermal efficiency gains represent a 1-3% increase over a baseline jet ignition engine that has already increased BTE by 20% over the baseline SI engine.
- While increased levels of charge motion resulted in higher in-cylinder heat transfer losses compared to the baseline, these losses were overcompensated by the net reduction in incomplete combustion losses under ultra-lean conditions with the tumble variant.
- Main chamber COV is most accurately predicted by the cycle-to-cycle standard deviation of chamber ΔP generated by the pre-chamber combustion event. The standard deviation of chamber ΔP is also a strong predictor of relative lean stability limit extension capability.
- For the baseline and especially the tumble variant, the tailoring of auxiliary pre-chamber fueling quantity can prevent pre-chamber combustion instability increases and even reverse it under ultra-lean conditions. Standard deviation of ΔP accurately predicted the relative ability of each charge motion variant to extend the lean limit.
- A common method for increasing pre-chamber and main chamber stability under ultra-lean conditions, increasing pre-chamber auxiliary fuel injection quantity, had only a limited effect with the swirl and swumble variants due to the influence of swirl on in-pre-chamber mixture dynamics.
- Simulations were generated that achieved macro-level main chamber pressure-based correlation with experimental engine results, providing relative and directional accuracy to help explain experimentally unobserved internal pre-chamber phenomena.
- The simulations showed that tumble motion in the main chamber does translate to the pre-chamber but counter-rotationally. Similarly, swirl can transfer from the main chamber to the pre-chamber, also counter-rotationally.

- Piston motion during the compression stroke forcing flow through the pre-chamber creates weak tumble motion in the pre-chamber even if the main chamber has negligible tumble motion.
- Swirl, tumble, and TKE have offset phasing between the main chamber and pre-chamber. The pre-chamber behaves similarly to IDI diesel swirl chambers, largely preserving the integrity of the charge motion during the compression stroke due to its fixed volume.
- The charge motion translated from the main chamber to the pre-chamber has a significant influence over mixing dynamics between the richer λ pocket in the pre-chamber created by the auxiliary fueling event and the incoming leaner charge from the main chamber. Translated tumble motion helps preserve a boundary between these two regions and creates an ordered mixing dynamic. Conversely, swirl motion in the pre-chamber provides an additional flow path for the incoming lean charge to interact with the rich pocket, compromising the integrity of the barrier between them. This dynamic allowed the baseline and especially the tumble variants to maintain a mildly rich and ignitable λ pocket around the spark plug, while the two swirl-based variants induced a leaner, less ignitable λ pocket around the spark plug.
- The mixture preparation conditions have an impact on the subsequent pre-chamber combustion event, as the flame avoids overly lean λ mixtures and consumes them slowly. Charge motion also has a direct influence over flame travel direction.
- The superior mixing dynamics and pre-chamber combustion in the tumble variant generated a peak average jet velocity of 220 m/s, approximately 10% higher than the ensemble average. This faster jet velocity resulted from a higher peak heat release rate in the pre-chamber, itself indicative a higher thermal efficiency of the pre-chamber combustion event.
- Main chamber combustion was influenced by both the jet characteristics and by the remaining motion in the chamber in the late burning phase. The tumble variant provided benefits on both ends, ultimately delivering a CA0-90 system burn duration 4-10% shorter than the other variants.

The results presented in this study confirm the benefits of increased tumble on homogeneous ultra-lean jet ignition engine operation in a variety of metrics including combustion efficiency, lean limit extension, and thermal efficiency, with a moderate increase in tumble providing a measurable BTE benefit across all relevant operating conditions.

7.2 Industry Relevance

The results of this study deepen the understanding of jet ignition engine operation, as well as provide an insight into the comprehensive influence of charge motion on mixing and combustion in homogeneous ultra-lean jet ignition engines. This study emphasized the importance of jet ignition applicability across the full engine map and quantified the low load limitations. An effective strategy for utilizing the additional flexibility offered by active jet ignition to address these limitations was demonstrated. And a roadmap for charge motion optimization to improve numerous engine performance metrics was provided.

The potential poor performance of swirl-based jet ignition combustion chambers should prove useful in the development of heavy duty natural gas applications. These engines tend to use diesel engine platforms as bases, with flat combustion chambers that generate high levels of swirl. In order to minimize the negative influence that swirl can have on pre-chamber mixing dynamics and pre-chamber combustion, steps must be taken to accommodate or manipulate the translation of main chamber swirl to pre-chamber swirl. Mitigation strategies include alternate pre-chamber geometry, alternate pre-chamber fuel injector location or spray pattern, and asymmetric pre-chamber nozzle geometry to induce stronger tumble motion and manipulate the level of swirl that can translate into the pre-chamber.

7.3 Recommendations for Future Work

As was established, the relative positive and negative impacts of differing levels and types of charge motion on pre-chamber mixing and combustion are somewhat specific to the pre-chamber geometry configuration used in this study. It would be instructive to understand how pre-chamber indexing and alternate geometries change the degree of this charge motion influence. This work could underpin the development of optimal pre-chamber geometries and auxiliary fuel injection strategies to match base engine charge motion, or at least establish its potential. Developing a jet ignition variant of an engine like the diesel-based natural gas engine described in the previous section may not afford the opportunity to adjust intake and combustion chamber design to reduce swirl and introduce tumble. In this case, it is instructive to understand if pre-chamber-based solutions could create the same effect by mitigating the translation of swirl to the pre-chamber and increasing the in-pre-chamber tumble generation. Ultimately a matrix of pre-chamber solutions required for each base engine charge motion level and type would provide engineers the ability to rapidly develop jet ignition engines with predictable performance output.

While this study examined four different type and level charge motion combinations, precise optimal tumble level for this engine, for instance, was not determined. A parametric study performed in CFD, underpinned by further experiments, is needed to identify precise optimal tumble ratio. Additionally, there are several ways to generate tumble, with varying levels of associated PMEP penalty. These should be explored in the context of this parametric study. Tumble can also be induced via active tumble flaps in the intake. The purpose of this technology is to vary the degree of tumble at different engine speeds and loads to respond to the fuel-air mixing needs in DI engines. It can be repurposed here to modulate the level of tumble in the jet ignition engine at different speeds, loads, and λ values in order to meet the pre-chamber mixture preparation needs without overly increasing in-cylinder heat transfer losses in the main chamber.

The CFD simulation tool used in this study satisfied the requirements for its stated use, but increasing CFD fidelity could substantially increase the value of the results. For this study, as in most work in this field, in-pre-chamber processes remain shielded from experimental observation. The CFD model therefore cannot be declared to accurately capture in-pre-chamber behavior, except, as in this study, in a comparative manner. In-pre-chamber optical diagnostics are necessary to capture pre-chamber mixing dynamics which, as this study proves, are highly prone to charge motion variations. Additionally, it is unclear if the simulation is accurately capturing the spray-wall interaction induced by the auxiliary pre-chamber fueling event. Optically observing this event and translating its behavior into the CFD model would substantially increase model validity and allow for multitude of optimization pathways including further charge motion refinement, injector spray pattern, pre-chamber wall geometry, and fuel injection parameters.

Finally, a full system-level optimization approach should be undertaken based on the results presented in this study. Shifting nominal peak BTE λ leaner, as the tumble variant did in this study, can enable the use of a higher CR as knock is mitigated further with shifts in nominal λ levels. The exact level of CR improvement potential was not explored in this study, but increasing CR even slightly above the value used here should increase BTE and likely also combustion efficiency. It could even provide a further minor shift in peak BTE λ to a leaner value and extend the lean limit. The addition of tumble motion provides lean limit extension benefits that could be leveraged differently in other industries, such as in the small engine segment where it might be leveraged to induce further emissions reduction rather than efficiency gain.

List of references

1) Yugo, M., Shafiei, E., Ellingsen, L., Rogerson, J., “Concawe’s Transport and Fuel Outlook Towards EU 2030 Climate Targets,” Concawe, Brussels, April 2021.
2) Van der Slot, A., Schlick, T., Pfeiffer, W., Baum, M., “Integrated Fuels and Vehicles Roadmap to 2030+,” Roland Berger GmbH, April 2016.
3) Bunce, M. and Blaxill, H., "Sub-200 g/kWh BSFC on a Light Duty Gasoline Engine," SAE Technical Paper 2016-01-0709, 2016.
4) Bunce, M., Blaxill, H., Kulatilaka, W., and Jiang, N., "The Effects of Turbulent Jet Characteristics on Engine Performance Using a Pre-Chamber Combustor," SAE Technical Paper 2014-01-1195, 2014.
5) Quader, A. A., “Lean Combustion and the Misfire Limit,” SAE Technical Paper 741055, 1974.
6) Yamamoto, H., “Investigation on Relationship Between Thermal Efficiency and NOx Formation in Ultra-Lean Combustion,” SAE Journal Paper JSAE 9938083, 1999.
7) Husted, H., Piock, W., Ramsay, G., “Fuel Efficiency Improvements from Lean Stratified Combustion with a Solenoid Injector,” SAE Technical Paper 2009-01-1485, 2009.
8) Germane, G., Wood, C., Hess, C., “Lean Combustion in Spark-Ignited Internal Combustion Engines – A Review,” SAE Technical Paper 831694, 1983.
9) Heywood, J., Internal Combustion Engine Fundamentals, McGraw-Hill, 1988.
10) Attard, W., Toulson, E., Fraser, E., Parsons, P., “A Turbulent Jet Ignition Pre-Chamber Combustion System for Large Fuel Economy Improvements in a Modern Vehicle Powertrain,” SAE Technical Paper 2010-01-1457, 2010.
11) Biswas, S., Tanvir, S., Wang, H., Qiao, L., “On ignition mechanisms of premixed CH4/air and H2/air using a hot turbulent jet generated by pre-chamber combustion”, Appl. Therm. Eng., 106:925-937, 2016.
12) Mastorakos, E., Allison, P., Giusti, A., De Oliveira, P., Benekos, S., Wright, Y. et al., "Fundamental Aspects of Jet Ignition for Natural Gas Engines", SAE Int. J. Engines 10(5):2429-2438, 2017.
13) Bureshaid, K., Feng, D., Zhao, H., Bunce, M., “Combustion and Emissions of Gasoline, Anhydrous Ethanol, and Wet Ethanol in an Optical Engine with a Turbulent Jet Ignition System,” *Proceedings of the Institution of Mechanical Engineers, Part D: Journal of Automobile Engineering* 233,13 (2019): 3528-3537.

14) Rodrigue, J-P., Comtois, C., Slack, B., *The Geography of Transport Systems – 2nd Edition*. New York: Routledge, 2006.
15) Environmental Protection Agency, "History of Reducing Air Pollution from Transportation in the United States," *EPA*, Accessed 2018, https://www.epa.gov/transportation-air-pollution-and-climate-change/accomplishments-and-success-air-pollution-transportation.
16) JATO, "Global Car Sales Up by 2.4% in 2017 Due to Soaring Demand in Europe, Asia-Pacific and Latin America," Press Release, 2/2018.
17) Doric, J., Klinar, I., Doric, Marko., "Constant Volume Combustion Cycle for IC Engines," FME Transactions 39, 97-104, 2011.
18) Ausserer, J., Rowton, A., Grinstead, K., Litke, P. et al., "Comparison of In-Cylinder Pressure Measurement Methods in a Small Spark Ignition Engine," SAE Technical Paper 2014-32-0007, 2014, doi:10.4271/2014-32-0007.
19) Bueno A. V., Velasquez J. A., and Milanez L. F., "Internal Combustion Engine Indicating Measurements," in Applied Measurement Systems, ed: InTech, 2012.
20) Lancaster, D., Krieger, R., and Lienesch, J., "Measurement and Analysis of Engine Pressure Data," SAE Technical Paper 750026, 1975, doi:10.4271/750026.
21) Taylor C. F., *The Internal Combustion Engine in Theory and Practice: Volume 1: Thermodynamics*, *Fluid Flow, Performance, 2nd, revised ed. Vol. 1*: First MIT Press, 1985.
22) Ferguson C. R. and Kirkpatrick A. T., *Internal Combustion Engines: Applied Thermosciences*. New York: John Wiley & Sons, Inc., 2000.
23) Naber, J., Johnson, J., "Internal Combustion Engine Cycles and Concepts," in *Alternative Fuels and Advanced Vehicle Technologies for Improved Environmental Performance*. Woodhead Publishing, 2014: Pages 197-224.
24) Stone, R., "Introduction to Internal Combustion Engines – 3rd Edition," Macmillan Press Ltd., 2002.
25) Zhao, F., Lai, M.-C., Harrington, D.L., "Automotive Spark-Ignited Direct-Injection Gasoline Engines," Progress in Energy and Combustion Science 25 (5), 2002: 437–562.
26) Oppenheim, A. K., "Combustion in Piston Engines: Technology, Evolution, Diagnosis and Control". New York: Springer, 2004.
27) Oppenheim, A.K., "Prospects for Combustion in Piston Engines," SAE Technical Paper 2002-01-0999, 2002, doi:10.4271/2002-01-0999.
28) Shudo, T., Nabetani, S., "Analysis of Degree of Constant Volume and Cooling Loss in a Hydrogen Fuelled SI Engine," SAE Technical Paper 2001-01-3561, 2001.

29) Kulzer, A., Christ, A., Rauscher, M., Sauer, C., Wurfel, G., Blank, T., “Thermodynamic Analysis and Benchmark of Various Gasoline Combustion Concepts,” SAE Technical Paper 2006-01-0231, 2006.
30) Gao, J., Wu, Y., Shen, T., “On-Line Statistical Combustion Phase Optimization and Control of SI Gasoline Engines,” Applied Thermal Engineering, Volume 112, 2017: Pages 1396-1407.
31) Zhang, Y., Shen, T., “Model Based Combustion Phase Optimization in SI Engines: Variational Analysis and Spark Advance Determination,” IFAC, Volume 49, Issue 11, 2016: Pages 679-684.
32) Zhao, F., Lai, M-C., Harrington, D., “A Review of Mixture Preparation and Combustion Control Strategies for Spark-Ignited Direct-Injection Gasoline Engines,” SAE Technical Paper 1997-02-24, 1997.
33) An, Y., Jaasim, M., Vallinayagam, R., Vedharaj, S., Im, H., Johansson, B., “Numerical Simulation of Combustion and Soot Under Partially Premixed Combustion of Low-Octane Gasoline,” Fuel, Volume 211, 2018: Pages 420-431,
34) Gatts, T., Liu, S., Liew, C., Ralston, B., Bell, C., Li, H., “An Experimental Investigation of Incomplete Combustion of Gaseous Fuels of a Heavy-Duty Diesel Engine Supplemented with Hydrogen and Natural Gas,” International Journal of Hydrogen Energy, Volume 37, Issue 9, 2012: Pages 7848-7859.
35) Zhao, J., Li, Y., Xu, F., “The Effects of the Engine Design and Operation Parameters on the Performance of an Atkinson Engine Considering Heat-Transfer, Friction, Combustion Efficiency and Variable Specific-Heat,” Energy Conversion and Management, Volume 151, 2017: Pages 11-22.
36) Sauer, C., Kulzer, A., Rauscher, M., Hettinger, A., “Analysis of Different Gasoline Combustion Concepts with Focus on Gas Exchange,” SAE Technical Paper 2008-01-0427, 2008.
37) Mattson, J., Depcik, C., “First and Second Law Heat Release Analysis in a Single Cylinder Engine,” SAE Technical Paper 2016-01-0559, 2016.
38) Farrell, J., Stevens, J., Weissman, W., “A Second Law Analysis of High Efficiency Low Emission Gasoline Engine Concepts,” SAE Technical Paper 2006-01-0491, 2006.
39) Rakopoulos, C., Giakoumis, E., “Second-Law Analyses Applied to Internal Combustion Engines Operation,” Progress in Energy and Combustion Science, Volume 32, Issue 1, 2006: Pages 2-47.
40) Singh, A., Wadhwani, D., Sharma, P., Rai, V., Sharma, V., “Technology to Achieve Engine Efficacy: Friction Reduction,” SAE Technical Paper 2018-01-0983, 2018.

41) Mabuchi, Y., Hamada, T., Kano, M., Yasuda, Y., Ariga, K., “Diamond-Like Carbon Coating for Reducing Valvetrain Friction,” SAE Technical Paper 2004-05-0188, 2004.
42) Wang, Z., Liu, H., Reitz, R., “Knocking Combustion in Spark-Ignition Engines,” Progress in Energy and Combustion Science, Vol 61, 2017, Pg. 78-112.
43) Turner, J., Pearson, R., Curtis, R., Holland, B., “Improving Fuel Economy in a Turbocharged DISI Engine Already Employing Integrated Exhaust Manifold Technology and Variable Valve Timing,” SAE Technical Paper 2008-01-2449, 2008.
44) Calabretta, M., Cacciatore, D., Carden, P., “Valvetrain Friction - Modeling, Analysis and Measurement of a High Performance Engine Valvetrain System,” SAE Technical Paper 2010-01-1492, 2010.
45) Xin, Q., Zheng, J., “Theoretical Analysis of Internal Combustion Engine Miscellaneous Heat Losses,” SAE Technical Paper 2009-01-2881, 2009.
46) Bassett, M., Hall, J., Hibberd, B., Borman, S. et al., "Heavily Downsized Gasoline Demonstrator," SAE Int. J. Engines 9(2):2016, doi:10.4271/2016-01-0663.
47) Stanton, D., “Systematic Development of Highly Efficient and Clean Engines to Meet Future Commercial Vehicle Greenhouse Gas Regulations,” SAE Technical Paper 2013-01-2421, 2013.
48) Zhou, F., Dede, E., and Joshi, S., "Application of Rankine Cycle to Passenger Vehicle Waste Heat Recovery - A Review," SAE Int. J. Mater. Manf. 9(2):224-235, 2016, https://doi.org/10.4271/2016-01-0178.
49) Dimopoulos, P., Rechsteiner, C., Soltic, P., Laemmle, C., Boulouchos, K., “Increase of Passenger Car Engine Efficiency with Low Engine-Out Emissions Using Hydrogen-Natural Gas Mixtures: A Thermodynamic Analysis,” Intl. J. of Hydrogen Energy 32, 2007, Pg. 3073-3083.
50) Sevik, J., Pamminger, M., Wallner, T., Scarcelli, R. et al., "Performance, Efficiency and Emissions Assessment of Natural Gas Direct Injection compared to Gasoline and Natural Gas Port-Fuel Injection in an Automotive Engine," SAE Int. J. Engines 9(2):2016, doi:10.4271/2016-01-0806.
51) Drake, M., Hawotrh, D., “Advanced Gasoline Engine Development Using Optical Diagnostics and Numerical Modeling,” Proceedings of the Combustion Institute, 31, 2007, Pg. 99–124.
52) Alkidas, A., Tahry, “Contributors to the Fuel Economy Advantage of DISI Engines over PFI Engines,” SAE Technical Paper 2003-01-3101, 2003.
53) Chincholkar, S., Suryawanshi, J., “Gasoline Direct Injection: An Efficient Technology,” Energy Procedia, Volume 90, 2016, Pgs. 666-672.

54) Yinhui, W., Rong, Z., Yanhong, Q., Jianfei, P., Mengren, L., Jianrong, L., Yusheng, W., Min, H., Shijin, S., "The Impact of Fuel Compositions on the Particulate Emissions of Direct Injection Gasoline Engine," Fuel, Volume 166, 2016, Pgs. 543-552.

55) Fraser, N., Blaxill, H. "Engine Downsizing and the Application of Gasoline Direct Injection to a High Specific Output Turbocharged Engine", Fuel Economy and Engine Downsizing Seminar Proceedings, 2004.

56) Bandel, W., Fraidl, G., Kapus, P., Sikinger, H. et al., "The Turbocharged GDI Engine: Boosted Synergies for High Fuel Economy Plus Ultra-low Emission," SAE Technical Paper 2006-01-1266, 2006, doi:10.4271/2006-01-1266.

57) Hancock, D., Fraser, N., Jeremy, M., Sykes, R. et al., "A New 3 Cylinder 1.2l Advanced Downsizing Technology Demonstrator Engine," SAE Technical Paper 2008-01-0611, 2008, doi:10.4271/2008-01-0611.

58) Lumsden, G., OudeNijeweme, D., Fraser, N., and Blaxill, H., "Development of a Turbocharged Direct Injection Downsizing Demonstrator Engine," SAE Int. J. Engines 2(1):1420-1432, 2009, doi:10.4271/2009-01-1503.

59) Kasseris, E., Heywood, J., "Charge Cooling Effects on Knock Limits in SI DI Engines Using Gasoline/Ethanol Blends: Part 1 – Quantifying Charge Cooling," SAE Technical Paper 2012-01-1275, 2012.

60) Atkinson, J., "Gas Engine", 1887, US Patent No. 367496.

61) Miller, R., "Supercharged Engine", 1957, US patent No. 2817322.

62) Li, Y., Khajepour, A., Devaud, C., "Realization of Variable Otto-Atkinson Cycle Using Variable Timing Hydraulic Actuated Valve Train for Performance and Efficiency Improvements in Unthrottled Gasoline Engines," Applied Energy, Volume 222, 2018, Pages 199-215.

63) Zhao, J., "Research and Application of Over-Expansion Cycle (Atkinson and Miller) Engines – A Review," Applied Energy, Volume 185, Part 1, 2017, Pages 300-319.

64) Shojaeefard, M., Keshavarz, M., "Mathematical Modeling of the Complete Thermodynamic Cycle of a New Atkinson Cycle Gas Engine," Applied Thermal Engineering, Volume 91, 2015, Pages 866-874.

65) Yu, R., Shahed, S., "Effects of Injection Timing and Exhaust Gas Recirculation on Emissions from a D.I. Diesel Engine," SAE Technical Paper 811234, 1981.

66) Komiyama, K., Heywood, J., "Predicting NOx Emissions and Effects of Exhaust Gas Recirculation in Spark-Ignition Engines," SAE Technical Paper 730475, 1973.

67) Li, T., Wu, D., Xu, M., "Thermodynamic Analysis of EGR Effects on the First and Second Law Efficiencies of a Boosted Spark-Ignited Direct-Injection

Gasoline Engine," Energy Conversion and Management 70, 2013, Pgs. 130-138.

68) A. Cairns, A., Blaxill, H., Fraser, N., "5 - Exhaust Gas Recirculation Boosted Direct Injection Gasoline Engines," in *Advanced Direct Injection Combustion Engine Technologies and Development*, Woodhead Publishing, Volume 1, 2010, Pages 105-132.

69) Ruhland, H., Lorenz, T., Dunstheimer, J., Breuer, A., Khosravi, M., "A Study on Charge Motion Requirements for a Class-Leading GTDI Engine," SAE Technical Paper 2017-24-0065, 2017.

70) Tang, Q., Liu, J., Zhan, Z., Hu, T., "Influences on Combustion Characteristics and Performances of EGR vs. Lean Burn in a Gasoline Engine," SAE Technical Paper 2013-01-1125, 2013.

71) Caton, J., "A Comparison of Lean Operation and Exhaust Gas Recirculation: Thermodynamic Reasons for the Increases of Efficiency," SAE Technical Paper 2013-01-0266, 2013.

72) Zel'dovich, Y., "The Oxidation of Nitrogen in Combustion Explosions". Acta Physicochimica U.S.S.R. 21: 577–628, 1946.

73) Miyamoto, N., Ogawa, H., Shudo, T., Takeyama, F., "Combustion and Emissions in a New Concept DI Stratified Charge Engine with Two-Stage Fuel Injection," SAE Technical Paper 940675, 1994.

74) Schweikert, J., Gumbleton J., "Emission Control With Lean Mixtures," SAE Technical Paper 760226, 1976.

75) Pozniak, D., "A Spark Ignition, Lean-Homogeneous Combustion, Engine Emission Control System for a Small Vehicle," SAE Technical Paper 760225, 1976.

76) Pauly, T., Franoschek, S., Hoyer, R., Eckhoff, S., "Cost and Fuel Economy Driven Aftertreatment Solutions -for Lean GDI-," SAE Technical Paper 2010-01-0363, 2010.

77) Peters, B., Quader, A., "Wetting" the Appetite of Spark Ignition Engines for Lean Combustion," SAE Technical Paper 780234, 1978.

78) Briggs, T., Alger, T., Mangold, B., "Advanced Ignition Systems Evaluations for High-Dilution SI Engines," SAE Technical Paper 2014-01-2625, 2014.

79) Forte, C., Bianchi, G., Corti, E., Fantoni, S., "Evaluation of the Effects of a Twin Spark Ignition System on Combustion Stability of a High Performance PFI Engine," Energy Procedia, Volume 81, 2015, Pages 897-906.

80) Altın, İ., Bilgin, A., "A Parametric Study on the Performance Parameters of a Twin-Spark SI Engine," Energy Conversion and Management, Volume 50, Issue 8, 2009, Pages 1902-1907.

81) Ricardo, H., Pitchford, J., "Design Developments in European Automotive Diesel Engines," SAE Technical Paper 370172, 1937.

82) Nunney, M.J., *Light and Heavy Vehicle Technology, Fourth Edition*. Butterworth-Heinemann; 2006.

83) "Prosper L'Orange and the modern diesel engine" http://media.daimler.com/marsMediaSite/en/instance/ko/Prosper-LOrange-and-the-modern-diesel-engine.xhtml?oid=9361309.

84) Nagao, G., Kakimoto, H., "Swirl and Combustion in Divided Combustion Chamber Type Diesel Engines," SAE Technical Paper 620558, 1962.

85) Taylor, J., *Land Rover Defender, 90 and 100 Range*, Wiltshire: Crowood Press Ltd, 2013.

86) Jääskeläinen, H., Khair, M., "Diesel Engines," from *DieselNet Technology Guide >> Engine Fundamentals*, Copyright © Ecopoint Inc., 2013.

87) University of Cambridge Department of Engineering, "A Pioneer of the Internal Combustion Engine Sir Harry Ricardo F.R.S.," 2000, http://www-g.eng.cam.ac.uk/125/achievements/ricardo/.

88) Turkish, M., "3-Valve Stratified Charge Engines: Evolvement, Analysis and Progression," SAE Technical Paper 741163, 1974, doi:10.4271/741163.

89) Noguchi, N., Sanda, S. and Nakamura, N., "Development of Toyota Lean Burn Engine," SAE Technical Paper 760757, 1976, doi:10.4271/760757.

90) Adams, T., "Torch Ignition for Combustion Control of Lean Mixtures," SAE Technical Paper 790440, 1979, doi:10.4271/790440.

91) Brandstetter, W., "The Volkswagen Lean Burn Pc-Engine Concept," SAE Technical Paper 800456, 1980, doi:10.4271/800456.

92) Garrett, T., "Porsche Stratified Charge Engine", Environmental Science & Technology, 1975. 9 (9), 826-830.

93) Wyczalek, F., Harned, J., Maksymiuk, S., Blevins, J., "EFI Prechamber Torch Ignition of Lean Mixtures," SAE Technical Paper 750351, 1975, doi:10.4271/750351.

94) Rittenhouse, J., "Thermal Loss Analysis for a Small Internal Combustion Engine," PhD Thesis, Air Force Institute of Technology, AFIT-ENY-14-M-41, 2014.

95) Gussak, L., Ryabikov, O., Politenkova, G., Furman, G., "Effect of Adding Individual Combustion Products on Combustion of Methane Air Mixture", Russian Chemical Bulletin (Historical Archive), 1973. 22 (9), 2128.

96) Gussak, L., Karpov, V., Tikhonov, Y., "The Application of the Lag-Process in Pre-chamber Engines," SAE Technical Paper 790692, 1979, doi:10.4271/790692.

97) Gussak, L., "High Chemical Activity of Incomplete Combustion Products and a Method of Prechamber Torch Ignition for Avalanche Activation of Combustion in Internal Combustion Engines," SAE Technical Paper 750890, 1975, doi:10.4271/750890.

98) Gussak, L., Karpov, V., Slutskii, V., Spasskii, A., “Burning Rate and Stability in Forechamber Flame Ignition in an Internal-Combustion Engine”, Combustion, Explosion, and Shock Waves (Historical Archive), 1984. 19 (5), 628-630.

99) Gussak, L., Ryabikov, O., Politenkova, G., Furman, G., “Yield of Atomic Hydrogen During Combustion of Methane and Hydrogen Mixtures with Air”, Russian Chemical Bulletin (Historical Archive), 1974. 23 (2), 451-452.

100) Gussak, L., “LAG-Process of Combustion and its Application in Automobile Engines”, IMechE C257/76, 1976, 137-145.

101) Gussak, L., “The Role of Chemical Activity and Turbulence Intensity in Pre-chamber-Torch Organization of Combustion of a Stationary Flow of a fuel-air Mixture,” SAE Technical Paper 830592, 1983, doi:10.4271/830592.

102) Date, T., Yagi, S., “Research and Development of Honda CVCC Engine,” SAE Technical Paper 740605, 1974, doi:10.4271/740605.

103) Norbye, J., Dunne, J., “Honda's New CVCC Car Engine Meets '75 Emission Standards Now”, Popular Science Magazine April, 1973, 79-81.

104) Breeze, P. (2014). Power Generation Technologies: 2nd Edition, Newnes.

105) American Public Gas Association, “A Brief History of Natural Gas,” https://www.apga.org/apgamainsite/aboutus/facts/history-of-natural-gas.

106) Evans, R., (1986). Automotive Engine Alternatives, Springer Science+Business Media, Inc.

107) Caterpillar, www.cat.com, 2020.

108) Snyder, B., Devine, M., “Beyond the Owner’s Manual: Getting the Most from Natural Gas-Fueled Engine Generator Sets,” white paper, Caterpillar, 2014.

109) Dale, J., Oppenheim, A., “Enhanced Ignition for I.C. Engines with Premixed Gases”, SAE Transactions, vol. 90, paper 810146, 1981.

110) Oppenheim, A., “Combustion in Piston Engines: Technology, Evolution, Diagnosis and Control”. 2004, Springer: New York.

111) Dainton, L., “Nikolai Nikolaevich Semenov. 16 April 1896-25 September 1986”, Biographical Memoirs of Fellows of the Royal Society. 36, 527-546 CR - Copyright © 1990 The Royal Society.

112) Zhao, F., Asmus, T., Assanis, D., Dec, J. E., Eng, J., Najt, P., “Homogeneous Charge Compression Ignition (HCCI) Engines Key Research and Development Issues”. 2003, SAE International: Warrendale, Pennsylvania.

113) Zhao, H., “HCCI and CAI Engines for the Automotive Industry”. 2007, Woodhead Publishing Limited: Cambridge, p. 544.

114) Dec, J., “Advanced Compression-Ignition Engines Understanding the In-Cylinder Processes,” Proceedings of the Combustion Institute, 2009. 32 (2), 2727-2742.

115) Murase, E., Hanada, K., “Enhancement of Combustion By Injection of Radicals,” SAE Technical Paper 2000-01-0194, 2000, doi:10.4271/2000-01-0194.
116) Murase, E., Hanada, K., “Control of the Start of HCCI Combustion by Pulsed Flame Jet,” SAE Technical Paper 2002-01-2867, 2002, doi:10.4271/2002-01-2867.
117) Yamaguchi, S., Ohiwa, N., Hasegawa, T., “Ignition and Burning Process in a Divided Chamber Bomb”, Combustion and Flame, 1985. 59 (2), 177-187.
118) Wakai, K., Kito, S., Isao, S., “Effect of Small Hydrogen Jet Flame on Augmentation of Lean Combustion,” SAE Technical Paper 931943, 1993, doi:10.4271/931943.
119) Watson, H.,“Internal Combustion Engine Ignition Device”, 1997 United States Patent No. 5611307.
120) Watson, H. C., “International Patent. Application PCT/AU92/00552”, 1992 Patent No. PCT/AU92/00552.
121) Dober, G. G. and Watson, H. C., “Modelling the Flame Enhancement of a HAJI Equipped Spark Ignition Engine”, IPC-10 Proceedings Paper Number 99091, 1999.
122) Lawrence, J., Watson, H., “Hydrocarbon Emissions from a HAJI Equipped Ultra-lean Burn SI Engine,” SAE Technical Paper 980044, 1998, doi:10.4271/980044.
123) Kyaw, Z., Watson, H., “Hydrogen Assisted Jet Ignition for Near Elimination of NOx and Cyclic Variability in the S.I. Engine”, Twenty-Fourth Symposium on Combustion, 1992. 24 (1), 1449-1455.
124) Glasson, N., Lumsden, G., Dingli, R., Watson, H., “Development of the HAJI System for a Multi-Cylinder Spark Ignition Engine,” SAE Technical Paper 961104, 1996, doi:10.4271/961104.
125) Lumsden, G., Watson, H., “Optimum Control of and S.I. Engine with a Lambda=5 Capability,” SAE Technical Paper 950689, 1995, doi:10.4271/950689.
126) Lumsden, G., *The Phenomena of Hydrogen Assisted Jet Ignition*, PhD Thesis in The Department of Mechanical Engineering, The University of Melbourne, 1995.
127) Bosecker, R., Webster, D., “Precombustion Chamber Diesel Engine Emissions - A Progress Report,” SAE Technical Paper 710672, 1971.
128) Attard, W., Kohn, J., Parsons, P., “Ignition Energy Development for a Spark Initiated Combustion System Capable of High Load, High Efficiency and Near Zero NOx Emissions,” SAE Journal Paper JSAE 20109088, 2010.

129) Attard, W., Blaxill, H., “A Gasoline Fueled Pre-Chamber Jet Ignition Combustion System at Unthrottled Conditions,” SAE Technical Paper 2012-01-0386, 2012, doi:10.4271/2012-01-0386.
130) Attard, W., Blaxill, H., “A Lean Burn Gasoline Fueled Pre-Chamber Jet Ignition Combustion System Achieving High Efficiency and Low NOx at Part Load,” SAE Technical Paper 2012-01-1146, 2012, doi:10.4271/2012-01-1146.
131) Bunce, M., Blaxill, H., Attard, W., “Turbulent Jet Ignition Pre-Chamber Combustion System for Spark Ignition Engines,” 2014, United States Patent No. 9,353,674.
132) Chinnathambi, P., Bunce, M., Cruff, L., “RANS Based Multidimensional Modeling of an Ultra-Lean Burn Pre-Chamber Combustion System with Auxiliary Liquid Gasoline Injection,” SAE Technical Paper 2015-01-0386, 2015.
133) Bassett, M., Reynolds, I., Cooper, A., Reader, S., and Berger, M., “MAHLE Modular Hybrid Powertrain,” Proceedings from the 28th Aachen Colloquium, 2019.
134) Bunce, M., Blaxill, H., Cooper, A., “Development of Both Active and Passive Pre-Chamber Jet Ignition Multi-Cylinder Demonstrator Engines,” Pischinger, S. and Eckstein, L. (eds.), in 28th Aachen Colloquium Automobile and Engine Technology, Aachen, 2019, 907-942.
135) Qi, Y., Ge, X., and Dong, L., "Numerical Simulation and Experimental Verification of Gasoline Intake Port Design," SAE Technical Paper 2015-01-0379, 2015, doi:10.4271/2015-01-0379.
136) Bozza, F., De Bellis, V., Berni, F., D'Adamo, A. et al., “Refinement of a 0D Turbulence Model to Predict Tumble and Turbulent Intensity in SI Engines. Part I: 3D Analyses,” SAE Technical Paper 2018-01-0850, 2018, doi:10.4271/2018-01-0850.
137) Ruhland, H., Lorenz, T., Dunstheimer, J., Breuer, A. et al., "A Study on Charge Motion Requirements for a Class-Leading GTDI Engine," SAE Technical Paper 2017-24-0065, 2017, doi:10.4271/2017-24-0065.
138) Loeper, P., Ra, Y., Foster, D., Ghandhi, J., "Experimental and Computational Assessment of Inlet Swirl Effects on a Gasoline Compression Ignition (GCI) Light-Duty Diesel Engine," SAE Technical Paper 2014-01-1299, 2014.
139) Patrie, M., Martin, J., Engman, T., "Inlet Port Geometry and Flame Position, Flame Stability, and Emissions in an SI Homogeneous Charge Engine," SAE Technical Paper 982056, 1998.

140) Hill, P., Zhang, D., “The Effects of Swirl and Tumble on Combustion in Spark-Ignition Engines,” Prog. Energy Combust. Sci. Vol 20, 1994, Pgs. 373-429.

141) Tong, Chao & Laramee, Robert. (2019). From Data Chaos to the Visualization Cosmos. 10.5772/intechopen.82159.

142) Qauder, A., “What Limits Lean Operation in Spark Ignition Engines-Flame Initiation or Propagation?,” SAE Technical Paper 760760, 1976.

143) Urushihara, T., Nakada, T., Kakuhou, A., Takagi, Y., “Effects of Swirl/Tumble Motion on In-Cylinder Mixture Formation in a Lean-Burn Engine,” SAE Technical Paper 961994, 1996.

144) Solomon, A., Szekely, G., “Combustion Characteristics of a Reverse-Tumble Wall-Controlled Direct-Injection Stratified-Charge Engine,” SAE Technical Paper 2003-01-0543, 2003.

145) Gombosuren, N., Yoshifumi, O., Hiroyuki, A., “A Charge Possibility of an Unfueled Prechamber and Its Fluctuating Phenomenon for the Spark Ignited Engine,” *Energies* 2020, 13, 303, doi:10.3390/en13020303

146) Bunce, M., Blaxill, H., Gurney, D., “Design and Development of a Jet Ignition Engine for Stable Ultra-Lean Operation,” *Proceedings of the Institution of Mechanical Engineers Internal Combustion Engines Conference*, London, 2017.

147) Jia, M. and Xie, M., “A Chemical Kinetics Model of Iso-Octane Oxidation for HCCI Engines”, Fuels 85, 2593-2604, 2006, doi:10.1016/j.fuel.2006.02.018.

148) Curran HJ, Gaffuri P, Pitz WJ, Westbrook CK. “A comprehensive modeling study of iso-octane oxidation”, Combust Flame 129: 253–80, 2002.

149) Knop, V., “Analysis of mixture structure and of its influence on combustion in a CAI engine”, International Journal of Engine Research, 19 (4), pp. 393-410, 2018.

150) Nazemi, M., Shahbakhti, M., “Modeling and analysis of fuel injection parameters for combustion and performance of an RCCI engine”, Applied Energy, 165, pp. 135-150, 2016.

151) Finney, C.E.A., Edwards, K.D., Stoyanov, M.K., Wagner, R.M., “Application of high performance computing for studying cyclic variability in dilute internal combustion engines”, Proceedings from the ASME 2015 Internal Combustion Engine Division Fall Technical Conference.

152) Amsden, A. A., “KIVA-3V: A Block Structured KIVA Program for Engines with Vertical or Canted Valves,” Los Alamos National Laboratory Report No. LA-13313-MS, 1997.

153) Gonzalez D., M., Lian, Z., and Reitz, R., “Modeling Diesel Engine Spray Vaporization and Combustion,” SAE Technical Paper 920579, 1992, doi:10.4271/920579.
154) Distaso, E., Amirante, R., Cassone, E., Catapano, F., De Palma, P., Sementa, P., Tamburrano, P., “Experimental and Numerical Analysis of a Pre-Chamber Turbulent Jet Ignition Combustion System”, Energy conversion and management, 2020-11-01, Vol.223, p.113257.
155) Kim, J., Scarcelli, R., Som, S., Shah, A., Biruduganti, M., Longman, D., "Assessment of Turbulent Combustion Models for Simulating Pre-Chamber Ignition in a Natural Gas Engine." Journal of Engineering for Gas Turbines and Power, 2021-03-12.
156) Zembi, J., Battistoni, M., Ranuzzi, F., Cavina, N., De Cesare, M., “CFD Analysis of Port Water Injection in a GDI Engine under Incipient Knock Conditions”, Energies, 12, 3409, 2019.
157) Sens, M., Binder, E., Reinicke, P.-B., Riess, M., Stappenbeck, T., Woebke, M., “Pre-Chamber Ignition and Promising Complementary Technologies”, 27th Aachen Colloquium Automobile and Engine Technology, 2018.
158) Brannys, S., Gehrke, S., Hoffmeyer, H., Hentschel, L., “Maximum Efficiency Concept of a 1.5L TSI evo for Future Hybrid Powertrains”, 28th Aachen Colloquium Automobile and Engine Technology, 2019.
159) Cao, Y., Li, L., “A Novel Closed Loop Control Based on Ionization Current in Combustion Cycle at Cold Start in a GDI Engine”, SAE Technical Paper 2012- 01-1339, 2012.
160) Bunce, M., Peters, N., Subramanyam, S.K.P., Blaxill, H., “Assessing the Low Load Challenge for Jet Ignition Engine Operation”, Proceedings of the Institution of Mechanical Engineers Internal Combustion Engines Conference, Birmingham, UK, 11-12 December 2019.
161) Qiao, A., Wu, X., “Research on the New Ignition Control System of Lean- and Fast-Burn SI Engines”, SAE Technical Paper 2008-01-1721, 2008.
162) Evans, R., (1986). Automotive Engine Alternatives, Springer Science+Business Media, Inc.
163) Pape, J., Getzlaff, J., Gruenig, C., Kuhnert, D. and Latsch, R., “Investigations on Pre-Chamber Spark Plug with Pilot Injection,” SAE Technical Paper 2007-01-0479, 2007, doi:10.4271/2007-01-0479.
164) Cooper, A., Harrington, A., Bassett, M., Reader, S., Bunce, M., “Application of the Passive MAHLE Jet Ignition System and Synergies with Miller Cycle and Exhaust Gas Recirculation”, SAE Technical Paper 2020-01-0283, 2020.

165) Bunce, M., Blaxill, H., “Methodology for Combustion Analysis of a Spark Ignition Engine Incorporating a Pre-Chamber Combustor”, SAE Technical Paper 2014-01-2603, 2014.

166) Peters, N., Krishna Pothuraju Subramanyam, S., Bunce, M., Blaxill, H., Cooper, A., “Optimization of Lambda across the Engine Map for the Purpose of Maximizing Thermal Efficiency of a Jet Ignition Engine,” *SAE Int. J. Advances & Curr. Prac. in Mobility* 2(6):3140-3150, 2020, doi:10.4271/2020-01-0278.